

HARVARD UNIVERSITY
Graduate School of Arts and Sciences



DISSERTATION ACCEPTANCE CERTIFICATE

The undersigned, appointed by the
Department of Physics
have examined a dissertation entitled

Microscopy of correlations at a non-equilibrium phase transition

presented by Matthew N. Rispoli

candidate for the degree of Doctor of Philosophy and hereby
certify that it is worthy of acceptance.

Signature A handwritten signature in black ink, appearing to read "Markus Greiner".

Typed name: Professor Markus Greiner, Chair

Signature A handwritten signature in blue ink, appearing to read "Mikhail Lukin".

Typed name: Professor Mikhail Lukin

Signature A handwritten signature in blue ink, appearing to read "Kang-Kuen Ni".

Typed name: Professor Kang-Kuen Ni

Date: May 9, 2019

Microscopy of correlations at a non-equilibrium phase transition

A DISSERTATION PRESENTED

BY

MATTHEW N. RISPOLI

TO

THE DEPARTMENT OF PHYSICS

IN PARTIAL FULFILLMENT OF THE REQUIREMENTS

FOR THE DEGREE OF

DOCTOR OF PHILOSOPHY

IN THE SUBJECT OF

PHYSICS

HARVARD UNIVERSITY

CAMBRIDGE, MASSACHUSETTS

MAY 2019

©2019 – MATTHEW N. RISPOLI
ALL RIGHTS RESERVED.

Microscopy of correlations at a non-equilibrium phase transition

ABSTRACT

One of the distinguishing achievements of physics has been the ability to describe the Universe based upon underlying microscopic principles. When there are many participating objects being governed by these microscopic principles, the resultant behavior often harbors emergent collective phenomena that may not be obviously related to the microscopic description. Phase transitions, quantum or classical, are a canonical example of such many-body phenomena that are understood in equilibrium through a framework of thermodynamic constraints, statistical ensembles, and a growth of system-wide correlations at the transition. However, a new class of quantum phase transitions has recently emerged for non-equilibrium systems with behavior that is not captured by this traditional framework. In the case of isolated quantum systems, these transitions occur among excited eigenstates and requires knowledge of the structure of these individual eigenstates in the quantum system. Understanding what drives such a phase transition requires a deeper microscopic knowledge of the role of correlations at the transition.

The use of ultracold atoms in optical lattices has paved the way for faithfully realizing quantum phase transitions. In particular, the advent of the quantum gas microscope realized an experimental platform that is highly controllable and provides microscopic access to the many-bodied wave

functions. All experiments presented in this thesis use such a quantum gas microscope architecture where a quantum degenerate gas of ^{87}Rb is used to probe the behavior of non-equilibrium quantum systems in one spatial dimension.

This thesis briefly discusses some studies of entanglement in equilibrium quantum phase transitions near the ground state of the system. In the first experiment, we directly measure the second-order Rényi entanglement entropy that develops as a Bose-Hubbard system transitions from a Mott insulator to a superfluid. This is followed by a study of entanglement growth at the transition in the transverse Ising model.

These studies progress to the investigation of two particular non-equilibrium quantum phases and their transition into one another: quantum thermalization and many-body localization. We investigate the development of entanglement entropy that mimics thermodynamic entropy for an isolated quantum system which locally thermalizes under its own unitary dynamics. We then investigate the only known robust exception to this thermalizing behavior by studying the onset of many-body localization due to disorder. We observe the breakdown of thermalization in this phase and the logarithmically slow growth of entanglement throughout the system, which identifies the localized system to be an interacting one. Lastly, we investigate the role of correlations in the critical dynamics that emerge at high-orders where the system transitions from thermalizing behavior to many-body localization.

Contents

o	INTRODUCTION	I
o.1	What we mean by “quantum”	2
o.2	Quantum simulation: probing quantum many-body problems	5
o.3	A non-equilibrium quantum phase	7
o.4	Outline	9
i	OPTICAL LATTICES AND THE BOSE-HUBBARD MODEL	II
i.1	Single-particle physics in optical lattices	12
i.2	The Bose-Hubbard model	25
i.3	Quantum phase transitions: superfluid to Mott-insulator	33
i.4	Discussion: beyond tight-binding Bose-Hubbard	37
2	QUANTUM GAS MICROSCOPE: AN OVERVIEW	39
2.1	Optical lattice potentials	42
2.2	Arbitrary potential generation	50
2.3	Imaging and readout	52
2.4	Calibration of energy scales	54
3	CORRELATIONS, ENTANGLEMENT, AND QUANTUM PHASE TRANSITIONS	64
3.1	Coherent superposition and statistical distributions	68
3.2	Correlations and Entanglement	72
3.3	Superfluid-to-Mott-insulator transition	83
3.4	Ising model phase transition	88
3.5	Discussion	94
4	ISOLATED QUANTUM SYSTEMS AND LOCAL THERMALIZATION WITHIN EIGENSTATES	95
4.1	Quantum thermalization	96
4.2	Protocol and Model	97
4.3	Non-equilibrium systems and highly excited eigenstates	99
4.4	Entropy from entanglement and thermalization	105

4.5	Discussion	110
5	CORRELATION DYNAMICS	
	IN MANY-BODY LOCALIZATION	113
5.1	Localization in the interacting Aubry-André model	116
5.2	Breakdown of thermalization	119
5.3	Localization of particles	122
5.4	Entanglement dynamics in an interacting, many-body localized system	125
5.5	Decoherence from scattering	139
5.6	Discussion	142
6	CRITICAL BEHAVIOR OF THE	
	MANY-BODY-LOCALIZATION TRANSITION	145
6.1	Critical behavior and phase transitions	147
6.2	Localization and transport	154
6.3	Critical transport behavior	157
6.4	Correlation Structure	161
6.5	High-order Correlations	163
6.6	Discussion	167
7	CONCLUSION	169
7.1	Summary	169
7.2	Outlook	171
APPENDIX A ATOMIC PROPERTIES OF ^{87}Rb		178
APPENDIX B NUMERICS		183
APPENDIX C EXPERIMENTAL SEQUENCES		184
APPENDIX D CHAPTER 1 CALCULATIONS		187
D.1	Optical lattice potential from laser light	188
D.2	Harmonic Oscillator Approximation	188
APPENDIX E CHAPTER 2 CALCULATIONS		190
E.1	Z -lattices from angled reflection	191
E.2	Calculations for Disorder and zero-point energy	192
APPENDIX F CHAPTER 3 CALCULATIONS		197
F.1	Mapping: Bose-Hubbard model to transverse Ising Model	198

APPENDIX G CHAPTER 4 CALCULATIONS	199
G.1 Predictions from thermodynamic ensembles	200
G.2 Entropies	204
APPENDIX H CHAPTER 5 CALCULATIONS	206
H.1 Scaling and limitations of configurational correlator	207
APPENDIX I CHAPTER 6 CALCULATIONS	209
I.1 Δx : Time Scaling Behavior (Power Law 12-Sites)	209
I.2 Spectral Statistics	211
I.3 Enhanced Thermalization	212
I.4 Subsystem-size fluctuations scaling	213
REFERENCES	232

TO MY PARENTS VALDA AND FRANK,
MY BROTHER STEPHEN AND MY SISTER-IN-LAW JEANINE,
AND MY PARTNER MELIS

Acknowledgments

Are we still having fun?

Dr. Daniel Greif

THE PHYSICS WE STUDY OCCURS IN A VACUUM, BUT OUR SCIENTIFIC SUCCESS DOES NOT^{*} –

There are an enormous number of people that are either directly or indirectly responsible for making all the results presented in this thesis possible.

I would like to thank my advisor, Markus Greiner, for six years of guidance and accepting me into his group considering that I arrived with zero AMO experience. You are an an endless supply of intuition and experimental voodoo that never ceases to amaze me.

Of course, my experience working in the Rubidium Lab has been predominantly related to my overlap with a group of very talented lab mates. I would like to thank them for not only keeping work in the lab fun, but also for teaching me a number of lessons over the years. Alex Ma taught me that everything will be “okay”. Philipp Preiss patiently taught me how to run the experiment and even walked me through simple calculations that were certainly only useful for one of us (me).

Not to mention he has continued to answer emails about the experiment years after having left and is always a pleasure to hang out with whenever conferences bring us back together. Eric Tai taught

*Thank you Christie for coining this very appropriate phrase.

me how to create – his attention to detail and care in fabrication is something I will always aspire to but probably never obtain. Thank you for your patience in listening to my ideas and work through problems with me. Not to mention all the time spent outside of the lab: going to the gym, cycling the Minuteman Bikeway, advice on getting a job, and going on adventures in Taiwan and Singapore. Alex Lukin taught me persistence and how to ask the correct conceptual questions. I have worked with no one else as closely in lab and I have no doubts that the latest experiments would have never succeeded without his help and guidance. He has independently provided an enormous amount of joy and entertainment both in and out of the lab – I think everyone would agree that life without him would have been significantly less memorable or fun.

Then there are the new-*ish* lab members who deserve significant credit and thanks too – they have already taught me a great deal and I am excited to see where their enthusiasm and talent will lead the experiment. Robert Schittko re-taught me English, how to actually makes figures beautiful, and to never stop asking questions. Sooshin Kim showed me what is *actually* numerically possible. The critical behavior paper would have certainly been less successful without him. Joyce Kwan has taught me how to be deliberate and persistent in conversations: both when looking for a job and with faculty members during grad school. Her diligence and optimism provided a significant improvement to the lab.

The Rubidium Lab has also been fortunate enough to have had a great number of talented post-docs that have led the experiment along a successful scientific path and kept the group harmonious and enjoyable to work in. Rajibul realized the first steps towards the subsequent measurements of entanglement in an isolated quantum system. I'm additionally thankful for his willingness to work

with me even during my first days in the lab. Adam's patience and willingness to talk about all things physical, political, pet related or otherwise not only significantly improved the quality of research in the lab, but the general work environment. He kept the lab organized and was a wonderful mentor. Julian brought in a great deal of experimental expertise and in-depth knowledge of equilibrium phase transitions. His guidance brought the MBL critical behavior paper to fruition and without him the lab would have been a disorganized mess.

Of course, the Greiner Group is composed of more than just the Rubidium Lab. My colleagues from the Lithium and Erbium labs have helped develop me both professionally and as an individual over the past six years. Not to mention that they have provided an endless amount of entertainment and fun through lunch conversations, group hikes, group skiing, and conferences. Thank you to the Lithium lab members over the years: Sebastian Blatt, Florian Huber, Max Parsons, Daniel Greif, Anton Mazurenko, Christie Chiu, Geoffrey Ji, Muqing Xu, and Justus Brüggenjürgen. Thank you to the Erbium lab members over the years: Susannah Dickerson, Greg Phelps, Anne Hébert, Aaron Krahn, Furkan Öztürk, Sepher Ebadi, and Emily Tiberi.

Even before coming to the Greiner Group, a number of professors and teachers influenced my educational path and academic career that brought me this PhD program: Stephen Sekula, Jodi Cooley, Randall Scalise, Nathan Huntoon, Janet Schofield, and Scott Wiley – just to name a few.

Additional acknowledgement and thanks also goes out to the administrators, staff, and technical experts in the department: Lisa Cacciabuado, Carol Davis, Stuart McNeil, Stan Cotreau, Jim MacArthur, Silke Exner, Manny & Danny, Samantha Dakoulas, and Clare Ploucha. Without them, not only would much of the group not successfully run, but the entire department would probably

fall apart. Jim MacArthur deserves a separate and special acknowledgement for his willingness to talk to me about all things that I brought up to him throughout the years – electronic and otherwise. He *always* set aside whatever he was doing and would spend time to discuss the topic with me. He additionally acted like a second advisor and helped me a great deal with figuring out what to do with my life after graduation.

The past six years have also been more than just research. I have been fortunate enough to have been supported and kept sane by all the good times from old friends. Some that go back as far as high school: Gabriel, Tony, Nick, Allen. Another group of friends, whom I was lucky enough to meet a bit later in life during undergrad: Cristina, Ali, Brian, Dan, Tori, Keith, and Isaac. Of course, the most recent and influential group of friends on my personal development during my PhD were found while here at Harvard: all of my entering class, my lab mates, and other students in the physics department either at Harvard or MIT that I've had the pleasure of meeting along the way: Ahmed, Annabelle, Fabian, Alp, Olivia, Ruffin, Ivan, Tim, Victor, and Lee.

Some of these friends deserve special individual acknowledgements for their significant contributions to my PhD experience:

Thank you Anne for being a constant source of joy, sanity, and support over the past years: eating raclette, joining me on cycling adventures, eating waffles, taking care of my cat, reading this thesis, and being a great desk neighbor – you're a wonderful friend and the entire Greiner Group is lucky to have you in it.

Thank you Christie, as my fellow previously-non-AMO colleague entering the same year into the Greiner Group, you have been a wonderful lab mate that has always been willing to share your

thoughts and support in both professional and personal matters over the years.

Thank you Julian for being such an inclusive postdoc and good friend. You not only supported me in professional matters in the lab but even welcomed me into your home when at conference in Germany. I am additionally very grateful for all the times you have selflessly offered to take care of my cat when I've been away.

Thank you Dom for being my first friend in grad school and being a great roommate over the years. Thank you for helping me through difficult times in my PhD: both work and non-work related problems. Thank you also for being the genesis of many great memories – including one where we opened a bottle of wine with a shoe.

Thank you Louis, Jae, Michael, and Ron for being a great friend group from my entering class in grad school. Louis is a fellow CUA member and AMO experimentalist with far more technical knowledge than I will ever have. You and Rachel have been a wonderful couple to hang out with – whether it was eating paella in Barcelona or having nearly-unrememorable experiences at beerfest here in Boston. Jae is the first person I met in grad school and was one of my first year officemates – you've not only been a great friend over the years, but your openness made me feel welcomed on the first day of the program. Michael was another officemate from my first year who introduced me to the importance of Cinnabon and the vastness of the internet – your friendship and empathy throughout the years has been invaluable and I hope you find your way back to the east coast in the years to come. Ron is another AMO physicist whose pragmatic down-to-earth-edness has always served as an example of how to live a less stressful life – separately, an example of how to bake amazing chocolate chip cookies.

Thank you Adam and Annalise (and Maddy), while I had the good fortune of working with Adam in lab, I had the even greater fortune of befriending all three of you! Adam is responsible for teaching me a great deal about physics and has kept an eye out for me both in and out of lab. Thanks to Adam, I was able to meet Annalise who, combined with her family, make up the sweetest group of people I have ever met – you’re an inspiration and example of the goodness possible in people. Maddy is, of course, amazing.

Thank you Daniel and Renate for being some of the closest friends I’ve had the pleasure of meeting in grad school. While Daniel and Renate are both AMO physicists, I have never had the pleasure of working together directly with them. However, they have always been willing to listen to me incessantly bug them about physics questions (especially Daniel about topology). Thank you for always reminding me that physics should be fun. Outside of the lab, the countless late nights of board games, waffle-seeking bike rides, and raclette dinners have made up a great deal of my fond memories for the past six years.

Thank you Anton and Caitlin (and Chloe) for being close friends in grad school. Anton deserves a separate acknowledgement for helping me land my job coming out of grad school – something I am extremely grateful for. Anton is the embodiment of selfless giving and was willing to help me with whatever often thankless lab-related task arose. Of course, this selflessness isn’t limited to lab: he has helped me move furniture more than once and listened to me complain and ask advice for all things job related. I’ll cherish many memories from grad school together (even the one where we opened a wine bottle with a fillet knife) and look forward to even more in New York. Thanks to Anton, I also got to meet his better thirds (yes it is a quasi-polyamorous relationship): Caitlin

and Chloe. Caitlin is, perhaps unsurprisingly as Anton's partner, another incredibly sweet individual that I look forward to now having the opportunity to spend more time with given my new job. And, of course Chloe, as the most opinionated cat I have ever met. She is responsible for some of the best cat stories that I know and, somehow, most of the cat photos in my phone are of her.

Pepper, as my own cat, of course deserves credit for providing a great deal of comfort and entertainment over the years. She has greeted me at the door almost every day and has spent the most time going over this thesis with me – either by sitting on me, the laptop, or the printed document itself and staring, perhaps carefully, into it.

My family have supported me with their unconditional love and support throughout my life. My parents Valda and Frank have always encouraged me to follow what I find interesting and provided me with every opportunity I could have ever hoped for – this would have not been possible without you. My brother Stephen and my sister-in-law Jeanine have supported me throughout my academic career and I am proud to finally be finishing a graduate degree in their footsteps.

There is a final, very special acknowledgement that goes to my partner Melis Tekant. The most important result of my entire PhD experience is that it introduced us! You have been my ceaseless supporter I don't believe I can ever truly deserve. A PhD can be a trying experience and it is thanks to your love, help, and good judgement that I have managed to successfully finish this degree at all. You are a loving companion that has picked me up when I've been down and taken me on a number of adventures that I will treasure forever. Through you, I have even gained a second family that has welcomed with open arms and shown me more warmth than I would have ever dreamed possible. I can't wait to see what the future has in store for us and look forward to every new experience we'll

share together. Seni çok seviyorum.

Simulation is a valid way of answering any question.

Professor Stephen Sekula

0

Introduction

The advent of a quantum mechanical theory of nature revolutionized our physical interpretation of the surrounding world. Its success in resolving outstanding questions and making new predictions over the past century has cemented it as the cornerstone of our microscopic understanding of nature. However, even though the theory and mathematical framework developed is well understood, solving quantum mechanical problems on classical computers is often exponentially difficult⁵⁷. Over

the past few decades, a powerful set of experimental tools have been developed in a wide variety of atomic physics platforms that enable insight into testing fundamental properties of these theories. In fact, some platforms have sufficiently matured in development that private companies (e.g. Atom Computing®, IonQ®, Google®, etc.) have begun their own research and development of these platforms to exploit their quantum mechanical properties for technological advancement. However, to appreciate the complexity of solving such quantum mechanical problems and their applicable virtues, we must first briefly discuss what properties we consider to be inherently quantum mechanical and their physical implications.

0.1 WHAT WE MEAN BY “QUANTUM”

0.1.1 SINGLE-BODY QUANTUM

Quantum mechanics was first realized as a necessary and accurate description of nature in the prediction of quantized energies of massless and massive single-bodied systems: e.g. energy of photons for black-body radiation¹⁴⁵ and the prediction of the electronic energy levels of hydrogen¹⁶⁵. This quantization resulted naturally for both systems due to the underlying constituents being described by a wave theory. Instead of these objects being described as point-like particles with properties whose values could change continuously, the boundaries of any given system admitted only a discrete set of solutions. This discreteness of these wave solutions meant the associated energies could also only take on discrete values with a bounded, non-zero lowest energy.

This wave formulation, however, did more than just solve a few open problems in the early 20th

century about the mismatch of nature’s behavior with known classical theories. It further implied some fundamental distinctions between previous classical frameworks that have observable consequences. One such example comes from the Heisenberg uncertainty principle, which determines that, due to the wave nature of the physical constituent, there is an inherent uncertainty in the ability to define the constituent’s physical properties: e.g. momentum and position – any wave with a well defined momentum cannot have a well defined position and vice versa.* This implies an inherent amount of fluctuations possessed by the quantum objects that are fundamental and can never be removed or “frozen out”.

Another example results from the quantum mechanical discretization of the constituent’s physical properties that render the possibility for multiple, independent objects to be fundamentally identical. In particular, if such identical objects are used as a resource for random variables, say coin flips, they will provide markedly different distributions from their classical counterparts.[†] Often however, our daily experience is among physics at high temperatures which provide a macroscopically large number of internal labels such that classical objects behave in accordance with the statistics associated with classical random variables, regardless of their underlying microscopic bosonic or fermionic nature.

*This property is analogous to the Fourier transform: a delta function in any basis is maximally distributed among all degrees of freedom in its complementary, Fourier transformed basis. This comparison is relevant since it accurately describes the behavior of waves – which all matter seems to be microscopically represented by.

[†]The exact outcomes will depend upon the underlying quantum statistics of the objects themselves too: bosonic or fermionic, which depend on the symmetries of the quantum mechanical object and will not be described here.

0.1.2 MANY-BODY QUANTUM

However, perhaps the most famous consequence of quantum mechanics can arise from the interaction of multiple objects that then globally act as a wave.* The implications of such behavior were recognized early on by Einstein, Podolsky, and Rosenste in a Gedankenexperiment⁵¹ of a pair of quantum mechanical objects whose internal properties are correlated. The correlations in this pair were famously shown by John Bell to generate physical implications for measured correlations that are indescribable by classical variables, which identifies these correlations as uniquely quantum²¹. These quantum correlations between the two objects are qualitatively described by the term “entanglement”.

This notion of entanglement leads to the concept of quantum many-body behavior that, as a whole, is described as a collective object with fundamentally wave-like properties. It additionally has a consequence that when measuring only some fraction of this many-bodied wave the remaining fraction’s properties become described by a truly classical, statistical ensemble. The coherences related to the wave-like nature of the many-bodied function are erased and can produce truly classical outcomes. This development of classicality due to a lack of access to such global information provides a deep conceptual framework for understanding our macroscopic experience from our microscopic picture of nature. In particular, this has been useful for drawing a link between the agreement

*This does not mean that many-particles act together simply like a single classical wave, like waves on the surface of water in the ocean. In this case all the particles are interacting with their neighbors through a linear response equation such that collective wave-like excitations can be made on the water. This classical wave is defined in a local, spatial basis where all interference in this wave happens only locally with itself or other waves. A many-bodied quantum wave function revolves around the global state itself having wave-like properties in the sense that it cannot be written as purely in a local basis and interference effects happen for this system on a global scale.

of thermodynamic properties from many-bodied classical systems in statistical mechanics and the behavior of a portion of a many-bodied wave function that behaves quantum mechanically^{48,177,99,43}. This suggests that it is not only the microscopic which behaves quantum mechanically, but the macroscopically large objects that we associate with classical laws of nature may actually naturally derive from the properties of many-bodied quantum mechanical systems – we simply do not have access to the global system to verify it.

0.2 QUANTUM SIMULATION: PROBING QUANTUM MANY-BODY PROBLEMS

In many cases for large systems, physicists have found effective theories that allow for accurate descriptions of macroscopically large objects such that we may ignore the complexity related to its microscopic principles. This is often not the case for many-bodied quantum mechanical systems. Additionally, the overhead then necessary to analytically or numerically calculate results from the understood microscopic descriptions quickly makes these systems intractable. To circumvent this problem, a suggestion attributed to Richard Feynman⁵⁷ is to use a type of analog calculator for such systems, which would be known as a “quantum simulator”. The crux of the suggestion being that to successfully find the correct answers to quantum mechanical questions, one should use a system that is already inherently quantum mechanical such that it naturally simulates the correct answer.

Experimental atomic physics platforms have undergone significant technological maturity in the past few decades that make attempting such quantum simulations possible. Trapped atomic ion systems²³ and superconducting qubits⁸² enable high-fidelity control of few-particle systems with

variable interaction strengths and geometries. These platforms harbor rapid experimental repetition rates that make them particularly promising for the purpose of quantum computation. However, they suffer from coupling to their surrounding environment: i) the static charge of atomic ions makes them sensitive to their surroundings due to the strength of the Coulomb force, and ii) superconducting qubits can be cooled down to extremely low temperature with dilution refrigerators, but are directly mounted to materials that harbor a finite phononic bath that can become relevant for the small energy gaps in many-body systems. This restricts their effective size in terms of quantum constituents and coherence times. New developments in waveguide manufacturing have enabled the study of correlated states in photonic systems and are well decoupled from their environment⁶⁰, but are not clearly scalable to the many-body limit.

A powerful platform for probing such fundamental questions about many-bodied quantum mechanics is provided by ultracold atoms in optical lattices^{25,24}. The versatility of these platforms, thanks to the variety of available atomic species, enables exploring systems with both bosonic and fermionic statistics. These atoms can be cooled to their motional ground state and controlled microscopically with almost arbitrary potential energy landscapes on top of several optical lattice geometries while remaining isolated from their surrounding environment¹³. Their inter-atomic interaction strength can be tuned by orders of magnitude and even change signs via Feshbach resonances³⁶. Due to the convenient length scales in such systems, traditional microscopy techniques can be used to image both bosonic^{15,173,127} and fermionic^{73,141,35} species in optical lattices with single-site resolution, gaining access to local observables and correlation functions⁵⁵ up to high orders¹⁵⁴.

One direction of quantum simulations with ultracold atoms concerns the realization of novel

quantum phases of matter and the transitions between them. Pioneering studies have observed quantum phases of matter both in equilibrium^{67,95,94,72,174} and in driven, non-equilibrium^{20,110,38,111} systems. The majority of such experiments have focused on the quantum phases themselves and measure their order parameters through macroscopic observables. However, it is the transition of these phases in the critical regime that is exceedingly difficult to access owing to a divergence of correlations as quantum fluctuations reorder the system from phase to another^{109,158}. Only recently have ultracold atoms experiments probed such critical scaling behaviors for equilibrium quantum phase transitions near the transition point^{9,41,100}.

0.3 A NON-EQUILIBRIUM QUANTUM PHASE

A new class of non-equilibrium quantum phase transitions has recently emerged with behavior that is not captured by this conventional framework of equilibrium phase transitions. In the case of isolated quantum systems, these transitions occur among excited eigenstates in the system and can be understood by considering typical excited states individually^{131,197,182,5,78}. * The experimental studies presented in this thesis will focus on two particular non-equilibrium quantum phases and their transition: *quantum thermalization* and *many-body localization*. These phases occur for isolated quantum systems that, while pure, are prepared far from equilibrium via a quantum quench¹⁶⁰ and are identified by their inherent dynamics from coherently populating many excited eigenstates^{131,43}. We exploit the microscopic access in our system to investigate one of the hallmarks of these quantum phases and their transition^{7,18,131,43} – entanglement properties of the many-body state.

*This is why these are sometimes referred to as “eigenstate phase transition” in the theory literature.

A quantum thermalizing phase is predicted generically for interacting, non-integrable isolated quantum systems by the Eigenstate Thermalization Hypothesis^{48,153,92,177}. These systems harbor excited eigenstates which individually possess ergodicity among their local degrees of freedom and whose dynamics resemble those of a classical thermodynamic systems: agreement with statistical ensembles constrained only by global thermodynamic ensembles^{92,48,177,153} and maximization of local entropy. Often, such a system is difficult to simulate theoretically due to the generation of a large amount of entanglement during the ensuing dynamics^{33,7,44,162}. Atomic physics experiments, however, have been successful in observing such thermalizing behavior: the ergodic character of eigenstates has been observed in few-qubit systems¹³² and, as presented in this thesis, the role of entanglement^{161,49} in generating such locally thermal states⁹⁹.

The only known robust exception to this description is many-body localization (MBL)^{131,43}. This exception can be realized by the application of disorder to this thermalizing phase causes a breakdown of ergodicity and thermalization at a finite disorder strength by localization of this many-body, interacting system^{8,166,22,155,107,45,88,105,91,47}. This breakdown can be understood as a fundamental change in the excited eigenstates, which results in logarithmically slow entanglement dynamics throughout the system – distinguishing these states as a separate non-equilibrium phase^{139,85}. Initial atomic experiments in this regime have tested the absence of thermalization by the memory of the initial states prepared far from equilibrium^{164,176,37}. This initial state localization is indeed a consequence of the many-body localized phase, but is not a unique characteristic^{8,131}. The results presented in this thesis provide evidence for such a unique characteristic by observing a logarithmically slow growth of correlations in the many-body state¹¹⁸.

While both non-equilibrium phases are well understood theoretically and can be successfully described by phenomenological models^{169,84,131}, the transition between these two phases remains an open question^{69,185,148,101,5,1,192}. Several experiments have probed slow transport properties through local observables near this critical regime^{120,26}. While such anomalous transport has been predicted theoretically^{2,171,192}, identifying anomalous transport as quantum critical dynamics is experimentally challenging, since similar behavior can also originate from stochastic effects: inhomogeneities in the initial state¹¹⁶ or the coupling to a classical bath^{130,119}. We overcome these challenges in our experiment with our protocol by evolving a pure, homogenous initial state under unitary dynamics where we additionally utilize post-selection to exclude coupling to the environment by atom loss^{119,118}. In the experiments presented in this thesis, we observe system-size dependent thermalization, anomalous transport, and correlations that span the entire system and persist up to high orders near the critical point¹⁵⁴. We additionally observe behavior in support of a proposed microscopic mechanism that leads systems at intermediate disorder strengths critically towards thermalization via a sparse resonant network^{148,101,154,77}.

0.4 OUTLINE

A quick summary of these studies are shown below as organized by their chapter:

- §1 serves as an introduction to and derivation of band physics associated with both solid state physics and neutral atoms in optical lattices. Additionally, this is then written in terms of the Bose-Hubbard model as an effective description. This serves as the underlying framework for all experiments in the thesis. Although, it is rarely explicitly referenced.
- §2 provides a brief overview of the quantum gas microscope as the experimental apparatus.

This chapter focuses on many of the details about how the lattice physics in §1 is physically realized as well as experimental protocols for calibrating the parameters of the Bose-Hubbard model.

- §3 introduces the concepts of entanglement and metrics used to quantify it. In this chapter, we then describe both conceptually and experimentally, how quantum phase transitions are realized in this system and measurements of entanglement in such phases. This will be discussed first for the superfluid-to-Mott-insulator transition and then for the paramagnetic-to-antiferromagnetic transition in the transverse Ising model.
- §4 summarizes the results and expands the techniques used in §3 to investigate and realize a highly entangled quantum mechanical system that locally mimics a classical system – both in local observables and entropy. At the same time: by utilizing a many-body interference technique the system can be verified to be describable by a single quantum mechanical wave function. These experiments are supported by the Eigenstate Thermalization Hypothesis, which predicts many thermodynamic behaviors emerge from entropy of entanglement generated by partial observation of a pure quantum mechanical system.
- §5 describes the only known robust exception to the generic prediction of locally thermalizing quantum mechanical systems – many-body localization. We study the breakdown of this thermalization in an interacting many-body system due to the application of a finite disorder strength, which realizes such many-body-localized states. We additionally quantify the separation of entanglement in the system that enable the first observation of the identifying property of this system: logarithmically slow growth of entanglement entropy throughout the system.
- §6 describes the properties of the transition from a quantum thermalizing system to a many-body-localized one. This transition is the focus of recent interest in the study of non-equilibrium phase transitions. In this regard, both the thermalizing and many-body-localized systems represent the quantum phases of highly excited eigenstates. We measure the growth of high-order correlations at the critical point when thermalization breaks down. Additionally, the observed structure of correlations in the system provides evidence for the suggested mechanism of a sparse resonant network that governs these critically thermalizing systems.
- §7 concludes with a summary and proposal for studying the possibility of other mechanisms governing this phase transition – a so called “avalanche” mechanism. We additionally study the concept of localization in Fock space and its dynamic properties.

Potential energy is just a word. It only has meaning if we provide it. For example, does this pen have potential energy?

::picks up pen and then drops it onto the floor::

Dr. Philipp Preiss

1

Optical Lattices and the Bose-Hubbard model

Ultracold neutral atoms in optical lattices provide a new paradigm in the ability to experimentally simulate quantum models. The level of control that can be applied to neutral atoms enables physicists to realize these quantum systems in their absolute ground states and create nearly defect free

lattice potentials engineered out of laser light. Additionally, the physical length scale of this physics admits the possibility of microscopic resolution of all degrees of freedom within a given measurement basis.

Such a framework for a quantum mechanical model maps most directly to condensed matter systems where the atom in the optical lattice takes the place of an electron in a crystal⁹⁰. For the sake of brevity, we will skip over most of the experimental footwork necessary to get to the point where such a relationship can be made. Instead, I will simply state that such a mapping is possible as long as the atoms can be made ultracold ($\sim 1\text{nK}$)^{17,16,149}. The average energy, or temperature, of the atom needs to be comparable to the kinetic energy and interaction energies within the optical lattice to probe the same physics. Another way of seeing the same relationship is to see if the thermal deBroglie wavelength, λ_{th} , of the atom is on the order of the lattice constant a such that it may be in a coherent superposition of occupying many lattice sites simultaneously and indistinguishable from other atoms within neighboring lattice sites. In our system, the quoted temperature provides $\lambda_{th} \approx 6\mu\text{m}$ which is ≈ 10 lattice sites. With this crude justification in mind, we will now derive the physics of a particle being described as a wave in such a periodic potential.

1.1 SINGLE-PARTICLE PHYSICS IN OPTICAL LATTICES

Optical coupling of orbital electronic states in neutral atoms provide a mechanism for both conservative and dissipative forces¹²⁶. These two processes can be thought of as elastic and inelastic scattering, respectively, of photons with the atom. The dissipative force is provided by the absorption of

a photon or emission of a photon and has been famously used for trapping and cooling of atomic gases^{40,152,39,126}. However, the vast majority of all work and models discussed in this thesis will rely on tailoring conservative potentials with almost arbitrary spatial control^{10,126,68}. Since the only external forces that interact with the atoms are optical and predominantly conservative, the system remains, to a very good approximation, isolated from the surrounding external environment.

I.I.I NEUTRAL ATOMS IN OPTICAL POTENTIALS

A neutral atom experiences a conservative external potential from optical photons when the frequency of the light is far from the atomic resonance. This light, rather than being absorbed by the atom, induces an electric dipole moment in the atom. The amplitude of the alignment, or anti-alignment, of this dipole moment with the external electrical field changes the energy of the atom and is known as the ac-Stark shift¹⁰. In the case of a two-level atom in a monochromatic laser field, where the laser detuning is large enough that the rotating wave approximation can be used, the conservative potential provided by the dipole atom-light interaction is given by:

$$V_{dipole}(r) \approx \frac{3\pi c^2}{2\omega_o^3} \frac{\Gamma}{\Delta} I(r) \quad (\text{I.I})$$

where the atomic transition frequency is ω_o , the linewidth of the transition is Γ , the intensity of the laser power is $I(r)$, and the detuning of the laser frequency from the atomic transition is $\Delta = \omega - \omega_o$. Note that the both the laser intensity, $I(r)$, and the detuning, Δ , are complimentary ways to change dipole potential depth. Additionally, the sign of the detuning Δ controls whether

the atom is attracted to or repelled from the high-intensity locations of the laser beam profile. This is commonly referred to as either red- or blue-detuning of the laser with respect to the atomic transition frequency due to their association with the colors in the visible spectrum. While (1.1) is written for a two-level atom approximation, additional energy levels can be included to provide a more accurate response¹²⁶.

However, even an off-resonant laser illuminating the atom does not act purely as a conservative potential since the photons still have a finite probability to exchange energy and momentum with the atom⁶⁸. The likelihood of such a dissipative process depends on both the intensity of the light, I , and the laser detuning with respect to the linewidth of the atomic transition Γ/Δ . The rate at which an atom scatters light is given by (1.2):

$$\Gamma_{sc}(r) \approx \frac{3\pi c^2}{2\hbar\omega_o^3} \left(\frac{\Gamma}{\Delta}\right)^2 I(r) = \frac{1}{\hbar} \frac{\Gamma}{\Delta} V_{dipole}(r) \quad (1.2)$$

By detuning the laser far from resonance, we see that the scattering rate, or dissipative contribution of the light-atom interaction, is reduced compared to the conservative contribution by a factor of (Γ/Δ) . This implies that for the same desired dipole potential depth V_o , it is always favorable to increase both the laser detuning and the intensity to reduce the scattering rate to more faithfully realize a purely conservative potential. This consideration of these two scalings provide some guidance in how to choose practical parameters for the lasers that produce the desired optical potentials (see §2.1.3).

1.1.2 BANDSTRUCTURE AND BLOCH WAVE FUNCTIONS

All experiments in this thesis will be realized in an effective 1-D optical lattice that is generated from interfering blue-detuned light. The potential generated from this light depends on the intensity of its interference pattern and is written as:

$$V(x) = -(V_o/2) \cos(2k_l x) \quad (1.3)$$

where k_l^* is the wavevector (or k-vector) of the laser light used to create the potential. The potential has been written with zero DC average for mathematical convenience. The total Hamiltonian then for a single-particle is written as:

$$H = \frac{\hat{p}^2}{2m} + V(x) \quad (1.4)$$

where m is the mass of the atom. In the case of zero lattice depth, $V_o = 0$, this Hamiltonian realizes a single-particle in free space whose eigenstates are described by a propagating wave with an eigenenergy that depends only on its momentum $\hbar k$: $\psi_k = e^{ikx/\hbar}$. A side note is that this potential-free Hamiltonian has a continuous translational symmetry in space and therefore conserves momentum which additionally implies that eigenstates of this Hamiltonian are also eigenstates of the

*This k-vector (k_l) is defined as $2\pi/\lambda$ when the light used to create the potential originates from two counter-propagating lasers where λ is the laser wavelength. However, this only provides an upper-bound for what k-vector can be produced by a given laser wavelength. What matters is the k-vector in the plane of the lattice formed by the lasers which can be tuned by their relative angle. This point will be further elucidated in §2.

momentum operator, \hat{p} . *

Once the lattice depth is non-zero, this symmetry is broken such that the Hamiltonian only retains a discrete translational symmetry. The Bloch theorem states that since the Hamiltonian (1.4) has a discrete translational symmetry from the periodic potential (1.3), then the eigenfunctions of the Hamiltonian will also be eigenfunctions of this discrete translation and hence will also be periodic (1.5).

$$\phi_q^{(n)}(x) = e^{iqx/\hbar} \cdot u_q^{(n)}(x) \quad (1.5)$$

The Bloch wave functions, $\phi_q^{(n)}$, are labeled by their band index n (which will become apparent later) and their quasi-momentum, or crystal momentum, q . This quasi-momentum is akin to the linear momentum of the free-particle case referenced to above except that it is now only defined within the Brillouin zone of the periodic potential $-\hbar k_l \leq q \leq \hbar k_l$ where k_l is the k-vector of the laser light. The function $u_q^{(n)}(x)$ is a Fourier series with a periodicity that correspond to integer multiples of the lattice period. Intuitively, the high-frequency cut off for $q = \pm \hbar k_l$ for defining $\phi_q^{(n)}(x)$ derives from the periodic potential that can only “detect” or “sample” spatial variation with a frequency equal to or less than its own.[†] Note that this does not define that the Bloch wave function cannot have local spatial variation with higher frequencies than the lattice periodicity, just that whatever this local high-frequency variation is, it must repeat periodically with the lattice period.

*This is, of course, obvious since the Hamiltonian is composed of only the momentum operator \hat{p} . However, the statement about symmetries and invariance relating to conserved quantities is a general one.¹⁸⁷

[†]This is akin to Nyquist frequency if you are an electrical engineer.

The remaining slowly varying envelope function is then defined by $e^{iqx/\hbar}$.*

To find the eigenfunctions of this new Hamiltonian with momentum states coupled by integer multiples of the lattice k-vector ($k_L = 2k_l$), we can more conveniently solve this problem in Fourier space and solve for the eigenenergies $E_q^{(n)}$. We first write both the potential and the periodic function $u_q^{(n)}(x)$ as Fourier series:

$$V(x) = \sum_m V_m e^{i2mk_l x/\hbar} \quad (1.6)$$

and

$$u_q^{(n)}(x) = \sum_r c_r^{(n,q)} e^{i2rk_l x/\hbar} \quad (1.7)$$

The periodic potential term $V(x)$ in (1.6) only has two non-zero terms that correspond to the lattice periodicity ($V_{m=-1} = V_{m=1} = -V_o/4$). To find the coefficients for the Fourier series of $u_q^{(n)}$ and the eigenenergies $E_q^{(n)}$, one should exploit the orthogonality relation between Fourier modes after taking the inner-product of $\langle e^{i2r'k_l x/\hbar} | H | \phi_q^{(n)} \rangle$. This procedure results in:

$$\sum_{r'} H_{r,r'} \cdot c_r^{(n,q)} = E_q^{(n)} c_r^{(n,q)} \quad (1.8)$$

*The presence of these high-frequency variations come through the Fourier series of $u_q^{(n)}(x)$ and will be apparent in the higher bands defined by the index n , which are related to the free-particle momentum states centered about an integer n of k_l displacements of momentum in Fourier space.

where

$$H_{r,r'} = \begin{cases} (2r + q/k)^2, & r = r' \\ -V_o/4, & |r - r'| = 1 \\ 0, & otherwise \end{cases} \quad (1.9)$$

Diagonalizing the Hamiltonian (1.9), where r and r' are matrix indices, will solve for the eigenenergies that depend on the continuous variable q and the discrete index n which labels the characteristic formation of *bands* in the spectrum. To gain some intuition for the system this Hamiltonian describes, we can again first think about the $V_o = 0$ case. In the case of no external potential, this Hamiltonian will realize a parabolic dispersion curve in k -space from the momentum of a free-particle. By turning on the lattice potential, $V_o \neq 0$, the external potential can now provide momentum “kicks” to the particle’s wave function in discrete quanta of $2\hbar k_l$ (when the indices r, r' differ by 1). In the case that the energy from the free-particle dispersion curve at q and $q \pm 2\hbar k_l$ are $\lesssim V_o$, then these two momentum states are strongly coupled and these states hybridize to form an eigenstate composed of a superposition of the two free-particle states. The first time this happens is at the $q = \pm\hbar k$ point in the dispersion curve and defines what is known as the Brillouin zone boundary in a crystal. Physically, this hybridization corresponds to perfect Bragg reflection of the particle’s wave function at the Brillouin zone boundary. This hybridization forms the familiar *gaps* associated between bands of energy as defined on a reduced Brillouin zone band diagram (1.1). Note that this also introduces a natural energy scale for this physics known as the lattice recoil energy. In essence, the Braggs scattering is an elastic scattering event by two photons within the plane of the

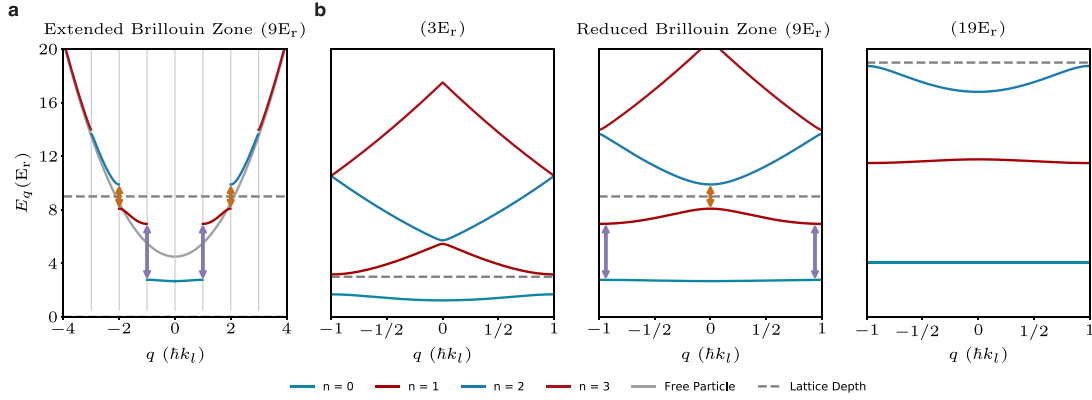


Figure 1.1: Dispersion with Bragg reflection. a) The left curve shows free-particle dispersion parabola (gray line) and the formation of gaps in the Bloch wave functions from Bragg scattering off the lattice. Additionally, the dashed-grey lines show the height of the lattice as it is centered about zero and determines when a state $|\psi_k^{(n)}\rangle$ is bound to the lattice. This depiction of the hybridization of the free-particle dispersion curve is known as the extended Brillouin zone scheme and is an intuitive way of how to reach the notion of bands from Bragg scattering. b) The reduced Brillouin zone scheme is associated with condensed matter physics and band structure and more common in the literature. This mapping is both compact and conceptually reflects the notion of periodic states that are described by Bloch wave functions $|\phi_q^{(n)}\rangle$ that are only well defined for quasi-momentum states q that are bounded by the lattice wave-vector k_L .

lattice that change the momentum of the particle in the lattice. For a given light k-vector defined in the plane of the lattice, k_l , this gives us the recoil energy defined as:

$$E_r = \frac{(\hbar k_l)^2}{2m} \quad (1.10)$$

Once the lattice depth, V_o , is deep enough that an entire band lies within its energy window, it conceptually makes sense to describe these as Bloch functions that are bound to the lattice. These original free-particle states are now sufficiently dressed by Bragg reflected states with momenta that differ by integer multiples of the lattice vector $\hbar k_L = 2\hbar k_l$ that they form a stationary wave with particle density maxima that reside deep in the potential minima. This is shown for both the ground

band and the first excited band in Fig. 1.1. This thesis will use the convention that $n = 0$ refers to the ground band. These periodic eigenstates of the Hamiltonian are plotted for various quasi-momentum states for both the ground band and the excited band in Fig. 1.2. A common physical picture given for the opening of a gap at the edge of the Brillouin zone, in the weak lattice limit, is given by the phase of the Bloch wave function's spatial structure. While,

$$\left| \phi_{q=\hbar k}^{n=0,1}(x) \right\rangle \approx e^{ik_l x/\hbar} + (-1)^n e^{-ik_l x/\hbar}$$

are both composed of the same free-particle momenta states, their symmetric versus anti-symmetric superposition either concentrates the density of the particle either in the minima or the maxima of the lattice potential (as shown in Fig. 1.2). This provides an obvious energy difference between the two combinations purely by the overlap of the wave function and the lattice potential – the kinetic energies should be approximately the same.

There are two primary quantities that are typically extracted from the band structure due to their physical relevance: the band width and the band gap. The band width, the energy difference between the maximum and minimum energy for a given band $(\arg \max_q \{E_q^{(n)}\} - \arg \min_q \{E_q^{(n)}\})$, describes the maximum kinetic energy of a particle confined to that band. The kinetic energy becomes substantially suppressed as bands become bound to the lattice and will appear to be approximately flat. The band gap, the energy difference between successive bands $\Delta = E_q^{(n+1)} - E_{q'}^{(n)}$, defines how well separated a particle in one band is energetically from another band. Practically speaking, all the physics in this thesis will assume a single-band model where all particles inhabit the

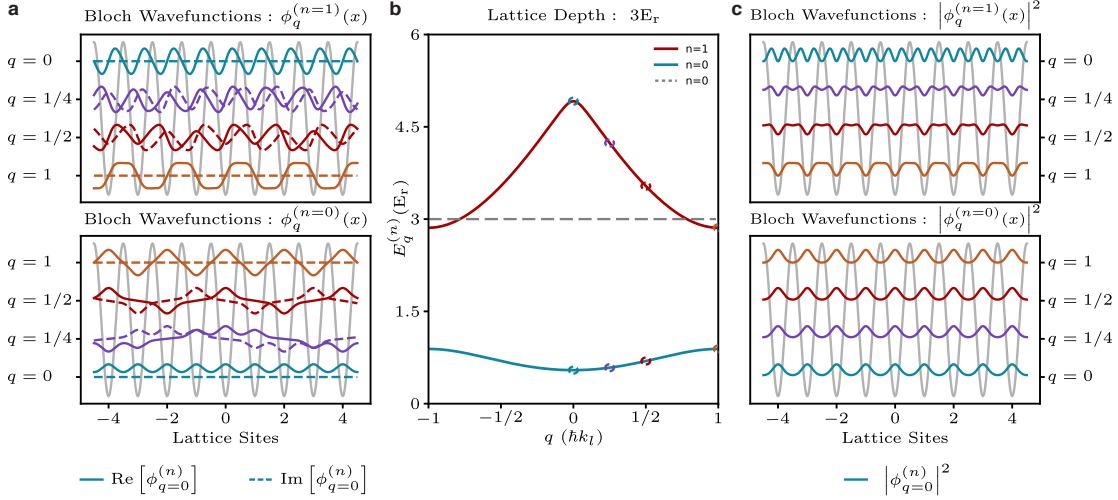


Figure 1.2: Bloch wave functions. a) The left plots depict the real and imaginary parts of the Bloch wave function's ($|\phi_q^{(n)}(x)\rangle$) spatial dependence as a function of distance for various quasi-momenta and both the $n = 0$ and $n = 1$ bands at a lattice depth of $4E_r$. b) Plots the band structure for at $4E_r$ and the quasi-momenta the plotted Bloch wave functions describe. c) These right plots depict the density distribution of the Bloch functions for the same quasi-momenta as the left plots and same bands. Note that only the ground-band, $n = 0$, is entirely bound to the lattice and relatively “flat”. Unlike the $n = 0$ band, $n = 1$ band has a significant deviation in its wave function across the band and has lots of particle probability that does not lie in the minima of the potential well and reflects its unbound nature.

ground-band of the lattice. This makes the band gap a relevant metric for determining how well the observed phenomena will be described by a single-band Hamiltonian and how susceptible the system will be to some form of heating that deposits energy into the system. The evolution of the band gap and band width can be seen from progression of band structure plots in Fig. 1.3 as well as the evolution of the band gaps between various successive bands as a function of lattice depth.

1.1.3 WANNIER WAVE FUNCTIONS

The Bloch wave functions, as the single-particle eigenstates, are a natural and convenient way to describe the physics of a particle in a periodic potential. They are a complete set of energy eigenstates

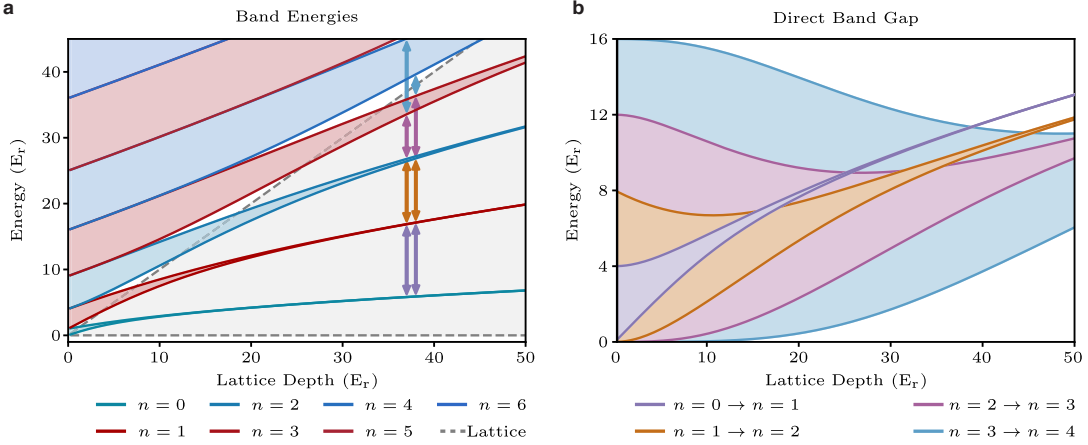


Figure 1.3: Band Gaps. a) The band structure of the four lowest bands are plotted for three lattice depths to depict how both the band widths and band gaps change as a function of lattice depth. Note that the lower bands both flatten and become gapped from the excited bands more quickly as a function of lattice depth. b) The band gap between successive bands can strongly depend on which quasi-momentum is being excited from and to ($\Delta_{q,q'}^{n,n+1} = E_q^{(n)} \rightarrow_{q'}^{(n+1)}$). In principle both direct, quasi-momentum preserving, and indirect, non-quasi-momentum preserving, excitations are possible in a lattice. However, in the case of a simple sinusoidal lattice, both the minimum and maximum band gaps are captured by just analyzing direct band excitations. The minimum and maximum band gaps are plotted as the solid lines and the distribution of all intermediate possible values are plotted as the shading.

and completely described by their band index n and quasi-momentum q . Since they are defined by a single quasi-momentum number q , they are maximally localized in momentum space and maximally delocalized in position space. A useful alternative, orthonormal basis for this system is given by the set of functions that describe the particle as localized in position space. These set of functions are known as Wannier functions and are a convenient way to describe the wave function of a particle in a band n that is maximally localized at a lattice site x_i . This basis can be constructed from a superposition of all Bloch wave functions within the Brillouin zone for a given band n :

$$w_n(x - x_i) = \frac{1}{N} \sum_q e^{-iqx_i} \phi_q^{(n)}(x) \quad (\text{I.II})$$

The normalization factor \mathcal{N} depends on the finite number of quasi-momentum Bloch wave functions summed over. Additionally, since the Bloch wave functions are eigenstates of the original Hamiltonian, they may have been solved with an arbitrary global phase that will become an important relative phase in the construction of the Wannier functions $w_n(x - x_i)$. Thankfully, there is a convenient recipe to follow that establishes how to choose the phases when constructing $w_n(x - x_i)$ that produces a wave function maximally localized on site x_i .

We have seen from the symmetry of the periodic potential, the hybridization of the free-particle states at the edge of the Brillouin zone, and the plots of the Bloch functions in Fig. 1.2 that the wave functions of even bands ($n = 2 \times m, m \in \mathbb{Z}$) are also even functions of x and the wave functions of odd bands are also odd functions of x . The Wannier functions will also retain this symmetry since they are constructed from the Bloch functions within a given band. To then construct a maximally localized wave function at lattice site x_i , we must find the necessary phases multiplied by the Bloch wave functions that constructively add at $x = x_i$. For even bands, we choose a phase for each Bloch function that makes it both real and positive at $x = x_i$.^{*} For odd bands, the Bloch wave functions are also odd about the center of each lattice site $x = x_i$. The recipe used above is modified such that the phase chosen is such that the first derivative of the Bloch wave functions are real and positive at site x_i . Including the recipes described above we can write down the Wannier functions construc-

^{*}It does not actually matter which phase you pick for this site, just that you rotate all Bloch wave functions such that their phase is the same at $x = x_i$: $\text{Arg} [\phi_q^{(n)}] = \text{const. } \forall q, \text{ where const. } \in \mathbb{C}$

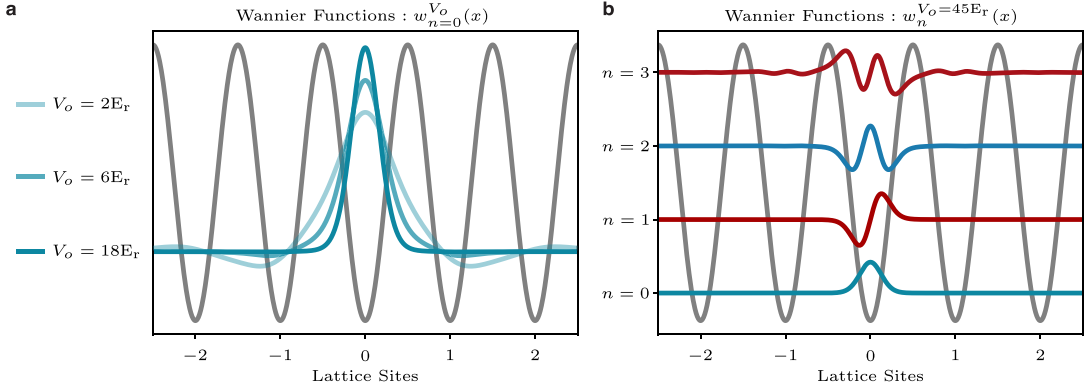


Figure 1.4: Wannier wave functions. a) The Wannier wave functions for the ground band ($n = 0$) are plotted for three different optical lattice depths. Note that this is plotted in the *field* of the Wannier function, not the density distribution of the atom on a given site. b) The Wannier wave functions are plotted here for band indices $n = [0, 3]$ for a deep lattice depth of $V_o = 45E_r$. Note that they are closely approximated by the harmonic oscillator solutions in this regime.

tion as follows:

$$w_n(x - x_i) = \begin{cases} \frac{1}{N} \sum_q e^{\left(-i\text{Arg}[\phi_q^{(n)}(x_i)]\right)} \cdot \phi_q^{(n)}(x), & n \text{ is even} \\ \frac{1}{N} \sum_q e^{\left(-i\text{Arg}[\partial\phi_q^{(n)}(x)/\partial x|_{x=x_i}]\right)} \cdot \phi_q^{(n)}(x), & n \text{ is odd} \end{cases} \quad (1.12)$$

The Wannier wave functions represent the maximally localized, conjugate basis to the Bloch wave functions. These Wannier states become more localized for increasing lattice depth, which is plotted in Fig. 1.4a for the ground band. We can additionally see in Fig. 1.4 that for a $45E_r$ lattice how the Wannier wave functions are also successively wider for higher bands in the lattice.

A useful, limiting case observation is that as the lattice depth becomes much larger than the band width of a given band, the Wannier functions approach the wave functions of a Harmonic oscillator, as can be seen by the similarity between the $w_n(x - x_i)$ plotted in Fig. 1.4b and Hermite Gaussians

solutions of the Harmonic oscillator.* This also implies that the Wannier functions become increasingly approximated by a superposition of free-particle states with a Gaussian envelope centered at an integer number of Bragg scattering events defined by the band index $n \times 2\hbar k_l$. Lastly, while the Wannier functions are not eigenstates of the original Hamiltonian, they become asymptotically close as $V_o \rightarrow \infty$, where both the corresponding band becomes flatter and the associated Bloch wave functions will be nearly degenerate.

1.2 THE BOSE-HUBBARD MODEL

The treatment for deriving band structure and Bloch wave functions describes the entire physical story for a single-atom in an optical lattice. However, it neglects the many-body physics associated with interacting particles that leads to celebrated exotic condensed matter systems. It additionally does not easily lend itself to describing the nature of inter-particle interactions that are often derived from a local, inter-particle potential. To incorporate these local dependencies, we will now reformulate the free-particle Hamiltonian from before into a local basis that utilizes our derivation of the Wannier functions in the previous section.

In particular, we will describe the overlap of an atomic wave function with a local Wannier function defined about a particular lattice site as the population of the atoms in an orbital defined about that site. This leads us towards adopting the tight-binding lattice model for bosonic particles that is

*This is additionally a conceptually comforting fact as the cosine potential providing the lattice can be approximated to lowest order as a quadratic potential. However, due to the finite depth of the lattice, there is always a non-negligible amplitude in the wings of $w_n(x - x_i)$ that is necessary for an accurate description of the system.

known as the Bose-Hubbard model. This is a renowned toy condensed matter model that faithfully incorporates strong inter-atomic interactions that lead to strongly correlated states that are otherwise absent in interaction corrected mean-field equations, such as the Gross-Pitaevski equation^{149,90}.

1.2.1 INTERACTING ATOMS IN AN OPTICAL LATTICE

In all our experiments, we work with dilute atomic gases. In these dilute gas regimes, the atom-atom interactions can be described by an effective inter-atomic potential between any two particles $V(r)$, where r is the inter-particle distance. This potential is strongly repulsive at distances on the order of a few Bohr radii, ($\sim a_0$), due to the strong Coulomb interaction between the respective atom electron clouds. However, since atoms are polarizable, they are attractive at long distances due to the mutually induced dipoles that lead to a van der Walls force¹⁸⁸.

In the case of the low temperatures utilized by ultracold atom experiments, these inter-atomic interactions primarily result in elastic scattering processes between the atoms. In this regime, it is not necessary to know the exact shape of the interatomic potential since the low kinetic energies of the atoms do not enable them to probe past the centrifugal barrier. This means that only the lowest partial wave scattering process, *s*-wave scattering, significantly contributes to the inter-atomic interactions. Therefore, this contribution can be well approximated by a contact interaction that is characterized by a single parameter that quantifies the *s*-wave scattering length, a_s :

$$V(r) = \frac{4\pi\hbar^2 a_s}{m} \delta(r) \quad (1.13)$$

These interactions are often tunable via Feshbach resonances where the interaction strength can be changed by many orders of magnitude and even change sign³⁶. Additionally, it can be tuned through a much narrower range via the lattice depth by increasing the wave function overlap between atoms.

1.2.2 DERIVING THE BOSE-HUBBARD MODEL PARAMETERS

We can derive the Bose-Hubbard model by incorporating the inter-atomic contact interactions into the Hamiltonian of a bosonic field $\hat{\Psi}(\vec{x})$ ^{*} and an external potential:

$$H = \int d^3x \hat{\Psi}^\dagger(\vec{x}) \left(-\frac{\hbar^2}{2m} \nabla^2 + V(\vec{x}) \right) \hat{\Psi}(\vec{x}) + \frac{1}{2} \frac{4\pi\hbar^2 a_s}{m} \int d^3x \int d^3x' \hat{\Psi}^\dagger(\vec{x}) \hat{\Psi}^\dagger(\vec{x}') \delta(\vec{x} - \vec{x}') \hat{\Psi}(\vec{x}) \hat{\Psi}(\vec{x}') \quad (1.14)$$

where $\vec{x} = (x_1, x_2, x_3)$.

Here the potential contains both the lattice potential and any additional potential term applied on top of the lattice that is relatively weak and spatially varies more slowly than the lattice itself:

$V(\vec{x}) = V_{latt}(\vec{x}) + V_{arb}(\vec{x})$. In the low temperature regime, the atoms only populate the ground band and we can restrict this derivation to involving only basis states that overlap with this band.

Since the interaction term is entirely local it is convenient to expand the bosonic field $\hat{\Psi}(\vec{x})$ in terms

*Note that by using this many-bodied bosonic field operator $\hat{\Psi}(\vec{x})$, we have implicitly moved into a second-quantized notation. This means that later when we populate this bosonic field with individual atoms as quantized excitations in the field (\hat{a}^\dagger), we have assumed these excitations to be indistinguishable from one another and will correctly incorporate the symmetrization necessary to accommodate these quantum statistics.

of ground band Wannier wave functions:

$$\hat{\Psi}(\vec{x}) = \frac{1}{N} \sum_i \hat{a}_i w_o(\vec{x} - \vec{x}_i) \quad (1.15)$$

Here \hat{a}_i (\hat{a}_i^\dagger) are the annihilation (creation) operators for a boson in the ground band Wannier function centered at a lattice site \vec{x}_i . These operators follow the typical bosonic commutation relation $[\hat{a}_i, \hat{a}_j^\dagger] = \delta_{i,j}$. This expansion allows us to rewrite (1.14) in terms of these bosonic annihilation and creation operators:

$$H = - \sum_{i,j} J_{i,j} \hat{a}_i^\dagger \hat{a}_j + \sum_{i,j,k,l} \frac{U_{i,j,k,l}}{2} \hat{a}_i^\dagger \hat{a}_j^\dagger \hat{a}_k \hat{a}_l + \sum_i (h_i - \mu) \hat{a}_i^\dagger \hat{a}_i \quad (1.16)$$

The additional potential that was added on top of the lattice, $V_{arb}(\vec{x})$, provides a variation in the on-site energy potential h_i . The chemical potential μ is a thermodynamic quantity that constrains the total particle number in the grand canonical ensemble description of the model. The $J_{i,j}$ term is known as the tunneling matrix element quantifies the tunneling rate between any two sites i and j and describes the kinetic energy of the atom. The $U_{i,j,k,l}$ term describes the various interaction matrix elements between atoms on sites i, j, k, l . Although the Wannier functions are constructed as an orthonormal basis, they were never eigenstates of the original Hamiltonian. Formally then, we can quantify these matrix elements via the overlap of the Wannier functions after the Hamiltonian

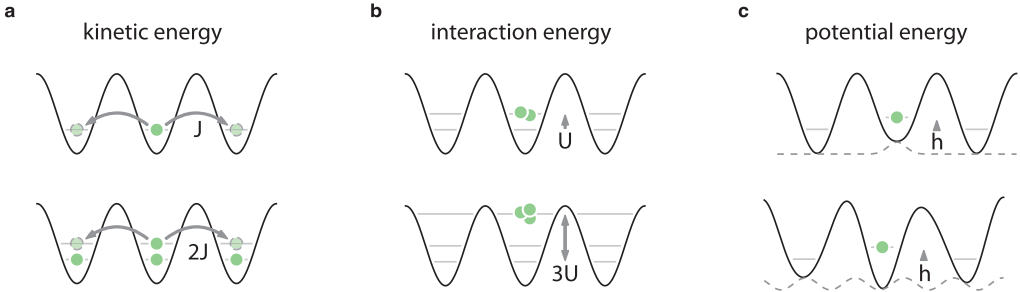


Figure 1.5: Bose-Hubbard terms. a) Each green disk represents a bosonic atom excitation of the many-body wave function that populates a Wannier function centered on a given lattice site x_i . The kinetic energy term J describes the coupling, or hopping rate, of the Wannier wave function to neighboring sites. In the presence of multiply occupied sites, this is energetically increased by bosonic enhancement. b) The interaction energy for multiply occupied sites is non-linear in the on-site occupation number \hat{n}_i since it depends upon the number of pair-wise scatterings on a given lattice site. c) On-site lattice potential variation, either intentional or unintentional, adds an additional energetic parameter for locally tuning the Bose-Hubbard model with optical potentials due to disorder or confining trap potentials.

has acted on them:

$$J_{i,j} = - \int d^3x w_0^*(\vec{x} - \vec{x}_i) \left(-\frac{\hbar^2}{2m} \nabla^2 + V_{latt}(\vec{x}) \right) w_0(\vec{x} - \vec{x}_j) \quad (1.17)$$

$$U_{i,j,k,l} = \frac{4\pi\hbar^2 a_s}{m} \int d^3x w_0^*(\vec{x} - \vec{x}_i) w_0^*(\vec{x} - \vec{x}_j) w_0(\vec{x} - \vec{x}_k) w_0(\vec{x} - \vec{x}_l) \quad (1.18)$$

For nearly all practical cases, we will work in the “tight-binding” regime of this ground band model. This approximation assumes that the Wannier functions are sufficiently localized that all higher order tunneling processes and higher order interaction terms may be ignored. This leaves the model with only a nearest-neighbor tunneling $J_{i,i\pm 1} \equiv J$ and on-site interaction $U_{0,0,0,0} \equiv U$ and

results in the standard form of the celebrated Bose-Hubbard model:

$$H_{BH} = -J \sum_{\langle i,j \rangle} \hat{a}_i^\dagger \hat{a}_j + \frac{U}{2} \sum_i \hat{n}_i (\hat{n}_i - 1) + \sum_i (h_i - \mu) \hat{n}_i \quad (1.19)$$

where $\hat{n}_i = \hat{a}_i^\dagger \hat{a}_i$ is the on-site number operator and the bracket sum, $\langle i, j \rangle$, refers to a sum only over neighboring indices. Physically, the mechanism that describes the exact contributions for the on-site interaction term comes from the sum of all pair-wise interactions of n atoms on site i , each of which contribute an energy cost of U : $U \sum_i \binom{\hat{n}_i}{2} = U \sum_i \frac{\hat{n}_i!}{(\hat{n}_i-2)!2!} = \frac{U}{2} \sum_i \hat{n}_i (\hat{n}_i - 1)$. All of these processes are illustrated below in Fig. 1.5.

Both parameters J and U change significantly as a function of the lattice depth V_o . The qualitative features of the states that are harbored by the Bose-Hubbard model depend only on the ratio of these two quantities U/J . Practically speaking, the absolute energy scales of these two parameters are important for defining relevant experimental time-scales. This conversion comes from defining all energies by \hbar as an *angular* frequency. In our experiment, the depth of the lattice is measured in lattice recoil $E_r/\hbar \approx 2\pi \times 1240\text{Hz}$ and sets these overall energy scales. The values for J and U , as calculated from the ground state Wannier wave functions (1.17, 1.18), are plotted for the parameters of our experimental parameters in Fig. 1.6.

In the deep lattice (tight-binding) limit, the dispersion of the ground band becomes well approximated by a cosine potential: $E_q = -2J \cos(2\pi q/k_l)$ where J is the Bose-Hubbard hopping parameter. In this regime, the analytical form for J can be solved for exactly and approximately decays

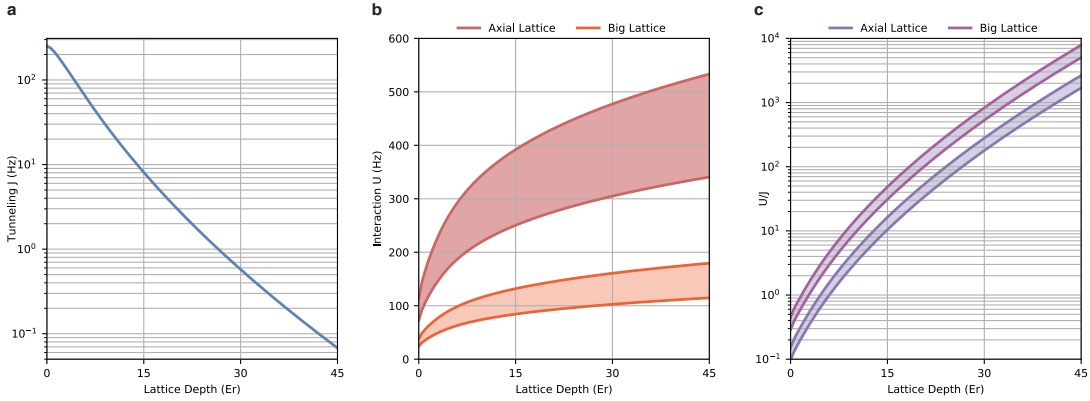


Figure 1.6: Bose-Hubbard Parameters. a) The hopping parameter J is evaluated for the optical lattice used in our experiments and is plotted here as a function of lattice depth. b) The interaction energy U is plotted as a function of lattice depth for a one-dimensional system. The absolute energy scale requires the knowledge of the amount of confinement in the other two spatial dimensions. The band of possible values plotted here relies on the two different z -confining optical lattices that each have different spacings and can be varied through different amounts of optical powers. This translates into a variable amount of compression of the wave function and hence interaction strength U . c) This plot shows the relevant ratio of U/J which qualitatively determines the physics investigated in the system. This plot is also for a one-dimensional system.

exponentially with lattice depth:

$$J = \frac{4}{\sqrt{\pi}} E_r \left(\frac{V_o}{E_r} \right)^{3/4} e^{-2(V_o/E_r)^{1/2}} \quad (1.20)$$

Additionally, the scaling of U with lattice depth can be estimated by approximating Wannier wave functions with the Harmonic Oscillator Gaussian states. In this limit the two relevant comparisons to the lattice can be given by the effective on-site trap frequency ω_{ho} and oscillator length l_{ho} that depend on the lattice depth:

$$\omega_{ho} = 2E_r \sqrt{V_o/E_r} \quad (1.21)$$

$$l_{ho} = \sqrt{\hbar/m\omega_{ho}} = \frac{a/2}{2\pi} \left(\frac{V_o}{E_r} \right)^{-1/4} \quad (I.22)$$

$$w_n(x - x_i) \approx \psi_{l_{ho}}^n = \frac{1}{\sqrt{2^n n!}} \left(\frac{1}{\pi l_{ho}^2} \right)^{1/4} e^{-x^2/(2l_{ho}^2)} H_n(x/l_{ho}) \quad (I.23)$$

where $H_n(x/l_{ho})$ are the Hermite polynomials of order n .

This leads to an approximate scaling of $U \propto V_o^{1/4}$. This elucidates the point that while both J and U are tunable with lattice depth, the relevant ratio of U/J is mostly determined by the exponential suppression of J with the lattice depth. However, one crucial difference is that $J_{x,y,z}$ should be defined per lattice direction and depends only on the lattice depth along this direction. This is not the case for U which depends upon the integral of the Wannier wave function in all three dimensions. This means that even without using a Feshbach resonance, there is some marginal tunability of U by just changing the lattice depth in the dimensions orthogonal to the dimension of interest for J . This is particularly relevant since the majority of the work described in this thesis is performed for one dimension. The lattices that provide confinement along the z -direction has the widest range of tunability and is plotted in Fig. I.6 as two-bands of experimentally accessible ranges for one-dimensional Bose-Hubbard physics parameters.

1.3 QUANTUM PHASE TRANSITIONS: SUPERFLUID TO MOTT-INSULATOR

Quantum phase transitions are a celebrated achievement in physics that differ from their classical counterparts since they can occur even at zero temperature. These quantum phase transitions are driven by quantum fluctuations in the ground-state wave function of a system since all thermal fluctuations are frozen out at zero temperature. The Bose-Hubbard model famously exhibits a quantum phase transition that depends on the relative strengths of the on-site interaction and tunneling terms. This will first be described by the ground-state wave function's behavior in the two extremes for a lattice with no additional potentials (i.e. $h_i = 0$), N atoms, and periodic boundary conditions.

1.3.1 SUPERFLUID PHASE: $J \gg U$

In the limit of very large J compared to U , the Hamiltonian favors the delocalization of atoms across the lattice. The ground-state wave function becomes simple to write down in the extreme case that $U \rightarrow 0$ and we simply recover N atoms occupying the Bloch band for $q = 0$ as defined from the band structure derived earlier in this chapter:

$$|\Psi_{SF}\rangle = \frac{1}{N} \left(\hat{a}_{q=0}^\dagger \right)^N |0\rangle \propto \frac{1}{N} \left(\sum_i \hat{a}_i^\dagger \right)^N |vac\rangle \quad (1.24)$$

where $|0\rangle$ is defined as the vacuum state with 0 bosons. In the case that we do not restrict the ground state to a specific number of particles N , the ground state is defined by a coherent state $|\alpha_i\rangle$ on every site i since this state is an eigenstate of the tunneling matrix elements \hat{a}_i ($\hat{a}_i|\alpha_i\rangle = \alpha_i|\alpha_i\rangle$).

In this regime of uncertain particle number, the ground-state becomes a product state of coherent states:

$$|\Psi_{SF}\rangle \approx \prod_i |\alpha_i\rangle = \prod_i e^{-|\alpha_i|^2/2} e^{\alpha \hat{a}_i^\dagger} |0\rangle \quad (1.25)$$

where the phase of α is well defined and constant across all sites in the lattice ($\hat{\phi}|\alpha_i\rangle = \text{Arg}[\alpha_i]$) and a fixed average density $\langle n \rangle = |\alpha|^2$. This approximation conceptually describes the superfluid as an array of Bose-Einstein condensates on each lattice site with a well defined phase that is locked across the entire lattice via the tunneling operators. The superfluid phase is defined by a non-zero order parameter $\psi \equiv \langle \alpha \rangle$ and has characteristic properties of having gapless excitations and finite compressibility $\kappa = \partial n / \partial \mu$.

1.3.2 MOTT-INSULATOR: $U \gg J$

In the opposite limit, as U becomes the dominant energy scale in the system, the eigenstates of the ground state become defined by the on-site atom number. This forms an insulating state that suppresses particle transport due to the strong inter-atom interactions. This becomes clear in the extreme limit as $J \rightarrow 0$ and the Hamiltonian is now defined by only the on-site number operator \hat{n}_i meaning that all the eigenstates of the Hamiltonian are also eigenstates of \hat{n}_i . Since the on-site particle number is quantized, the atom-number on a given site i is determined by the ratio of μ/U .

In the case of a commensurate total atom number N with the number of lattice sites L ($N/L = \nu$),

the Mott-insulator wave function is written as:

$$|\Psi_{MI}\rangle = \prod_i \left(\hat{a}_i^\dagger \right)^\nu |0\rangle \quad (1.26)$$

In the Mott-insulating state, the order parameter of the superfluid goes to zero since all phase coherence between lattice sites is lost. In the case of commensurate filling*, this state forms plateaus of fixed on-site atom number ν and the lowest excitations are defined by moving a particle to its neighboring site at the cost of the on-site interaction energy U . This defines this state as having gapped excitations and points to its *incompressibility*.

1.3.3 PHASE DIAGRAM

The two variables, phase ($\hat{\phi}$) and on-site atom number (\hat{n}_i), are conjugate variables that describe the quantum phases described above. The diagram that determines the boundary between the phases can be understood from a mean-field approach. The superfluid to Mott insulator transition is a

*A subtlety when attempting to reach the Mott-insulating state in a real system is fulfilling this commensurability requirement. If one is using a box-like potential (rather than a harmonic trap), the system *must* have commensurate filling to reach a true Mott-insulating plateau. Otherwise the system will be effectively described by two competing effects: a Mott-insulating plateau with closest lower integer on-site filling ($n = \lfloor \nu \rfloor \rightarrow |MI_n\rangle = \prod_{i=1}^L \left(\hat{a}_i^\dagger \right)^n |0\rangle$) that is accompanied by an overlapping superfluid that lives on top of this Mott-insulating plateau with the remaining delocalized atoms ($|SF_{(n-\nu) \times L}\rangle = \left(\hat{a}_{q=0}^\dagger \right)^{(\nu-n) \times L} |0\rangle$). Realizing a state that is similar to a combination of the two and can be difficult to realize the underlying state ($|\Psi_o\rangle \sim |MI_n\rangle \otimes |SF_{(n-\nu) \times L}\rangle$). However, in *most* ultracold atom experiments, such a potential is not used. Instead, the varying trap potential can be approximated as a slowly varying chemical potential (known as the local density approximation) and spatially redistributes atoms to form true integer filling Mott plateaus in a canonical “wedding cake” structure (Fig. 1.7b) with superfluid regions living between the Mott-insulating layers of the “cake”. This is more thoroughly described in these two theses^{66,149}.

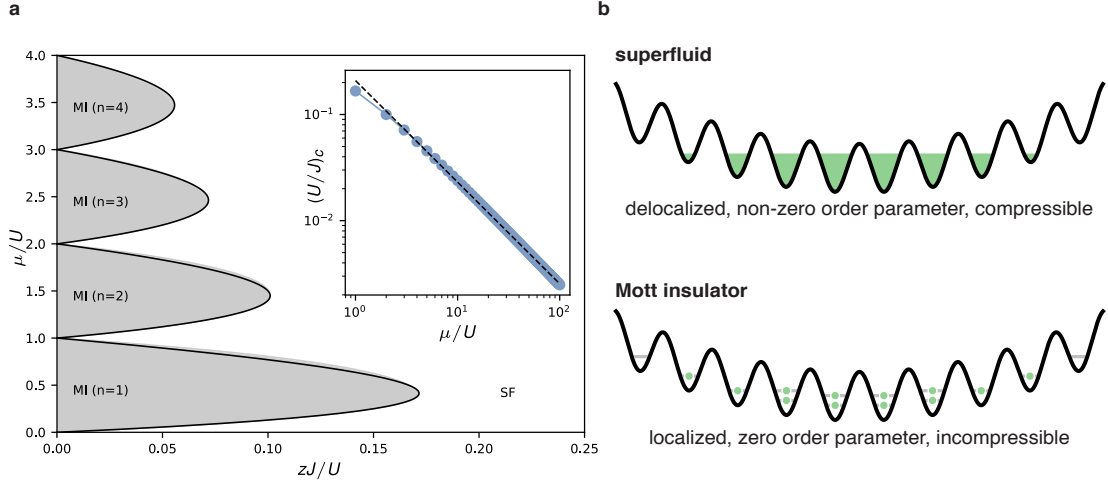


Figure 1.7: Mean-field phase diagram. a) The mean-field phase diagram is shown here for the break down of the superfluid phase into the Mott-insulating lobes (gray) as a function of J/U and μ/U . The coordination number, z , corresponds to the number of neighboring sites in a system and in this way accounts for dimensionality. This phase diagram works relatively well for ≥ 2 spatial dimensions. The inset is a plot of the scaling of the peak of the Mott lobes as a function of μ/U and demonstrates its suppression with increase in filling ν^{-1} . b) These illustrations demonstrate the qualitative features of the regimes of this phase diagram: i) a superfluid regime which is described by delocalized particles, gapless excitations (for dimensionality ≥ 2), and non-zero order parameter and ii) a Mott-insulating regime where the particles are localized by inter-particle interactions, the order parameter is zero, and the state contains a finite gap.

second-order phase transition and therefore can be described by the traditional approach *a la* Landau¹⁰⁹.

The mean-field phase diagram is plotted in Fig. 1.7 with axes given by the relative chemical potential μ/U and relative tunneling strength zJ/U where z is the coordination number, the number of neighbors to each lattice site, which is linear with the physical dimensionality in a square lattice ($z = 2 \times D$, where D is the dimensionality). The lobes on the left plot of Fig. 1.7 define plateaus of a given atom number which become smaller, or experimentally more fragile, as a function of on-site occupation number.

It can be seen intuitively that the critical, finite value of U/J_c depends on the on-site occupation

number by comparing the kinetic energy scales to the gap in the system. We first start in a Mott-insulating plateau $|\Psi_{MI}\rangle$ with n atoms per site which has a total energy of $E_0 = L \cdot \frac{U}{2}n(n - 1)$. The first excitation from this state involves moving an atom from site i to its neighbor and has a total energy of $E_1 = (L - 2) \cdot \frac{U}{2}n(n - 1) + \frac{U}{2}(n + 1)(n) + \frac{U}{2}(n - 1)(n - 2)$. The gap between these two states is given by $\Delta = E_1 - E_0 = U$ and notably is independent of the on-site occupation number n_i . Since the atoms are bosonic and identical, the kinetic energy term J that connects these two states has a bosonic enhancement factor of $\sim n$ and means that the relevant comparison for distinguishing these two phases is $(U/J)_c \propto U/(nJ)$. The peaks of the lobes in Fig. 1.7 and are plotted as a function of half integer chemical potential in the inset and agree with a power law exponent n^{-1} .

1.4 DISCUSSION: BEYOND TIGHT-BINDING BOSE-HUBBARD

The derivations of the chapter encompass the simplest incarnation of physics relating to a solid state physics system. We derived how a single-particle is diagonalized within a rather simple, but very physically relevant sinusoidal lattice. Incorporating more complex lattice geometries is conceptually the same but can lead to subtle changes in the band structure such as a honeycomb lattice which harbors Dirac points⁶².

Additionally, even within the currently studied model, when not residing deep in the tight-binding limit, one needs to include the hopping terms to non-nearest neighboring sites to accurately describe the observed physics in the lattice^{149,151} (§2.4.2). In the case of relatively strong inter-particle

interactions, energy shifts from high on-site occupancy can induce hybridization with higher bands and create anharmonic, on-site occupation number dependent changes in the interaction energy¹²¹.

The presence of significant on-site, or inter-site potential deviations from disorder in the optical potential can additionally modify the canonical Bose-Hubbard parameters considered earlier. While the predominant deviation comes in directly as on-site energy offsets, h_i , the fractional change to the lattice depth between sites will also create a distribution of J_i values, and the fractional change to local site curvature will incur small changes of the interaction strength U_i . This is systematically explored for an optical speckle disorder in *White, et al.*¹⁸⁹. Later in this thesis, we will also apply an engineered on-site potential distribution derived from a quasi-periodic potential with respect to the physics lattice. We found that the variation in Bose-Hubbard parameters in this regime were negligible other than the on-site offsets h_i (§5).

Lastly, several experimental groups have moved on to atoms from the lanthanide group that host a large number of useful internal states and additionally harbor a strong dipolar magnetic moment that is $\approx 10\times$ larger than that of standard alkali atoms. These magnetic atoms admit a whole host of interesting quantum phases within optical lattice systems and can be included in the Bose-Hubbard model as additional terms. This construction has been termed the extended Bose-Hubbard model with some recent theoretical interest and experimental progress^{50,14}.

It is hard for me to empathize with an atom.

Dr. M. Eric Tai

2

Quantum gas microscope: an overview

All experiments presented in this thesis are performed using an apparatus designed in a quantum gas microscope architecture for bosonic atoms.* We conduct all experiments with a degenerate,

*Traditional microscope naming conventions typically refer to the method by which they probe the phenomena of interest (i.e. *optical* microscopy, *electron* microscopy). Although this microscope may seem

quantum gas of ^{87}Rb atoms in either one or two spatial dimensions by confining the atoms to a single-plane in a three-dimensional optical lattice. This single-plane of ultracold atoms lies at the focus of an imaging system with a high numerical aperture (NA) of 0.8. The occupation of these lattice sites can be read out with single-site resolution via an in-situ fluorescence imaging technique. A far more detailed description of this apparatus is provided in a number of other theses and publications^{63,142,16,121,149,194,180,117} and only the core components necessary to explain the successive work of this thesis will be explained here.

While all ultracold atom machines are an amalgamation of many parts that collectively record the successes of atomic physics for the past several decades, the schematic in Fig. 2.1 only represents the latest addition and the heart of the microscopic access in this experimental apparatus. This schematic shows the high-NA imaging objective that sits outside an evacuated glass cell in which the degenerate quantum gas is formed. The custom objective that sits outside the glass cell has an NA \approx 0.55. The in-vacuum hemispherical lens is made of fused silica with a refractive index of $n = 1.45$ and increases the combined NA to ≈ 0.8 . We create a Bose-Einstein condensate (BEC) of ^{87}Rb by conventional evaporation in a magnetic trap in the glass cell. The BEC is then transported to the focus of this imaging system which is $\approx 10\mu\text{m}$ below the bottom surface of the hemisphere. The z -confining lattices enter into the glass cell from the sides while the x - y plane lattices are projected through the objective itself (Fig. 2.2). The occupations of the lattice sites are imaged onto an

dissimilar to this naming convention, an important point of this apparatus is that it is using the quantum properties of the degenerate atomic gas to probe physics that is harbored by Hamiltonians of interest. While I do not think this name was intentionally chosen to reflect this approach, I think it is a surprisingly appropriate/accurate description.

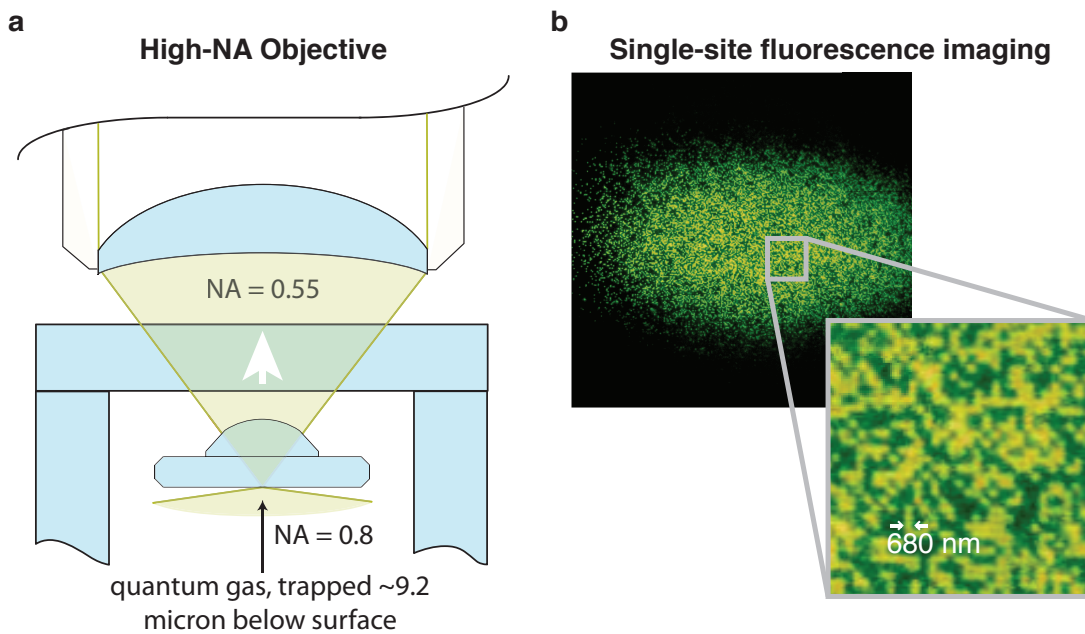


Figure 2.1: Schematic of microscope objective, glass cell, and imaging. **a)** The heart of the quantum gas microscope revolves around the combined high-NA (0.8) microscope objective built constructed from an out of vacuum objective (0.55 NA) and an in-vacuum hemispherical lens. The gas is trapped in a single plane of an optical lattice approximately $9.2\mu\text{m}$ below a super-polished glass substrate. This substrate and all surrounding glass cell surfaces have no optical coatings. **b)** This example of a single-site fluorescence image of the atoms in the optical lattice displays the size of the atomic cloud that can be seen by the camera with its current magnification. The zoomed in inset demonstrates the ability to resolve the occupation of single lattice sites. Their approximate spacing is given by the lattice constant $a \sim 680\text{nm}$.

EMCCD camera (Ixon X-3313) using fluorescence imaging from polarization gradient cooling via optical molasses beams. These two paths are the two generic options for optical access to the atoms and all other beams are combined onto these paths by either beam-splitters or dichroic filters.

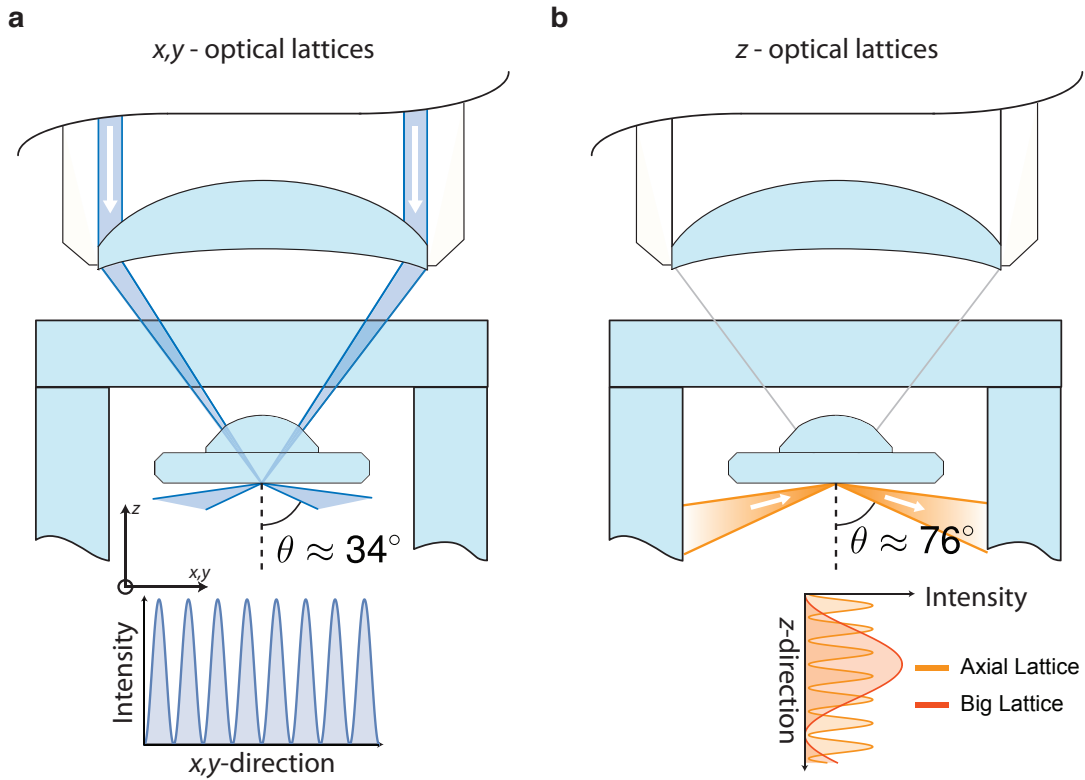


Figure 2.2: Optical lattices and optical access. a) The x , y -optical lattices are projected onto the atoms through the microscope objective. Both directions, x and y , are imaged onto the atoms from their own separate phase holograms. Since these beams are not generated by retro-reflection, both their wavelength ($\lambda \approx 758\text{nm}$) and their angle of incidence $\theta \approx 34^\circ$ determine the lattice spacing $a \approx 680\text{nm}$. b) The z -confining lattice is produced by reflecting a single beam off the bottom of the super-polished substrate at a steep angle. Since the beam is not retro-reflected, it only produces a standing wave along the z -direction. There are actually two different lattice spacings created in this configuration by changing the angle of incidence. The large spacing lattice, termed the “big” lattice, has a spacing of $\approx 9.2\mu\text{m}$ to match the magnetic trap position holding the BEC. This BEC is then compressed by turning on the tighter lattice, termed the “axial” lattice which has a spacing of $\approx 1.5\mu\text{m}$. All the optical lattice potentials in this setup are produced by spectrally broad light ($\approx 3\text{nm}$). This is possible for the x , y -lattices since they are imaged onto the atoms. The z -lattices still have relatively high contrast due to the high-reflection coefficient at such steep angles and since the lattice planes are well within the coherence length ($\approx 100\mu\text{m}$).

2.1 OPTICAL LATTICE POTENTIALS

The dominant potential landscape experienced by the atoms is defined by optical lattices in three dimensions. The atoms are loaded from the BEC in a magnetic trap into a single two-dimension plane

by being confined by a single node of a vertical (z -direction) lattice. All studied physics relating to the Bose-Hubbard model derived in the previous chapter is restricted to within this two-dimension plane (x, y -directions). All lattices are formed by interfering two beams along a given axis which produces a square lattice in all directions with a sinusoidal shape.

Nearly all optical potentials in the setup are regulated by sampling the beam intensity with a photodiode with a logarithmic amplifier (AD8304) which is set to $\sim 0.5\text{V}/\text{decade}$. This has two important effects in the system: i) the logarithmic amplification of the photodiode signal provides a wide dynamic range which is useful for alignment procedures, and ii) that all optical intensity ramps shown in any of the documented experimental sequences refer to how this photodiode voltage is changed. This means that a “linear” ramp seen by the PID that regulates the optical power in a beam to the photodiode output results in an exponential ramp seen by the atoms. This is compensated in some sequences by logarithmic ramps, although often such an exponential ramp is desirable since the most sensitive Bose-Hubbard parameter, the tunneling element J , also scales exponentially with the lattice depth.

2.1.1 z -LATTICES

The loading of the BEC into a single node of the z -confining lattices is performed by a two-step process and requires two different z -lattices. Both of these lattices are generated from a single beam that is reflected off the uncoated, flat surface of the hemispherical, in-vacuum lens as shown in Fig. 2.2.

The first step comes from a beam illuminating this surface from a very shallow angle and forms a large spacing lattice with a lattice constant of $\approx 9.2\mu\text{m}$ which corresponds to a recoil energy $E_r \approx$

$2\pi \times 7\text{Hz}$. This large spacing lattice is denoted as the “big” lattice. The atoms are loaded into the 1^{st} minimum of the lattice away from the surface of the glass surface, which provides the reference for defining all z -positions in the apparatus. While this bottom surface is uncoated, the angle is sufficiently shallow ($\approx 88^\circ$ from normal) such that the Fresnel intensity reflection coefficient is reasonably large ($R_s \approx 0.85$). This reflection coefficient produces a lattice with a contrast $\left(\frac{2\sqrt{R_s}}{1+R_s}\right)$ of ≈ 0.997 . This means that for a measured lattice depth of V_o^{big} , the corresponding DC offset will be $\approx 0.002 \times V_o^{big}$.

The second step involves a hand-off with a second beam that illuminates the surface from the opposite direction at a less shallow angle ($\approx 75.6^\circ$) to produce a lattice with a smaller lattice constant of $\approx 1.5\mu\text{m}$ which corresponds to a recoil energy $E_r \approx 2\pi \times 255\text{Hz}$. This smaller spacing lattice is denoted as the “axial” lattice. The atoms lie in the 6^{th} minimum of this lattice which overlaps with 1^{st} minimum of the “big” lattice. The uncoated surface has a more detrimental effect at this illumination angle where the Fresnel intensity reflection coefficient is significantly smaller ($R_s \approx 0.39$). However, since the beam interferes with itself upon reflection, the interference contrast still remains relatively high at ≈ 0.90 . This means for a measured lattice depth of V_o^{axial} , the corresponding DC offset will be $\approx 0.056 \times V_o^{axial}$. The angle dependencies of both of these parameters, minimum offset and contrast, are plotted in Fig. 2.3.

Both of these z -confining lattices are generated from an amplified Superluminescent Light Emitting Diode (SLED) source (EXALOS® EXS210025-01) centered at $\lambda \approx 755\text{nm}$. The bandwidth of this light is relatively wide $\approx 3\text{nm}$ such that the light is approximately temporally *incoherent*. The corresponding coherence length is $\approx 100\mu\text{m}$ which is much longer than the z -lattice spacing

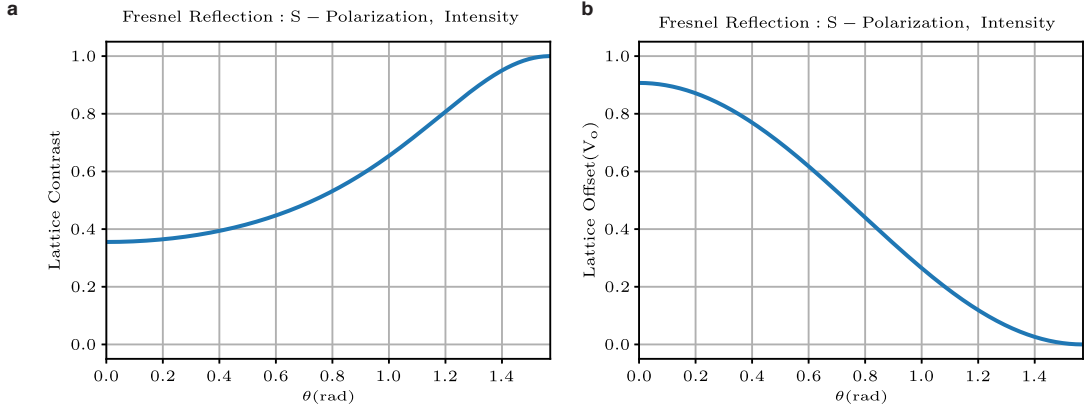


Figure 2.3: Lattice parameters vs. angle. a) The lattice contrast, $\left(\frac{2\sqrt{R_s}}{1+R_s}\right)$, plotted as a function of angle of incidence for a beam reflecting off an uncoated glass surface. The reflection coefficient is derived from the Fresnel reflection coefficient defined for intensity R_s . b) The potential energy offset incurred by non-unity reflection of a beam off an uncoated glass surface as a function of the angle of incidence. The offset is plotted as a fraction of the lattice depth seen by the atoms.

and allows for relatively high-contrast interference quoted above. This short coherence length, while allowing the creation of a high contrast lattice at the length scales of interest, prevents interference of any of the conservative potential beams with one another or with unwanted reflections from surfaces more than $100\mu\text{m}$ away.

2.1.2 x, y -LATTICES

In the $x-y$ plane, the lattices are imaged onto the atoms from a holographic mask through the objective (Fig. 2.2). The spacing of this lattice is $\approx 680\text{nm}$ which corresponds to a recoil energy $E_r \approx 2\pi \times 1240\text{Hz}$. The holographic mask is a phase hologram that imprints a square wave of alternating 0 and π phase onto the profile of the illuminating beam^{63,142}. This phase profile onto the beam nearly eliminates the 0^{th} order of the light emanating from the hologram in the far field

and only the ± 1 orders are imaged on to the atoms. This produces a sinusoidal lattice with relatively high contrast since the imaging condition is well met by the microscope and optical setup. However, it additionally means that any unwanted artifacts (e.g. dust on the hologram) is additionally imaged onto the atom potential and creates local disorder. To alleviate some of this disorder, the beams are spatially filtered in the Fourier plane of the imaging system¹⁴².

The same SLED source used to produce the z -confining lattices is also used to produce these lattices in the x - y plane. Since the lattices are imaged onto the atoms, a more temporally incoherent source could, in principle, be used.

2.1.3 DISORDER (UNINTENTIONAL) AND HEATING RATES

The use of temporally incoherent light alleviates the contribution of stray reflections to unwanted interference, and hence unwanted disorder, in the system. However, since the lattices themselves are imaged from a holographic mask onto the atoms, the fidelity of the lattice potentials is very sensitive to local scatters in the image plane of the imaging system. There are two approaches to alleviate this problem: spatial filtering of the lattice beams in the Fourier plane of the system (currently implemented), or the illumination of the mask with spatially incoherent light that would average out any local scatterer.

Within the context of a faithful realization of the Bose-Hubbard model, the dominant effect from this disorder corresponds to a modulation in the on-site potential height h_i in the tight-binding limit. However, the choice of blue- or red-detuned lattices affect the relationship of h_i to the actual intensity of the scattered beam. In the case of red-detuned lattices, the atoms reside at the intensity

maxima which means that, in the tight-binding limit, the on-site potential contains both the lattice depth $-V_o$ and the zero-point energy $\propto V_o^{1/2} \propto \hbar\omega_{ho}/2$. In a blue-detuned lattice, the atoms reside at the intensity minima and hence are sensitive to only the zero-point energy shift $\propto V_o^{1/2}$. The light used to produce the lattice potentials in the experiment has a center frequency of $\lambda = 755\text{nm}$ which is far blue-detuned from atomic resonances of $\lambda_{D1} = 795\text{nm}$ and $\lambda_{D2} = 780\text{nm}$.

The other relevant consideration for the faithful realization of the Bose-Hubbard model in optical lattices depends on residual spontaneous scattering of light from the lattices by the atoms. This light will necessarily impart some kinetic energy onto the atom and begin to populate higher bands in the lattice. This may appear, at first glance, to not be a significant issue in the case of a blue-detuned lattice since the atoms sit at the intensity minima where there is no light to scatter. While the scattering rate is indeed significantly different for the blue- and red-detuned cases, the “heating” rate (rate at which atomic population is moved to higher bands) is not necessarily different¹⁴⁴. This result of equivalent “heating” for both blue- and red-detuned lattices corresponds only to the increase in average energy for an atom. However, as shown in *Pichler et al.*, this does not reflect the increase in entropy related to the dephasing of a many-body state evolving under the Bose-Hubbard model¹⁴⁴. This will become the metric of interest and therefore the scattering rate is the more appropriate quantity for comparing between lattice detunings (Fig. 2.4).

We compare several methods for calculating the spontaneous scattering rate in the lattice. The first estimate that will be considered follows an assumption of deep lattices and being deep within the Lamb-Dicke regime^{68,144}. By including the Lamb-Dicke parameter, $\eta^2 = (4V_o/E_r)^{-1/2}$, the

estimated heating rate for deep lattices becomes:

$$\gamma = E_r \frac{\Gamma}{2\Delta} \left(\frac{V_o}{E_r} \right)^{1/2} \quad (2.1)$$

where Γ is the linewidth of the D₂ transition in ⁸⁷Rb (nearest resonance for the blue lattice), Δ is the detuning of the lattice light from the D₂ transition, and E_r is the lattice recoil energy. In the case of the *x-y* lattices, which should have no appreciable offset, this will become a good estimate of the spontaneous scattering rate as shown in Fig. 2.4. However, it is a poor description of the spontaneous scattering rate with an offset and so we take a more general approach that accounts for these DC potential offsets (2.2).

$$\gamma = E_r \frac{\Gamma}{\Delta} \int dx (V_{latt}(x) + V_{offset}) |\psi(x)|^2 \quad (2.2)$$

where the considered $\psi(x)$ is either the Wannier wave functions, $w_n(x)$, or the Harmonic oscillator wave functions. These more accurate estimates from (2.2) are plotted in Fig. 2.4. The relevant lattice depths are: $\approx 2 - 45E_r^{x,y}$ for the *x, y* lattices, $\approx 40 - 250E_r^{axial}$ for the axial lattice, and $\approx 3,000 - 20,000E_r^{big}$ for the big lattice.

In the case of choosing laser parameters to make optical lattices, a natural comparison for the red and blue detuned lattices can be made in the deep-lattice limit when the Lamb-Dicke regime is reached. The relationship finds the necessary detuning in a red-detuned lattice for the same scattering rate of a given blue-detuned lattice depth (given by Lamb-Dicke parameter η^2) and detuning

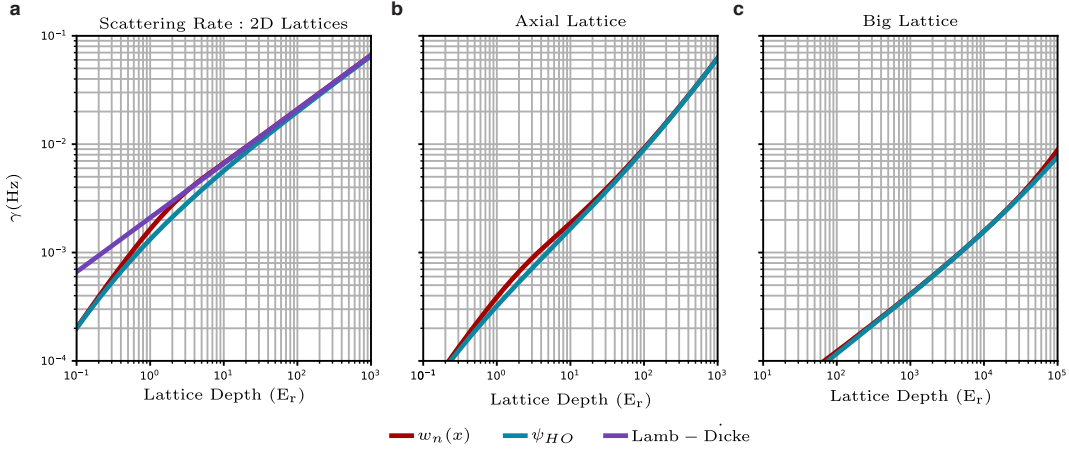


Figure 2.4: Spontaneous scattering rate from optical lattices. **a)** The optical lattices that provide the confinement in the x , y directions have a negligible offset and can be compared in three regimes: the Harmonic oscillator wave function overlap (blue), the Wannier wave function overlap (orange), and the Lamb-Dicke approximation (green). The relevant parameter range for the physics contained in this thesis ranges from $\approx 2 - 45E_r^{x,y}$. **b)** The spontaneous scattering from the “axial” lattice differs from the naive Lamb-Dicke expectation due to the residual offset from imperfect reflection. The relevant parameter regime for this thesis is $\approx 40 - 250E_r^{axial}$. **c)** The spontaneous scattering from the “big” lattice differs from the naive Lamb-Dicke expectation due to the residual offset from imperfect reflection. The relevant parameter regime for this thesis is $\approx 3,000 - 20,000E_r^{big}$.

(Δ_B) :

$$\Delta_R = \Delta_B(1 + \eta^2)/\eta^2 = \Delta_B \left(1 + \left(\frac{4V_o}{E_r} \right)^{1/2} \right) \quad (2.3)$$

In short, (2.3) shows that a red-detuned lattice needs to be $\approx (1 + 2\sqrt{V_o/E_r}) \times$ more detuned than a blue-detuned lattice to obtain the same spontaneous scattering rate at a given lattice depth. While red-detuned lattices have some benefits in terms of being globally confining as an optical trap, they are often worse in terms of scattering and decoherence of the atomic system.

2.2 ARBITRARY POTENTIAL GENERATION

The ability to realize interacting, many-body systems at ultracold temperatures in optical lattices has been the work horse of atomic gases and allows the observation of exotic physics such as the superfluid to Mott-insulator transition^{67,25,24}. The addition of a microscope to these systems enables single-site resolution and microscopic access to the lattice sites in the system. Not only can this be used for imaging of the atoms to determine which lattice sites are occupied, but by symmetry enables the microscope to be used in reverse to project local optical potentials on the order of a lattice site.

Using this capability for single-site optical potential projection has enabled a series of pioneering experiments that allow Hamiltonian engineering on top of the bare Bose-Hubbard model. This is implemented in our apparatus via a Digital Micromirror Device (DMD) that is located in the Fourier plane of our imaging system. Even though the DMD only provides a binary mask for projecting patterns onto the atoms, the fact that it is in the Fourier plane enables finer resolution for single-site features that are spread out across a significant portion of the DMD. Only a brief description of this setup will be mentioned here such that it provides context for how it is used in the successive experiments detailed in this thesis. A more detailed description of this setup can be found in the cited articles and theses^{195,149,194,117}.

The DMD is illuminated with a laser that is blue-detuned from the D₁ and D₂ transitions with a center wavelength $\lambda_{DMD} = 765$ nm. By placing the DMD in the Fourier plane of the imaging system, all desired potentials must be programmed as the Fourier transform of the desired potential at

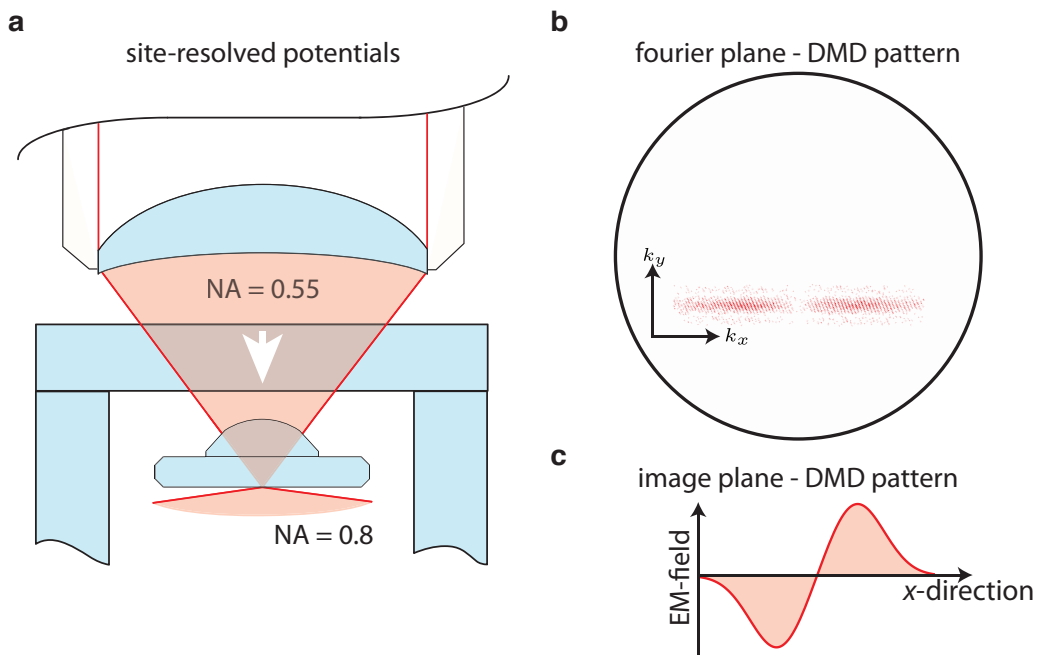


Figure 2.5: Schematic of the DMD. a) This schematic simply demonstrates that the arbitrary potentials created in the Fourier plane of the imaging system by the DMD are imaged through the microscope objective. b) This is an example of a binarized mask that is displayed by the DMD (red pixels). The underlying grating can be seen by the diagonal stripes that live within the envelope of the pattern. This pattern makes a Hermite Gaussian along one-direction (x -direction) and an approximate rectangular envelope along the orthogonal direction (y -direction). c) The field of the laser is what the DMD determines by the displayed binarized pattern. Here is an illustration of a through-cut of the Hermite Gaussian described in its field (rather than intensity) at the image plane where the atoms reside. Note that the atoms themselves will respond to the intensity of this pattern for all intents and purposes. This provides some degrees of freedom when actually designing a desired local potential to display on the atoms.

the atom plane. Additionally, the potential generation on the DMD incorporates a secondary grating in the projection that allows for both amplitude and phase control of the light. Since it is really the *field** of the light that is tunable with the DMD, the patterns produced can be pre-compensated for aberrations in the imaging system such that the desired potentials are produced to a high fidelity. Aberrations in this system can be reduced to $\approx \lambda/10$ at the atom plane^{194,117}.

*Meaning both amplitude and phase.

2.2.1 DISORDER (INTENTIONAL)

The DMD is used for two primary functions for the experiments in this thesis: 1) wall-like potentials that act to isolate sections of the optical lattices and 2) the generation of local, tunable “disorder” for the realization of localized states in the Bose-Hubbard model. For all experiments in this thesis the applied potential used to localize the wave functions is sampled from a quasi-periodic distribution of on-site potentials and will be discussed in §5.

2.3 IMAGING AND READOUT

At the end of every experimental sequence, the atoms are imaged via fluorescence imaging by optical molasses beams. The recoil of this near-resonant light necessarily and significantly excites the atoms to higher-bands in the optical lattice. Even though the optical molasses light provides polarization gradient cooling to the photon recoil limit, the average energy of the atoms would not remain trapped very long in the far from resonant lattices used for studying Bose-Hubbard model physics. To keep the atoms trapped to a single lattice site during imaging we use near-resonant lattices that are blue-detuned by ≈ 55 GHz from the $\lambda_{D1} = 795$ nm transition. The depth of this “imaging” or “pinning” lattice is $\approx 5000 E_r$.

During the fluorescence imaging process, an additional complication occurs for multiply occupied sites. The absorption of a photon by the atom leads to the formation of an electron dipole moment with the excited state. This, in turn, induces a dipole in a nearby atom on the same lattice site such that they form an attractive molecular potential and causes the atoms to gain kinetic energy

via their mutual attraction. However, the excited state will then rapidly decay and leave both atoms with enough energy to escape even the deep imaging lattice; a phenomenon that is known as photo-assisted collisions^{46,15}.* Importantly, this results in pair-wise loss of atoms from a lattice site during imaging such that only the parity of the on-site occupation number is imaged and is colloquially referred to as “parity projection.”

This parity projection imaging can be circumvented for one-dimensional slices of the lattice by using the DMD. The DMD is used to create two wall-like potentials that isolated a single row or column of the lattice. The corresponding lattice is then reduced in depth such that all other atoms outside of this isolated tube escape the system. Then the atoms within the isolated tube are expanded along the orthogonal direction for a brief time such that they are very spread out over the orthogonal direction during the imaging sequence⁹⁹. This makes it very unlikely, in a probabilistic sense, for the atoms to occupy the same site and be ejected from the lattice due to the photo-assisted collisions. This expansion allows for on-site occupation number resolution. For a one-dimensional, many-body wave function this amounts to a projective measurement onto the particle number basis or Fock basis.

This resolution of the on-site number distribution enables several important key features for probing quantum many-body systems. It enables readout of the entire diagonal of the full system’s density matrix which allows for probing correlations within this basis. It also enables higher-fidelity

*Note that this effective 3-body interaction is what allows for the photon to impart such a significant amount of energy into the atoms as kinetic energy. In a 2-body scattering event between the atom and the photon, the atom only receives only a recoil of energy from the photon changing momentum, but not wavelength.

state readout in two ways: i) during the imaging process there is a finite probability in a densely occupied lattice, that an atom hops to a neighboring site which can result in photo-assisted collisions and appears as two “holes” in the image that are artifacts of the imaging and not the physics being probed, and ii) it also enables post selection on total atom number which becomes paramount to quantifying atom loss during the experimental sequence. The latter is an essential tool for reducing the heating that contributes to measurements in the experiments described later on in this thesis.

2.4 CALIBRATION OF ENERGY SCALES

The ability to accurately determine all experimental parameters in the system is an invaluable benefit that contributes to the precision of the results generated by this experiment. I have briefly described several of the standard calibration steps that were used ubiquitously throughout this thesis to accurately determine Bose-Hubbard parameters for conducting experiments and will not be described otherwise. Additionally, many of these methods are built upon previous results using the apparatus and in some cases are thoroughly detailed in those publications, which will be cited in the appropriate locations.

2.4.1 LATTICE DEPTH: KAPITZA-DIRAC SCATTERING

A particularly efficient method to calibrate the lattice depth experienced by the atoms is via Kapitza-Dirac scattering^{106,137,179,70,59}. This method requires that the atoms have Bose-condensed so that their many-body wave function has a well defined phase across the entire cloud. The lattice is then

turned on very diabatically* and illuminates the atoms for a tunable, but brief time period. This brief illumination of the atoms is such that the atoms only experience a potential that evolve the local phase of their wave function but the atoms have not had time to move yet. The imprinted phase on the atoms has a spatial structure that is proportional to the lattice potential and can be probed easily via common time of flight measurements which map the spatial Fourier components, or wavevectors of the wave function, to momentum.

This mapping of the imprinted spatial phase on the BEC to momentum has a convenient and clean analytical form that results from the spatial phase always being commensurate with periodicity of the lattice. This results in the atomic momentum only existing at integer multiples of the lattice wavevector. The population in these integer multiples then follows the analytic form given by:

$$P_{|\nu|}(t) = \left| J_\nu \left(\pi E_r \frac{V_o}{E_r} t \right) \right|^2 \quad (2.4)$$

where J_ν is the Bessel function of the 1st kind, ν denotes the integer of the lattice vector and the order of the Bessel function, V_o is the lattice depth in Hz, E_r denotes the recoil energy of the lattice, and t is the time the atoms have evolved in the presence of the lattice. The evolution of the population into these modes is shown as a function of time in Fig. 2.6. As can be seen in this figure, the dynamics stop following the predicted evolution due to the presence of the additional trap confinement and that the wave function will also begin to redistribute atomic population in the presence of this lattice on the order of the lattice-site trap frequency ω_{Latt} .

*This means the new Hamiltonian is turned on significantly faster than all the inverse energy scales in the system such the wave function itself has not evolved during the turn on time.

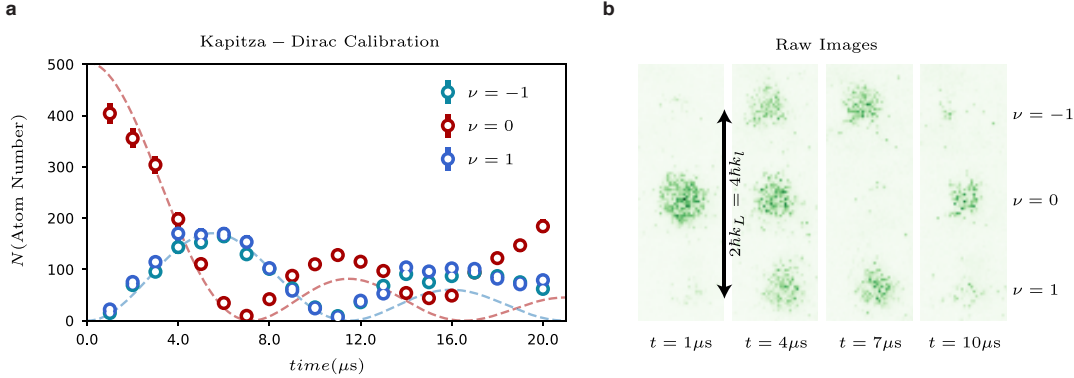


Figure 2.6: Kapitza-Dirac scattering. **a)** The plotted points denote the total atom number in the various time-of-flight peaks that are separated by integer numbers of the lattice wavevector: $\nu = 0$ (red), $\nu = \pm 1$ (light/dark blue). The dashed lines are the fitted, analytic forms up to $\approx 10\mu\text{s}$. **b)** Example of the raw, in-situ atom images before being processed.

2.4.2 TUNNELING J : SINGLE-ATOM QUANTUM WALKS

The tunneling matrix element (tunneling strength), J , can be calibrated from the quantum walk of single atoms in one-dimensional lattices. This protocol involves first isolating a single-atom at a particular site per one-dimensional lattice. These dynamics have been explored extensively in a number of publications^{74,108,3,124,149} and are of significant interest in their own right. While the tunneling strength and the lattice depth have a well defined theoretical relationship that could make this calibration seem redundant, practically speaking this method provides a far more accurate estimate of the local tunneling strength.* The analytic form is quite similar to the Kapitza-Dirac scattering form. The physics of the quantum walk is, in a sense, exactly complimentary to Kapitza-Dirac scattering.

*This is partially due to some of the systematic biases in the lattice depth calibration that uses Kapitza-Dirac scattering that limit the precision of the measurement. However, the other issue is that the optical lattices used in this apparatus have local variation in disorder that can locally modify the tunneling strength J . Since the vast majority of experiments in this system work with appreciably large-lattice depths and small systems, this is a significant consideration for calibrating experimental parameters.

A single-particle which is localized in real space (completely delocalized in k-space) is evolved forward in time by unitary evolution of a new quenched Hamiltonian which has a cosine dispersion curve in k-space (real space). This necessarily realizes the same analytic result for the population of the different reciprocal orders in real space, which are now lattice sites:

$$P_{|\nu|}(t) = |\mathcal{J}_\nu(2 \times 2\pi J t)|^2 \quad (2.5)$$

where \mathcal{J}_ν is the Bessel function of the 1st kind, ν denotes the integer lattice sites away from the origin and the order of the Bessel function, and J is the tunneling strength. There is an additional formulation that includes the possibility for local potential gradients that can provide a better fit and is the corresponding form for what are known as Bloch oscillations:

$$P_{|\nu|}(t) = \left| \mathcal{J}_\nu \left(\frac{2J}{\pi E} \sin(\pi E t / h) \right) \right|^2 \quad (2.6)$$

where E is the local potential gradient. For a given evolution time t , a corresponding lattice size can be fit where $|\nu| \leq L/(2\pi J)$. * These fits and averaged site-occupation data are shown in Fig. 2.7. Note that at very low-lattice depths, the tight-binding, nearest-neighbor coupled Bose-Hubbard model becomes a less accurate description of the physics in the lattice and hence higher-order tunneling terms become significant. The deviation, both theoretical and measured, is shown in Fig. 2.7.

*This bound is determined by the Lieb-Robinson velocity, which for a single-atom in a lattice is determined by the steepest slope (maximum group velocity) of its corresponding band.

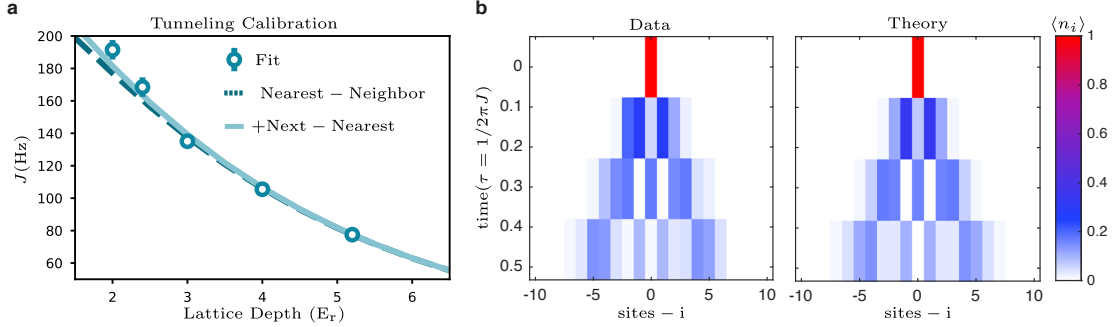


Figure 2.7: Quantum Walk Calibration. a) The calibrated tunneling strength J are plotted as the blue points for various measure lattice depths by fitting the time evolution of the particle's wave function to the analytical form (2.5) The analytical result for the nearest-neighbor tunneling strength J as a function of lattice depth is plotted as the dashed black line. The orange line describes the expected deviation of the calibration fits to the data based upon the contributions of higher-order tunneling terms that include tunneling beyond nearest neighbors. b) The raw data is shown as a function of time and lattice site index i for a $5.2 E_r$ deep lattice. The analytical dynamics that fits best to it is shown on the right.

2.4.3 INTERACTION U AND LINEAR TILT E : PHOTON-ASSISTED TUNNELING

Determining the on-site interaction strength U and local potential variation from local disorder can be determined from a single protocol that utilizes photon-assisted tunneling¹²². This method first starts deep in a Mott-insulating regime where there is exactly an integer number of atoms per lattice site. Then a potential gradient is applied to the system such that it increases the on-site potential energy by E Hz/site such that is larger than the interaction energy U . Then the lattice depth is lowered to intermediate lattice depth $\approx 15E_r$ where the tunneling J is still much smaller than U or E . The lattice depth is then sinusoidally modulated at small amplitudes at various frequencies to restore tunneling between the sites that are currently far away from resonance. When the frequency matches the energy difference between two sites, it restores tunneling and appears as strong on-site fluctuations away from the Mott-insulating state.

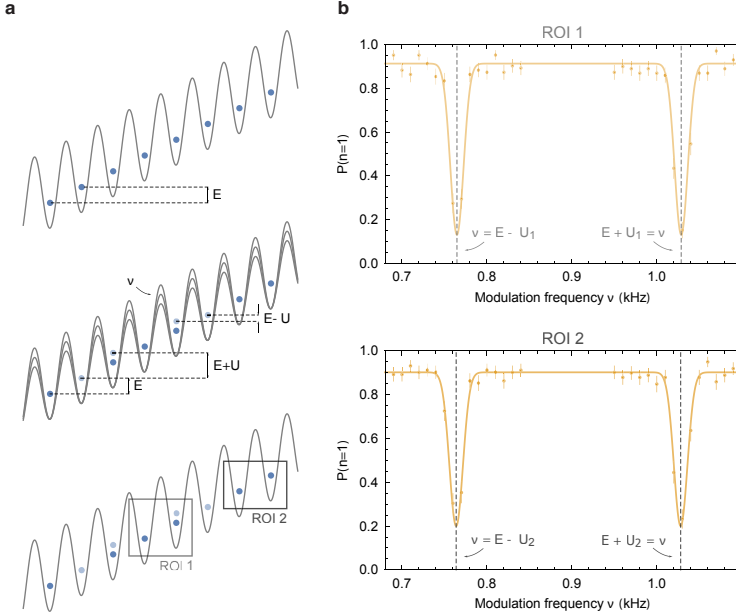


Figure 2.8: Protocol for modulation spectroscopy. a) This illustration describes the protocol for this tilt and modulation experiment. By analyzing the system by local regions of interest (ROIs), not only can the global interaction strength be measured, but also the local variation in on-site potential offsets. b) Two potential ROIs are plotted as a function of the modulation frequency and the measured on-site occupancy between neighboring sites. The solid lines are fits from a two Gaussian model to extract the resonance frequencies.

There is a useful asymmetry in this protocol due to the on-site interactions. In the regime where $E > U$, the energy difference for an atom to hop to neighboring sites will cost either $E + U$ or $E - U$ energy depending upon the direction of increasing gradient potential. This means that by measuring out both resonance conditions both E and U can be calibrated locally. This is demonstrated in Fig. 2.9 where the two resonances are measured, and the variance of the tilt E and the interaction U across the measured region reveal residual on-site disorder and on-site curvature.

While the tilt E here is described as purely a part of a process that is necessary to suppress tunneling such that U and on-site differences can be measured, the tilt itself is also sometimes the quantity of interest. In some experimental schemes that implement synthetic magnetic fields in ultracold atom experiments, a potential gradient is used to suppress the bare, resonant tunneling in the lattice J along one direction which is then restored with a spatially varying phase. This has been explored

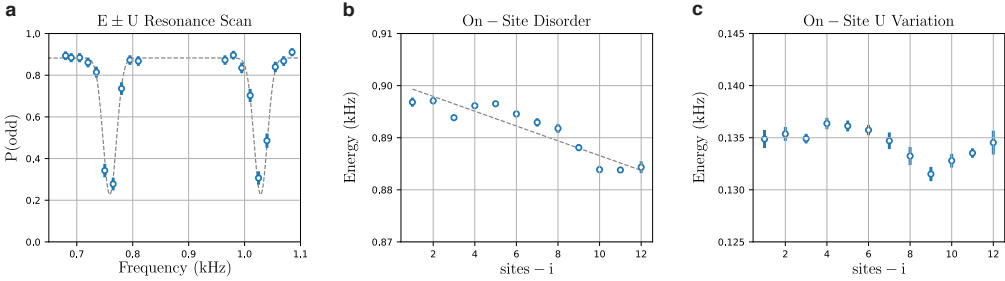


Figure 2.9: Calibration of interaction (U), tilt (E), and variation in on-site potential (h_i). **a)** The same ROI plot as shown in Fig. 2.8 is demonstrated for a system with the interaction strength defined by the z -confinement derived from the “big” lattice. **b)** Variation of tilt as a function of the lattice site of interest. The linear fit here suggests a residual curvature of the on-site lattice offsets since it is the derivative of the on-site potential offset profile that is measured by this protocol. **c)** Variation of interaction as a function of lattice site index. Note that this varies only on the order of 1 Hz since it is effect by the on-site variation in curvature.

in several cold atom experiments in real space^{4,128} and was implemented in this system to probe the Harper-Hofstadter model¹⁸¹ and is described in significant detail in the cited thesis¹⁸⁰.

2.4.4 ON-SITE POTENTIAL OFFSETS h_i : ADIABATIC TRANSFER

The generation of single-site resolved potentials h_i are created via the DMD installed in the apparatus and are used extensively for state initialization and site-occupation readout during imaging. In both of these cases, the absolute depth of the potentials used is not particularly important since both procedures are relatively insensitive to them. However, some of the experiments in this thesis rely on a particular relationship of the on-site potential offsets h_i , to both the tunneling strength J and interaction strength U . By calibrating these potential offsets using the atoms we can both compare how precisely the DMD can produce a desired optical potential and the absolute height of these potentials in Hz.

We used a similar protocol to the U calibration method mentioned above in §2.4.3 and is a hy-

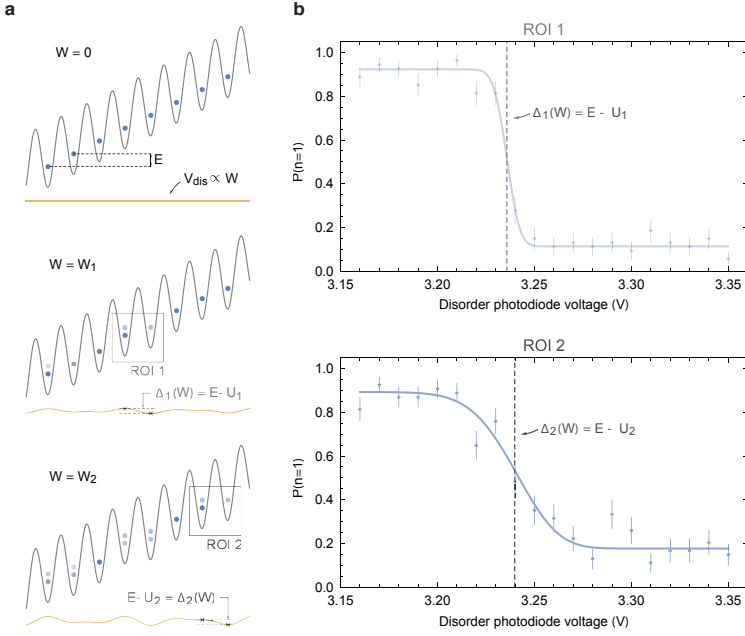


Figure 2.10: Calibration of on-site potential offsets (h_i).

a) This illustration demonstrates the protocol for finding the on-site potential offset by adiabatic passage of an atom onto its neighbor. b) By finding the crossing point of these Landau-Zener like crossings, we are able to fit the resonance crossing to extract the local potential offset between neighboring sites. Note that the x -axis is the voltage on the photodiode that is logarithmically sensitive to the power in the beam with 0.5V/decade as the calibrated slope.

brid of the protocols used in previous studies^{122,174}. The method starts with a unity-filled Mott-insulating state. A tilt of strength E Hz/site is then applied to the system to bring all sites far from resonance with their neighbors. The lattice depth is then reduced to an intermediate depth with appreciable but small tunneling. The additional potential pattern is then turned on approximately adiabatically with respect to only the nearest neighbor tunneling strength J . Since the potential that is applied has varying on-site potentials h_i , the resonance condition is again re-established when the energy difference between neighboring sites, $\Delta_i = h_i - h_{i-1}$, compensates for the energy offset $E - U$. The signal for this transition is finding when the average on-site occupation changes from $n = 1$ atom to $n = 0, 2$. This is actually measured in-situ as a change in parity. The example for this method shown in Fig. 2.10 is performed for an on-site potential sampled from a quasi-periodic distribution: $h_i = W \cos(2\pi\beta i + \phi_o)$, where β is the golden ratio ≈ 1.618 , i is the site-index, and

ϕ_o is an arbitrary phase factor. This protocol is also described in the supplementary information of *Lukin et al.*¹¹⁸.

2.4.5 HEATING RATES : SPONTANEOUS SCATTERING

As discussed earlier in §2.1.3, the spontaneous scattering rate provides a limit on the lifetime of many-body coherent processes. To estimate this limit, we determine the contribution of the spontaneous scattering rates present from all the confining optical potentials in the system. The approximate background lifetime related to background collisions with hot atoms (this is related to the vacuum quality in the glass cell) is a lifetime of $\tau_{Bkg} = 33(3)$ s or scattering rate $\gamma_{Bkg} = 0.03(3)$ Hz. By measuring the atom loss rate from relatively weak traps as a function of optical potential depth, we can measure the contribution of the additional optical potential to heating and the offset that comes from background gas collisions. In general, this loss will follow an exponential form $\sim n(t) = N_o e^{-\gamma_{Bkg}t - \gamma_{Optical}(V_o)t}$. By holding the atoms in just an optical harmonic potential (a large Laguerre-Gauss beam) and the axial confinement lattice, we were able to find good agreement with the predicted spontaneous scattering rate and the approximate background collision rate estimated by previous works (Fig. 2.11)^{63,16,149}. These measurements put an approximate single-atom lifetime bound due to the combination of all decay mechanisms in the experiments presented in this thesis to be $\tau_{all+axial} \approx 14$ s in the axial-lattice configuration and $\tau_{all+big} \approx 19$ s in the big-lattice configuration.

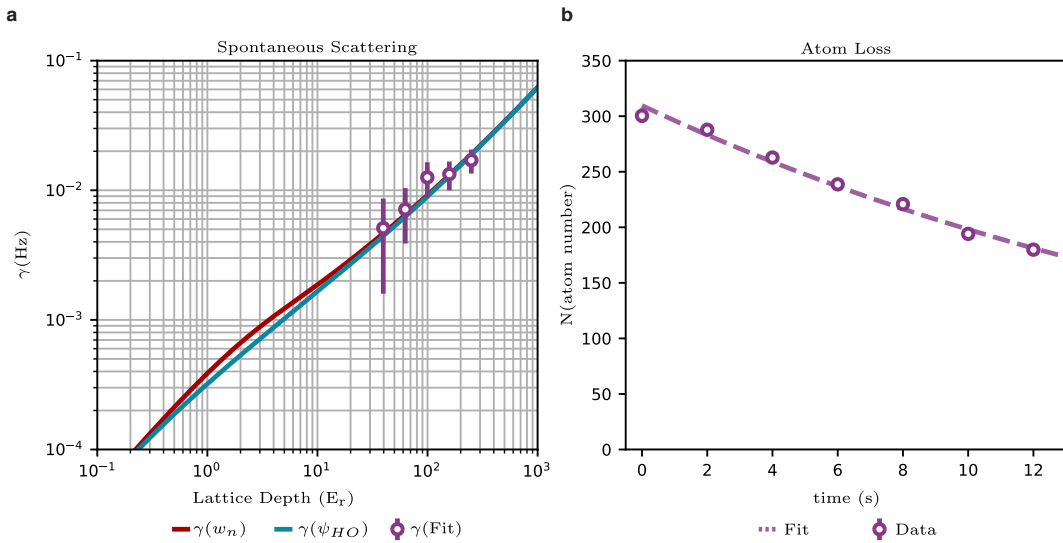


Figure 2.11: Axial lattice heating rate. **a)** The plotted data points are determined directly from the fit of an exponential decay to the atom loss from the optical trap at various axial lattice depths after removing the static contribution from the background lifetime independent of lattice depth. **b)** The atom loss from the optical trap as a function of time. The dashed line represents the fitted exponential decay.

Even two shoes in the box are correlated!

Dr. Alexander Lukin

3

Correlations, Entanglement, and Quantum Phase Transitions

Phase transitions, classical or quantum, are a celebrated paradigm in physics for describing the macroscopic properties of many-body systems independent of their microscopic parameters. These phases are described by a canonical diagram that distinguishes between an “ordered” and “disor-

dered” macroscopic phase of the system via a quasi-local observable known as an “order parameter”. This parameter possesses a non-zero value in the “ordered” regime and becomes zero when it enters the “disordered” regime. The transition of the macroscopic system from one phase to another is often performed by tuning a thermodynamic constraint such as the equilibrium temperature of the system: the solid to liquid transition at the melting point, the ferromagnetic to paramagnetic transition at the Curie point, or the condensing of bosonic atoms into a Bose-Einstein condensate (BEC) at the critical temperature of a trapped, ultracold atomic gas^{143,158,97,96}.

In classical systems, these thermodynamic transitions occur at a particular temperature when the thermal energy per constituent is comparable to a microscopic interaction parameter that governs the ordering of the system. This leads to a non-analyticity of the thermodynamic free energy and defines the point of the phase transition^{97,96}. The ability of the system to actually change its macroscopic ordering requires that the system possesses microscopic fluctuations, in this case driven by the microscopic thermal fluctuations that accompany a given temperature. The ability of these fluctuations to drive the system from a disordered state towards an ordered one requires the correlation of these fluctuations across the system such that they bring the system collectively towards a macroscopically ordered state. As such, a length scale can be defined that associates the spatial extent of these correlations in the system and gives rise to many of the characteristic associations with phase transitions such as the correlation length diverging at the critical point. This divergence of correlations at the critical point represent, perhaps, one of the best examples of a many-body system that cannot be accurately described by only looking at a few of its microscopic constituents.

The most remarkable aspect of this phase transition paradigm being that, while many phase tran-

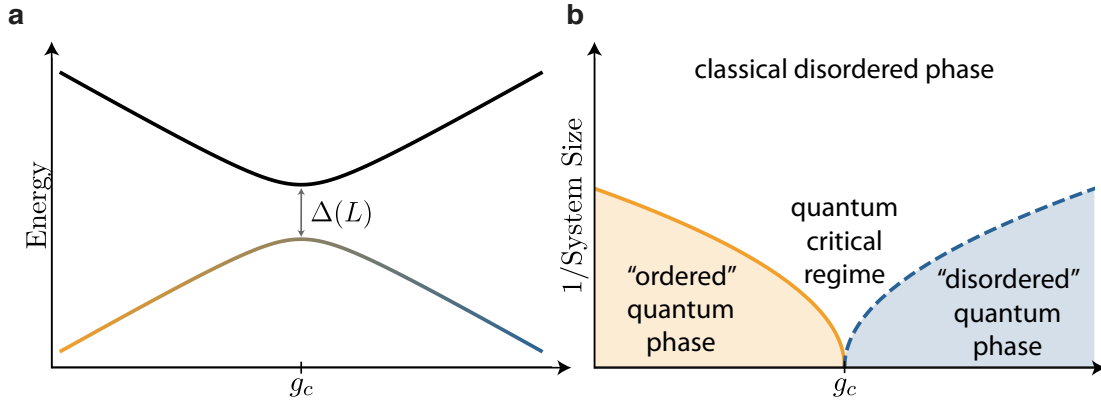


Figure 3.1: Schematic of a Quantum Phase Transition. a) The canonical schematic for a quantum phase transition occurring at $T = 0$ for the ground state as a function of a tuning parameter g . The avoided crossing shown between the ground state and the excited state in this diagram are separated by the coupling between the two terms in the Hamiltonian: H_0 and H_1 . Each dominating character of the ground state in their respective regimes. The color of the ground state denotes whether it lies in the “ordered” or “disordered” phase. b) The canonical phase diagram associated for a quantum phase transition has an “ordered” and a “disordered” phase that cross at a critical point g_c when $T = 0$ and the size of the system is very large (referred to the “thermodynamic limit”). The left diagram, a, is a plot of the eigenstates along a finite system size cross section of this diagram. As the system size is increased, this gap goes to zero. As the temperature is increased, more eigenstates in the system become incoherently populated and conceptually the quantum fluctuations, $\hbar\omega_c$, that attempt to order the system compete with the thermal fluctuations $k_B T$ that drive the system towards a disordered phase. The closing gap near the critical point extends this classically disordered phase downward into the critical “fan” shape associated with critical behavior and quantum phase transitions.

sitions may differ in absolute values, their qualitative scaling behaviors for such transitions depend only upon a few global constraints such as dimensionality or underlying symmetries. This means that given some appropriate rescaling of different systems, their macroscopic (thermodynamic) behavior will be identical and therefore the behavior of the transition is actually “universal”.

Many of these concepts from classical phase transitions can be related to quantum phase transitions. The study of quantum phase transitions involves the tuning of a coupling parameter, g , in a

Hamiltonian between two non-commuting terms as schematically shown in:

$$H = H_0 + gH_1 \quad (3.1)$$

where $[H_0, H_1] \neq 0$. The transition of this system occurs at a critical coupling point g_c and is only considered at equilibrium which can occur even when $T = 0$.^{*} Fundamentally, the system still needs fluctuations even at $T = 0$ to allow for the macroscopic ordering at the phase transition. The difference being that these fluctuations are now driven as purely “quantum” fluctuations that persist even at $T = 0$ due to the Heisenberg uncertainty principle. These quantum fluctuations also lead to a divergence in a correlation length across the system at the critical point. The question that then naturally arises is “how much are these correlations purely quantum?” This notion of uniquely quantum correlations is intimately related to the concept of entanglement in quantum systems – perhaps the most celebrated hallmark of “quantum-ness.” In some cases, the entropy induced in a system due to its entanglement has been used to distinguish the uniquely quantum aspect of these phase transitions. Analytical and numerical results for this entanglement behavior have been studied theoretically for both spin systems (Ising and Heisenberg models) and lattice models of itinerant particles (bosonic and fermionic)^{7,136,135}.

This mapping of the language and Landau-Ginzburg framework of phase transitions, however, does not apply ubiquitously to all quantum phase transitions. Notably, in the case of fractional quantum hall states^{103,112,93} or spin liquids^{193,88} their is not a clear notion of a local order parameters

^{*}It is at this point, the assumption of a system at equilibrium and $T = 0$, that all quantum phase transitions are typically assumed to refer to the transition in the ground state properties.

that distinguishes these phases, but rather their non-local entanglement that captures their behavior.

This section will start off with a generic discussion about correlations and entanglement in quantum systems. The presence of such correlations and their relation to quantum phase transitions will be discussed in the context of experiments measuring entanglement in the superfluid-to-Mott-insulating transition in the Bose-Hubbard model and the paramagnetic-to-ferromagnetic transition in the transverse Ising model – both of which are realized in one dimension. While the transverse Ising model will harbor much of the generic behavior discussed above, the Bose-Hubbard model in one dimension belongs to the class of topological BKT-type transitions.

3.1 COHERENT SUPERPOSITION AND STATISTICAL DISTRIBUTIONS

This section provides the mathematical formalism and concepts that naturally arise in the context of correlations and entangled states. For simplicity, we start with a single-particle state to develop some intuition. If we imagine a single-spin that is prepared in the $+x$ direction, we can write it as an eigenstate of the x -basis or a superposition in the z -basis:

$$| \rightarrow \rangle \equiv \frac{1}{\sqrt{2}} (| \uparrow \rangle + | \downarrow \rangle)$$

This equal superposition in the z -basis would result in a 50%/50% z -measurement distribution that would give rise to an expected average value $\langle \sigma^z \rangle = 0$. However, representing this state in this ket-vector notation actually makes an implicit assumption that the state is pure and therefore describable by a single vector that represents this coherent superposition of states in some basis. A

more convenient and versatile notation that avoids this assumption is with density matrices. The density matrix for the pure state above is simply the ket-bra product:

$$\rho = |\rightarrow\rangle\langle\rightarrow| = \frac{1}{2}(|\uparrow\rangle\langle\uparrow| + |\uparrow\rangle\langle\downarrow| + |\downarrow\rangle\langle\uparrow| + |\downarrow\rangle\langle\downarrow|)$$

When written in matrix form where the basis states $\{|\uparrow\rangle, |\downarrow\rangle\}$ define the row and column indices of the matrix:

$$\rho = \frac{1}{2} \begin{bmatrix} |\uparrow\rangle\langle\uparrow| & |\uparrow\rangle\langle\downarrow| \\ |\downarrow\rangle\langle\uparrow| & |\downarrow\rangle\langle\downarrow| \end{bmatrix} = \begin{bmatrix} 1/2 & 1/2 \\ 1/2 & 1/2 \end{bmatrix}$$

The diagonal of this matrix is simply the probability of a given state outcome, in this case either $+z$ or $-z$ each happen with 50% probability and give an average measured value of $\langle\sigma^z\rangle = 0$. This also implies that the diagonal must necessarily sum to unity $\text{Tr}[\rho] = 1$. In general then, the expectation outcome of a given observable $\hat{\mathcal{O}}$ is evaluated by the trace of the density matrix with this operator: *

$$\langle\hat{\mathcal{O}}\rangle = \text{Tr}[\hat{\mathcal{O}}\rho]$$

Notably, this notation shows that a measurement along any particular, single basis (in this case the z -basis) is agnostic to the presence of a coherent superposition of given outcomes. In other

*Conceptually, once this density matrix is written down in the measurement basis, only the diagonals of this matrix are accessible to the observer since all measurements involve a contraction with a given bra/ket-vector.

words, the presence of the off-diagonal matrix elements does not play a role in this measurement.

If, instead of $\rho = |\rightarrow\rangle\langle\rightarrow|$, we simply had a 50%/50% statistical distribution of either $+z$ or $-z$, then our density matrix, now ρ' , is given by $\rho' = \frac{1}{2}|\uparrow\rangle\langle\uparrow| + \frac{1}{2}|\downarrow\rangle\langle\downarrow|$. In matrix form simply being:

$$\rho'_z = \begin{bmatrix} 1/2 & 0 \\ 0 & 1/2 \end{bmatrix}$$

Note that this density matrix would have all the same statistics and expectation values along the z -axis. However, if we were to measure along another axis, say in the x -basis, then we have to first rotate our state about the y -axis by an angle of $-\pi/2$ or simply express $|\pm z\rangle$ in the x -basis:

$$|\uparrow\rangle = \frac{1}{\sqrt{2}}(|\rightarrow\rangle + |\leftarrow\rangle)$$

$$|\downarrow\rangle = \frac{1}{\sqrt{2}}(|\rightarrow\rangle - |\leftarrow\rangle)$$

For ρ , we know that it is actually defined as $|\rightarrow\rangle\langle\rightarrow|$ and therefore an exact eigenstate of this measurement basis would be measured as 100% in the $+x$ -direction. In the case of ρ' , this expands to be $\rho'_x = \frac{1}{2}|\rightarrow\rangle\langle\rightarrow| + \frac{1}{2}|\leftarrow\rangle\langle\leftarrow|$, which in matrix form, is still:

$$\rho'_x = \begin{bmatrix} 1/2 & 0 \\ 0 & 1/2 \end{bmatrix}$$

The lack of off-diagonal, coherence terms is what differentiates this statistical distribution from

before as a physically different object. This extreme case when these coherence terms are zero defines this system as a completely mixed state since the probabilities and measurements solely arise from a classical, statistical mixture of outcomes.

A very common metric used to differentiate and quantify these two types of systems is by measuring the associated purity of a given density matrix. This purity is defined as the trace of the second moment of the density matrix:

$$P \equiv \text{Tr}[\rho^2] \quad (3.2)$$

Note that this purity relies on the matrix product of ρ for the second moment. In the case of a state described by a single vector, $|\psi\rangle$, this metric can easily be shown to sum to unity, since $\rho^2 = |\psi\rangle\langle\psi||\psi\rangle\langle\psi| = |\psi\rangle\langle\psi| = \rho$ and $\text{Tr}[\rho] = 1$. However, in the case of a completely mixed state, such as ρ' , the density matrix is diagonal and so $\text{Tr}[\rho_{i,i}^2] = P < 1$ as long as there is more than one non-zero diagonal entry. The particularly powerful property of this formalism is that it is basis-independent, meaning that regardless of what basis is chosen to express the wave function or statistical mixture, the purity will give the same numerical answer¹³³.

While this was a specific, single-spin example, this provides some intuition for some very general properties for physical systems that are either quantum, classical, or a mixture of both. The important implication being that the purity of a system is actually invariant under any unitary operation that can be performed on the system. One way to understand this is to think of the mixed state as a statistical mixture of different truly pure states, and as vectors with a length given by their probabil-

ity, unitary operations (e.g. a rotation about an arbitrary axis) preserve this length.

This framework of density matrices, purity, and statistical mixture provides the mathematical tools to now understand the celebrated concepts and properties associated with many-bodied wave functions. The important implication being that the constituents of the wave function can be physically separated from one another while still belonging to the same coherent many-bodied state. These same arguments from above can be applied to both the joint and local distributions such that even correlations developed among these constituents are encoded in the field of their many-bodied wave function and give rise to their uniquely quantum correlations.

3.2 CORRELATIONS AND ENTANGLEMENT

Entanglement is one of the most counterintuitive and truly unique consequences of quantum mechanics. It was famously shown by John Stewart Bell that entangled quantum particles can exhibit correlations that are stronger than physically possible in classical, local theories²¹. * The canonical examples of these highly entangled quantum states that exhibit such classically violating correlations are known as Bell states and were first verified experimentally by *Aspect, et al.*,^{12,11} and rule out proposed “hidden variable” theories. Until recently, various “loop-holes” were brought forward as arguments such that the system could still admit a classical explanation. However, recently experiments have additionally implemented various loop-hole free versions of the Bell test^{76,64,172} – more

*In fact, a very common question asked of any result from a quantum simulation experiment is how “quantum” are the results. As in, how uniquely can the observed behavior be attributed to the system being a quantum one and not just one, for example, described by a classical wave theory. The violation of Bell’s inequality by a system is one of these few cases that is simply unrealizable in a purely classical world.

stringently identifying quantum mechanics as a successful description of nature.

Correlations and the presence of entanglement in a quantum system are intimately linked. For the purpose of clarity in this thesis, I will describe entanglement as a qualitative descriptor for pure, many-body quantum states that are inseparable. This inseparability means that the joint description of the quantum state is necessary and that attempting to describe the system as the product of its separated parts is insufficient. To gain some intuition about these statements, we will first consider a canonical example – the anti-symmetric Bell state:

$$\begin{aligned} |\Psi^-\rangle &= \frac{1}{\sqrt{2}} (|\uparrow_A\rangle \otimes |\downarrow_B\rangle - |\downarrow_A\rangle \otimes |\uparrow_B\rangle) \\ &= \frac{1}{\sqrt{2}} (|\uparrow_A\downarrow_B\rangle - |\downarrow_A\uparrow_B\rangle) \end{aligned} \tag{3.3}$$

which is intentionally constructed to be inseparable. That is to say, that this state cannot be decomposed into a product of single-particle states of spin A and spin B, $|\Psi^-\rangle \neq |\psi_A\rangle \otimes |\psi_B\rangle$. This can additionally be seen by noting the state $|\Psi^-\rangle$ is not an eigenstate of any single-particle operator which acts only locally on the spatially separated spins. We now analyze this state to find the emergent implications of this inseparability in a quantum state composed of this two-spin state where spin A and spin B can be spatially separated. As in the previous section (§3.1), it will again prove useful to rewrite this state as a density matrix:

$$\begin{aligned} \rho &= |\Psi^-\rangle \langle \Psi^-| \\ &= \frac{1}{2} \left(|\uparrow_A\downarrow_B\rangle \langle \uparrow_A\downarrow_B| + |\downarrow_A\uparrow_B\rangle \langle \downarrow_A\uparrow_B| - |\downarrow_A\uparrow_B\rangle \langle \uparrow_A\downarrow_B| - |\uparrow_A\downarrow_B\rangle \langle \downarrow_A\uparrow_B| \right) \end{aligned} \tag{3.4}$$

which in matrix form is expressed as:

$$\rho = \frac{1}{2} \begin{bmatrix} |\uparrow_A\downarrow_B\rangle\langle\uparrow_A\downarrow_B| & -|\downarrow_A\uparrow_B\rangle\langle\uparrow_A\downarrow_B| \\ -|\uparrow_A\downarrow_B\rangle\langle\downarrow_A\uparrow_B| & |\downarrow_A\uparrow_B\rangle\langle\downarrow_A\uparrow_B| \end{bmatrix}$$

The coefficients associated with the diagonal entries of this matrix are the joint probability outcomes of both spins for this given Bell state. Note that ρ is only showing a fraction of the total Hilbert space – the spin configurations of $|\uparrow_A\uparrow_B\rangle$, $|\downarrow_A\downarrow_B\rangle$ are not written since they have zero population.

As stated above, any single-particle operator (e.g. $\sigma_{A,B}^z$) changes the wave function and therefore demonstrates the state is not an eigenstate of local operators. However, there is a clear relation of the two spins in the state $|\Psi^-\rangle$ that are captured by the spin-spin correlation operator $\hat{\mathcal{O}} = -\hat{\sigma}_A^z\hat{\sigma}_B^z$. This two-spin operator is often referred to as the total two-point correlator.^{*} For the aforementioned ρ we obtain $\langle\hat{\sigma}_A^z\hat{\sigma}_B^z\rangle = 1$. We can see that this correlation is significant since a single-point operator would have a value of zero, $\langle\sigma_{A,B}^z\rangle = 0$. However, measuring these correlations does not distinguish our entangled Bell state from classically correlated variables (e.g. two correlated coins that are constructed classically by a hidden operator to always flip together where one is heads and the other tails) since the measurement only relies on the diagonals. The distinguishing property of

^{*}This naming convention can be a bit confusing but is common. The statistical definition for a correlator is generically written as $\frac{\langle xy \rangle - \langle x \rangle \langle y \rangle}{\sqrt{\langle x^2 \rangle - \langle x \rangle^2} \sqrt{\langle y^2 \rangle - \langle y \rangle^2}}$. This statistical definition inherently removes both offsets in the single-point measurements, $\langle x \rangle$, $\langle y \rangle$ and normalizes by dividing by the single-point variances. In practice for the given Bell state above, this is not necessary since the state has unit fluctuations and is centered about zero. However, later on in this thesis these distinction will become important for distinguishing between “total”, “connected”, and “disconnected” correlations.

the correlations encoded in our Bell state $|\Psi^-\rangle$ is the fact it is again described by a coherent superposition; geometrically, the many-body state is again described by a single vector.

We can explore the difference by considering a simplified test from Bell's proposal. After preparing the two-spin state $|\Psi^-\rangle$, spin A and spin B are spatially separated and given to two different observers to be measured at the same time. Each observer is allowed to either measure their spin in the z or the x basis and can choose which randomly (based upon a classical random variable) as long as the observer keeps track of the result and chosen measurement axis. All of the two-spin measurements possible are $\{\mathcal{O}^{z,z} = -\sigma_A^z \sigma_B^z, \mathcal{O}^{x,z} = -\sigma_A^x \sigma_B^z, \mathcal{O}^{z,x} = -\sigma_A^z \sigma_B^x, \mathcal{O}^{x,x} = -\sigma_A^x \sigma_B^x\}$. Each joint measurement will happen with equal probability. For the case of our Bell state $|\Psi^-\rangle$ the expectation values of these four observables after an ensemble of measurements are $\{\langle \mathcal{O}^{z,z} \rangle = 1, \langle \mathcal{O}^{x,x} \rangle = 1, \langle \mathcal{O}^{x,z} \rangle = 0, \langle \mathcal{O}^{z,x} \rangle = 0\}$. We could then construct some integrated quantity that combines these measurements into a single metric: e.g. $C = \frac{1}{4} \sum_{i,j \in x,z} \mathcal{O}^{i,j} = 1/2$.

However, if we had instead shared two classically correlated spins with each observer, we would produce a mixed density matrix ρ' :

$$\rho' = \frac{1}{2} \begin{bmatrix} |\uparrow_A \downarrow_B\rangle \langle \uparrow_A \downarrow_B| & 0 \\ 0 & |\downarrow_A \uparrow_B\rangle \langle \downarrow_A \uparrow_B| \end{bmatrix}$$

Physically, this would amount to some classical intermediary that randomly (perhaps based upon the toss of a fair coin) prepares the anti-correlated spins and gives one to either observer A or observer B. If observers A and B again perform the same random x, z measurements, they would obtain the outcome $C = \frac{1}{4} \sum_{i,j \in x,z} \mathcal{O}^{i,j} = 1/4$ which is certainly less than $1/2$! It is the in-

terference of the coherent superposition of the many-body state that results in the enhanced correlations measured in the case of the prepared Bell state $|\Psi^-\rangle$. This ability of having many-body coherences that enable the interference of global states under rotations of the state is what leads to the non-classicality of these correlated quantum states and a valuable resource for computation.*

This difference between the two cases, the classically correlated ρ' and the quantum state $|\Psi^-\rangle$, can be understood mathematically a bit more easily via the same purity formalism discussed previously. This way, even with measuring the same $\langle \mathcal{O}^{z,z} \rangle$ for both ρ and ρ' , the purity tells us in a basis independent way that one state is pure, $\text{Tr}[\rho^2] = 1$, and that the other is mixed $\text{Tr}[\rho'^2] = 1/2$.

3.2.1 ENTROPY

The distinction between correlations originating from pure and mixed states can be described by concepts originating from information theory and thermodynamics. Let us first start with the concept of entropy which is the logarithm of the number of microscopic states populated by a given probability distribution. For an arbitrary probability distribution, the classical definition for the entropy is given by the Shannon entropy:

$$H(P) = - \sum_i P_i \log[P_i] \quad (3.5)$$

where P_i is the probability of microstate i occurring. The entropy of a probability distribution describes the amount of information in base e (in bits for \log_2) needed to describe the distribution.

*As a caveat, however, that should be mentioned here is that this thought experiment exploits a property of the particular Bell state chosen which is that it is also an eigenstate of any global rotation. The experiment proposed by Bell is more general than this and does not rely on such a specific property.

In the case that our probability distribution P_i is built out of two constituents, say A and B, then we consider this a joint distribution which we will now write as $P_{A,B}$. The individual distribution outcomes that are possible if just A or B is measured are known as the marginal distributions and can be determined from the joint distribution by summing over (or ignoring) the other constituent (e.g. $P_A = \sum_{b \in B} P_{A,b}$). In the case that $P_{A,B}$ is produced by two uncorrelated constituents A and B, then it reduces to the product of the two marginal distributions $P_{A,B} = P_A \times P_B$. From an entropic point of view, we find that the joint entropy is just the sum of the parts:

$$\begin{aligned}
H(P_{A,B}) &= - \sum_{A,B} P_{A,B} \log[P_{A,B}] \\
&= - \sum_{A,B} P_A P_B (\log[P_A] + \log[P_B]) \\
&= - \sum_B P_B \times \sum_A P_A \log[P_A] - \sum_A P_A \times \sum_B P_B \log[P_B] \\
&= H(P_A) + H(P_B)
\end{aligned} \tag{3.6}$$

In words, that amount of information needed to describe a joint distribution built from two independent marginal distributions is just the sum of the information needed for each independent distribution respectively. This consequence changes in the presence of correlated outcomes between A and B and the joint distribution is no longer separable. The amount of information that is shared between the two distributions A and B is known as the mutual information:

$$I(P_A : P_B) = H(P_A) + H(P_B) - H(P_{A,B}) \tag{3.7}$$

This quantity describes the amount of information that is shared between constituents A and B which is then intimately related to the correlations that exist between A and B. In the case of the completely correlated, but classical example, $\rho' \rightarrow P_{A,B}$, we find that all the entropies are the same $H(P_{A,B}) = H(P_A) = H(P_B) = \log[2]$ which additionally implies the mutual information $I(A : B) = \log[2]$. These two extreme cases for the classical system, maximally correlated and independent, provide some intuition about the possible entropies – namely that:

$$\arg \max\{H(A), H(B)\} \leq H(P_{A,B}) \leq H(P_A) + H(P_B)$$

$$0 \leq I(A : B) \leq \arg \min\{H(A), H(B)\}$$

These relationships can be seen intuitively from Fig. 3.2 that graphically describes the information shared between A and B.

The translation of the information concepts of Shannon entropy to quantum mechanical states is provided through the definition of the von Neumann entropy. Instead of finding the classical microstates populated by a probability distribution, the von Neumann entropy acts on the density matrix of a state:

$$S(\rho) = \text{Tr} [\rho \log[\rho]] \quad (3.8)$$

While this definition is basis independent and can be computed as long as one is careful with acting on a matrix with the $\log[]$ function, it is easiest to compute the von Neumann entropy in the

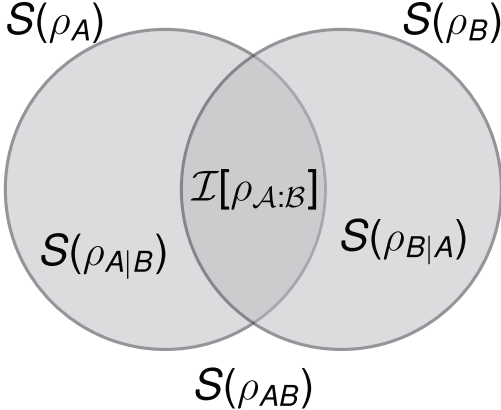


Figure 3.2: von Neumann entropy and mutual information. This Venn diagram graphically describes the total information needed to separately describe the constituents $\{S(\rho_A), S(\rho_B)\}$, as well as the information they share $I[\rho_{A:B}]$, and the amount of information that is independent of knowing everything about the other constituents $\{S(\rho_{A|B}), S(\rho_{B|A})\}$. Since these are quantum states and not classical ones, the bounds are different than those derived for the Shannon entropy can be difference since $S(\rho_{AB})$ can be zero.^{34,80,81} The classical and quantum bounds described in this chapter can be understood from this diagram by taking this global entropy bound into account.

diagonalized (or Schmidt basis) of ρ in which the matrix is diagonal.* This description of a system by a matrix ρ with the possibility for coherent superposition of many-bodied states fundamentally changes the entropy bounds shown for the classical case. To start with, let us consider the total entropy in a pure state as defined by the Bell state $|\Psi^-\rangle$ above. Since we can choose to rotate ρ to any basis, it is most convenient to express it in the Bell state basis, in which case it is simply a single entry defined by $\rho = |\Psi^-\rangle\langle\Psi^-|$. The fact there is only a single microstate populated means that the total entropy of this system is zero. To understand the significance of this result though, we need to first address the concept of the partial trace of a system – this is akin to finding the marginal distribution P_B by summing over all possibilities for A : $P_B = \sum_A P_{A,B}$. In the density matrix case this is performed by an inner product with the basis states of system A:

$$\rho_B = \text{Tr}_A[\rho] = \sum_{a \in A} \langle \phi_a | \rho | \phi_a \rangle \quad (3.9)$$

*This is diagonalization of the density matrix is equivalent to determining the number of pure, many-body quantum states (akin to global microstates) the density matrix populates.

where $|\phi_a\rangle$ defines a complete, orthonormal basis of subsystem B. If we apply this partial tracing to the originally investigated Bell state $|\Psi^-\rangle$, where $|\phi_a\rangle \in \{|\uparrow_A\rangle, |\downarrow_A\rangle\}$ then we have constructed ρ_B which is known as the reduced density matrix since it only spans the subspace of spin B:

$$\rho_B = \frac{1}{2} \begin{bmatrix} |\uparrow_B\rangle\langle\uparrow_B| & 0 \\ 0 & |\downarrow_B\rangle\langle\downarrow_B| \end{bmatrix}$$

The partial trace, conceptually, is considered the “ignoring” of information present in the other subsystem, in this case the orientation of spin A. The originally pure, entropically zero many-body state ρ is now locally a completely mixed state with $S(\rho_B) = \log[2]$. This result elucidates the difference in entropy bounds of the quantum case as compared to the classical one: $S(\rho)$ is no longer bounded from below by $\arg \max\{S(\rho_A), S(\rho_B)\}$ and the maximum mutual Information has a much larger upper bound $0 \leq I(A : B) \leq S(\rho_A) + S(\rho_B)$.

This regime of $S(\rho) < S(\rho_A), S(\rho_B)$ is often used to identify the qualitative statement of *entanglement* for a state and defines that some of these correlations are quantum in origin. There are several significant remarks to be noted about such systems. This enhancement of the maximally available mutual information between two subsystems is why entanglement is considered an important and exploitable resource for quantum information and quantum computation purposes¹³³. Another important observation is that in the case of a pure quantum state, the entropy observed for a subsystem is entirely generated by the loss of information related to the initial coherent, many-body superposition of the state. Lastly, these states are not trivial to generate. This is for two reasons: 1)

the many-body state has to start off as a relatively pure one* and then 2) become correlated such that it is inseparable and therefore entangled. As it will turn out, unitary evolution of an initially separable, pure quantum state through a phase transition is one way generate such entangled states§3.3, 3.4, 4.

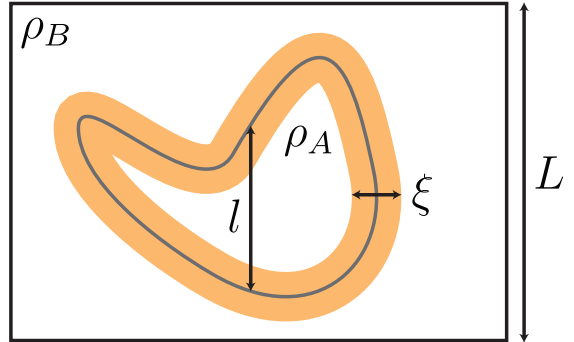
3.2.2 ENTANGLEMENT AND QUANTUM PHASE TRANSITIONS

From the previous brief discussion of phase transitions: the growth of correlations near the critical point seems like a clear and natural manifestation of entanglement if the phase transition is a quantum one. However the exact relationship can be a bit subtle. In the case of a $T = 0$ phase transition, the system is described by a single eigenstate, namely the ground state, and therefore has zero total entropy. The generation of correlations in the ground-state near the phase transition will make it inherently inseparable and therefore generate entropy among its subsystems – which indeed makes them entangled on a qualitative level^{183,7,158}.

However, some of the same notions, such as diverging correlation lengths at the critical point, do not straight-forwardly manifest in a quantitative way for the discussed entanglement metrics. For instance, the entropy of a single spin in a many-spin state does not necessarily relate to the number of other spins with which it is correlated. The local entropy is bounded from above by $\log[2]$ and therefore the entanglement of the individual spin with the rest of the system can be distributed arbitrarily via its correlations as long as it respects this bound. This is often referred to as the “monogamy” of entanglement and refers to the fact that there is a finite amount of this resource that can be dis-

*In comparison with the locally generated entropy from the partial trace.

Figure 3.3: Area law in ground-state phases. As demonstrated in Vidal, et al., the entanglement entropy due to a bipartition of the total many-body system into subsystems ρ_A, ρ_B realized a scaling relationship known as an area law. This area law determined that the amount of entanglement entropy probed by the bipartition scaled linearly with the boundary size $\propto l^{D-1}$ of the bipartition rather than the volume $\propto l^D$ for dimension D. This area law's relation to the correlation length was found in critical systems by a logarithmically slow divergence of the entropy with system size l inherited from the diverging correlation length ξ .



tributed among the system. If two spins are maximally entangled, as in the case of the Bell state $|\Psi^-\rangle$, then for them to become entangled with a third spin, they must inherently reduce some of the entanglement they initially shared with one another, even though they may still be just as “correlated”. This property is particularly important when attempting to evaluate the length scale over which entanglement is distributed in a quantum system at a quantum critical point. The first numerical studies addressing this problem, while finding a familiar universal scaling behavior of correlations at the critical point, had difficulty defining the properties of the length scale over which entanglement was spread in the system^{136,135,7}.^{*} Further studies showed that by always partitioning the system into two macroscopically large subsystems (known as a bipartition), rather than looking at the entanglement between two individual spin subsystems, provided a direct relation of the correlation length to the entanglement entropy near the critical point¹⁸³. The entropy for the ground-state transitions was found to scale with the area⁵², or boundary, of the subsystem due to the finite correlation length ξ in the system(see Fig. 3.3).

*This was partially compounded in difficulty due to the wide number of numerical metrics meant to quantify entanglement and the fact that the monogamy of entanglement made many entanglement measures peak around but not necessarily at the transition.

Despite the ubiquitous use and study of entanglement in theoretical physics, current traditional condensed matter experiments do not have a direct probe for measuring it. In a few other similar AMO experiments, entanglement has been probed via entanglement witnesses²⁸: specifically constructed observables that probe inseparability of a quantum state that violates a particular bound. Such witnesses are state-specific and do not necessarily scale in a meaningful way with the degree of entanglement in the state. In systems of trapped ions⁷¹ and superconducting qubits¹³², an exhaustive reconstruction of the entire density matrix can be performed, known as state tomography, from which the entanglement entropy can be directly computed. There is not a known scheme for mapping this technique to lattice systems of itinerant particles. Instead, we will demonstrate the use of a many-body interference technique that forgoes the aforementioned techniques. We use this technique to investigate the entanglement developed in ground-state phase transitions^{54,129,140,44}. Recently, a new method involving measuring the variation in observable outcomes after random quenches on a single realization have also been demonstrated to measure entanglement entropy³¹.

3.3 SUPERFLUID-TO-MOTT-INSULATOR TRANSITION

The superfluid to Mott-insulator transition is one of the most celebrated manifestations of a quantum simulator generating and measuring a quantum phase transition^{67,17,158}. While these experiments were able to explore the properties of the different quantum phases and probe the local order parameter, they were unable to directly measure the entanglement generated in the system. In this experiment, we directly measure the global and local purities of a finite size system in the

Bose-Hubbard model through a many-body interference technique^{54,129,140,44,98,89,99}. This purity measurement allows us to directly compute the second-order Rényi entropy:

$$S_2(\rho) = -\log[\text{Tr}[\rho^2]] \quad (3.10)$$

which is a quantitative lower bound to the more traditional von Neumann entropy. The same inequalities used for the discussion of the von Neumann entropy above additionally apply to the Rényi entropy for measuring entanglement in a system:

$$S_2(\rho) < S_2(\rho_A) \quad (3.11)$$

$$S_2(\rho) < S_2(\rho_B) \quad (3.12)$$

The technique used to measure the Rényi entropy relies on the interference of two identical but independent quantum many-body states. This allows one to extract observables that are quadratic in the density matrix which is used here to access the system purity^{54,129,30,140,29,186,163,44}. The capability to directly measure the Rényi entropy is a powerful technique for several reasons: i) it does not rely on violating particular correlation measurement inequalities such as the Clauser-Horne-Shimony-Holt (CSCH) inequality^{80,29}, ii) quantum state tomography requires a measurement of a prohibitively large Hilbert space and has no known scheme for itinerant systems, iii) in principle requires few measurements to verify low entropies and can be quickly used to bound the global purity

of a state. The exact experimental implementation of this technique is thoroughly detailed in *Islam et al.*^{89,149,117} and is not extensively discussed here. The results presented below not only directly measure the development of entanglement in a quantum system, but provide some instructive insights on its origin.

The experiment begins in a Mott-insulating state with unity filling ($U \gg J$) in a finite 1D system of 4 sites. This means that the initial many-body state is described by a product state of exactly one atom per-site:

$$|\Psi_{MI}\rangle = \prod_{i=1}^{L=4} \otimes |1_i\rangle$$

Since this state is a product state, it is inherently separable and therefore unentangled * and both the sub-systems and full-system are pure. As the ratio of U/J is reduced towards the superfluid regime ($J \gg U$) the ground-state becomes a spatially delocalized state:

$$|\Psi_{SF}\rangle \propto \left(\sum_{i=1}^{L=4} a_i^\dagger \right)^{\otimes N=L} |vac\rangle$$

The superfluid ground state with a finite particle number is spatially delocalized and therefore is inseparable among the lattice sites which leads to entanglement entropy when measuring the purity of a subsystem. The Rényi entropy measurements shown in Fig. 3.4 show that on the superfluid

*There is a common use of the phrase “strongly-correlated” when referring to the Mott-insulating state which would appear unjustified given the above description. However, as a point of clarification, remember that the concept of entropy from entanglement is always with respect to a given partitioning of the system, while, for any given partition, the metric is basis invariant. In the case of a Mott-insulator, any real-space separation of many-body state generates no entropy.

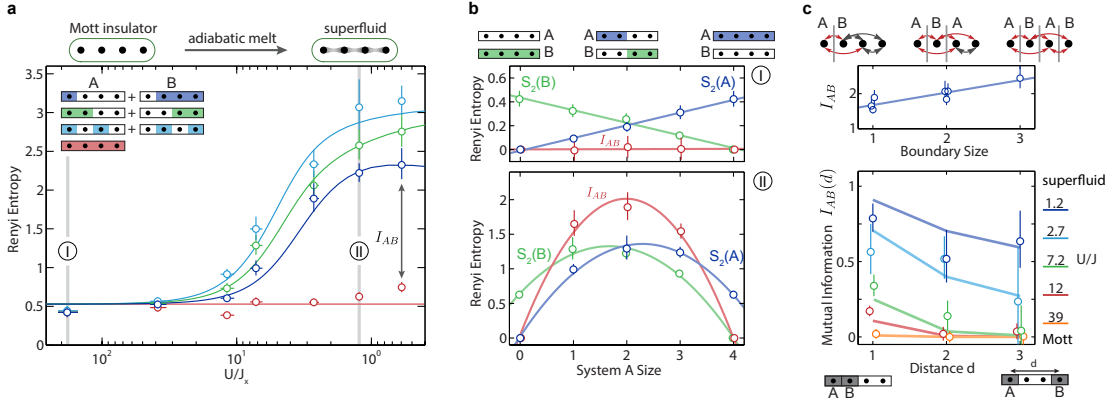


Figure 3.4: Measured Rényi entropy in the Mott-insulating-to-superfluid transition. a) The measured global and subsystem entropies are shown for various partition volumes and arrangements. The area between the subsystem entropies and the global entropies quantify the amount of mutual information generated in the system during the adiabatic ramp to the superfluid state. Note that the entropy inequality that would determine the bound on entanglement in this plot lies close to 1. The different partitions shown are to illustrate the difference area versus volume laws. b) Illustrates the extensive, volume law scaling, of the background classical entropy injected in the system through residual heating or non-unity fidelity interference contrast. c) The top plot demonstrates the area law behavior of the entropy with partitioning of the subsystems. The lower plot demonstrates the decrease in correlations as a function of distance between non-bipartite subsystems – as would be expected from a decaying correlation length. All solid lines in a,c are numerics performed by exact diagonalization. The error bars are the s.e.m.

side of the transition there exists verifiable entanglement among all possible subsystem sizes and partitions.

The many-body interference technique performed here shows the measurable development of entanglement entropy. It additionally illustrates its versatility as a technique by its capability to measure variable subsystem sizes and arbitrary partitioning in real-space as a single measurement scheme. Note that while these measurements indeed perform a remarkable job in measuring entanglement, it does not seem to follow the intuition we developed and discussed in the previous section for quantum phase transitions. The reason for this stems from the fact that the system has a conserved particle number that manifests as strong, inherent particle number correlations between a

subsystem and the remainder. As an example, imagine a subsystem of one-site. This single-site can have only $N+1$ possible microstates bounded by the total particle number: $0 \leq \hat{n}_i \leq N$. However, more importantly, due to the particle number conservation, there are no coherences in the single-site reduced density matrix and it is purely a diagonal matrix. This is because the sub-systems are a bipartition of the total system and therefore the number of atoms in the two subsystems are unique numbers $n_A, n_B = N - n_A$. This is actually not a generic feature of the superfluid state, and is dependent upon having a conserved particle number. In the limit of the superfluid being composed of a product of local coherent states:

$$|\Psi_{SF}\rangle = \prod_i |\alpha_i\rangle$$

the total particle number is not conserved, the state is an eigenstate of the Bose-Hubbard model, and a product state of the lattice sites. However, for this experiment where we start in a Mott-insulating state, one must always start with a number of atoms that is commensurate with the lattice size. Therefore, it is not possible to have a coherent superposition of total particle numbers which is required by this coherent state superfluid.

Schemes have been developed for this protocol that probe only the entropy related to the diverging correlation length at the transition that effectively remove the correlations from fixed global particle number^{190,125}. This entanglement that follows our intuition of quantum phase transitions, however, is rather small. In the absence of this modal entanglement from particle delocalization, this particular transition would make experimental demonstration of entanglement entropy very

challenging.

3.4 ISING MODEL PHASE TRANSITION

This section starts with a brief overview of another canonical phase transition that occurs in the Ising model with both longitudinal and transverse magnetic fields. Importantly, the implementation of this model in our Bose-Hubbard system has characteristics that are more akin to the phase transition behavior expected without any conservation rules such as conserved particle number.

Through the use of our DMD, we can access the full-counting statistics of the quantum state in the Fock basis. This allows us to directly probe the order parameter of the quantum phase, the single-site entropy, and the reversibility of the transition which probes its overall adiabaticity and purity.

This model has been previously realized in this same experimental apparatus¹⁷⁴ and is more thoroughly discussed in the following theses^{16,121}. The mapping from the Bose-Hubbard model to a spin model was first proposed by *Sachdev et al.*¹⁵⁹ and is accomplished by working in a reduced Hilbert space via a strong potential gradient in the optical lattice. The primary ingredients of this mapping are shown in Fig. 3.5.

This mapping starts in a regime where $U \gg J, U/2 < E < U^*$: $U \approx 410\text{Hz}$ and $J = 6\text{Hz}$. This realizes a set of eigenstates that are approximately described by the Fock basis. The gradient potential, E , starts at a low value $E_- \approx 307\text{Hz}$ is then increased till $E_+ \approx 512\text{Hz}$. This ramp passes through a regime where every site is on-resonance with its neighbor when the offset is equal

*The lower bound forgoes the contribution of second-order hopping processes that incorporate states outside of the prescribed basis for a faithful mapping to the Ising model. This was found to be a necessary step since these second-order processes provided a non-negligible fraction of population into these states.

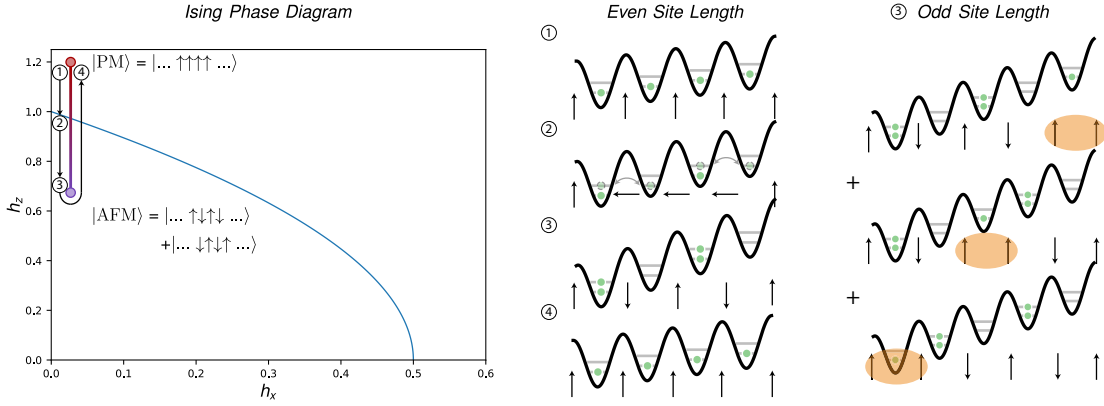


Figure 3.5: Bose-Hubbard to Ising model mapping. a) The phase diagram is shown on the left with the adiabatic path taken that leads to the transition from the paramagnetic phase $|PM\rangle$ to the antiferromagnetic $|AFM\rangle$ ones. The mapping of on-site occupations to spin alignment is shown for total system sizes of both even- and odd-site lengths. b) These boundary conditions only effect the $|AFM\rangle$ states. In the even-site regime there is a single ground-state orientation, while in the odd-site regime the ground state contains a delocalized domain wall (denoted as the orange bubble).

to the energy U . However, the important aspect of these dynamics arise from the collusion of all the particles in the system such that they transfer in a many-body coherent way and the system remains in the global ground state. All Bose-Hubbard-to-Ising-model mappings are listed in Appendix: F.

After following the mapping prescribed by Sachdev *et al.*¹⁵⁹, the resultant spin Hamiltonian is given by:

$$H = J \sum_i S_z^i S_z^{i+1} - (h_z + \delta_z^i) S_z^i - h_x S_x^i \quad (3.13)$$

where the transition in this Hamiltonian is approximately at $h_z = 1 - 0.66h_x$.

Importantly, the ground states of the system are approximately locally factorable on either side of the transition. In the paramagnetic (PM) phase, which is the unity filling Mott insulator we start with, the system is separable both in the spin mapped Hilbert space and the bare Hilbert space of

lattice-site occupations. The spin mapping here is that $|n_i = 1\rangle \rightarrow |\uparrow\rangle$. After going through the $E \approx U$ resonance, atoms that hop to their neighboring site will be considered the spin-flipped atoms. This implies that lattice-site occupations $|n_i = 0\rangle \rightarrow |\downarrow\rangle$, while $|n_i = 1, 2\rangle \rightarrow |\uparrow\rangle$. This phase is known as the antiferromagnetic (AFM) phase of the transition. This corresponds to a charge-density wave in the bare basis of on-site occupation number.

While the initial state is independent of boundary conditions, the final state is sensitive to the bounds of the system. In the case of periodic boundary conditions, the final state is a superposition of two possible AFM configurations: $|\Psi_{AFM}\rangle = |\dots \uparrow\downarrow\uparrow\downarrow \dots\rangle + |\dots \downarrow\uparrow\downarrow\uparrow \dots\rangle$. While this case is useful theoretically for computation, it is rather unphysical. The experiment is always a finite size system with open boundary conditions. This imposes two generic types of ground states that depend upon whether the system size includes an even or odd number of lattice sites (Fig. 3.5). In the case of an even number of lattice sites, there is a single state for both the paramagnetic and antiferromagnetic ground states. This is the case shown in Fig. 3.6a for an $N = 4$ site system. In contrast to previous work¹⁷⁴, we now resolve the on-site number which enables us to directly measure the exact ground state for the PM or AFM phases on either side of the transition and the order parameters (e.g. Néel order parameter):

$$\langle \hat{\mathcal{O}}_{AFM} \rangle = \left\langle \left(\sum_j (-1)^j \hat{s}_j^z \right)^2 \right\rangle \quad (3.14)$$

Additionally, since we are working with a conserved particle number for a finite size system, the correlations related to the particle number distribution on a single-site can be directly related to the

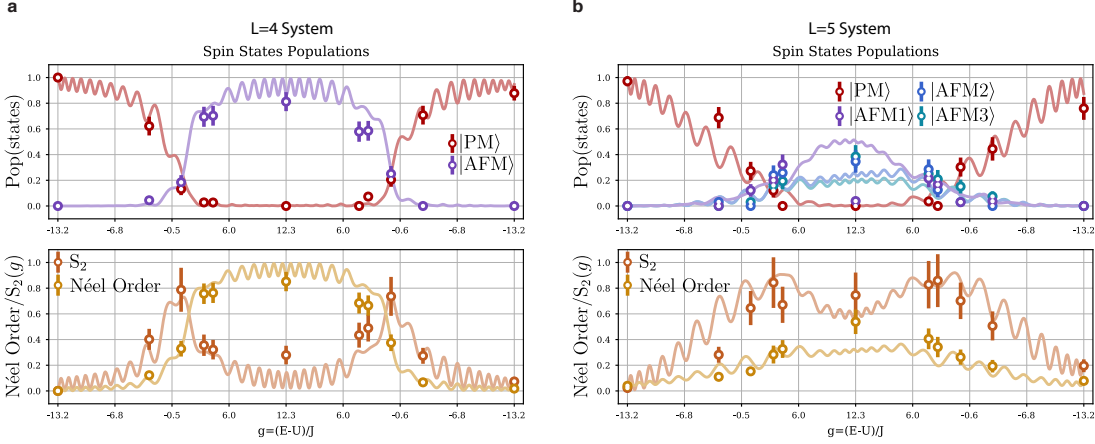


Figure 3.6: Measured population in magnetic states, order parameter, and single-site entropies. a) The top plot shows the population in the paramagnetic state and antiferromagnetic state as a function of the tuning parameter g for the $N = 4$ system. The system is shown ramping through the transition and back to demonstrate the adiabaticity of the process and bound the amount of entropy generated at the transition due to diverging correlation length at the critical point. The lower plot shows the increase of entropy near the critical point (orange) and the measured Néel order (blue) that occurs in the AFM phase. b) The top plot shows the population in the paramagnetic state and antiferromagnetic states as a function of the tuning parameter g for the $N = 5$ system. Note that now the three possible AFM states that admit a single domain wall are now plotted. This inherent domain wall incurs a reduction in the order parameter presented in the lower plot and the increase in the entanglement entropy in the AFM phase. All solid lines are exact numerics performed by Trotterized time evolution. The error bars are the s.e.m.

single-site entropy. This provides a metric with which to probe the enhanced quantum fluctuations that occur at the critical point of the phase transition which are also shown in Fig. 3.6.

In the case of an odd number of lattice sites, there is always a single domain wall somewhere in the system due to the frustration of trying to anti-align all neighboring spins. This leads to an AFM ground state composed of the $N - 2$ possible configurations with a single domain wall. This superposition of this domain wall leads to an additional residual entropy in the AFM phase that can be seen by both a non-zero entropy in the single-site entropy and a reduced Néel order parameter. This is shown for an $N = 5$ site system in Fig. 3.6b.

We scale the system size for both the even and odd site cases to see how the transition depends

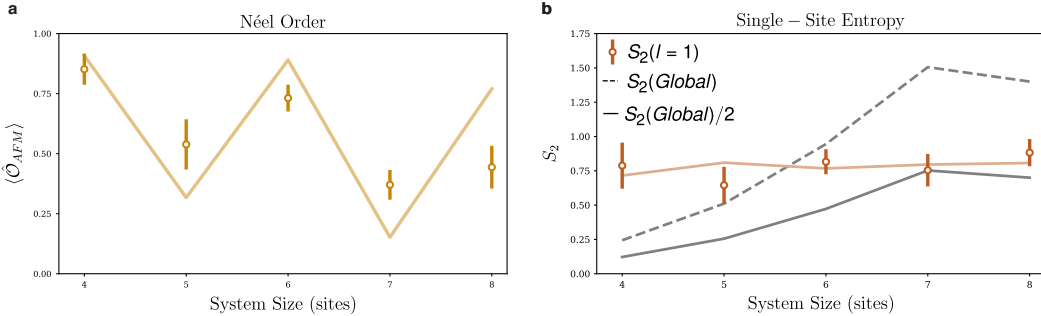


Figure 3.7: System size scaling: order parameter and single-site entropy. **a)** The Néel order parameter is plotted for the tuning parameter ($g \gg g_c$) deep in the AFM phase as a function of system size. The staggered structure reflects the domain wall excitations in the odd-site system size ground states. The additional suppression of the expected order parameter value for the even-site system reflects the shrinking gap at the critical point that restricts the maximum correlation length possible in a finite time ramp. **b)** The single-site entropy remains nearly maximized for all explored system sizes. Importantly, we can use this to distinguish whether the system's change in order arise due to quantum fluctuations by comparing this entropy the global purity estimates (black solid and dashed lines). All solid,colored lines are exact numerics performed by Trotterized time evolution. The error bars are the s.e.m.

upon the total system size. The finite size of the system is related to the minimum gap in the system and is associated with a shrinking of the critical region(Fig. 3.1) that lies between the two quantum phases¹⁵⁸. This shrinking gap size with system size will require longer ramp times to maintain adiabaticity during transition. The on-site atom number resolution affords us the ability to measure the local order parameter and peak single-site entropy of this transition for system sizes $4 \leq L \leq 8$ which are plotted in Fig. 3.7.

To determine whether the entropy measured at the critical point is due to entanglement, we have to compare this single-site entropy to the global entropy of the system. In the even site case, the ground state on either side of the phase transition is approximately an eigenstate of the many-body Fock state in our system and enables us to directly estimate an upper bound on the global entropy in the system by simply estimating the purity from the diagonal of the measured density matrix (3.15)

in an arbitrary basis.

$$\text{Tr}[\rho^2] \leq \sum_i \rho_{i,i}^2 \quad (3.15)$$

In the case of an odd-site system, it is more insightful to reverse the transition back to the initial state. By estimating the entropy from either one of these cases at the end of the initial sweep, we can make a stricter statement about whether the entropy at the critical point is due to the entanglement of the quantum state. We see that based upon the estimate on the global purity after reversing the dynamics that we can strictly make this statement about this transition up to the system size $N \leq 5$. Although, if we assume that the non-adiabaticity of the ramp that leads to this lack of purity occurs from ramping through the transition twice, then a closer estimate would show this to be true for system sizes $N \leq 7$.

There is an additional influence on these dynamics that derives from residual disorder in the optical lattice. Inhomogeneous potential offsets on individual lattice sites correspond to local variation in fields h_z in (3.13). If these local fields are on the order of the coupling strength between sites, the minimum gap will significantly decrease and one can effectively think of several, nearly, disconnected chains undergoing the transition. These will create a set of chains that are effectively incoherently populated with respect to one another and may not reversibly map back to the PM state.

A last comment to be made from looking at the odd-numbered lattice sites in Fig. 3.6 is that not all single-domain wall states are equivalent in the AFM phase. This actually becomes an intuitive outcome of this frustration if one considers the single-domain wall like a single-particle or excitation

in a box. The wave function of this single-excitation on top of the AFM background will have a ground state minimized by its kinetic energy within a confined volume – akin to the typical cosine solution for a single-particle in a box.

3.5 DISCUSSION

The demonstrated measurements of entanglement entropy in ground-state phases provide a basis for experimental exploration of entanglement and quantum criticality in ground-state quantum phases. The microscopic access available to the system allows for a direct measurement of the microscopic entropy, the order parameter, and could be extended to extract the corresponding correlation length in the system. Additionally, other proposals for multipartite entanglement witnesses through the quantum Fisher information can be applied that also have access to the global entropy through dynamic susceptibilities⁷⁵. These techniques could be applied to measure the Kibble-Zurek mechanism that governs the expected critical behavior^{146,196}. Experimentally, such scaling behavior has been seen for both strongly interacting system and those captured by a mean-field approach^{56,9,41,100}.

Lastly, this chapter has only focused on the concept the role of entanglement and fluctuations in the context of equilibrium systems. In all of the successive chapters of this thesis, the same concepts will be used and applied for pure quantum systems that are far from equilibrium. This will inherently involve eigenstates other than the ground-state of the system. We will now focus on the characteristic behavior of these excited eigenstates and how they, too, harbor many-body physics similar to the concepts discussed here.

*The only problem with testing ETH is you need another
copy of the Universe to interfere with!*

Professor Markus Greiner

4

Isolated quantum systems and local thermalization within eigenstates

Having discussed entanglement and correlation properties in the context of equilibrium systems in the previous section of this thesis, we will now focus on the development of these properties in a pure, isolated quantum non-equilibrium system. The system's non-equilibrium dynamics will be

used to probe the nature of its excited eigenstates. We will see that these excited eigenstates also have a generic, local behavior with characteristic dynamics that identify these eigenstates as belonging to a non-equilibrium quantum phase.

4.1 QUANTUM THERMALIZATION

When an isolated quantum system is strongly perturbed, for example by a sudden change in the Hamiltonian (a so-called quantum quench), the ensuing dynamics are determined by the population of eigenstates in the final Hamiltonian after the quench.¹⁶⁰ at any given time, the evolving quantum state will have amplitudes that depend only on the eigenstates populated by the quench, their respective phases, and their energy eigenvalues in the final Hamiltonian. In many cases, such a system would be difficult to simulate exactly due the generation of a large amount of entanglement during the ensuing dynamics^{33,7,44,162}. Remarkably, however, the same isolated quantum system can locally thermalize under its own unitary dynamics – unaided by an external reservoir – meaning that the tools of statistical mechanics apply in describing the long-time, saturated behavior of the system^{48,153,53}. In this case, most local observables of a quantum state that is coherently evolving according to the Schrödinger equation can be predicted from a thermal ensemble and thermodynamic quantities. Even with infinitely many copies or realizations of this quantum state, these local observables are fundamentally unable to distinguish whether the global system is a single, many-body quantum state or a thermal ensemble. This statement is remarkably powerful: a globally pure quantum system is locally indistinguishable from a mixed, globally entropic thermal ensemble^{92,48,177,153}.

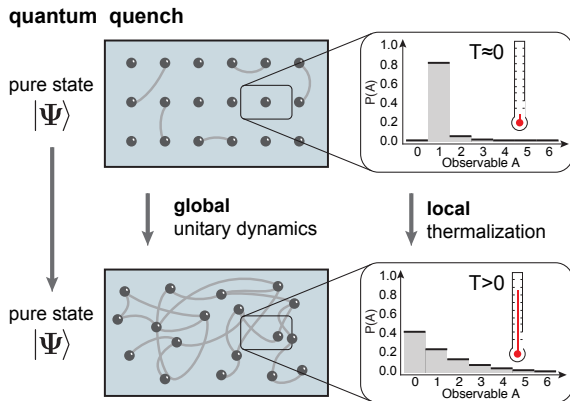


Figure 4.1: Quantum thermalization. The characteristic thermalizing behavior of our closed quantum system is probed via a quantum quench. The system initially starts at equilibrium with both a global and local entropy that is approximately zero. The system is then strongly perturbed by a sudden change in the Hamiltonian. As the system evolves only under its unitary evolution, it comes to a local equilibration that is indistinguishable from that of a globally entropic ensemble even though it is verifiably still part of a globally pure quantum state. This local agreement with a thermal ensemble is mediated by the growth of entanglement with the remaining system and generates local entropy.

The dynamic convergence of the pure quantum state via unitary evolution towards the predictions of a thermal ensemble and the entanglement that drives it are the focus of this chapter.

Many theoretical studies have helped clarify the role quantum mechanics plays in statistical physics^{48,153,92,177,161,49,43}. The questions surrounding the agreement of local observables in pure quantum many-body states with extensively entropic thermal distributions are resolved by the implications of quantum entanglement in the pure state. The generation of local entropy by ignoring parts of a globally pure quantum system is the conceptual glue that connects how a pure quantum state can appear locally like a thermal ensemble. The key point is that this local entropy does not derive as some fraction of the globally entropic system. Rather, it originates from the ignoring of the quantum correlations shared between the local subsystem and the remainder of the full system.

4.2 PROTOCOL AND MODEL

The work presented in this chapter directly measures the global purity of a thermalizing quantum system through quantum many-body interference^{44,89,99}. We experimentally verify that a globally

pure quantum state dynamically loses local purity to entanglement, and, in parallel becomes locally thermal. Other recent experiments have demonstrated aspects of quantum thermalization through the relationship between classical chaotic dynamics and entanglement in a superconducting qubit system¹³² and the dynamics of thermalization within an ion system⁴².

All quench experiments are initialized from a 2×6 size plaquette of a larger low-entropy Mott insulator with unity filling (Fig. 4.2a). The separability of the Mott insulator implies that the entire state is initialized as a product state of single-atom Fock states on each lattice site. This separability allows us to think of the 2×6 size plaquette as two copies of identical 1×6 site systems. The subsequent dynamics of this system will be given by a two-dimensional Bose-Hubbard Hamiltonian shown below:

$$\hat{H} = -\left(J_x \sum_{x,y} \hat{a}_{x,y}^\dagger \hat{a}_{x+1,y} + J_y \sum_{x,y} \hat{a}_{x,y}^\dagger \hat{a}_{x,y+1} + h.c.\right) + \frac{U}{2} \sum_{x,y} \hat{n}_{x,y}(\hat{n}_{x,y} - 1) \quad (4.1)$$

As illustrated pictorially in Fig. 4.2a, the quench dynamics are initiated by suddenly switching on the tunneling in the x direction, whereas tunneling in the y direction remains suppressed. These dynamics are restricted to a one-dimensional 6-site chain for both copies. This quench realizes a projection of the initial state onto many highly excited energy eigenstates in the final Hamiltonian. Each chain represents an identical and independent copy of a quenched system of six particles on six sites, which evolves in the quenched Hamiltonian for a variable duration. At the end of this evolution time, the dynamics are frozen and one of the two protocols depicted in Fig. 4.2c is performed.

To measure the local occupation number on each site of the copy, we perform a one-dimensional time-of-flight measurement along the y direction while a barrier remains between the two copies. To measure the global and local purity of the system, the tunneling along the y direction between the two copies is rapidly increased to realize a many-body–interference measurement as mentioned in §3⁸⁹. Two examples of such results are shown in Fig. 4.2c for both the local on-site occupation statistics and the global many-body purity.

The ability to verify the quantum purity and presence of entanglement in the studied quantum many-body state is crucial for discerning the role of entanglement in the system. Fundamentally, the two-copy interference technique used directly provides access to observables that are quadratic in the density matrix and hence to the system’s local and global purity⁸⁹. Other techniques to extract this quantity, such as quantum-state tomography, would be particularly challenging due to the large size of the full 462-dimensional Hilbert space defined by the itinerant particles in the system.

4.3 NON-EQUILIBRIUM SYSTEMS AND HIGHLY EXCITED EIGENSTATES

Much of our conceptual understanding about the link between entanglement entropy and the expected thermal entropy of an ensemble^{161,49} is provided by the eigenstate thermalization hypothesis (ETH)^{48,153,92,177}. ETH provides an explanation for how closed quantum systems come to local agreement with a globally entropic thermal ensemble and is often framed in terms of the small variation of observables associated with eigenstates that are close in energy^{48,153,177}. The role of entanglement in the eigenstates is paramount to this agreement⁴⁹. Fundamentally, the ETH implies

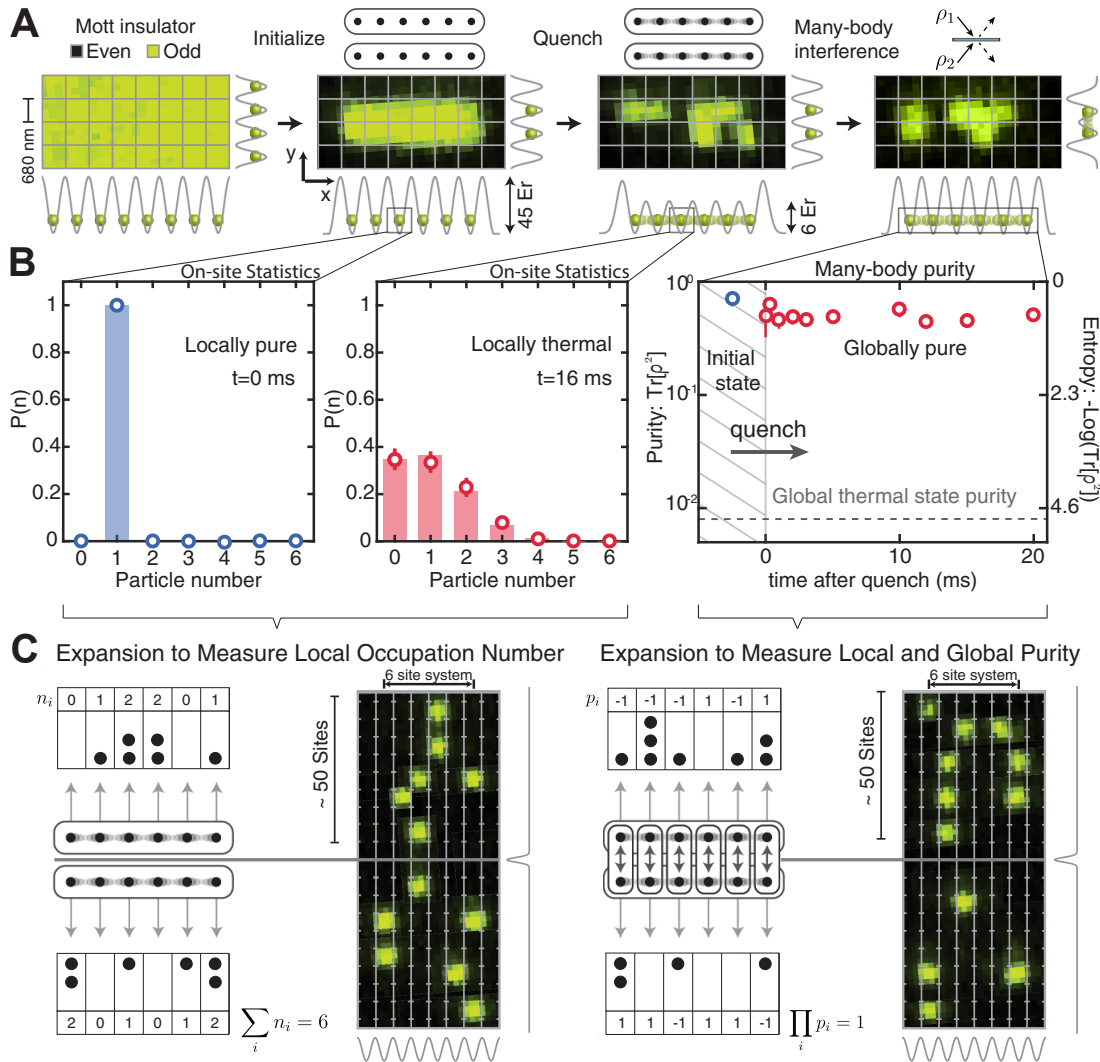


Figure 4.2: Protocol. a) The experimental protocol starts with a unity filled Mott insulator, from which a 2×6 plaquette is sliced out with the installed DMD. The thermalizing unitary dynamics is realized by a sudden quantum quench of the lattice depth down to 6Er . The system is then either imaged in a site-resolve, number-sensitive fluorescence scheme shown in c or a many-body-interference operation is performed on the system to obtain the global and local purities of the system (shown in c). b) The resultant local on-site distributions are shown for the very non-thermal initial state and the thermalized quenched state. The global purity is plotted on the far right to demonstrate how unitary the dynamics are in preserving the global purity (red) of the initial state (blue). c) The two final protocols are shown here: the left) demonstrates a time-of-flight technique used to expand the one-dimensional systems into an orthogonal dimensions such that they may be imaged while avoiding parity projection; the right) demonstrates the same readout protocol after having performed the many-body-interference operation.

an equivalence of the local, reduced density matrix of a single excited energy eigenstate and the local reduced density matrix of a globally thermal state¹³¹.^{*} This equivalence is made possible only by entanglement and the local entropy it induces locally within a globally pure state.

Since we cannot experimentally populate a single, excited eigenstate in the system, we do not probe how the ETH applies at the single eigenstate level. Instead, we perform a quench (Fig. 4.2) which brings the global system far from equilibrium and study the unitary dynamics of the many excited eigenstates populated by this quench. However, since these eigenstates all individually are thermal according to ETH and vary slowly from eigenstate to eigenstate with energy, the quantum average over this superposition of states provide a qualitatively similar result to the single eigenstate.

We examine the presence of thermalization by performing a series of measurements of local observables and comparing them to thermal predictions of various ensembles. The eigenstate distribution resulting from a quench, Fig. 4.3a, determines the resulting dynamic values of the observables and their subsequent saturated values. Importantly, the final values of the Hamiltonian are $U/J_x < (U/J)_c$ where $(U/J)_c$ is the critical point in the superfluid-to-Mott-insulator transition. This is relevant because the eigenstates below this transition point are known to be non-integrable and therefore can be ergodic within global thermodynamic constraints. The underlying explanation for the ETH is that these excited eigenstates in the thermalizing, non-integrable system are nearly like random vectors or, equivalently, are described by a Hamiltonian that is described by random matrix theory^{48,43}. The diffuse probability distribution of eigenstates in most bases, in this case the

^{*}Conceptually, this single eigenstate acts as the minimal version of a microcanonical ensemble and resembles the traditional equilibrium frameworks.

Fock state basis, is analogous to the chaotic dynamics of a closed classical mechanical system that passes through all allowed points of phase space. This chaotic eigenstate assumption, like in the classical system, can be adapted to explain the saturated values of measured local observables, agreement of these saturated values with thermal ensembles, and the presence of a volume law in the entanglement entropy^{48,43,138,86}. The distinction between the classical and quantum cases is that the classical case experiences chaos in its temporal dynamics which realizes both entropy maximization and thermalization as a time-averaged effect. While in the quantum case, these characteristics are directly encoded into the properties of nearly every individual excited energy eigenstate.

In Fig. 4.3c & d, we compare our measurements to the predictions of several thermal ensembles as illustrated in Fig. 4.3b. We also compare our results to a grand-canonical ensemble truncated to our total atom number (see Appendix: G). The grand-canonical ensemble most closely models how well the many-body state can act as a reservoir for its constituent subsystems. For both the single-site and three-site subsystem observables, we show the atom number distributions for two different effective temperatures: $T = 3.8J$ and $T = 11J$. These effective temperatures are achieved by the final quench parameters of the Hamiltonian to $J/U = 0.64$ and $J/U = 2.6$ respectively. The effective temperature is determined by matching the average energy of the quench system with the calculated average energy originating from the population of the global energy eigenstates by a canonical ensemble at temperature T .

For the smallest subsystem considered, the single site, the data are in good agreement with all ensembles considered. This conceptually agrees with our intuition as well since the single site can use all of the remaining system as an effective bath with which to share information and become locally

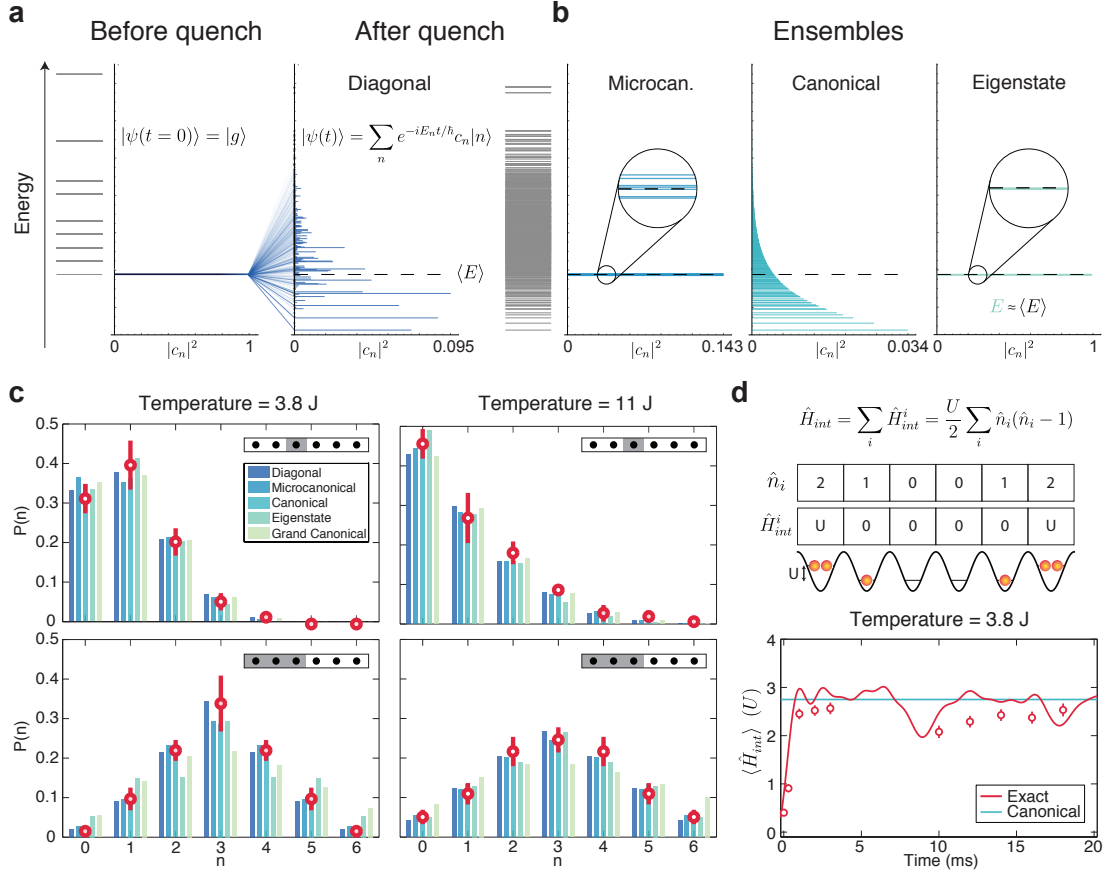


Figure 4.3: Statistical mechanical ensembles. a) The quantum quench populates the initial state across many of the eigenstates in the final Hamiltonian. b) We compare the results of our dynamics to several statistical ensembles: a microcanonical ensemble of a few eigenstates closest to the average global energy, the canonical ensemble where the temperature is chosen such that it has the same average energy, and a single eigenstate in the limit where we take the microcanonical ensemble to admit only the closest eigenstate to the average energy. c) The number distributions are plotted as a function of subsystem size and statistical ensemble prediction. d) The average interaction energy of the full state, a relatively global observable, is also plotted as a function of time which also agrees with the thermal prediction. All data are averaged in the saturated regime 10 – 20ms. error bars are the s.e.m. Eigenstates are found by exact diagonalization.

thermal. Remarkably, despite the fact that the quenched state is a large distribution of eigenstates,

our data show agreement with a microcanonical ensemble* consisting of a single eigenstate which is

*This wording is a bit confusing since a single eigenstate is by definition not an ensemble. However, we use this terminology to relate to the language of statistical mechanical ensembles in the limiting case that a microcanonical ensemble admits only a single eigenstate.

chosen to be the eigenstate with the closest energy to the average. This illustrates the key principle of the ETH; the reduced density matrix and its associated observable values vary slowly from eigenstate to eigenstate and are therefore relatively insensitive to the width of the distribution of populated states from the quench. This agreement between the ensembles and the measured values is relatively good even up to the subsystems of half the system size. The enhanced deviation hints at the fact that this larger sub-system is more sensitive to the fact that the global system is not truly a thermal ensemble.

Since the above measurements rely on the full Fock-state read out, this technique allows for the extraction of other global observables (Fig. 4.3d). Since the interaction term is diagonal in the measured basis (4.1), our measurements allow the computation of the expectation value of the interaction energy $\langle \hat{H}_{int} \rangle = \langle \frac{U}{2} \hat{n}_i(\hat{n}_i - 1) \rangle$. For the $T = 3.8J$ data, we show a time series of both the initial growth of this quantity after the quench and its long-time agreement with the canonical prediction. Since this measurement is sensitive to the entire six-site system, it might at first glance seem to be sensitive to the global state purity and be unlikely to agree with thermalization. However, $\langle \hat{H}_{int} \rangle$ indeed thermalizes because it is a sum of local operators that all agree with thermal predictions and are insensitive to the global purity of the full system. This observation emphasizes that only a small number of global operators, such as global purity, are sensitive enough to truly distinguish the globally pure state from a thermal one.

4.4 ENTROPY FROM ENTANGLEMENT AND THERMALIZATION

While the above results and predictions by the ETH provide a relationship between local predictions of single eigenstates and thermal ensembles, they do not provide any intuition for how the remainder of the system acts as a functional bath. To answer this question, we study the dynamics of entanglement entropy immediately after the quench for a variety of subsystem sizes (Fig. 4.4). Initially, we observe a rapid and approximately linear rise in the entropy with time with a similar slope among all considered subsystems (Fig. 4.4 inset)³³. After a subsystem-size-dependent evolution time, the entanglement entropy saturates to a steady-state value, about which there are small residual temporal fluctuations. The origin of these small residual temporal fluctuations is the finite size of the system.

These observed entanglement entropy dynamics agree well with exact numerical calculations with no free parameters. The data show how the considered subsystems acquire entropy with time even though, crucially, the system as a whole retains only a finite, time-independent entropy that is smaller than the subsystem entropies. The high purity of the global system proves that the dynamical increase in entropy in the subsystems originates in the production of entanglement between the system's constituents. Furthermore, in analogy to the growth of thermodynamic entropy in an equilibrating classical mechanical system, such as a gas in a closed container, we observe the growth of local entropy in a closed quantum mechanical system. The distinction being that in the quantum mechanical case, the mechanism for generating this entropy is through entanglement throughout the global system.

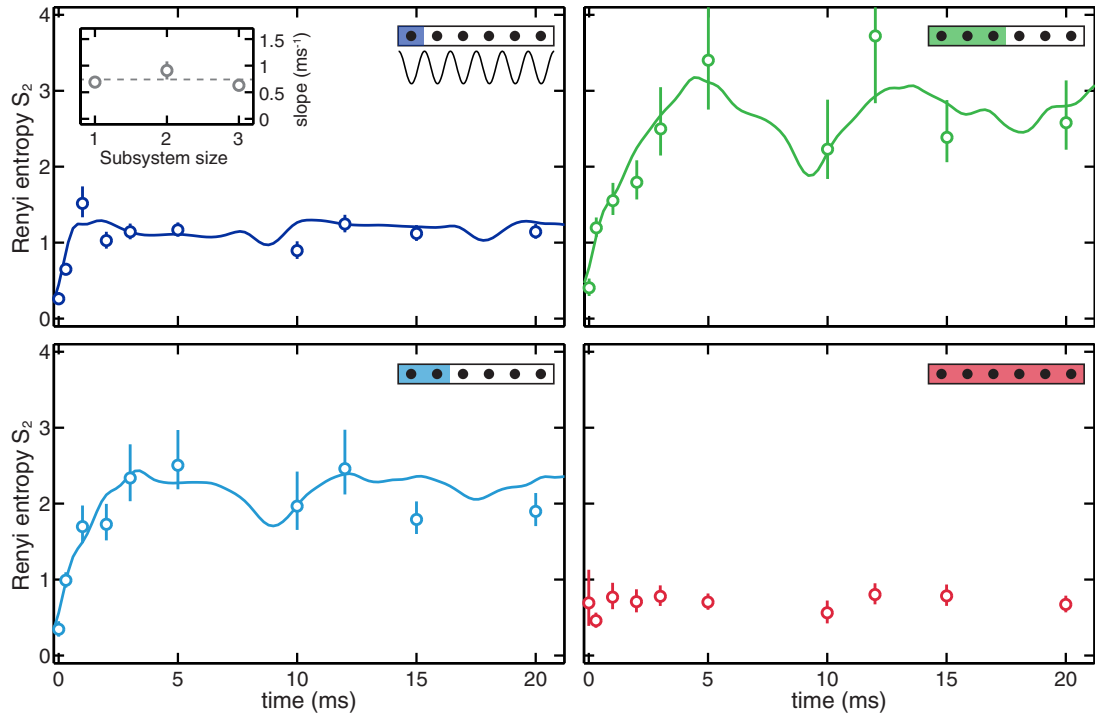


Figure 4.4: Entanglement entropy dynamics and saturation. The second-order Rényi entropy is plotted for three different subsystem sizes as a function of evolution time. Both the time necessary for saturation scales and the fluctuations about the saturated value scale with the system size. The global entropy, plotted in the bottom right (red), remains substantially lower than all the measured local entropies and therefore satisfies that the local entropy is indeed due to entanglement. All error bars are the s.e.m. The solid lines are determined by exact diagonalization with an additional offset added due to extensive classical entropy as measured by the global entropy.

When a system thermalizes, we expect that the saturated values of local observables should correspond to the predictions of a statistical ensemble. By analogy, if the entanglement entropy plays the role of thermal entropy in these ensembles, then in a thermalized pure state, we expect extensive growth in the entanglement entropy with subsystem volume. The linear scaling of the entanglement entropy with the volume of the subsystem being considered is commonly referred to as a volume law. In the case of the studied one-dimensional system this volume is defined by the length of the subsystem considered. Theoretical work using conformal field theory has shown that for

quenched, infinite, continuous systems the long time entanglement entropy should follow a volume law^{32,33,52}. This differs from the ground state entropy scaling considered in the previous chapter (§3) which follows an area law^{183,32,33,52}. Characterizing the large amount of entanglement associated with such a volume law scaling is challenging because it results from small but important contributions of entanglement from many of the available degrees of freedom in a given subsystem.

We observe that the measured entanglement entropy shows a near-volume law behavior with subsystem size. A linear growth with volume in the entanglement entropy occurs when the reduced density matrix of a subsystem incoherently populates a number of its states that approximately scales exponentially with the physical size. This is true for this system since the Bose-Hubbard model has a Hilbert space that scales approximately exponentially with the system size. This results in $S_2(A) = -\log[\text{Tr}(\rho_A^2)] \propto L_A$. While this scaling proportionality of a thermal system is robust, the exact slope of the scaling depends on the average energy of the thermalized pure state^{184,61}.

We can contrast this scaling behavior with the ground state by adiabatically reducing the lattice depth to the same final values as the quenched Hamiltonian. In the case of the superfluid ground state of the Bose-Hubbard model, the system is predicted to have an area law with logarithmically slow correction that depends on the subsystem size³². These two cases are clearly distinguished by our measurements. The bending-over of the entanglement-entropy curve after the half-size subsystem indicates that the state is a globally pure one. Note that this entanglement-entropy curve additionally deviates at the half-size subsystem from the volume-law expectation. This deviation is expected as a result of random pure quantum states and is known as the Page correction¹³⁸.

In the spirit of comparison between thermodynamic ensembles and the local properties of pure

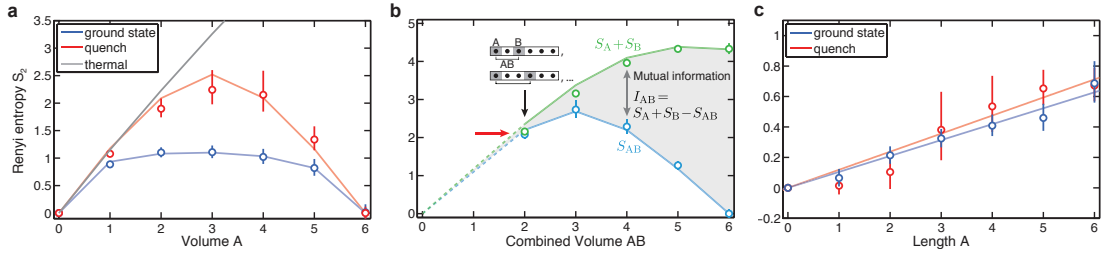


Figure 4.5: Scaling behavior. a) The measured entanglement entropy is plotted as a function of considered subsystem size for both the thermalizing quenched state (red) and the equilibrium ground state (blue). The quenched state has entanglement scaling that qualitatively agrees with a volume and the predicted thermodynamic entropy (gray line). The ground state exhibits a scaling that is consistent with only an area law. Both curves must bend over at the mid point (volume $A = 3$) since they are both pure quantum states. b) In order to look for whether locally thermal systems appear independent, the mutual information between subsystems of sizes less than or equal to the total system size are compared. Once the combined system size is approximately half the system size, the subsystems begin to demonstrate their lack of independence. c) The measured extensive, classical entropy injected into the system during the experiment is determined by subtracting off the expected entanglement entropy from the measured values. The remaining entropy should reflect this truly classical entropy which appears to follow a true volume law up to the system size. The solid lines in a,b are calculated from exact diagonalization. The solid lines in c are from a linear fit. All error bars are the s.e.m.

quantum states, we compare the measured entanglement entropy as a function of subsystem volume with the thermodynamic entropy predicted by a canonical thermal ensemble ρ^T (where T is the effective temperature and ρ^T is determined the same way as written above). We find a near-quantitative agreement between the entanglement entropy and thermal entropy for a subsystem volume smaller than the half-system size. Unfortunately, the total system size limits this comparison to only a few points.

Despite their quantitative similarity, it is worth emphasizing the disparate character of the thermal and entanglement entropies. The entanglement entropy is an instantaneous quantity that is present in a pure state even for an infinitely precise measurement time. It arises from the non-separability of the quantum state between the subsystem and its traced-out degrees of freedom. This realizes an instantaneously truly classical ensemble. This differs in a fundamental way from the clas-

sical case. The von Neumann entropy of a subsystem from a mixed thermal state is the thermodynamic entropy in statistical mechanics and can be extracted from irreversible heat flow experiments on the system⁴⁹. Additionally, from a physical point of view there is another important conceptual difference. At any given instant of time, a classical system resides in a well defined microstate and therefore would actually have zero entropy. Practically speaking however, no measurement is instantaneous and any such attempt to show this exact microstate would result in a time average that would provide the same thermodynamic prediction of a true instantaneous probability distribution. The quantum system, in some sense, actually provides a conceptually simpler picture for nature since the tracing out of any local subsystem will realize a truly mixed ensemble that is valid even instantaneously.

This behavior of entanglement entropy not only provides a useful framework for describing thermalizing closed quantum systems, but also alleviates the need for the ad hoc statements for describing the behavior of classical ensembles. The quantum description encompasses the quantum properties we know to be true for isolated pure quantum systems and can also locally generate the classical properties we know phenomenologically to be true for classical thermodynamic systems. Remarkably, this also implies that one of the most well-known features of entanglement, the presence of non-local correlations, must somehow play a role in this behavior. In particular, the large amount of entanglement implied by the observed volume law suggests a large amount of correlations between disparate parts of the system, whereas a key feature of a thermal state is the absence of such long-range correlations. A useful metric for determining the amount of correlation between two subsystems, both classical and quantum, is the mutual information $I_{AB} = S_A + S_B - S_{AB}$ ^{191,89}.

The mutual information in the presence of a volume law would find vanishing correlations between the two subsystem volumes, as would be the expectation for a thermodynamic statistical ensemble. Our data agrees with this prediction when the total volume considered is less than half the system size ($L_A + L_B \leq L/2$). This agreement breaks down once the total considered volume is a majority of the system size. There are additional bounds on the classically allowable mutual information described in §3 that are violated in Fig. 4.5b. This demonstrates that while two local subsystems will agree with being uncorrelated, as predicted in the thermodynamic case, once their joint subsystem volume grows to encompass a majority of the system, the correlations related to the system being an entangled quantum state are revealed.

4.5 DISCUSSION

These observations and measurements provide a natural link between thermalizing quantum mechanical systems and classical thermodynamic systems composed of itinerant particles. In fact, they allow for an interpretation of the known classical thermodynamic framework as a natural consequence of the quantum-mechanical behavior. They provide some of the justification for the necessary assumptions for classical statistical mechanics: a classical system in thermal equilibrium can be found in any microstate that is compatible with the thermodynamic constraints imposed on the system. The theoretical work related to the ETH demonstrates how this is true for the individual eigenstates of a thermalizing isolated quantum system. The ergodicity associated with exploring all available microstates is also justified even for instantaneous measurements by a quantum system

and does not require time-averaging or multiple realizations of a system to generate a truly entropic ensemble^{43,83,123}. In fact, the superposition of states realizes a truly instantaneous, locally entropic ensemble that requires no additional statements.

This study hints at a microscopic origin for the maximization of entropy in a single quantum state. The ergodic nature of the eigenstates implies the system's entanglement is caused by scrambling correlations among all available degrees of freedom in the system. This scrambling of correlations is what realizes the thermal entropic scaling behavior when considering a small subsystem: a volume law occurs for small subsystem sizes since the amount of information (correlations) gained by including a larger subsystem is outweighed by the amount of new information lost among the all-to-all sharing of information. This fact is captured by the vanishing mutual information between subsystems whose joint volume is still small compared to the total system size.

These frameworks help establish the possibility for many-bodied classical behavior, namely statistical mechanics, to be interpreted as a subset of quantum-mechanical phenomena. The principles postulated classically out of practicality and physical agreement are now implied as the result of only resolving highly entangled quantum systems locally.* While these eigenstate characteristics are not generically predicted for ground states, they are generically predicted for almost all excited eigenstates in itinerant, interacting many-body quantum systems that do not harbor some form of integrability that prevents ergodicity. In the next chapter we will study the only known robust exception to this phenomena, which is known as many-body localization^{131,43}. This exception turns

*To put it bluntly, but not carefully, if the Universe were a non-integrable, interacting many-body quantum system in an excited but pure state, we would still realize a classical world on all practical human length scales.

out to be the only known robust exception to the ETH paradigm and harbors excited eigenstates with characteristic behavior that appears to belong to another phase of eigenstates. This phase forms an extensive number of locally conserved quantities in the Hamiltonian that causes the ETH to fail and harbors unique entanglement dynamics^{18,170,169,84,131}.

*What is different between many-body localization and
the atoms in this table?*

Professor Adam Kaufman

5

Correlation dynamics in many-body localization

In the previous section, the generic behavior for a pure quantum state of an interacting many-body system was presented in the context of the eigenstate thermalization hypothesis (ETH). This hypothesis predicts that when such a system is brought far from equilibrium, it will locally equilibrate

to the prediction of a thermal ensemble while remaining in a pure quantum state. This prediction relies on the fact that the eigenstates themselves are chaotic and are in a superposition of all (many) of the available microstates that satisfy global thermodynamic constraints^{48,177,153,132,99}. A consequence of this eigenstate property is that local information about the initial state is scrambled and transferred into non-local correlations that are only accessible through a few special global observables.

A narrower class of systems that do not exhibit such chaotic eigenstates are known as integrable systems. They harbor an extensive set of locally conserved quantities that prevent the ergodic phase space exploration required for the ETH and classical statistical ensembles⁴³. In the case of non-interacting systems, the addition of local disorder was shown to create all eigenstates of the system to be constructed out of localized orbitals^{8,166,22,155,107,45,58,105,91,47}. These localized orbitals become the extensive set of locally conserved quantities that makes the system an integrable one. The addition of inter-particle interactions was thought to generically lead to the breaking of this integrability by allowing for hybridization between these localized orbitals return the system to a thermalizing one.* However, as speculated by *Anderson*⁸ it turns out that even in the case of relatively strong interactions, the addition of sufficiently strong disorder can make the system integrable and inhibit thermalization. This paradigmatic example of such an integrable, many-body system is known as many-body localization (MBL)^{131,8,104,168,65,19,134,185}. Since the system does not thermalize, its dynamics do not lead to relaxation of an initial state through the scrambling of all local information

*In a classical sense, the thought would be that inter-particle interactions would allow for ergodic exploration of phase space since interactions would allow the particles to exchange energy and eventually equilibrate in their potential landscape – although it may take a very long time.

throughout the remaining system – using it as a functional bath like. Such an onset of localization has previously been probed by a lack of thermalization (i.e. lack of ergodic space exploration) in a system of interacting particles^{164,176,37}.

We will explore many-body localization for a Bose-Hubbard system where on-site disorder is used to suppress the transport of particles in the system and, in doing so, preserves a memory of the initial state that signals a lack of ergodic exploration of the system. We observe this onset of integrability at a finite disorder strength and can independently probe the localization of particles. Importantly, we additionally verify the system is an interacting, many-bodied one: even though particle transport has been suppressed, the interactions in the system continue the spread of non-local correlations throughout the system¹¹⁸. These non-local correlations exist within the manifold of available states that are limited by particle localization. These dynamics are considered to be the hallmark of MBL are absent for a localized, non-interacting system. These characteristics are due to the change in the behavior of nearly all the eigenstates in the system and realize a non-equilibrium phase of the quantum system. It is additionally the only known robust form for breaking ergodicity and the application of the ETH in an interacting system¹³¹. Unlike other integrable, interacting systems, MBL is not fine tuned and small perturbations applied to the system do not destroy its integrability.

5.1 LOCALIZATION IN THE INTERACTING AUBRY-ANDRÉ MODEL

In our experiments, we study MBL in the interacting Aubry-André model for bosons in a one-dimensional lattice^{84,13}. This model is described by the Hamiltonian:

$$\hat{H} = -J \sum_i \left(\hat{a}_i^\dagger \hat{a}_{i+1} + h.c. \right) + \frac{U}{2} \sum_i \hat{n}_i (\hat{n}_i - 1) + W \sum_i h_i \hat{n}_i \quad (5.1)$$

where the on-site potential offsets are derived from an incommensurate (quasi-periodic) distribution described by $h_i = \cos(2\pi i \beta + \phi)$ with a spatial frequency of $\beta \approx 1.618 \text{ sites}^{-1}$ as an approximation of the golden ratio ($\beta_{GR} = \frac{\sqrt{5}+1}{2}$). * The phase offset ϕ is changed for different measurements such that the results are characteristic of a general phenomena and not descriptive of a single potential realization. We use the DMD discussed earlier in this thesis (§2.2) to project this on-site potential offsets onto the bare lattice with some overall scaling strength represented by W in (5.1).

Observing the slow coherent dynamics in the many-body localized system additionally requires the quantum system remains well isolated from the environment for long experimental times. Since the optical path for the optical lattice and the projected on-site potentials are not the same, any residual physical vibrations on the optical table or air currents in the optical path will result in relative

*This is often called “quasi-periodic disorder” to describe this distribution of offsets. While the function is, of course, exactly periodic, its ratio is incommensurate with the physics lattice periodicity and hence any given on-site offset will never be resampled in the system on any length scale. This intrinsic prevention of resampling adds inherent structure to the system that lead to spatial correlations that should discourage one from thinking of it as truly “disorder” as investigated for the Anderson localization problem. However, for a practical comparison of both localizing phenomena, it is the on-site potential that leads to localization and hence inherits the common terminology of “disorder”.

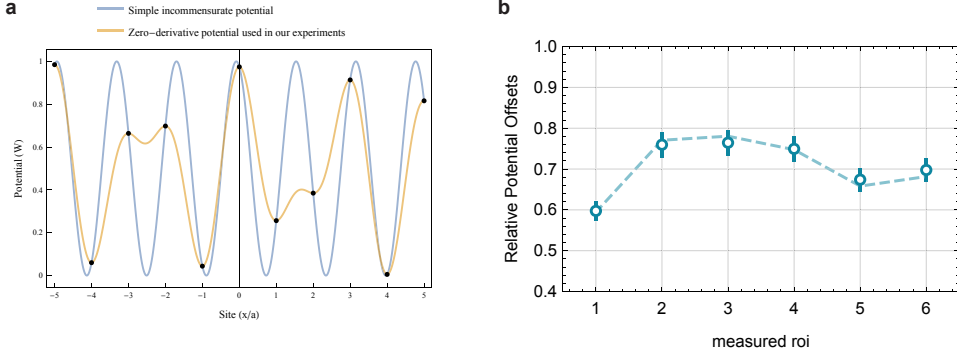


Figure 5.1: Applied on-site potential and calibration. a) The theoretically prescribed quasi-periodic potential (blue) and the physically implemented potential (yellow) are plotted together to show that they sample the same points at every physical lattice site. Importantly, the implemented potential has extrema at each lattice site which is locally quadratic and is therefore insensitive to shaking at first order. b) The applied DMD potential was calibrated by a method mentioned in §2.4.4 where we find excellent agreement between the predicted relative potential offsets and the measured ones. All error bars are the s.e.m.

shaking between the two potentials. In the bare formulation of h_i , as written above, some sites additionally have a non-zero potential gradient ($dh(x)/dx|_{x=x_i} \neq 0$). Any shaking of the optical path will realize this on-site potential gradient into an on-site potential modulation $h_i(t)$ that prevents the system from being time-independent; effectively, this weakly couples the system to an infinite temperature bath on every site of the lattice. We adjust this original potential formulation to a new functional form, \tilde{h}_i that realizes the same on-site potential but additionally has zero slope at each lattice site:

$$\begin{aligned}\tilde{h}_i &= (2 - \beta) \cos^2 \left(\pi(\beta - 1) \frac{(x - x_i)}{a} + \phi \right) + (\beta - 1) \cos^2 \left(\pi(\beta - 2) \frac{(x - x_i)}{a} + \phi \right) \\ &= \frac{(2 - \beta)}{2} \left[e^{i(\pi(\beta-1)\frac{(x-x_i)}{a}+\phi)} + e^{-i(\pi(\beta-1)\frac{(x-x_i)}{a}+\phi)} \right]^2 \\ &\quad + \frac{(\beta - 1)}{2} \left[e^{i(\pi(\beta-2)\frac{(x-x_i)}{a}+\phi)} e^{-i\pi/2} + e^{-i(\pi(\beta-2)\frac{(x-x_i)}{a}+\phi)} e^{-i\pi/2} \right]^2\end{aligned}\quad (5.2)$$

where ϕ is the same phase offset as in the original formulation of h_i and a is the lattice constant.*

This potential is realized by projecting two lattices with different periodicities ($\beta - 1, \beta - 2$) but with a fixed, relative optical phase difference of $\pi/2$ that allows one to add the two potentials incoherently in (5.2). This physically will appear like the projection of two overlapping optical lattices as shown in Fig. 2.2 that have a varying angle of incidence to the atoms to control these new spacings. However, both sets of lattices are implemented via a phase hologram displayed on the DMD (Fig. 2.5). If this were performed with two retro-reflected lattices where the periodicity and temporal frequency are a fixed relationship, then this would provide the same effective potential due to the rapidly rotating terms from interference of the two beams averaging to zero. An example realization of this potential is shown in Fig. 5.1 along with the calibrated neighboring, relative potential offsets as demonstrated in §2.4.4.

The agreement with our calibrated disorder patterns and intended on-site potential patterns demonstrate the precision with which the system is understood. We use 197 different on-site potential patterns for almost all of the measured observables in the following experiments by uniformly choosing $\phi \in [0, 2\pi)$. These implemented potentials have on-site statistics and neighboring potential offsets that are very close to a truly quasi-periodic distribution (Fig. 5.2). The difference between the ideal distribution and the sampled one is a lack of a strong peak in Fig. 5.2a at $W_i = 0$ that mimics the one at $W_i = 1$. For all intents and purposes, this mostly effects the width of the distribution

* Any integer change of β will realize an incommensurate potential that has the same on-site values with respect to the optical lattice periodicity. This allows for effectively decomposing an idealized incommensurate on-site offsets in a Fourier series to reduce all higher order effects and realizes a step like change between sites. This process is unnecessary in this case and would be physically limited by the wavelength of the light used.

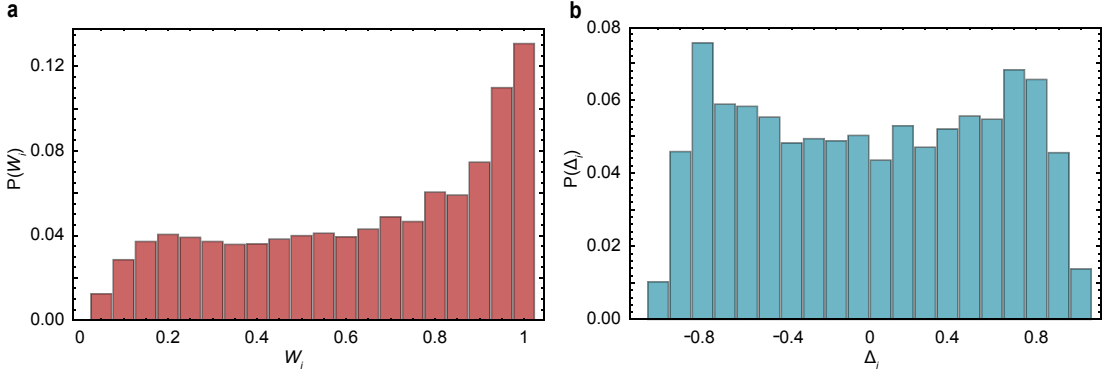


Figure 5.2: On-site potential histograms. a) A histogram of the expected on-site potentials (red) from the applied quasi-periodic distribution. b) A histogram of the expected neighboring potential differences (blue) from the applied quasi-periodic distribution.

in Fig. 5.2b. The qualitative physics of MBL remains the same, however to compare results quantitatively with an ideal quasi-periodic distribution, one must increase the disorder strength by ≈ 1.25 .

5.2 BREAKDOWN OF THERMALIZATION

Our experimental protocol is very similar to that described in §4.2 and is shown in Fig. 5.3b. Our experiments begin in the Mott-insulating state with unity filling in a two-dimensional optical lattice. We first use the DMD to isolate a single, one-dimensional chain from the Mott insulator and then add the on-site potential offsets h_i . We then abruptly switch on the tunneling by reducing the lattice depth within a fraction of a tunneling time which realizes a quantum quench as in our previous study (Fig. 5.3c). The final Hamiltonian parameters are given by a tunneling time $\tau = \hbar/J = 4.3(1)\text{ms}$ and $U = 2.87(3)J$ and remain constant for all experiments. We allow the system to evolve by unitary evolution in this Hamiltonian for a variable amount of time at the end of which we perform the same number-resolved imaging as in the previous chapter (§4.2). Since particle loss

during the evolution of the system realizes a form of coupling to an external bath, we post-select on all images such that they contain the same number of atoms as intended for state initialization. In this way, we realize an on-site single-particle occupation fidelity of 99.1(2)%. This is limited by the fraction of doublon-hole pairs in the initial Mott insulator.*

We first investigate the breakdown of thermalization in a subsystem that consists of a single lattice site. The conserved total atom number N enforces a one-to-one correspondence between the particle number outcome on a single site n_a and the outcome in the remainder of the system $n_b = N - n_a$ – entangling the two subsystems via tunneling dynamics. Ignoring information about the remaining system makes the single-site a completely mixed state of different on-site occupation numbers. The associated number entropy is given by $S_n^{(1)} = -\sum_n p_n \log(p_n)$, where p_n is the probability of finding n atoms on the single-site. Due to the one-to-one correspondence mentioned above, this implies the lack of any off-diagonal (coherence) terms in the reduced density matrix. This is equivalent to saying that measuring the on-site number occupation for a single-site extracts all information available to that subsystem's reduced density matrix. Hence, $S_n^{(1)}$ is the single-site von Neumann entanglement entropy $S_{vN}^{(1)}$ as long as the system is globally pure.

Counting the atom number on an individual lattice site in different experimental realizations allows us to obtain the probabilities p_n and compute $S_{vN}^{(1)}$. We perform such experiments for various evolution times. At a low disorder strength ($W = 1.0(1)J$), the entropy grows over a few tunnel-

*This number differs from the measured in-situ occupations of the unity-filling Mott-insulating shell. However, this is largely due to the loss during imaging that reduces this on-site fidelity and is not due to thermal excitations in the Mott insulator.

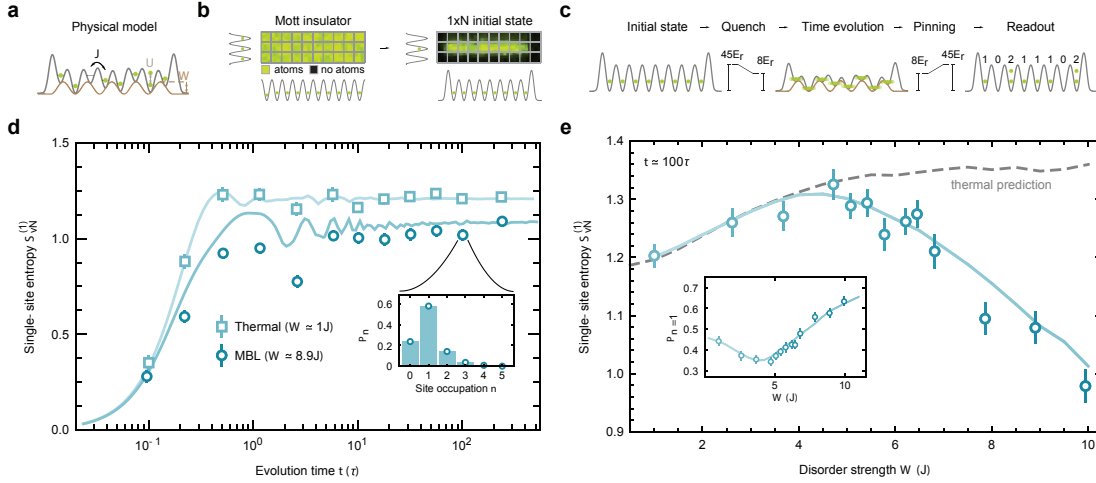


Figure 5.3: Breakdown of thermalization. a) The physical model is illustrated here as an interacting Bose-Hubbard model with on-site potentials sampled from a quasi-periodic distribution. b) All experiments start from a unity-filling Mott-insulating state. The DMD is then used to create a single 1×8 site system. c) The quench protocol is outlined here where the 1×8 site initial state is evolved by unitary dynamics for a variable evolution time t in the interacting Aubry-André Hamiltonian. The state is then read out with single-site and number-resolved fluorescence imaging technique elucidated in §4. d) The single-site von Neumann entropy, $S_{VN}^{(1)}(t)$, is plotted as a function of time for two different disorder strengths: ($W = 1J$), which corresponds to the thermalizing regime, and ($W = 8.9J$), which corresponds to the many-body localized regime. Note that the MBL regime has suppressed single-site entropy that persists up the longest evolution times. e) The measured single-site entropies at the end of the unitary evolution are then compared to the prediction by a thermal ensemble as a function of the applied disorder W . The single-site entropy agrees with the thermal prediction up to a finite disorder strength, at which point it becomes sub-thermal and consistent with numerics. The inset shows the probability of the site retaining exactly one atom, which is akin how well the site remembers the initial state. All solid lines are calculated by exact diagonalization. All error bars are the s.e.m.

ing times and then reaches a stationary value (Fig. 5.3).^{*} This stationary value is suppressed for larger disorder ($W = 8.9(1)J$) and remains constant over two orders of magnitude in evolution time. The lack of entropy increase indicates the absence of heating from an external source in the system – as indicated by the agreement with the exact diagonalization calculations of the coherent dynamics up to longest measured evolution times.

*The naive assumption would be that the non-disordered regime should saturate in approximately a single tunneling time τ . However, the plot in Fig. 5.3a curiously saturates for this regime in $t \approx \frac{1}{2}\tau$. This is because of the fact that J is defined for the field of the wave function and has the same consequence in the traditional Rabi problem where the oscillations happen with a frequency twice as fast as the driving field Ω .

To determine the effect of disorder strength on this saturated value, we measure the $S_{vN}^{(1)}(W, t = 100\tau)$ in Fig. 5.3e. To evaluate the degree to which this agrees with local thermalization, we compare the result with the prediction of a microcanonical thermal ensemble for our system (compare predictions from previous chapter §4.3). For weak disorder, the measured entropy agrees with the prediction of a thermodynamic ensemble up to a finite disorder strength – we use this agreement to identify this regime a “thermalizing” one. As disorder is increased, we observe an increasingly large departure from the prediction of thermal equilibrium. This sub-thermal regime retains memory of the initial state which initially has no on-site fluctuations and therefore reduced entropy in comparison to the thermal prediction. The degree to which the single-site relaxation differs from this thermal prediction increases for stronger disorder. This memory of the initial state (Fig. 5.3e inset) is the same metric by which other experiments of localization in interacting systems have measured a lack of thermalization^{164,27,176,37,120}.

5.3 LOCALIZATION OF PARTICLES

This observed breakdown of thermalization is expected to be a consequence of the spatial localization of the constituent particles in the system. For point-like interactions between particles, particle transport becomes a necessary condition for exchange of energy to allow relaxation towards equilibrium. The lack of such transport has been previously observed as a localization length of an initially prepared density step into empty space³⁷. We simultaneously measure this localization as well as the breakdown of thermalization by directly probing density-density correlations within

the system while maintaining the average density in the system. These correlations are captured by

$G^{(2)}(d) = \langle n_i n_{i+d} \rangle - \langle n_i \rangle \langle n_{i+d} \rangle$, where $\langle \dots \rangle$ denotes simultaneously averaging over different disorder realizations as well as all sites i of the chain. The particle number on two sites at distance $d > 0$ are uncorrelated for $G^{(2)}(d) = 0$. If a particle is coupled to a site a distance d away, then the sites become anti-correlated, and the correlator decreases to $G^{(2)}(d) < 0$.

An important contribution to these correlations relates to the structure of the applied on-site potentials themselves. The on-site potential h_i has a non-vanishing autocorrelation function $A(d) = \langle h_i h_{i+d} \rangle_i$ (Fig. 5.4b) at all distances that is inherited by the fluctuations in the density-density correlations that we need to account for when extracting the localization length ξ . From this we construct an ansatz fit function:

$$G^2(d) = (a + b \times A(d))e^{-d/\xi} \quad (5.3)$$

which is shown on top of the data and exact theory in Fig. 5.4c. We exemplify how we extract a length scale from the measured the density-density correlations $G^{(2)}(d)$ in Fig. 5.4: we show a comparison of the measured correlations, the exact diagonalization, and the ansatz for the functional form (5.3) of the correlations.

From these fits we extract the correlation length ξ from the long-time saturated correlations to probe the relationship between disorder strength and localization. At low disorder ($W = 1J$), we find these correlations to be independent of distance and at a constant, negative offset. This indicates that the particles are able to tunnel across the entire system and hence are delocalized (Fig. 5.5c).

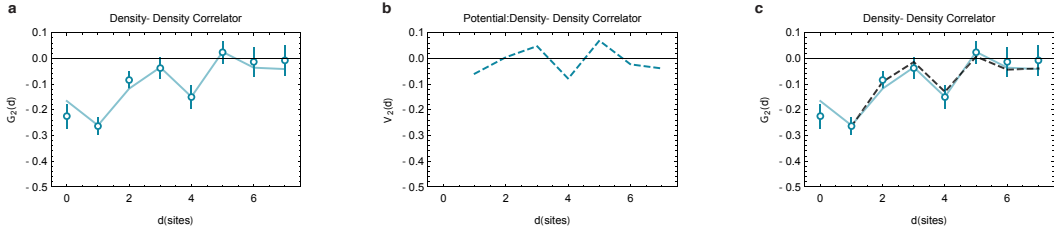


Figure 5.4: G_2 data, theory, and fit function. **a)** The raw data and exact theory are plotted after an evolution time $t = 100\tau$ at a disorder strength $W = 4.8(1)J$. **b)** The autocorrelation function of the on-site potential distribution, $A(d) = \langle h_i h_{i+d} \rangle_i$, is plotted as a function of inter-site distance. **c)** Combines the measured data, the exact theory, and the ansatz fit function (5.3) that incorporates the autocorrelation function of the on-site potentials. The theory is calculated by exact diagonalization. The error bars are the s.e.m.

In the regime of strong disorder ($W = 7.9J$), only nearby sites show significant correlations and demonstrate the suppression of particle motion across large distances. We thus conclude that the particles are localized in this regime. We then plot the extracted localization length ξ as a function of disorder in Fig. 5.5c where the correlation length exists at the system size limit until a finite disorder strength where it is reduced to the smallest measured value of ≈ 1 site.

The observation of localized particles is consistent with the description of MBL in terms of local integrals of motion^{170,169,84}. This model was initially formulated for MBL in a spin system, but can be extended to lattice bosons. It describes the global eigenstates as a product of exponentially localized orbitals. The correlation length extracted from our model is a measure of these orbitals. Since the latter form a complete set of locally conserved quantities that prohibit an ergodic exploration of all available phase space with respect to global thermodynamic constraints (total energy, total particle number, etc.), this picture connects the breakdown of thermalization in MBL with integrable systems.

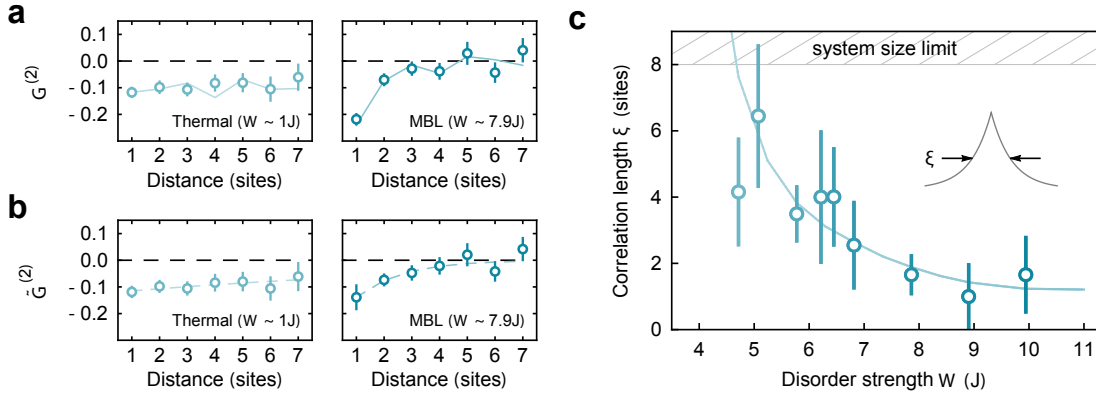


Figure 5.5: Localization. **a)** The measured two-point correlations, $G^{(2)}(d)$, are plotted for both the thermalizing ($W = 1J$) and MBL ($W = 7.9J$) regimes. **b)** By removing the non-monotonic behavior of the on-site potential correlations we visualize the localization of the distribution $\tilde{G}^{(2)}(d) = G^{(2)}(d) - b \times A(d)e^{-d/\xi}$. **c)** The extracted correlation length ξ is then plotted as a function of disorder depth W . This correlation length ξ becomes smaller than the system size at the same finite disorder at which thermalization breaks down in the system. All solid lines are calculated from exact diagonalization. The dashed lines are the results of a fit (5.3). The error bars are the s.e.m.

5.4 ENTANGLEMENT DYNAMICS IN AN INTERACTING, MANY-BODY LOCALIZED SYSTEM

Up till this point, the role of interactions in this many-body system has been solely related to the concept of thermalization and non-integrable systems. However, since non-interacting systems are already known to Anderson localize it may seem like purely a competition of two effects in this system: i) thermalization when disorder is low and interactions and transport realize ergodic, thermal eigenstates, and ii) localization when disorder is so large that it dominates energy scale and effectively breaks up the system into a series of disconnected, localized, non-interacting chunks. However, this picture was shown by Bardarson *et al.*¹⁸ as an inaccurate description of the system. In this pioneering theory work, it was shown how the bipartite entanglement entropy dynamics of a disordered spin system differs between a non-interacting and an interacting system. A non-interacting

system only realizes the rapid relaxation akin to the observed single-site entropy measured in Fig. 5.3.

However, any infinitesimal interaction between particles/spins will lead to long term entanglement growth that is logarithmically slow with time. This result led to the identification of the logarithmically slow entanglement growth as the distinguishing behavior that realizes the unique characteristics of a strictly interacting*, many-body localized system.[†]

Discerning the unique entanglement growth in a many-body localized system requires a precise understanding of how correlations can develop due to unitary evolution of this pure quantum state.

In a Bose-Hubbard chain with fixed global particle number, there are two classes of degrees of freedom that contribute to the bipartite entanglement entropy: i) the number of particles in a given subsystem, and ii) the way those particles are configured among the available lattice sites in the subsystem. Mathematically, this can be separated exactly for the von Neumann entropy, $S_{vN} = S_n + S_c$. This becomes clear if we consider the reduced density matrix ρ_A of subsystem A in the Schmidt basis ρ_{ii} :

$$S_{vN} = \sum_i \rho_{ii} \log (\rho_{ii}) \quad (5.4)$$

*Nearly all literature or researchers in this field will exclude this “interacting” descriptor. Strictly speaking, a system of many, non-interacting bodies would also localize (i.e. Anderson localization) and is the exact comparison given in Bardarson, *et al.*. However, it is the fact that the many-bodies interact at all that give rise to the unique dynamics and so I add this qualifier here for emphasis and clarity only.

[†]An additional comment is that a significant distinction here is that *both* regimes, delocalized and the localized, can be provably shown to be interacting ones. Non-interacting systems without disorder will be delocalized but are also strictly non-thermalizing systems: the energy per particle is an additional, extensive constraint on the system and once again realizes an integrable system. Therefore, simply demonstrating that a system delocalizes or localizes are *insufficient* observables – although they are considered to be necessary ingredients for thermalization and its breakdown, respectively. In a many-body localized system, it is the logarithmically slow entanglement growth that defines the system as being localized in the presence of interactions.

Since the global particle number is conserved, the same argument for a single-site having no coherences between different particle numbers in a subsystem holds also for larger subsystems; there is again a one-to-one, unique relationship between with a given number of particles in subsystem A and subsystem B ($N_A, N_B = N - N_A$). This permits us to break up (5.4) into a double sum over the particle number n in a given subsystem and then all states i within that manifold:

$$S_{vN} = \sum_{n=0}^N \sum_i p_n \rho_{ii}^{(n)} \log(p_n \rho_{ii}^{(n)}) \quad (5.5)$$

where p_n refers to the probability of a populating the manifold of n atom states in subsystem A. This can be understood graphically (see Fig. 5.6a) as the reduced density matrix being a block diagonal matrix where the population of each block is given by p_n and each respective block within the n atom manifold $(\rho_{ii}^{(n)})$ may be individually diagonalized and normalized $(\sum_i \rho_{ii}^{(n)} = 1)$.* By exploiting the lack of coherences between blocks and the normalization of each block, S_{vN} can be

*In the single-site regime, each of these blocks $\rho_{ii}^{(n)}$ is reduced to containing only a single state. Since this block has only one entry it cannot have any internal coherences. Hence, measuring single-site occupation number is all the information available.

reduced to a sum of two separate contributions: S_n and S_c (5.6).

$$\begin{aligned}
S_{vN} &= \sum_{n=0}^N \sum_i p_n \rho_{ii}^{(n)} \left[\log(p_n) + \log(\rho_{ii}^{(n)}) \right] \\
&= \sum_{n=0}^N p_n \log(p_n) \sum_i \rho_{ii}^{(n)} + \sum_{n=0}^N p_n \sum_i \rho_{ii}^{(n)} \log(\rho_{ii}^{(n)}) \\
&= \sum_{n=0}^N p_n \log(p_n) + \sum_{n=0}^N p_n \sum_i \rho_{ii}^{(n)} \log(\rho_{ii}^{(n)}) \\
&= S_n + S_c.
\end{aligned} \tag{5.6}$$

This separation of contributions to entanglement by types of correlation between the two subsystems gives rise to exactly the separation of identifying behavior in many-body localization (Fig.5.6).

It also qualitatively reflects the original results presented in *Bardarson, et al.*¹⁸ and distinguishes between the contributions to entanglement from atom delocalization, which can arise in a non-interacting system (S_n), and the contribution from atom-atom interactions that gives rise to a persistent growth of entanglement (S_c).

The entropy generated by fluctuations in particle number in a given subsystem is suppressed by the presence of localization and has the same early-time saturation behavior as for single-site in the system. The entropy associated with configurations of particles within a given block of the density matrix, however, can still slowly develop correlations with the remainder of the system and is solely responsible for the logarithmically slow entropy growth used to distinguish interacting, many-body-localized systems.

This separation of correlation contributions additionally provides some intuition for discerning

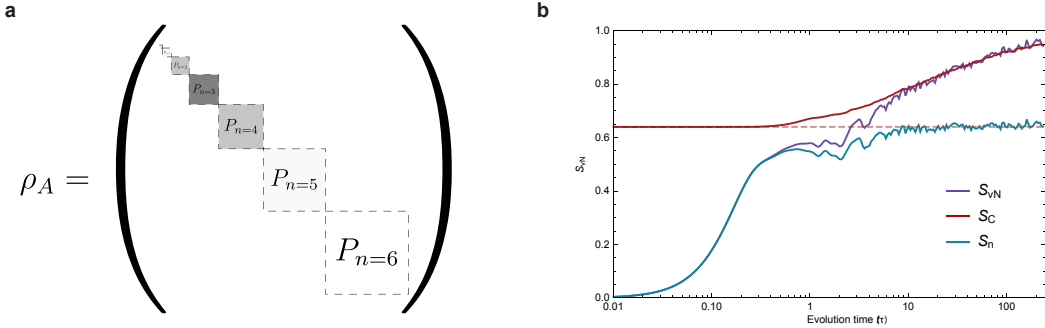


Figure 5.6: Degrees of freedom and entropy. a) Shows an illustration for the reduced density matrix ρ_A of a system where the subsystem size is larger than a single lattice site. The size of the blocks in this system refer to the Hilbert space within the manifold of states that contain n atoms in the subsystem. The shading refers to the probability of populating states in that block, P_n . b) The bipartite von Neumann entropy plotted is for half-size subsystem with a total size of $L = 6$ sites. The separate contributions to this entropy, S_n and S_c , provide independent metrics for distinguishing the rapid relaxation and the slow, non-local correlations built up by the presence of interactions in the system. The solid lines are produced for exact diagonalization.

the difference in the dynamics of Anderson localized, many-body localized, and thermalizing systems. In a thermalizing system, the lack of disorder allows for particle to rapidly transport through the whole system, and build correlations between the two subsystems by both particle exchange across the subsystem boundary, and interactions between particles that cause correlations between particular configurations in the two subsystems.

5.4.1 PHENOMENOLOGICAL DESCRIPTION OF LOCALIZED ORBITALS: NON-INTERACTING

To better elucidate how entanglement develops in these localized systems, we will refer to a phenomenological model adapted from spin systems to a Bose-Hubbard, which is written in the physical on-site basis below:

$$\hat{H} = -J \sum_i (\hat{a}_i^\dagger \hat{a}_{i+1} + h.c.) + W \sum_i h_i \hat{n}_i \quad (5.7)$$

In this Anderson localized (i.e. non-interacting) regime, the particles are exponentially localized to their initial site by disorder. We will assume we are in the regime $W \gg J$ for simplicity. This localization hints to the fact that eigenstates of the system may be built out of a product of creation operators that populate such localized orbitals with individual atoms $\hat{\mathcal{A}}_k^\dagger$.^{*} We can find much of the phenomenological physics by expressing such an exponential orbital a superposition of on-site creation operators with exponentially decreasing amplitude. We can think of eigenstates of this system as being built out of quasi-local creation operators:

$$\hat{\mathcal{A}}_k^\dagger \sim \frac{1}{N} \sum_j \hat{a}_j^\dagger e^{i\phi_j} e^{-|x_j - x_k|/\xi} \quad (5.8)$$

where the only degree of freedom being the phase ϕ_j of the exponentially decaying amplitude on these sites and enables these orbitals to be constructed such that they are orthogonal $(\langle 0 | \hat{\mathcal{A}}_{j \neq k} \hat{\mathcal{A}}_k^\dagger | 0 \rangle = 0)$. In the Anderson localized case, the exponentially localized particles are eigenstates of the non-interacting disordered Hamiltonian and only these many-body phases evolve in time. This evolution happens because of the local potential offsets \tilde{W}_k they experience and therefore can be described by an effective Hamiltonian:

$$\hat{H}^{eff} \sim \sum_k \tilde{W}_k \hat{\mathcal{A}}_k^\dagger \hat{\mathcal{A}}_k \quad (5.9)$$

Note that this effective Hamiltonian is diagonal in the basis of the occupation number of lo-

^{*}This concept is intentionally presented to be similar to populating local Wannier functions in a lattice with \hat{a}^\dagger , which it will reduce to in the infinitely-deep disorder limit as $\xi \rightarrow 0$.

calized orbitals $\hat{\mathcal{A}}_k^\dagger \hat{\mathcal{A}}_k$ and therefore, in this localized orbital basis, creating such an eigenstate will evolve in a global phase. Let us consider a simple initial state that is separable but in a superposition of these localized orbitals:

$$|\psi_o\rangle = \frac{1}{\mathcal{N}} \left(I + \hat{\mathcal{A}}_0^\dagger \right) |0_0\rangle \otimes \left(I + \hat{\mathcal{A}}_1^\dagger \right) |0_1\rangle \quad (5.10)$$

In the case of a non-interacting system, the temporal dynamics of this initial state simply depend upon the local orbital occupation number:

$$|\psi_o(t)\rangle = \frac{1}{\mathcal{N}} \left(|0_0\rangle + e^{i\tilde{W}_0 t} |1_0\rangle \right) \otimes \left(|0_1\rangle + e^{i\tilde{W}_1 t} |1_1\rangle \right) \quad (5.11)$$

In the basis of the localized orbitals, the dynamics of the system are entirely contained in the local phase evolution of the populated orbital and preserve the separability of the initial state – they remain unentangled at all times. Importantly, however, in the basis of physical lattice sites, such a state would still retain some entanglement from particle number fluctuations across a real-space bipartition that cuts through all the $\hat{\mathcal{A}}_k^\dagger |0\rangle$ states at some physical site index. In fact, our original formulation of $\hat{\mathcal{A}}_k^\dagger$ (5.8) as an exponentially decaying amplitude of on-site creation operators \hat{a}_k^\dagger suggests (correctly it turns out) that eigenstates have an area-law scaling of entanglement entropy (§3). Importantly, though this entanglement does not grow as a function of time (5.11).

5.4.2 PHENOMENOLOGICAL DESCRIPTION OF LOCALIZED ORBITALS: *INTERACTING*

We will use conceptually expand the framework presented above to think about the interacting regime by adding very weak but non-zero interactions:

$$\hat{H} = -J \sum_i (\hat{a}_i^\dagger \hat{a}_{i+1} + h.c.) + \frac{U}{2} \sum_i \hat{n}_i (\hat{n}_i - 1) + W \sum_i h_i \hat{n}_i \quad (5.12)$$

In this many-body localizing Hamiltonian, we will work in the regime where $W \gg J \gg U$.

We see from the formulation above that the interaction occurs for multiply occupied sites in the physical basis. Attempting to adapt our intuition of the eigenstates from the non-interacting basis, we would suspect that in this weakly interacting limit the system will still be constructed out of localized orbitals. The difference being that where orbitals overlap they will see an energy shift due to the particle-particle interaction that exists in our bare physical basis:

$$U_{j,k}^{eff} \sim \frac{U}{2} \sum_i e^{-|x_i - x_k|/\xi} e^{-|x_i - x_j|/\xi} \sim \tilde{U} e^{-|x_j - x_k|/\xi} \quad (5.13)$$

where we only include overlap from two orbitals centered about sites- j and k since overlap with successively more orbitals will exponentially decrease in strength.* It remarkably turns out that this concept is approximately true and we can again reconstruct eigenstates form localized quantities^{170,169,84†} which we will now construct from new creation operators $\hat{\mathcal{L}}_k^\dagger$. We can incorporate this

*They may need to be considered in terms of finding the correct quantitative values for the dynamics of a system, but to see the phenomenological dynamics we can stop at this second-order non-local interaction.

†It is very tempting to assume $\hat{\mathcal{L}}_k^\dagger \sim \hat{\mathcal{A}}_k^\dagger$. However, this is importantly not the case. It is the many-body states that are hybridized by the interactions (i.e. $\hat{\mathcal{L}}_j^\dagger \hat{\mathcal{L}}_k^\dagger |0\rangle \sim (\hat{\mathcal{A}}_j^\dagger \hat{\mathcal{A}}_k^\dagger + \alpha \hat{\mathcal{A}}_j^\dagger \hat{\mathcal{A}}_j^\dagger + \alpha' \hat{\mathcal{A}}_k^\dagger \hat{\mathcal{A}}_k^\dagger + \dots) |0\rangle$).

interactions into our new Hamiltonian built out of our new localized creation operators below:

$$\hat{H}^{eff} \sim \sum_k \tilde{W}_k \hat{\mathcal{L}}_k^\dagger \hat{\mathcal{L}}_k + \sum_{j,k} U_{j,k}^{eff} \hat{\mathcal{L}}_j^\dagger \hat{\mathcal{L}}_j \hat{\mathcal{L}}_k^\dagger \hat{\mathcal{L}}_k \quad (5.14)$$

While this Hamiltonian also has eigenstates that are constructed out of quasi-local creation operators ($\hat{\mathcal{L}}_k^\dagger$), the evolution of the phases now depends upon a non-local interaction term between the population of spatially separated, localized orbitals. In particular, if we return to our original initial state example, $|\psi_o\rangle$, the dynamics of the many-body states will no longer remain separable:

$$|\psi_o(t)\rangle = \frac{1}{\mathcal{N}} \left(|0_0 0_1\rangle + e^{i\tilde{W}_1 t} |0_0 1_1\rangle + e^{i\tilde{W}_0 t} |1_0 0_1\rangle + e^{i(\tilde{W}_0 + \tilde{W}_1)t} e^{iU_{0,1}^{eff}t} |1_0 1_1\rangle \right) \quad (5.15)$$

There is now an additional phase evolution from $e^{iU_{0,1}^{eff}t}$ that will make the system inseparable in this localized orbital basis and the physical site basis – exemplifying the entangling of the states due to the interaction term. This interaction is physically derived from the the additional energy offset that atoms experience from multiply occupied sites that, in this case, will depend on the relative overlap of exponentially localized particles. This simple, phenomenological model not only describes how the system becomes entangled but qualitatively characterizes from the phase $e^{iU_{x_j,x_k}^{eff}t}$ that this entanglement will happen logarithmically slowly throughout the system since the interaction is ex-

The new localized quantities will share atoms from these original non-interacting orbitals and make it difficult to directly compose in these non-interacting terms. Although, they will appear relatively close if only looking at on-site occupation number. This example is further explained in Appendix : I.

ponentially weak between distance sites d apart:

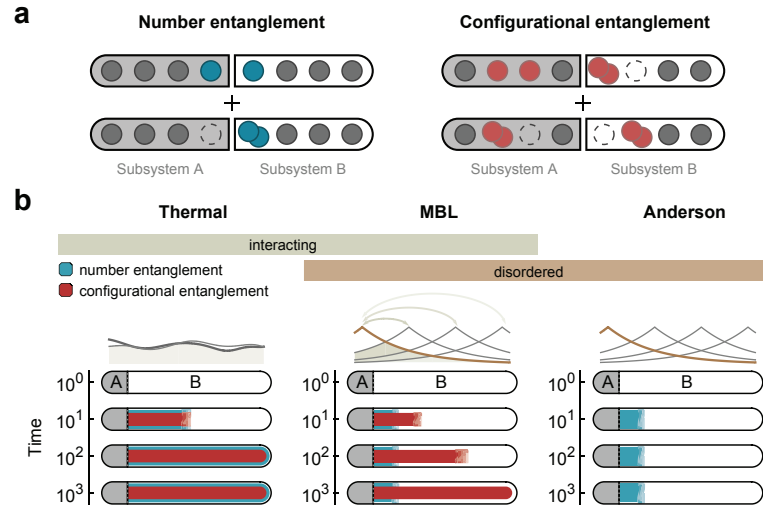
$$\tau_{ent} U_{x_j, x_{j+d}}^{eff} = \tau_{ent} \tilde{U} e^{-d/\xi} \sim 1 \rightarrow \log [\tau_{ent} \tilde{U}] \xi \sim d \quad (5.16)$$

This framework is adapted from the “l-bit” description used to provide a phenomenological picture for the entanglement dynamics of many-body localization in a spin system^{170,169,84}.^{*} The implication of the framework presented above is that the magnitude of local fluctuations in particle number are entirely restricted by the localization length scale ξ . The scaling behavior of entanglement within a single eigenstate of this many-body localized is again an area law – like the Anderson localized case discussed above. However, if the initial state is a superposition of several of these local creation operators ($\hat{\mathcal{L}}_k^\dagger$) the system will eventually become entangled by this interaction term and converge to a volume law.

Importantly, our initial state is not an eigenstate of the final Hamiltonian in this localized basis and hence the relative phase evolution of eigenstates that are sensitive to the exact population of these localized orbitals that results in the slow entanglement among the localized constituents of the system. From this framework we can additionally find an intuitive description of the spread of

*Strictly speaking, the “l-bit” (localized bit) picture from spins is somewhat inadequate since the on-site degree of freedom in the Bose-Hubbard case can take on more than two values. This is why an attempt at a modification to this picture has been added above for the population of these localized orbitals with a creation operator \mathcal{L}_k^\dagger where multiple on-site occupations can apply. The additional translation of this model is that the “p-bits” (physical bits) are now defined as the bare on-site occupation basis given by creation operators \hat{a}_k^\dagger . Lastly, the original “l-bit” picture, as written for spins, is that quasi-local operators are defined as to be comprised of eigenstates that commute with a product of local Pauli operators (e.g. $\dots I_{k-2} \sigma_{k-1}^{(z)} \sigma_k^{(x)} \sigma_{k+1}^{(y)} I_{k+2} \dots$) in the “p-bit” basis. However, it should be repeated once more that this is purely a phenomenological picture to help with intuitively writing down a mathematical description of the observed behavior in the system, not a literal diagonalization.

Figure 5.7: Separation of entanglement in Bose-Hubbard. a) These illustrations depict the separate contributions to the entanglement (5.6) in a Bose-Hubbard system. b) The role of these contributions qualitatively differ for these regimes: i) in a thermalizing system, both the number and configurational entanglement grow rapidly together and throughout the entire system, ii) the Anderson localized regime possesses only number entanglement which remains local, iii) the many-body-localized regime possesses local number entanglement but also harbors a logarithmically slow growth of configurational entanglement throughout the system.



entanglement after a quench throughout the system for the thermalizing, Anderson localized, and many-body-localized systems (Fig. 5.7). In the thermal case, the system rapidly develops entanglement of both types that extend across the entire system. The Anderson-localizing system develops entanglement only due to the finite extent of particle delocalization across a boundary and therefore all entanglement is additionally local in the system. The many-body-localized system develops initial entanglement due to the particle number fluctuations, similar to that of the Anderson-localized system, but also develops entanglement among the local configurations of particles in the system that slowly spreads across all length scales. This entanglement of local configurations of particles is in part possible because it respects the locally conserved integrals of motion. However, it can still scramble initial phase relationship of these quasi-local operators throughout the entire system, albeit logarithmically slowly due to the exponentially small overlap between distant orbitals.

5.4.3 MEASURED ENTANGLEMENT DYNAMICS

While we have access to the atom number in a given subsystem, p_n , which allows us to directly compute S_n for any given subsystem, we do not have access to the entropy of configurations S_c . Therefore, we probe this entanglement from the underlying correlations of configurations between the bipartite subsystems. This correlation of configurations must be performed respective to the local manifold of conserved atom number in a given system. We define this configurational correlator as a measure of non-separability between configurations A_n and its compliment $B_{n'}$ with n particles in A and $n' = N - n$ particles in B:

$$C = \sum_{n=0}^N p_n \sum_{\{A_n\}, \{B_{n'}\}} |p(A_n B_{n'}) - p(A_n) p(B_{n'})| \quad (5.17)$$

where $p(A_n B_{n'})$ is the joint probability of a particular Fock state configuration $A_n B_{n'}$ occurring and $p(A_n), p(B_{n'})$ are the marginal probabilities of the local Fock state configurations A_n , $B_{n'}$ occurring independently. A non-zero C provides a strict statement that the two subsystems are not separable within their configurational degrees of freedom and therefore implies entanglement of the configurational type. What this non-zero value implies mathematically is an upper bound on the magnitude of the coherence terms within the blocks of the reduced density matrix in Fig. 5.6. Importantly, this configurational correlation C is numerically found to be almost linearly proportional with S_c for our parameter regimes (Fig. 5.8). However, this proportionality is not always linear and some discussion about the mathematical bounds involving this correlator (C) are discussed in Ap-

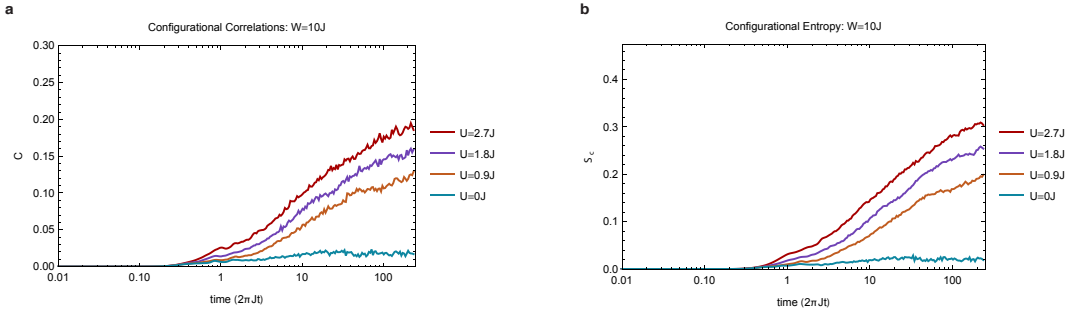


Figure 5.8: C and S_c . a) The calculated configurational correlations are plotted for various interaction strengths in the MBL regime ($W = 10J$). b) The calculated configurational entropy are plotted for various interaction strengths in the MBL regime ($W = 10J$). Both calculations are for a 6-site system where we find excellent qualitative agreement between the two metrics. Note that a small amount of configurational correlation exists in the non-interacting case, but never grows. The finite value here is due to the many-body nature of the non-interacting system which still harbors bosonic statistics that effect this configurational correlation. However, since it requires overlap of the particles, it is highly suppressed with localization length ξ . In the interacting case this changes the final saturation value but not the growth. All calculations are performed by exact diagonalization.

pendix H.

Due to the ability to resolve the exact Fock state distribution with our microscope, we study the time dynamics for both the particle number entropy (S_n) and the configurational correlations (C). We study all temporal dynamics within a 6-site Bose-Hubbard system. Without disorder, we find that both S_n and C indeed grow rapidly and reach a stationary value within a few tunneling times (Fig. 5.9a). In the presence of strong disorder, we find a qualitatively different behavior for both quantities. Again, S_n reaches a stationary state, although after longer evolution time due to reduced effective tunneling. Additionally, the stationary value is significantly reduced (approximately a factor of 2 in Fig. 5.9a,b) and indicates the suppression of particle transport in the system. The correlator C , in contrast, shows a persistent slow growth up to the longest evolution times reach by our measurements (Fig. 5.9b). The growth is consistent with logarithmic behavior over two decades

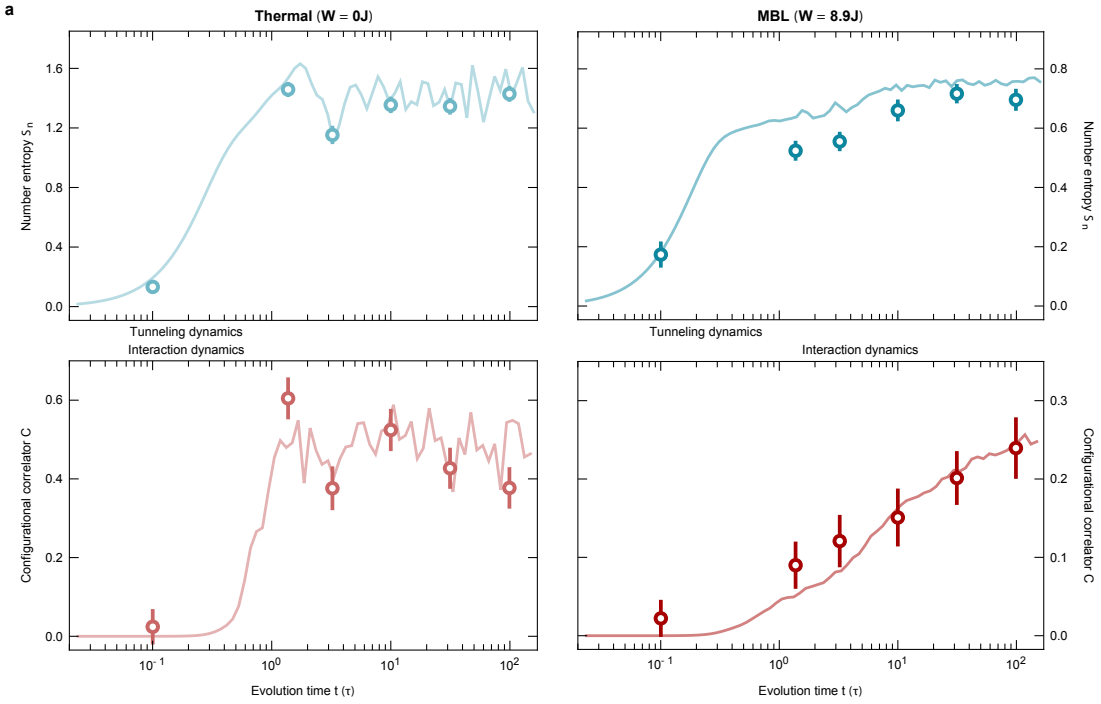


Figure 5.9: Separation of entanglement. **a)** Both the measured number entanglement entropy (blue) and the configurational correlator (red) are plotted for a 6-site Bose-Hubbard system after a quench with no disorder – realizing a thermalizing system. Note that both contributions to the entanglement in the system rapidly grow and saturate within a single tunneling time τ . The configurational correlations, requiring some amount of local number fluctuations, turning on more rapidly, but after the start of the number entropy growth. **b)** Both the measured number entanglement entropy (blue) and the configurational correlator (red) are plotted for a 6-site Bose-Hubbard system after a quench with strong disorder ($W = 8.9J$) – realizing a many-body-localized system. The number entanglement entropy rapidly grows and saturates within 10τ while the configurational correlations give rise to a logarithmically slow growth consistent with the phenomenological model expectations of MBL. All solid lines are calculated by exact diagonalization. All error bars are the s.e.m.

of evolution time. We conclude that we observe the interaction-induced entanglement dynamics in the MBL regime, which is additionally consistent with the phenomenological model presented earlier^{18,170,169,84}. The agreement of the longterm dynamics of S_p and C with numerical calculations in the MBL regime confirms the unitary evolution of the system and is consistent with very few scattering events that could decohere the system ($\gamma \leq 1$ photon / (second · atom number), §5.5).

Considering the scaling of this entropy in subsystems of different sizes provides us additional insights into the spatial distribution of entanglement in the system: in a one-dimensional system, locally generated entanglement results in a subsystem size independent entropy, whereas entanglement from non-local correlations causes the entropy to increase in proportion to the size of the subsystem. In reference to the subsystem's boundary and volume, these scalings are called area law and volume law. We find almost no change in S_n for different subsystems of an 8-site MBL system (Fig. 5.10a) – indicating an area law scaling to the localization of the particles and confirming the suppression of particle transport. In contrast, the configurational correlations C increase until the subsystem reaches half the system size (Fig. 5.10b). Such a volume-law scaling is also expected for the entanglement entropy and demonstrates that the observed logarithmic growth indeed stems from non-local correlations across the entire system. *

5.5 DECOHERENCE FROM SCATTERING

There are a few comments to be made about the sensitivity of the observed quantities in the system due to coupling to the external environment. There are three dominant ways that the external environment couple into the system as a bath: i) atom loss due to background gas collisions, inter-band scattering from spontaneous emission, or lattice depth modulation, ii) on-site modulation from physical vibrations between the optical paths, and iii) intra-band scattering that does not add energy

*This volume-law scaling of the configurational correlations, and therefore the von Neumann entropy, is a result of the unitary dynamics in the system. In fact, each individual eigenstate in the MBL system actually only harbors area-law entanglement. It is the unitary evolution of a superposition of many MBL eigenstates that give rise to this volume-law scaling.

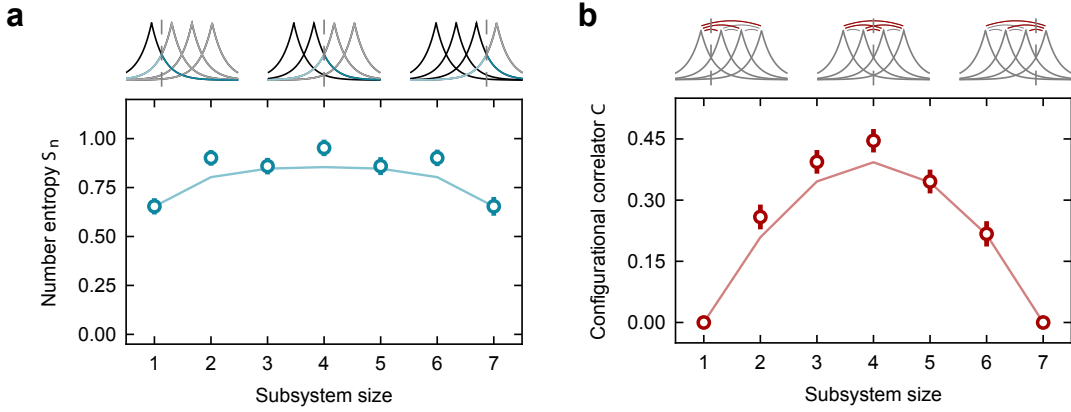


Figure 5.10: Subsystem-size scaling of entanglement entropy. a) The particle number entropy, which is most sensitive to the distance over which particle number fluctuations are possible, proves very insensitive to subsystem-size scaling and indicates the existence of an area law caused by particle localization. b) The configurational correlations, however, derive from a non-local interaction term that allows the system to become entangled extensively with subsystem size and reveals an volume-law scaling up to the half-system size. All solid lines are calculated by exact diagonalization. All error bars are the s.e.m.

to the system but does measure the atom location and decreases coherences of the many-body state.

The first contribution, atom loss, we can remove by post-selection of the atom number such that we retain the atom number we intended to load. This post-selection reduces the fidelity of an experimental run but is also necessary for the calculation of more complicated quantities such as the configurational correlations. However, if one only considered the single-site entanglement entropy, you can continue to calculate such local quantities and normalize for the total number of particles^{164,37}. Conceptually though, such excitations should be thought of as a strong measurement of the particle number and randomly projects the system into a subspace with global particle number $N - 1$. We found experimentally that not including such post-selection causes an overall offset in the entropy. This includes an offset in the entropy from atom loss due to imaging or loading, as well as a more troubling slow growth of entropy on the single-site level from continued atom loss during the dy-

namics. We cannot distinguish between background gas collisions or excitations to higher bands in the system since only the lowest band is trapped by the confining walls we apply.*

The second contribution, on-site modulation, we eliminate by using an on-site potential that has zero first derivative at each lattice site. This, to first order, removes the contribution of optical table vibrations and air currents that shake the relative position of the projected on-site potentials and the optical lattice. We found this reduces the residual entropy growth we measured in initial runs of the experiment.

The third contribution, intra-band scattering, should in principle be highly reduced due to the fact that we use blue-detuned optical lattices that should predominantly contribute to only inter-band excitations¹⁴⁴. However, as mentioned in §2.1.1, the z-confining lattices and applied disorder provide on-site offsets that restore this intra-band spontaneous scattering. This type of heating does not necessarily add energy into the system and therefore cannot be post-selected away. While this may not add any energy, we still call this “heating” since it increase the global entropy of the system by scattering events that act as a local measurement in the system and erase some of the many-body coherences which reduce the overall purity. Since a Bose-Hubbard system that populates all Fock states equally and incoherently has no configurational entropy (classical infinite temperature), we numerically investigated at what scattering rate our measured configurational correlations could provide numerical bounds on this contribution (Fig. 5.11). The most likely assumption was that the sites

*We find the correct height of the confining walls by determining the optical potential power that retains all atoms at early times after performing a hard quench without disorder such that we should populate many excited eigenstates. This power is then increased by approximately a factor of two that still prevents us from trapping the next highest band but trapping all particles in the lowest band.

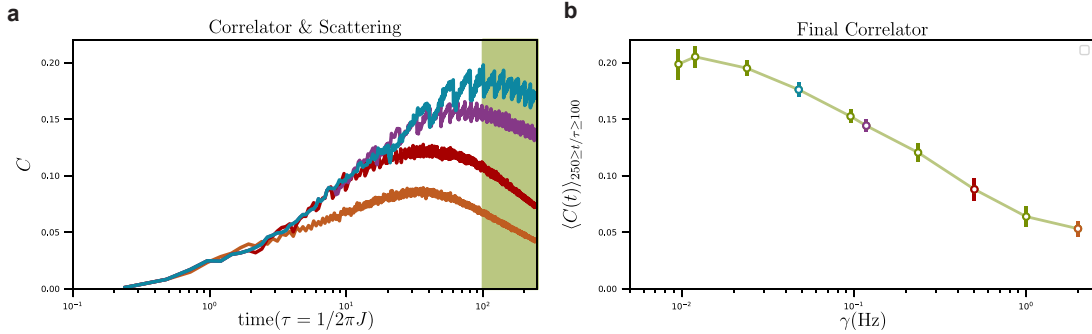


Figure 5.11: Correlator sensitivity to decoherence. **a)** The time dynamics of the configurational correlator C when sampled at a periodic rate γ . The scattering here is modeled to measure the atom-number on a single-site that sees the highest on-site potential offset from the disorder. While the system does not immediately begin to erase the coherences, they are all strongly effected by the final measurement time in our system ($t = 100\tau$). **b)** The averaged correlation value for measurements that happen at a time $100\tau \leq t \leq 250\tau$. This final correlation vale is then plotted as a function of scattering rate in units of the tunneling rate J . Note the experimental measured value was $C \approx 0.25$. All simulations are calculated by exact diagonalization for the half-size subsystem of a 6-site Bose-Hubbard chain.

with higher on-site potential would be most likely to scatter and measure the local atom number. In particular, a worry had been that perhaps the quasi-random, but structured sampling of the system might unintentionally create correlations – it turns out it does not (Fig. 5.11). We conclude from our measured correlations and numerical comparison that our intra-band scattering rate $\gamma_{intra} \leq 1$ photon / (second · atom number).

5.6 DISCUSSION

Investigating the growth of non-local quantum correlation has been a long-standing experimental challenge for the study of MBL systems. In addition to achieving exceptional isolation from the classical, external environment and local access to the system, such a measurement requires access to the entanglement entropy^{18,131}. Our work provides a novel technique to characterize the entanglement properties of MBL systems, based on measurements of the particle number fluctuations and their

configurations. The observation of slow coherent many-body dynamics along with the breakdown of thermalization allows us to ambiguously identify and characterize the MBL state in our system.

Resolving the genuine growth of correlations related to the logarithmically slow growth of entanglement in the system additionally requires some care in how one averages measurements in the system. Since the configurational correlations, unlike the density-density correlations, are not spatially locked to the underlying correlation of the applied on-site potentials, one has to be careful to always compute C from the quantum average of a given Hamiltonian realization first. Then, the averaging over different disorders realizations can be performed. Otherwise, effectively all configurations will be explored equally among different disorder realizations and the slow entanglement growth will be erased out by the average. This effect does not happen on a qualitative level for the particle number entropy S_n and only changes this observable quantitatively¹⁸.

This distinction in averaging actually provides some additional insight into these correlations as well. In some crude sense, the number fluctuations are a more classical measure that probe thermalization in the system since the eigenstates explore all thermodynamically allowed number states. Then the quantum average over eigenstates and the average over disorders are not particularly different in a qualitative manner.

Another qualitative way to think about MBL system is that while it does not ergodically explore all number states, it does allow ergodic exploration of the remaining degree of freedom: the configurations of particles restricted to a manifold of local particle number. This, in some sense, sounds like thermalization within a manifold of states where the system can scramble initial phase information*

*This refers to the phase information in the superposition of local “l-bit” creation operators immediately

among the remainder of the system. So while the MBL system does not resolve local observables that agree with the global thermodynamic constraints of a thermodynamic ensemble, the system does use a manifold of states as a type of bath for only a subset of states. This additionally implies that while the transport of particles are suppressed in the disordered system, the interactions enable the transport of phase information and has been predicted as a system that enables quantum teleportation of only “l-bit” phase information.

However, the most fundamental question about this system is whether the transition in behavior of these highly excited eigenstates can be described within the conceptual framework of quantum phase transitions. While this appears as an appealing way to describe the behavior of excited eigenstates, such a relationship has remained elusive due to the difficulty in theory to either compute the behavior of the intermediate disorder regime both numerically or analytically. We will explore such a regime experimentally in an attempt to utilize our quantum simulator to shed some additional light on to this question in the following chapter¹⁵⁴.

after the quench.

There is nothing sharp in nature.

Dr. Julian Léonard

6

Critical behavior of the many-body-localization transition

We have, up till now, described quantum thermalization and MBL in terms of their resultant dynamical behavior from the integrability, or lack there of, of the quantum system. This behavior is a consequence of a qualitative change of the properties of the eigenstates at a finite disorder value

where the two phases, thermalizing and many-body localized, have been theoretically predicted in the extreme value cases for short-range interacting systems in one-dimension^{139,19,85,131,87,43}. This type of non-equilibrium phase transition is often referred to as an eigenstate phase transition since the properties of the individual excited eigenstates themselves change qualitatively at a finite value^{139,85}. However, understanding the exact transition behavior requires the ability to exactly diagonalize the entire Hamiltonian since it relies on access to these highly excited eigenstates.* Such numerical approaches, while exact, are limited to relatively small finite sizes based upon the exponential growth of Hilbert space dimensionality with physical size^{171,101}. Other numerical approaches, such as renormalization group theories (RG)^{148,185,192} work on significantly larger sizes but are implemented via a self-consistent set of rules that may not accurately capture the critical behavior due to the expected large, non-local entanglement at the critical point^{5,1}. These same set of limitations do not restrict our experimental realization of an MBL system and in principle can faithfully perform exact simulations of the correct behavior for large systems. Although, a new practical limit emerges experimentally based on coherent evolution time. The practical limit of measuring out successive decades of time evolution require exponentially more experimental runs to overcome the increased post-selection rates.[†] All results in this chapter will derive from time evolution up till $t \approx 100\tau$.

While both non-equilibrium phases are well understood theoretically and can be successfully described by phenomenological models^{169,84,131}, the transition between these two phases remains an

*There are many theoretical proposals for this critical behavior that do not use exact diagonalization, but the validity of their results is unknown without either comparison to exact diagonalization or experimental results.

[†]Additional estimates of evolution time can be made from using the spontaneous scattering rate measurements in §2.1.3.

open question^{69,185,148,101,5,1,192}. Several experiments have probed slow transport properties through local observables near this critical regime^{120,26}. While such anomalous transport has been predicted theoretically^{2,171,192}, identifying anomalous transport as quantum critical dynamics is experimentally challenging, since similar behavior can also originate from stochastic effects: inhomogeneities in the initial state¹⁶ or the coupling to a classical bath^{130,110}. We overcome these challenges in our experiment with our protocol by evolving a pure, homogenous initial state under unitary dynamics where we additionally utilize post-selection to exclude coupling to the environment by atom loss^{119,118}. In this chapter, I present our results in this critical regime where we observe system-size dependent thermalization, anomalous transport, and correlations that span the entire system and persist up to high orders near the critical point¹⁵⁴. We additionally observe behavior in support of a proposed microscopic mechanism that leads systems at intermediate disorder strengths critically towards thermalization via a sparse resonant network^{148,101,154,77}.

6.1 CRITICAL BEHAVIOR AND PHASE TRANSITIONS

Quantum phases are described by their local order parameter and their transition from one order to another, in any physical system, happens smoothly. This smooth cross over is typically limited by either the system size or temperature of the system. This regime of the smooth cross over tends to sharpen (shrink) as the system is either cooled to lower temperatures or the system size is increased. This shrinking of the smooth crossover demonstrates that the system was only critically limited by an external property; it will approach a particular phase in the $T = 0$ or infinite-size limit. This

smoothness has to do with the relationship of the finite correlation length at the transition as compared to the system size or the temperature to the minimum gap in the system. The scaling behavior of these transitions are dependent upon only global properties such as dimensionality and internal symmetries – making the theory describing this critical behavior universal: it applies across a wide variety of physically different transitions as long as they have these same global properties¹⁵⁸.

6.1.1 CRITICAL DYNAMICS IN EQUILIBRIUM PHASE TRANSITIONS

The dynamics at non-equilibrium phase transitions are inherently different from those associated with critical behavior at equilibrium phase transitions.* A traditional approach for the theory of ground state phase transitions has seen wide success in describing phase transitions within a set of universal classes with qualitative distinctions only changed by symmetries, interaction range, and dimensionality of the system. Therefore, it is natural to try and understand which, if any, of these traditional concepts may apply to non-equilibrium phase transitions and their critical behavior. In the following sections, the behavior associated with criticality in a traditional equilibrium quantum phase transition is discussed.

To probe all ground-state phase transitions, a system is typically prepared in one phase at equilibrium, then a parameter in the Hamiltonian, e.g. λ , has to be swept as a function of time through the transition point. These are also known as equilibrium phase transitions since the assumption is that this parameter is swept adiabatically. Since the Hamiltonian will not be time-independent dur-

*However, one might consider that all phase transitions are eigenstate transitions and equilibrium quantum phase transitions focus only on the lowest energy eigenstate – the ground state.

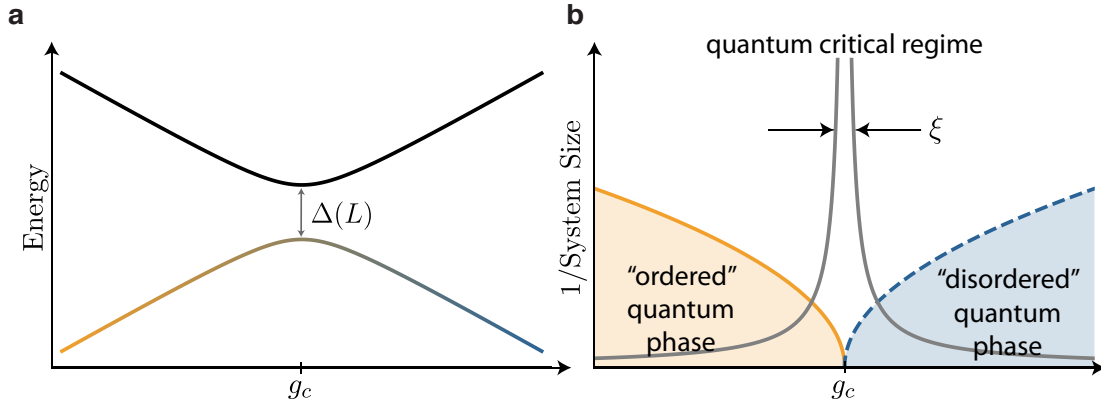


Figure 6.1: Equilibrium quantum phase transition. a) The canonical schematic for a quantum phase transition occurring at $T = 0$ for the ground state as a function of a tuning parameter g . The avoided crossing shown between the ground state and the excited state in this diagram are separated by the coupling between the two terms in the Hamiltonian: H_0 and H_1 . Each dominating character of the ground state in their respective regimes. The color of the ground state denotes whether it lies in the “ordered” or “disordered” phase. b) The canonical phase diagram associated for a quantum phase transition has an “ordered” and a “disordered” phase that cross at a critical point g_c when $T = 0$. The left diagram, a, is just plot of the eigenstates along the $T = 0$ cross section of this diagram. As the temperature is increased, more eigenstates in the system become incoherently populated and conceptually the quantum fluctuations, $\hbar\omega_c$, that attempt to order the system compete with the thermal fluctuations $k_b T$ that drive the system towards a disordered phase. The closing gap near the critical point extends this classically disordered phase downward into the critical “fan” shape associated with critical behavior and quantum phase transitions. A similar diagram can be made for the Temperature rather than inverse system size.

ing this sweep, the approximate requirement for adiabaticity is given by the Landau-Zener problem that the change in the energy due to the sweep of a parameter $(d\lambda/dt) \times (dE/d\lambda) < g$ where $(d\lambda/dt) \times (dE/d\lambda)$ is the change in the energy as a function of time and g is the coupling between the ground and excited states. Experimentally, any ramp will be finite in time, and any finite ramp time will always inject a finite amount of entropy into the system during the sweep. Additionally, even if these systems are prepared at $T \approx 0$, the degree to which this sweep is not adiabatic will result in non-equilibrium dynamics. The presence of these non-equilibrium dynamics are characteristic of the energy gap in the system defined by parameter $\lambda(t)$ when this adiabatic criterion breaks

down due to the finite ramp time. This is additionally linked to the correlation length in the system which is dependent to the energy gap in the system and therefore defines the average size of domain size in a system¹⁸⁸. The relationship between this domain size, correlation length, and dynamics is known by the Kibble-Zurek mechanism^{146,196} and have recently been seen experimentally¹⁰⁰.

6.1.2 A NON-EQUILIBRIUM PHASE TRANSITION

The thermal-to-MBL eigenstate phase transition is also known as an out-of-equilibrium phase transition.* Since it is not physically possible, while remaining in thermodynamic equilibrium, to populate a single highly excited eigenstate, the quantum quench performed in the experiment will populate many excited eigenstates which will lead to dynamics. However, an important point is that the many-body gaps between eigenstates are related to the properties of the eigenstates themselves and therefore the observed unitary dynamics probe the inherent characteristics of the eigenstates^{85,131,5,1}.

In the thermalizing case (§4), the ergodic nature of the eigenstates of the system imply that most relatively local properties change smoothly across the eigenstates as a function of energy. This can be intuited from the fact that by the property of being ergodic, small perturbations applied to any eigenstate will hybridize energetically nearby eigenstates. This property additionally leads to level repulsion between eigenstates and applies generically across the majority of the spectrum⁴³. † It is precisely the non-ergodic character of a many-body-localized eigenstate that prevents a generic

*This term additionally covers another class of “dynamical phase transitions” that are qualitatively different from the thermalizing to MBL transition discussed here.

†This level repulsion is nothing other than avoided level crossing in a two-level system when they are generically coupled by some parameter. For these thermalizing systems this applies generically between almost any two eigenstates since they are constructed out a nearly ergodic superposition of states that are constrained only by global, thermodynamic quantities.

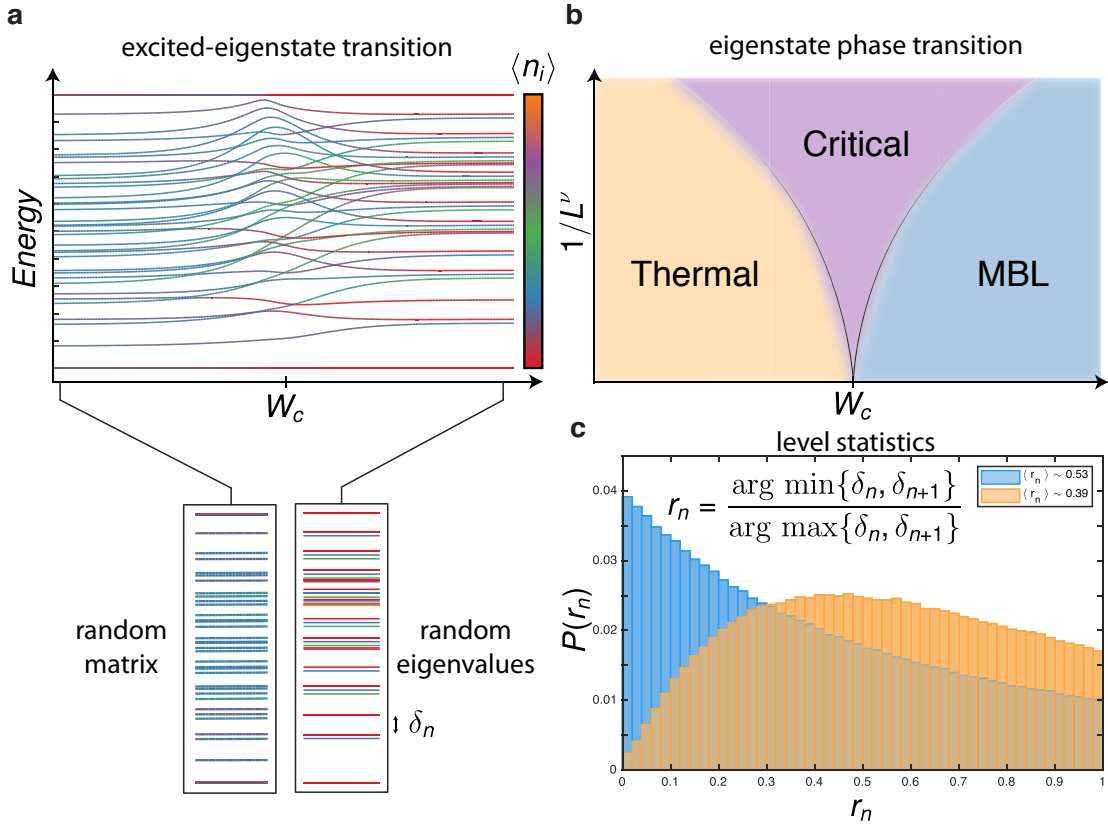


Figure 6.2: Excited eigenstate phase transition and spectral statistics. a) The entire spectrum (normalized in bandwidth) is plotted for a small, disordered Bose-Hubbard chain as a function of disorder strength W . The color of the eigenstates denote the local particle number on a single-site. Not only do we see a large number of crossings near the critical point, but the color of the eigenstates, which was very uniform for low disorder ($W < W_c$), changes dramatically as it cross the transition ($W > W_c$). By zooming into the spectrum on either side we can see the differences in gaps: on the low-disorder side there are level-repelled eigenstates that are characteristic of the eigenvalues of a random matrix and ergodic eigenstates, and on the high-disordered side we see gaps that change dramatically across the spectrum that is characteristic of random eigenvalues and non-ergodic eigenstates. b) The association of these characteristic gaps and local parameters expressed in a are associated with the generic behavior attributed to the excited eigenstates in the thermalized and many-body-localized phases. c) The common metric used to differentiate these two phases from their spectrum is by computing the level statistics ratio r_n . The histogram of values are plotted for a random matrix (orange, thermalizing regime) and randomly selected eigenvalues (blue, localized regime).

perturbation from coupling nearby energy eigenstates. Consequently, or simultaneously, this means

that eigenstates also can change drastically in their local character from eigenstate to eigenstate and

do not exhibit level repulsion. This internal character of these two phases is inherently related to their relative gaps in the system and hence their dynamics⁸⁵. A convenient metric, known as the level statistics ratio, captures the existence of this level repulsion and characterizes the transition of eigenstates from ergodic to non-ergodic:

$$r_n \equiv \frac{\min\{\Delta_n, \Delta_{n+1}\}}{\max\{\Delta_n, \Delta_{n+1}\}} \quad (6.1)$$

where $\Delta_n = E_n - E_{n-1}$ is the energy difference between neighboring eigenstates indexed by n in order of increasing energy. In the regime where the states are ergodic, the eigenenergies match those of the eigenvalues from a random matrix and the eigenstate average, $\langle r \rangle$ takes on the Wigner-Dyson value $\langle r \rangle \approx 0.53$. In the many-body localized regime the eigenvalues look as though sampled from a random distribution and are then characterized by the Poisson value $\langle r \rangle \approx 0.39$. The transition of a system's level statistics ratio is typically the way theory identifies these two regimes, however we will look at the resultant dynamic behavior of the system that is inherently linked to the structure of the eigenstates that are captured by this statistic (Fig. 6.2).

Since this metric requires access to all the eigenstates and their relative gaps, it is mostly used as a theoretical tool^{85,131}. Although, recently in a small qubit system the excitation spectrum was probed such that the spectrum could be reconstructed¹³⁷. Lastly, as it is the gaps in the many-body spectrum that give rise to all observable dynamics, this change in eigenstate characteristics will be observable in the dynamics of the system.

6.1.3 OBSERVING NON-EQUILIBRIUM CRITICAL DYNAMICS

Qualitatively, we can see the overlap of several characteristic traits between equilibrium quantum phase transitions and the thermal-to-MBL transition. In both cases, for some parameter regime, there exists a phase that is described by a local observable (order parameter or localization of initial state) and the eigenstates of both the ground state phases and excited states in MBL follow an area-law in entanglement entropy. However, several other characteristics seem difficult to relate, such as the notion of a diverging correlation length at the critical point in equilibrium transitions since eigenstates change from an area-law in the MBL phase to a volume-law in the thermal phase – where correlations are scrambled among all constituents and therefore extended. Some of these comparisons are schematically shown in Fig. 6.2 and Fig. 6.1.

Conceptually, though, the mechanisms may be similar in how the eigenstates change: phase transitions are driven by collective fluctuations of a system’s constituents that emerge at a critical point^{182,158,109}. We will probe the critical behavior of this non-equilibrium phase transition by observing the correlation dynamics that emerge at intermediate disorder near the critical point. By comparing multiple system sizes at fixed evolution time, we can probe which local behavior is critically dependent upon the system size and how the emergent correlation dynamics lead to this critical behavior.

We will again focus on the interacting Aubry-André model¹³:

$$H = -J \sum_{\langle i,j \rangle} (\hat{a}_i^\dagger \hat{a}_j + \hat{a}_j^\dagger \hat{a}_i) + \frac{U}{2} \sum_i \hat{n}_i(\hat{n}_i - 1) + W \sum_i h_i \hat{n}_i \quad (6.2)$$

where, $h_i = \cos(2\pi\beta x_i + \phi)$ and with a spatial frequency of $\beta \approx 1.618 \text{ sites}^{-1}$ as an approximation of the golden ratio ($\beta_{GR} = \frac{\sqrt{5}+1}{2}$). We will follow the same quench protocol shown in the previous chapter §5 and pictorially shown in Fig. 5.3. All experiments will use a unity-filling Mott insulator for the initial state for a system size of $L = 8$ or $L = 12$.

6.2 LOCALIZATION AND TRANSPORT

We will first characterize the system's dynamical behavior by studying its transport properties at different disorder strengths. This will be similar to asking how local perturbations explore the remainder of the system and should characterize the thermalizing regime. Since the initial state has exactly one atom per site, the system starts with zero density correlations at all length scales. However, during the Hamiltonian evolution, the tunneling dynamics build up anti-correlated density fluctuations between coupled sites of increasing distance. Motivated by this picture, we quantify the particle dynamics by defining the transport distance:

$$\Delta x = 2 \sum_d d \times \langle G_c^{(2)}(i, i+d) \rangle \quad (6.3)$$

as the first moment of the simultaneously disorder and site- i averaged two-point density correlations, $G_c^{(2)}(i, i+d) = \langle \hat{n}_i \hat{n}_{i+d} \rangle - \langle \hat{n}_i \rangle \langle \hat{n}_{i+d} \rangle$. This two-point density correlation function correctly maps out the effective probability distribution of a single-particle in the non-interacting limit of the Aubry-André model. Additionally, by calculating the first moment of the distribution we do not assume a particular functional form for the localization of particles. However, it is useful

to compare to the analytical results for the non-interacting case to see how such a metric converges to the localization length.

In the large detuning limit, one can find that all states are localized by the large site-to-site detuning quantified by on-site disorder W :

$$\psi \sim \frac{1}{N} \sum_d (2J/W)^d = \frac{1}{N} \sum_d e^{-d/\xi}$$

where $\frac{1}{\xi} = \log(2J/W)$. Analytically, it was shown by Aubry and André that $\frac{1}{\xi} = \log(\lambda/2)$ where $\lambda = W/J$ ¹³. We then extract the first moment of this localized function:

$$\langle x \rangle = \frac{1}{N} \sum_i x_i e^{-x_i/\xi} = -\frac{\partial}{\partial(1/\xi)} \frac{1}{N} \sum_i e^{-x_i/\xi} = \frac{1}{e^{1/\xi} - 1}$$

By expanding the exponential of this result we see that the localization length and the first moment, $\langle x \rangle$ converge in the large localization length limit.

$$1 + \frac{1}{\langle x \rangle} = e^{1/\xi} \approx 1 + \frac{1}{\xi} + \mathcal{O}(2)...$$

It also allows us to compare the expected first moment at a given disorder strength in the non-interacting limit:

$$\langle x \rangle = \frac{1}{w/2 - 1}$$

However, this last dependence on the disorder strength will not prove quantitatively precise in our case since the localization point significantly changes in the case of an interacting system and

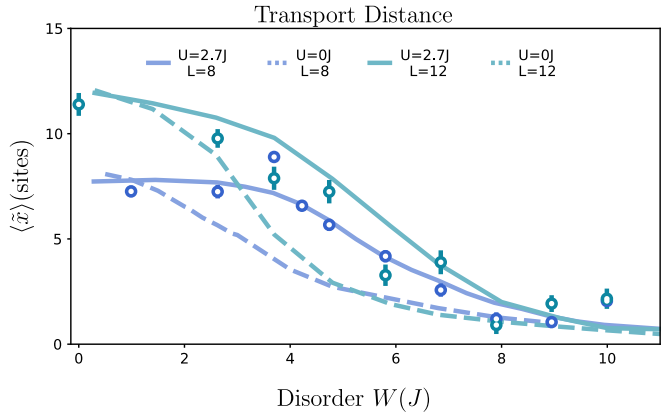
it is not known if the scaling behavior should be the same in the interacting system. Qualitatively though, it provides a usable metric that is model independent and maps onto the correct quantity when the system is exponentially localized. There is an additional complication in the interacting case: when comparing this value across different disorder strengths, the injected energy by the quench changes the number of participating particles.* We normalize this effect by adding an additional normalization constant to create the normalized first moment $\Delta\tilde{x}$:

$$\Delta\tilde{x} = \frac{2L}{L-1} \left(\frac{\sum_d G_c^{(2)}(d) d}{\sum_d G_c^{(2)}(d)} - 1 \right) \quad (6.4)$$

This function is normalized such that in the thermalizing regime, where particles are completely delocalized, that the normalized first moment $\Delta\tilde{x}$ is equal to the system size L . We measure this quantity for several disorder strengths after long evolution times, $t/\tau \approx 100$, such that the system's dynamics should have saturated for our system sizes. We show this in Fig. 6.3 both experimentally and numerically to demonstrate how these quantities differ for the interacting and non-interacting regimes. Note that the point where the single-particle localization transition should occur is $W_c = 2J$ and is approximately where the single particle normalized transport distance decreases from the system size. In the deep disorder regime, the transport distance is similar for both system sizes. Additionally, the agreement of the theoretically predicted transport distance for an interacting and non-interacting system indicates the negligible role of interactions in transport in

*Since the particles harbor repulsive interactions, high on-site occupancy costs more injected energy. Therefore by injecting a finite amount of energy only favors lower on-site occupations and effectively appears as though only a fraction of the particles are participating in the delocalization.

Figure 6.3: Transport distance: interacting and non-interacting. The first moment is plotted as a function of disorder strength W for both the interacting (solid, points) and the non-interacting (dashed) cases for both the 8, 12-site systems. The first moment remains close to the system size till $W \approx 5J$ when it begins to localize for the interacting case. The first moment remains close to the system size till $W \approx 2J$ when it begins to localize for non-interacting. The solid lines are computed by exact numerics. The error bars are the s.e.m.



the strongly localized regime. Although we expect this might be true asymptotically, it could be the closeness of convergence at this disorder depth is finite-time limited.

6.3 CRITICAL TRANSPORT BEHAVIOR

Now that we have an idea of where the system changes phases from delocalized to localized, we can probe the inherent dynamics involved at the transition point of such a non-equilibrium phase transition. We additionally only evaluate these critical dynamics for the $L = 8$ system size since we can only locate the finite-size critical regimes by comparison to larger system size. This will be further clarified below.

6.3.1 ANOMALOUS DIFFUSIVE TRANSPORT

At low disorder, we observe that anti-correlations rapidly build up and saturate with a time scale of $t/\tau \approx L/2$. Note that this is the approximate time it takes for a ballistic density excitation to travel across the entire system size L since the tunneling time $\tau = 1/(2\pi J)$ where J is defined in

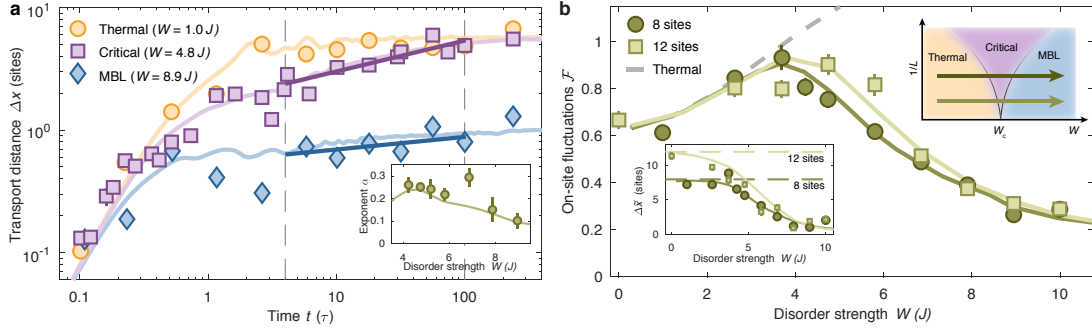


Figure 6.4: Critical Thermalization. **a)** Particle transport slows down at intermediate disorder, consistent with a power-law evolution with exponent $\alpha < 0.5$, demonstrating subdiffusive dynamics (inset). These data were taken on an eight-site system. **b)** The critical nature of these dynamics is determined from the behavior of on-site density fluctuations \mathcal{F} and transport distance $\Delta\tilde{x}$ (lower left inset) for both considered system sizes. The thermal regime is determined by the agreement of the measured \mathcal{F} with the prediction from a thermal ensemble (dashed grey). The system-size dependence at intermediate disorder is consistent with the reduced size of a quantum critical cone (upper right inset). These data were measured for both an eight-site and twelve-site system. The solid lines denote the prediction of exact numeric time calculations without any free parameters. The errorbars are the s.e.m.

the hopping rate of the field of the quantum many-body wave function. With increasing disorder, we observe a slowdown of particle transport that is consistent with a power-law growth $\Delta x \sim t^\alpha$ (Fig. 6.4)^{2,171,192,61}. We extract the power-law exponent α from the data points after the initial transient dynamics cease ($L/2 < t/\tau \leq 100$) (Fig. 6.4 inset). We find that this exponent α is reduced by successively higher disorder strengths such that it is only anomalously diffusive in the intermediate disorder regimes and demonstrates the suppression of transport in the MBL regime at high disorders.* We cannot experimentally verify the functional form of the transport behavior, but can find a very suggestive relationship numerically which is shown in Appendix: I.

*Note that the thermal regime is expected to eventually become $\alpha = 0.5$ in the infinite size limit. However, finite size effects limit both our experiment and numerical simulations which attempt to probe this regime.²

6.3.2 CRITICAL THERMALIZATION

In order to identify the anomalous diffusion as a signature of quantum critical behavior, we measure the system-size dependence of two observables in the long-time limit ($t=100\tau$): the on-site number fluctuations $\mathcal{F} \equiv G_c^{(2)}(d=0)$ as a probe of local thermalization and the corresponding transport distance $\Delta\tilde{x}$ as a measure of localization (Fig. 6.4). At low disorder, the fluctuations agree with those predicted by a thermal ensemble and particles are completely delocalized for both system sizes ($L = 8, 12$). This demonstrates that local quantum thermalization in our system is system-size independent at low disorder and identifies this disorder regime as the thermal phase. At strong disorder, the physics is governed by the formation of an intrinsic length scale, namely the localization length $\xi \sim \Delta\tilde{x}$ ^{37,118} (§6.2). We observe system-size independent, sub-thermal fluctuations that measure the onset of an intrinsic length scale. This identifies the strong disorder regime as the localized phase. However, at intermediate disorder, our data are consistent with a system-size dependence for both observables. This simultaneously demonstrates the absence of an intrinsic length scale and the presence of finite-size-limited fluctuations and hence finite-size-limited thermalization, therefore identifying the presence of a critically thermalizing regime. These measurements of system-size dependent, enhanced thermalization can be visualized as two horizontal cuts in a finite size phase diagram. The observed finite-size dependence is consistent with the physics associated with a critically thermalizing intermediate phase and a shrinking quantum critical cone (Fig. 6.4).*

*This, however, only demonstrates that the $L=8$ system is critically sub-thermal for the intermediate disorder regime and continues to thermalize in the presence of a larger system. Without having any other measurement, a strict statement about the $L = 12$ system being critical cannot be made.

6.3.3 FLUCTUATIONS SCALING

One complication with scaling the thermal predictions to larger system sizes is that the classical ensemble prediction still requires knowing all the energy eigenstates in the Hamiltonian. However, there is an analytical approach to finding the particle-number fluctuations per particle for a given sub-system at infinite temperature that will help provide some intuition:

$$\mathcal{F}(l, N)_L/N = \left(\frac{(L-l)l}{L^2} \right) \left(\frac{1 + N/L}{1 + 1/L} \right) \quad (6.5)$$

where l is the sub-system size, L is the total system size, and N is the total particle number (see Appendix: I for derivation). Note that in the limit that $N \rightarrow 1$ this reduces to the fluctuations per particle given by a Bernoulli distribution:

$$\mathcal{F}(l, N)_L/N = \left(\frac{(L-l)l}{L^2} \right)$$

The factor of N/L (typically denoted as the filling of the system ν) arises from indistinguishability of the bosons and their enhanced likelihood to occupy the same quantum-mechanical state (known as bosonic enhancement). However, since our system is always at some finite energy density, the number of excitations in the system that then participate in these fluctuations becomes limited to some effective number $N \rightarrow N_{eff}$. We do not know of any literature that defines what the correct energetic suppression of this N should be. This scaling of such subsystem fluctuations also contain the physics of the localization length in the system and can additionally be used

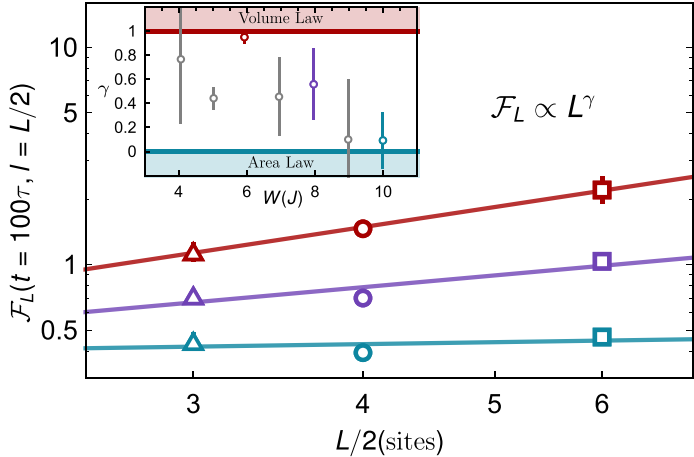


Figure 6.5: Scaling of bipartite fluctuations. The scaling of half-system size, bipartite fluctuations ($\mathcal{F}_L(l = L/2, t = 100\tau)$) are plotted here for data taken at three system sizes: $\{L = 6, L = 8, L = 12\}$. These data are always measured after long evolution times ($t = 100\tau$) and then fit with a power law as a function of half-system size L . The fitted exponents are then plotted in the inset. The solid lines denote the fitted values from a power law. The error bars are the s.e.m.

to probe the transition point. In the thermal regime, the particles are delocalized and so the fluctuations are qualitatively similar to the expression above (I.2) up to an overall scaling. Therefore, by evaluating the half-size subsystem fluctuations we expect the fluctuations to scale with the volume of the total system ($\mathcal{F}(l = L/2, N = L)_L \sim L$). Conversely, as the particles become localized the system forms an intrinsic length scale ξ that particles can delocalize over that does not scale with the total system size. This intrinsic length scale would give rise to a strict area law ($\mathcal{F}(l = L/2, N = L)_L \sim \text{const.}$)¹⁷³. We explore the scaling behavior of these half-system size fluctuations for three system sizes: $\{L = 6, L = 8, L = 12\}$ in Fig. 6.5. A possible relationship between the scaling behavior and the localization length ξ is discussed in Appendix: I.

6.4 CORRELATION STRUCTURE

In order to reveal the microscopic origin of this anomalous transport, we now investigate the site-resolved structure of correlations in the many-body state (Fig. 6.6a). We first study how much each

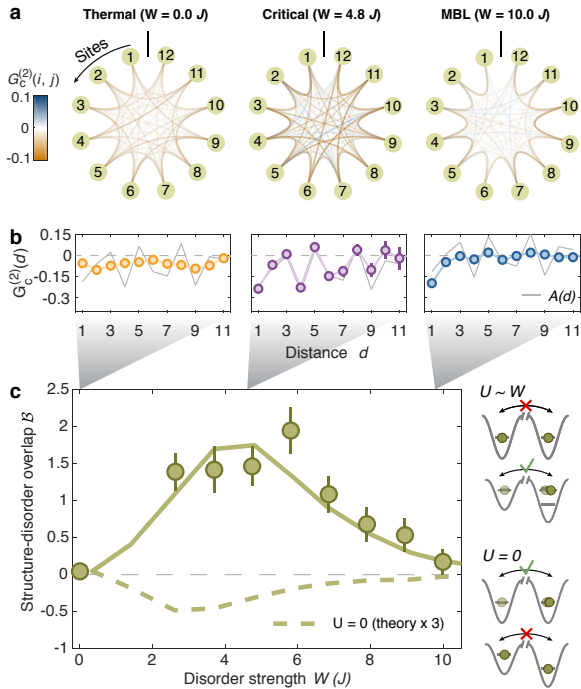


Figure 6.6: $G^{(2)}(d)$ Structure. **a)** The measured site-dependent two-point correlations $G_c^{(2)}(i, j)$ differ for the three disorder regimes. In the quantum critical regime, correlations preferably form at specific distances, showing a network-like structure. This contrasts with homogeneous correlations in the thermal regime and nearest neighbor correlations in the MBL regime. **b)** The structure of the correlation network is revealed by the averaged correlation function $G_c^{(2)}(d) = \langle G_c^{(2)}(i, i + d) \rangle_i$. Its similarity to the autocorrelation $A(d) = \langle h_i h_{i+d} \rangle_i$ of the quasi-periodic potential (solid grey) indicates interaction-induced tunneling processes that are enhanced when the interaction energy compensates for the chemical potential difference. **c)** We quantify the similarity by the overlap $\mathcal{B} = \sum_d G_c^{(2)}(d) A(d)$, which is maximal in the quantum critical regime. The sign of the overlap would be opposite for non-interacting particles (dashed line), which favors tunneling between sites with similar potential energies. The solid lines in b,c denote the prediction of exact diagonalization calculations without any free parameters. The error bars are the s.e.m.

lattice site contributes to the transport by considering the site-resolved two-point correlations in the long-time limit ($t = 100\tau$). In the thermal regime, we find similar correlations between all lattice sites, which correspond to uniformly delocalized atoms. In contrast, density correlations are restricted to nearby sites in the MBL regime due to localization. Intriguingly, we observe a sparse structure of correlations at intermediate disorder, which involves only specific distances between lattice sites, yet spans the entire system.

The sparse resonant structure is expected to be linked to the applied quasi-periodic potential. The average energy offsets of distances d apart in the system are correlated by this potential. The correlation is then inherited by the system's fluctuations when the interaction energy U compensates for these correlated offsets. To investigate this structure, we compare the two-point density correla-

tions with the autocorrelation function, $A(d) = \langle h_i h_{i+d} \rangle_i$, of the quasi-periodic potential. Indeed, we find that the site-averaged density correlations $G_c^{(2)}(d) = \langle G^{(2)}(i, i + d) \rangle_i$ inherit their spatial structure from $A(d)$ (Fig. 6.6b). We quantify this contribution by taking the overlap of these two-point correlation functions, $\mathcal{B} = \sum_d \langle G^{(2)}(i, i + d) \rangle_i A(d)$. We find that this contribution is maximal in the critical regime but is strongly reduced in both the thermal and MBL regimes (Fig. 6.6c). These observations contrast with the behavior of a non-interacting system, where the sign of the structure is opposite since resonant tunneling is favored for zero potential energy difference between sites (Fig. 6.6c). These results illustrate microscopically how the interplay of strong interactions and disorder can lead to anomalous diffusion. However, this picture of effective single-particle hopping that couples distance sites neglects the potential many-body nature of these systems and the emergence of collective fluctuations between many particles over long distances.

6.5 HIGH-ORDER CORRELATIONS

We investigate the contribution of multi-particle fluctuations to the thermalization in the critical regime to probe the presence of enhanced quantum fluctuations when the system changes phases. For this study, we employ the n -point connected density-correlation functions^{114,167,79,150}:

$$G_c^{(n)}(\mathbf{x}) = G_{tot}^{(n)}(\mathbf{x}) - G_{dis}^{(n)}(\mathbf{x}) \quad (6.6)$$

which acts on lattice site positions $\mathbf{x} = (x_1, \dots, x_n)$. The disconnected part of this function, $G_{dis}^{(n)}$ is fully determined by all lower-order correlation functions, and therefore does not contain

new information at order n . By removing these disconnected contributions from the total measured correlation function, $G_{tot}^{(n)} = \langle \prod_i^n \hat{O}_i \rangle$, we isolate all n -order correlations that are independent of lower-order process (§Appendix: I). This approach gives a direct handle on the level of complexity of the underlying correlation structure of the many-body wave function and characterizes its entanglement via its non-separability into subsystems of size $< n$. We quantify the relevance of order n processes by computing the mean absolute value of all correlations arising from both contiguous and non-contiguous n sites in the system (Fig. 6.7). This is similar to looking at the width of the distribution of correlations at a given order since the average correlation value converges to zero. This is conceptually similar to investigating the network structure at higher disorders since this width will disappear in the thermal and localized phases as all correlations will be equivalent or only local, respectively. The distributions of the correlations for high-orders for various disorder strengths and sampling sizes are plotted in §Appendix: I.

We find that in the thermal and the many-body-localized regimes, the system becomes successively less correlated at higher order. The behavior in the quantum critical regime is strikingly different: we observe that the system is strongly correlated at all measured orders. There is an additional interpretation to the presence of correlations at high order that relates to the length scale of entanglement in the system. Since all high-order correlations in this system inherently involve n unique sites, it is also implying that there is non-negligible correlations across n sites in the system and can be thought of as an increasing length scale of correlations in this critical regime. Similar behavior has been seen in theory when performing a cluster analysis of entanglement among spins⁷⁷ and is reminiscent of the canonical phase transition behavior expected for equilibrium phase transitions^{7,136,135}.

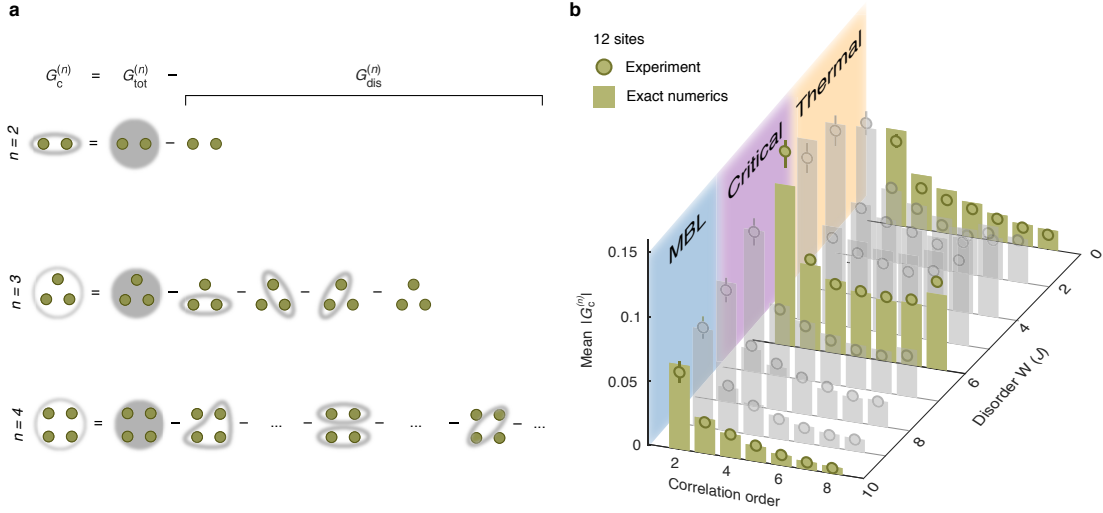


Figure 6.7: Higher Order Connected Correlations. a) We obtain the genuine many-body processes of order n from connected correlations $G_c^{(n)}$ by subtracting all lower order contributions $G_{\text{dis}}^{(n)}$ from the total correlation function $G_{\text{tot}}^{(n)}$. b) In the quantum critical regime, we find enhanced collective fluctuations at all measured orders by computing the mean absolute value of $G_c^{(n)}$ for different disorder strengths. These data were measured on a twelve-site system. The bars denote the prediction of exact numeric time calculations without any free parameters. The error bars are the s.e.m.

In order to further investigate the system's many-body structure, we examine the site-resolved contributions of the three-point correlations. Since all non-zero contributions to the three-point correlations involve correlated hopping of at least two particles, they are a signature for multi-particle entanglement¹⁶⁷. In the quantum critical regime, we find that these correlations span the entire system and are highly structured, taking on both positive and negative values (Fig. 6.8). In contrast to the pattern in the second-order correlation function, this third-order structure is not directly recognizable as the quasi-periodic correlation functions. In fact, the quasi-periodic correlation function is exactly zero at third-order. In order to gain further insight into the structure, we analyze the contributions of all possible particle configurations that contribute to non-zero connected correlations

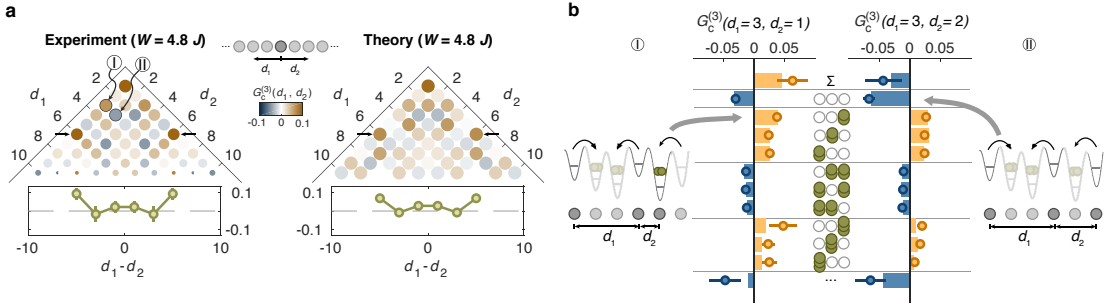


Figure 6.8: Microscopy of $G_c^{(3)}(d_1, d_2)$. **a)** The connected correlation function, $G_c^{(3)}(d_1, d_2)$, for three lattice sites spaced by distances d_1 and d_2 in the quantum critical regime ($W = 4.8 J$), showing the strongly interacting nature of the state. We find that the three-point correlations show a characteristic structure that is governed by the contribution of the number states on the considered sites. The arrows indicate the cut in d_1, d_2 space plotted below. **b)** To exemplify the relevant processes of order $n=3$, we show the contributions of the number states on lattice sites at distance $d_1 = 3, d_2 = 1$ (left) and $d_1 = 3, d_2 = 2$ (right). While there is a wide distribution of contributing configurations, the relative dominance of a particular process provides the overall structure in a. The illustration of atoms undergoing a highly correlated hopping process in the lattice describe how such correlations can contribute to either positive or negative correlations among the three considered sites. The theory plot in a and bars in b are calculated from exact numeric time calculations without any free parameters. The inverse marker size in the experimental plot in a, and the error bars in both a and b denote the s.e.m.

in Fig. 6.8. In particular, for $G_c^{(3)}(d_1 = 3, d_2 = 1)$, which is positive, we see that the dominant contributions comes from a particular process that favors multiple atoms hopping to the same site. In contrast, $G_c^{(3)}(d_1 = 3, d_2 = 2)$, which is negative, has a dominant process that favors all atoms leaving the three considered sites. While this provides some intuition for the emergent many-body resonances, the three-point correlations are, in fact, the result of a superposition of many correlated processes. These observations further demonstrate how the interactions between multiple atoms can compensate for the disorder via correlated tunneling of several atoms. In this way we can see the additional role interactions play in the disordered system: they supply high-order many-body resonances that preserve transport where lower-order processes are energetically suppressed.

6.6 DISCUSSION

These results¹⁵⁴ demonstrate how a many-body sparse resonant structure drives the quantum critical behavior at the MBL transition. The observed microscopic description is consistent with the theoretically suggested mechanism of a sparse *backbone* of resonances that can act as a functional bath for the system that is critically sub-thermal^{101,69,148}. However our results provide a new perspective on this description by mapping out the prevalence of higher-order process in the system that facilitate this critical thermalization.

Since we use a quasi-periodic localizing potential, our system has no rare regions and prevents other proposed thermalizing mechanisms from playing a role, such as rare Griffiths regions that act as local thermal baths. In that respect, we are able to isolate a class of thermalizing mechanisms and observe them in-situ as the dominant way that the system critically thermalizes at intermediate disorder. These results do not, however, rule out any other possible mechanism that may also lead to critical thermalization at intermediate disorder regimes. Further studies of larger system sizes and different localization potentials would better elucidate whether proposed mechanisms (e.g. quantum avalanches) would also lead to qualitatively similar behaviors^{148,185,192,156,115,147}. This would additionally open up the possibility for studying the role of universality and whether there exist multiple classes for the thermal-to-MBL transition that depend upon the disorder type¹⁰².

A last comment to make is about what is considered a natural route of continued exploration, which would be to evaluate the same type of system at larger sizes. It is worth noting here that, at least for all known current experimental apparatuses, larger system sizes are not actually the limita-

tion. The ability to evolve the quantum many-body system coherently for exponentially long time is the current limitation. The danger being that, in most cases, coupling to the external environment will add an energy reservoir attached to every site in the system that will always lead the system to an infinite temperature state given enough time. One of the crucial steps in the reported results from this thesis being that we are able to verifiably provide a bound on how coherent the system is (§5.5).

Humility has negative impact factor.

Professor Rajibul Kazim Islam

7

Conclusion

7.1 SUMMARY

In this thesis, I have presented results that discern the behavior of quantum correlations in both equilibrium and non-equilibrium phase transitions. A framework is presented for distinguishing between quantum-thermalizing and many-body-localized phases by observing the dynamics of such correlations in a Bose-Hubbard system. Additionally, the observations of spatial correlations persist-

ing to high orders in the critical regime demonstrates the value of using a quantum gas microscope to observe highly correlated, novel quantum phenomena.

For the case of the equilibrium quantum phase transition of the transverse Ising model, we can directly measure the order parameter as we cross the phase transition and the effect of boundary conditions on the ground state. We additionally measure an increase of entanglement entropy near the critical point that qualitatively aligns with the phenomenology of traditional phase transition behavior¹⁵⁸. In the case of the superfluid-to-Mott-insulator transition, we directly measure the entropy via the second-order Rényi entropy and verify that it arises from modal entanglement of the many-body quantum state⁸⁹.

In the context of a non-equilibrium phase transition, we directly measure that, after a quantum quench, an isolated quantum many-body system rapidly approaches local agreement with predictions given by a statistical ensemble. The entanglement entropy measured via the Rényi entropy in this system is analogous to the thermal entropy expected for a truly thermal system. These observations agree with the predictions of the eigenstate thermalization hypothesis that isolated quantum systems locally resemble classical ensembles⁹⁹. However, the robust exception to this behavior is generated by the application of on-site disorder potentials that prevent the system from thermalizing and qualitatively changes its entanglement dynamics. We observe a logarithmically slow growth of entanglement in such a many-body-localized system and measure the subsystem-size scaling behavior of entanglement in both the thermalizing and localized phases¹¹⁸.

We additionally explore the transition between these two non-equilibrium phases. We find a system-size dependence in the thermalization of these isolated quantum systems that identifies their

critical behavior. In the two extremes of low and high disorder, we find system-size independent thermalization and localization, respectively. Near the critical point of the transition we observe an increase in correlations that persists up to high orders. Additionally, these correlations are highly-structured and suggest that it is not all sites in the system that contribute to this critical thermalization, but it is a sparse-resonant network of sites that leads the system towards equilibration. These results lay the foundation for experimentally studying the critical behavior of non-equilibrium phase transitions and whether many of the same concepts from traditional equilibrium phase transitions framework can be applied to these systems¹⁵⁴.

7.2 OUTLOOK

The results in this thesis have demonstrated novel measurement techniques, long coherence times, precise system-size scalability, and framework for understanding the growth of correlations in a non-equilibrium system. However, many open questions about the thermal-to-MBL phase transition still remain. Some of these questions can be straight-forwardly implemented in our system through several new studies:

7.2.1 LOCALIZATION IN DIFFERENT DISORDER DISTRIBUTIONS

For all the experiments involving localization in this thesis, the on-site potential offsets used for localization of the many-body states were drawn from a quasi-periodic distribution. This effectively realizes many-body localization in the interacting Aubry-André model. While localization is not unique to this distribution, it has been predicted by numerical studies that different disorder distributions

may lead to different universality classes of such a transition^{102,192}. The DMD used for applying the on-site potentials in the presented experiments can be easily adjusted to generate different potential distributions (e.g. binary disorder, uniform-random disorder, etc.). Studying the critical behavior of this system in different potential distributions will help shed light on the presence of universality in these non-equilibrium systems^{102,192,171}.

7.2.2 MECHANISMS FOR THERMALIZATION

Additionally, the microscopic mechanism that leads to thermalization in different disorder distributions may qualitatively differ. The microscopic resolution of correlations in these systems afforded by the quantum gas microscope would allow for an extended study of the microscopic picture for how such systems thermalize^{148,185,192,156,115,147}.

As a preliminary study of a particular mechanism, we experimentally implement the effect of anomalously low-disorder regions that would exist in truly random on-site disorder. It is believed that such regions will behave like thermal systems and create a so-called “avalanche” that drives the remaining system towards thermalization^{156,115}. To probe such a mechanism, we measured the local number fluctuations in a many-body-localized system that is in contact with a variable-size ergodic grain. The many-body-localized system experiences quasi-periodic disorder and in a system with no bath remains localized for long times. We observe that in the two studied cases, a bath size of 2-sites and a bath size of 6-sites, the smaller system remains localized for all measured times while the system with the larger bath size shows a slow relaxation towards thermal equilibrium with a spatial dependence that mimics the proposed “avalanche” mechanism.

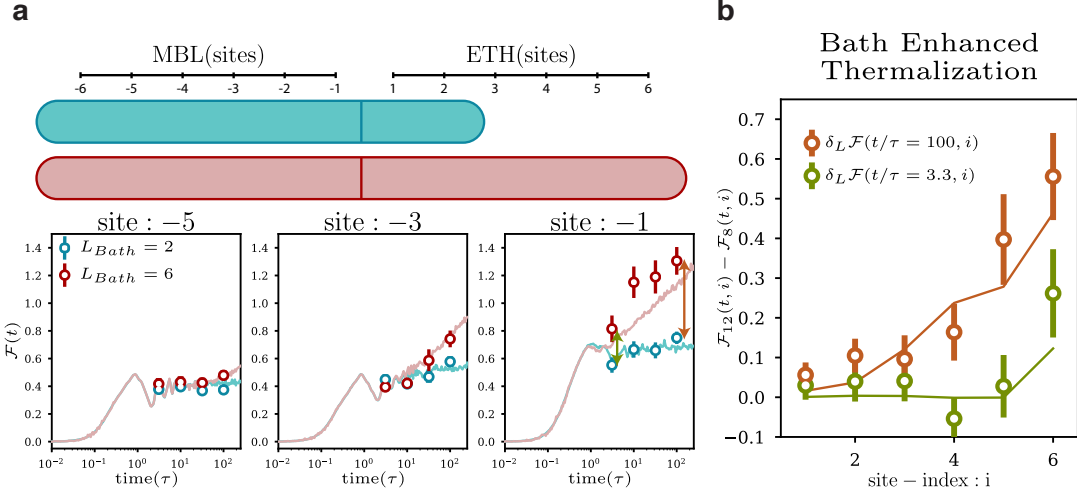


Figure 7.1: Thermalization from bath. **a)** The thermalization of a 6-site MBL system due to local contact with a thermal bath is compared for two different bath sizes : a 2-site bath (blue) and a 6-site bath (red). The site indices reflect their distance from the left-most end of the MBL system: $i = 6$ is the first MBL site closest to the bath, $i = 1$ is the MBL site furthest from the bath. We find that only the larger bath size causes a slow growth of the on-site fluctuations which typically herald the agreement with a thermal ensemble. **b)** The difference between the on-site fluctuations of the two different bath sizes are compared site-by-site for two different times: $t = 3\tau$ (green) and $t = 100\tau$ (orange). The green line (early time) demonstrates a near agreement at early times between the two different system sizes, while the orange line (late time) shows a significant, site dependent thermalization away from the bath. The solid lines are calculated from exact numerics. The error bars are the s.e.m.

The enhanced thermalization in the larger bath-size system grows as a function of distance away from the bath-MBL interface. This is consistent with the avalanche process acting as a bath that incorporates nearby non-thermal systems that then enhance the bandwidth of thermalizing bubble that then spatially drives the system as a whole towards equilibrium. This can be visualized by comparing the penetration depth of the bath into the localized system where we see the larger system has a penetration depth that grows with time – unlike the smaller bath system (as seen in Fig 7.2).

These preliminary studies suggest that the avalanche-like process is likely a viable mechanism for thermalizing disordered systems. This mechanism seems like a conceptually natural method for systems with random disorder to eventually thermalize since sufficiently large systems will contain large

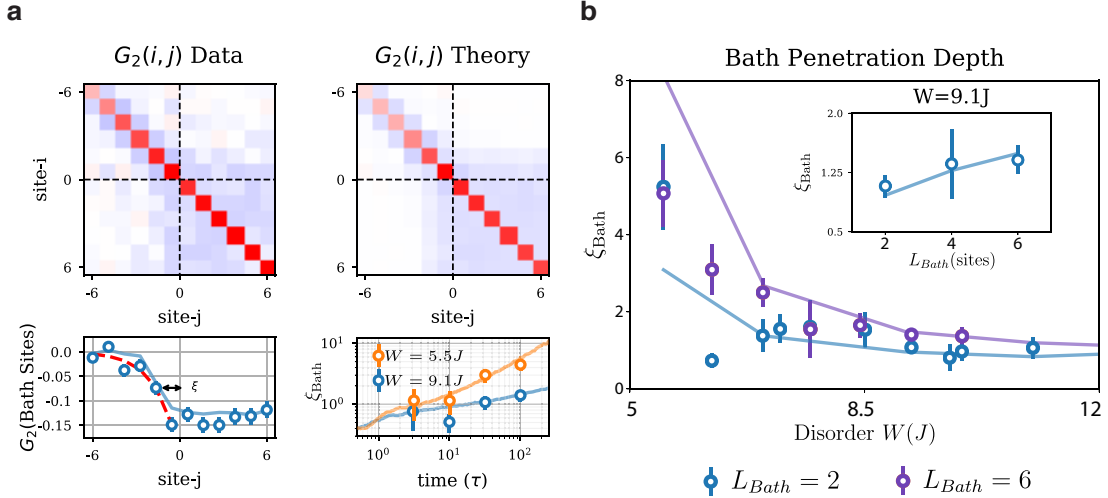


Figure 7.2: Penetration depth. a) We directly probe the bath penetration depth by averaging over the two-point correlations from bath sites to MBL sites ($G_c^{(2)}(i,j)$). The extracted correlation length (bottom left) is then calculated by the first moment and plotted as a function of time for a critical system (orange, $W = 5.5J$) and an MBL system (blue, $W = 9.1J$). b) We then compare the extracted localization length ζ_{Bath} at long times ($t = 100\tau$) for both the 2-site bath system (blue) and the 6-site bath system (orange) as a function of disorder. We then compare this length scale as a function of total bath size for the MBL disorder regime (inset).

ergodic grains known as Griffiths regions. In this study, this hybrid system of a quasi-periodic disordered system in physical contact with an ergodic grain is similar to adding such a non-disordered Griffiths region in a randomly disordered system.* There is an additional caveat to this physical implementation that relates to a suggestion that the critical behavior for quasi-periodic and random potentials might be of different universality classes^{102,192}, in which case it is unclear whether the observed behavior will quantitatively agree with either. This emphasizes the importance of further

*Griffiths regions often refer to a rare region of anomalously large disorder that acts like a bottle neck for hindering the spread of information in a system. These regions will exist in large random-disorder systems due to the stochastic likelihood of sampling several significantly different on-site potential values that are also neighboring in space. However, in this case I am referring to the opposite likelihood of sampling very similar values for on-site potential values for neighboring sites in space that would allow for anomalously low disorder regions that would look locally thermal and potentially act as a bath for the remaining system.

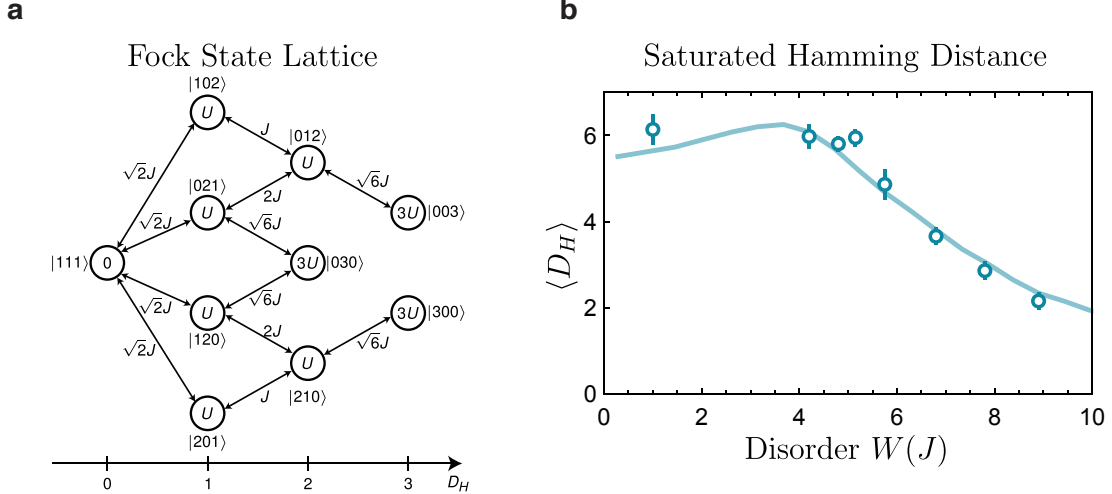


Figure 7.3: Hamming distance (D_H). **a)** A schematic of the mapping to a Fock state lattice of 3-sites at unity filling. Each node in this lattice represents a given Fock state. The nodes have an on-site energy determined by their interaction and potential offsets. They are still coupled by the tunneling matrix elements J . This effectively casts the many-body problem into a multi-dimensional, single-particle problem. The number of hops away from the initial state are encoded along the x -axis and are labeled as the Bose-Hubbard version of the Hamming distance (D_H). **b)** The Hamming distance is measured at late times ($t = 100\tau$) and plotted as a function of disorder strength W for an 8-site Bose-Hubbard system after the protocol defined in §5. The decrease in final Hamming distance as a function of W indicates localization in Fock space.

studies of thermalization in such disordered systems by engineering the presence of ergodic grains and also realizing multiple disorder distribution classes.

7.2.3 LOCALIZATION IN FOCK SPACE

One of the first approaches taken to solve the MBL problem was to cast it back to a single-particle problem by looking at the system in Fock space⁶⁵. This then makes every Fock state a single node in a large, multi-dimensional space where the on-site disorder for each node both depends upon the interaction energy U and the experienced on-site disorder W_i . This is shown schematically in Fig. 7.3.

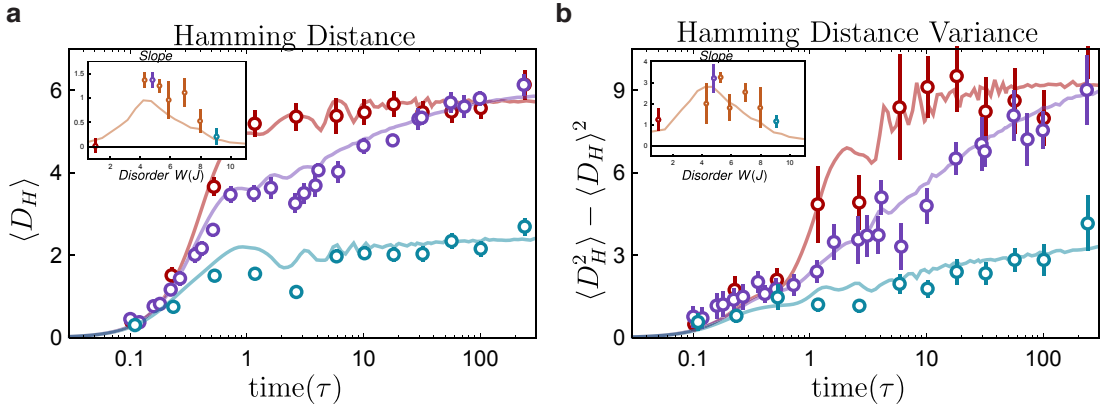


Figure 7.4: First and second moments of Hamming distance. **a)** The first moment of the Hamming distance, $\langle D_H \rangle$ is plotted as a function of time for the thermalizing (red), critical (purple), and MBL (blue) regimes. The slopes of these growth curves are extracted from a semi-log plot for $L/2\tau < t \leq 100\tau$ and shown in the inset as a function of disorder. **b)** The second moment of the Hamming distance, $\langle (D_H - \langle D_H \rangle)^2 \rangle$ is plotted as a function of time for the thermalizing (red), critical (purple), and MBL (blue) regimes. The slopes of these growth curves are extracted from a semi-log plot for $L/2\tau < t \leq 100\tau$ and shown in the inset as a function of disorder.

Since we have direct access to the many-body state in the Fock basis at the end of each experimental run, we can experimentally verify the localization of the system in Fock space. In some preliminary experiments, we quantify the localization of the state through the Fock-space Hamming distance. Traditionally, the Hamming distance is a concept from computer science that defines how many bit flips away a string of bits is from its original configuration. This is modified to the case of bosons hopping in a lattice by determining the minimum number of hopping events a state has moved away from its initial state (D_H). In Fig. 7.4 we show the evolution of the first and second moments of D_H in the thermalizing, MBL, and critical regimes of disorder as a function of time. This preliminary study seems to show a persistence of evolution in the diffusion of the system in Fock space while the first moment remains stationary at a finite value.

However, since the original intention was to look at whether the system localizes in Fock space,

one needs to normalize this system by the density of states at a given Hamming distance. This approach is only marginally more complicated than in real space since the dimensionality, or connectivity, of the system changes as a function of a given node. This density of states as a function of D_H , as well as the measured, long-time probability distributions have not been normalized. Note that when normalized by the density of states, all quench experiments will appear to be localized to some finite value. This is partially due to the cost in energy associated with multiple occupancies in Fock space, which appears as an effective trapping potential in this basis. Therefore, all finite energy density quench experiments will likely have a finite localization length less than the total system size.

A

Atomic Properties of ^{87}Rb

Below are a useful set of physical constants and atomic properties for ^{87}Rb .¹⁷⁸

Table 1: Fundamental Physical Constants (2006 CODATA recommended values [2])

Speed of Light	c	$2.997\ 924\ 58 \times 10^8$ m/s (exact)
Permeability of Vacuum	μ_0	$4\pi \times 10^{-7}$ N/A ² (exact)
Permittivity of Vacuum	ϵ_0	$(\mu_0 c^2)^{-1}$ (exact) $= 8.854\ 187\ 817\dots \times 10^{-12}$ F/m
Planck's Constant	h	$6.626\ 068\ 96(33) \times 10^{-34}$ J·s $4.135\ 667\ 33(10) \times 10^{-15}$ eV·s
	\hbar	$1.054\ 571\ 628(53) \times 10^{-34}$ J·s $6.582\ 118\ 99(16) \times 10^{-16}$ eV·s
Elementary Charge	e	$1.602\ 176\ 487(40) \times 10^{-19}$ C
Bohr Magneton	μ_B	$9.274\ 009\ 15(23) \times 10^{-24}$ J/T $h \cdot 1.399\ 624\ 604(35)$ MHz/G
Atomic Mass Unit	u	$1.660\ 538\ 782(83) \times 10^{-27}$ kg
Electron Mass	m_e	$5.485\ 799\ 0943(23) \times 10^{-4}$ u $9.109\ 382\ 15(45) \times 10^{-31}$ kg
Bohr Radius	a_0	$0.529\ 177\ 208\ 59(36) \times 10^{-10}$ m
Boltzmann's Constant	k_B	$1.380\ 6504(24) \times 10^{-23}$ J/K

Table 2: Rubidium 87 Physical Properties.

Atomic Number	Z	37	
Total Nucleons	$Z + N$	87	
Relative Natural Abundance	$\eta(^{87}\text{Rb})$	27.83(2)%	[3]
Nuclear Lifetime	τ_n	4.88×10^{10} yr	[3]
Atomic Mass	m	86.909 180 520(15) u $1.443\ 160\ 648(72) \times 10^{-25}$ kg	[4]
Density at 25°C	ρ_m	1.53 g/cm ³	[3]
Melting Point	T_M	39.30 °C	[3]
Boiling Point	T_B	688 °C	[3]
Specific Heat Capacity	c_p	0.363 J/g·K	[3]
Molar Heat Capacity	C_p	31.060 J/mol·K	[3]
Vapor Pressure at 25°C	P_v	$3.92(20) \times 10^{-7}$ torr	[5]
Nuclear Spin	I	3/2	
Ionization Limit	E_I	33 690.804 80(20) cm ⁻¹ 4.177 127 06(10) eV	[8]

Figure A.1: Physical constants reference and atomic physical properties ¹⁷⁸

Table 3: Rubidium 87 D₂ ($5^2S_{1/2} \longrightarrow 5^2P_{3/2}$) Transition Optical Properties.

Frequency	ω_0	$2\pi \cdot 384.230\,484\,468\,5(62)$ THz	[9]
Transition Energy	$\hbar\omega_0$	$1.589\,049\,462(38)$ eV	
Wavelength (Vacuum)	λ	$780.241\,209\,686(13)$ nm	
Wavelength (Air)	λ_{air}	$780.033\,330(23)$ nm	
Wave Number (Vacuum)	$k_L/2\pi$	$12\,816.549\,389\,93(21)$ cm ⁻¹	
Isotope shift	$\omega_0(^{87}\text{Rb}) - \omega_0(^{85}\text{Rb})$	$2\pi \cdot 78.095(12)$ MHz	[10]
Lifetime	τ	$26.2348(77)$ ns	[18–21]
Decay Rate/ Natural Line Width (FWHM)	Γ	$38.117(11) \times 10^6$ s ⁻¹ $2\pi \cdot 6.0666(18)$ MHz	
Absorption oscillator strength	f	$0.695\,77(29)$	
Recoil Velocity	v_r	5.8845 mm/s	
Recoil Energy	ω_r	$2\pi \cdot 3.7710$ kHz	
Recoil Temperature	T_r	361.96 nK	
Doppler Shift ($v_{\text{atom}} = v_r$)	$\Delta\omega_d(v_{\text{atom}} = v_r)$	$2\pi \cdot 7.5419$ kHz	
Doppler Temperature	T_D	145.57 μK	
Frequency shift for standing wave moving with $v_{\text{sw}} = v_r$	$\Delta\omega_{\text{sw}}(v_{\text{sw}} = v_r)$	$2\pi \cdot 15.0839$ kHz	

Table 4: Rubidium 87 D₁ ($5^2S_{1/2} \longrightarrow 5^2P_{1/2}$) Transition Optical Properties.

Frequency	ω_0	$2\pi \cdot 377.107\,463\,380(11)$ THz	[10]
Transition Energy	$\hbar\omega_0$	$1.559\,591\,016(38)$ eV	
Wavelength (Vacuum)	λ	$794.978\,851\,156(23)$ nm	
Wavelength (Air)	λ_{air}	$794.767\,119(24)$ nm	
Wave Number (Vacuum)	$k_L/2\pi$	$12\,578.950\,981\,47(37)$ cm ⁻¹	
Isotope shift	$\omega_0(^{87}\text{Rb}) - \omega_0(^{85}\text{Rb})$	$2\pi \cdot 77.583(12)$ MHz	[10]
Lifetime	τ	$27.679(27)$ ns	[18, 19, 21]
Decay Rate/ Natural Line Width (FWHM)	Γ	$36.129(35) \times 10^6$ s ⁻¹ $2\pi \cdot 5.7500(56)$ MHz	
Absorption oscillator strength	f	$0.342\,31(97)$	
Recoil Velocity	v_r	5.7754 mm/s	
Recoil Energy	ω_r	$2\pi \cdot 3.6325$ kHz	
Recoil Temperature	T_r	348.66 nK	
Doppler Shift ($v_{\text{atom}} = v_r$)	$\Delta\omega_d(v_{\text{atom}} = v_r)$	$2\pi \cdot 7.2649$ kHz	
Frequency shift for standing wave moving with $v_{\text{sw}} = v_r$	$\Delta\omega_{\text{sw}}(v_{\text{sw}} = v_r)$	$2\pi \cdot 14.5298$ kHz	

Figure A.2: Optical transition properties for ^{87}Rb ¹⁷⁸

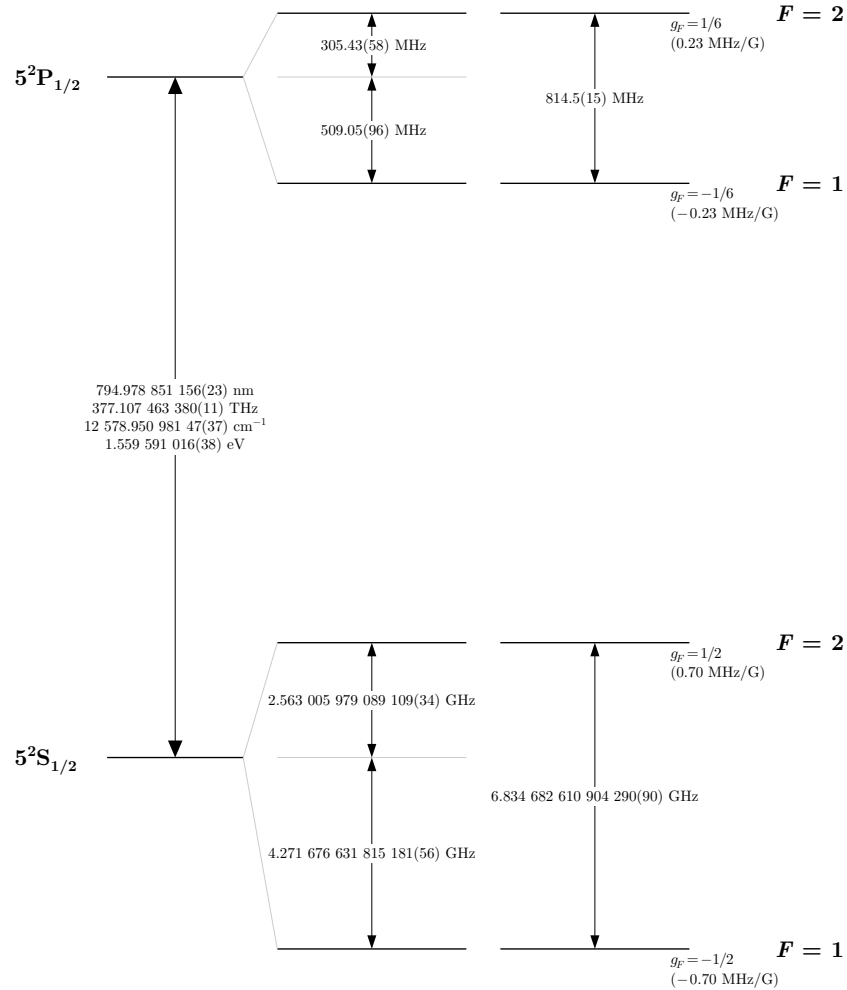


Figure 3: Rubidium 87 D₁ transition hyperfine structure, with frequency splittings between the hyperfine energy levels. The excited-state values are taken from [10, 11, 26], and the ground-state values are from [29]. The relative hyperfine shifts are shown to scale within each hyperfine manifold (but visual spacings should not be compared between manifolds or to the optical splitting). The approximate Landé g_F -factors for each level are also given, with the corresponding Zeeman splittings between adjacent magnetic sublevels.

Figure A.3: Optical D1 transition diagram ¹⁷⁸

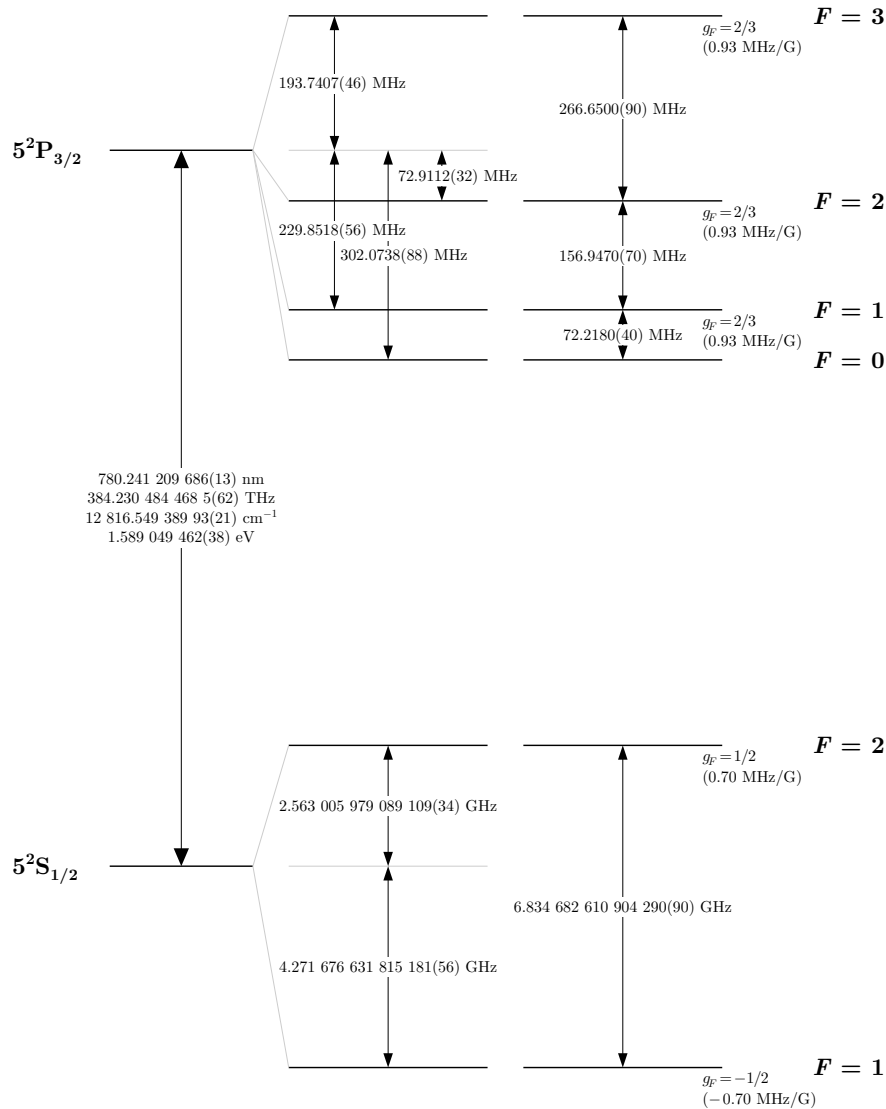


Figure 2: Rubidium 87 D₂ transition hyperfine structure, with frequency splittings between the hyperfine energy levels. The excited-state values are taken from [9], and the ground-state values are from [29]. The relative hyperfine shifts are shown to scale within each hyperfine manifold (but visual spacings should not be compared between manifolds or to the optical splitting). The approximate Landé g_F -factors for each level are also given, with the corresponding Zeeman splittings between adjacent magnetic sublevels.

Figure A.4: Optical D2 transition diagram ¹⁷⁸

B

Numerics

All L^AT_EX, PYTHON, MATLAB, and MATHEMATICA files related to this thesis can be found at –

<https://github.com/mnrispoli/Dissertation/>

C

Experimental Sequences

Below are the experimental sequences used for all non-equilibrium experiments:

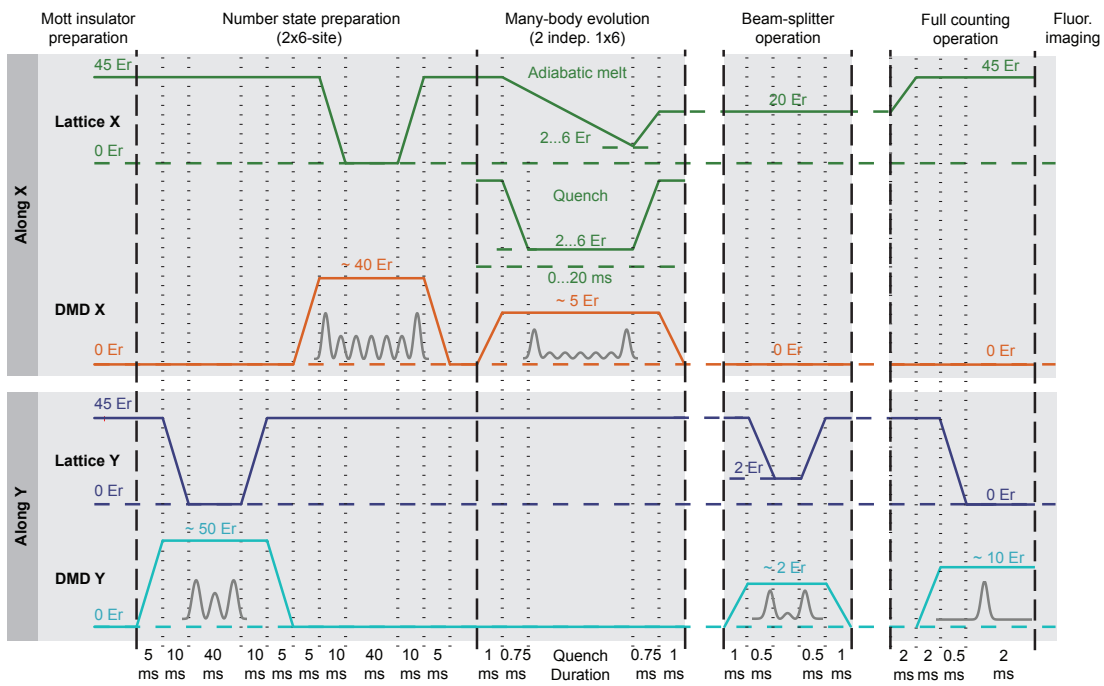


Figure C.1: Experimental sequence for probing quantum thermalization⁹⁹

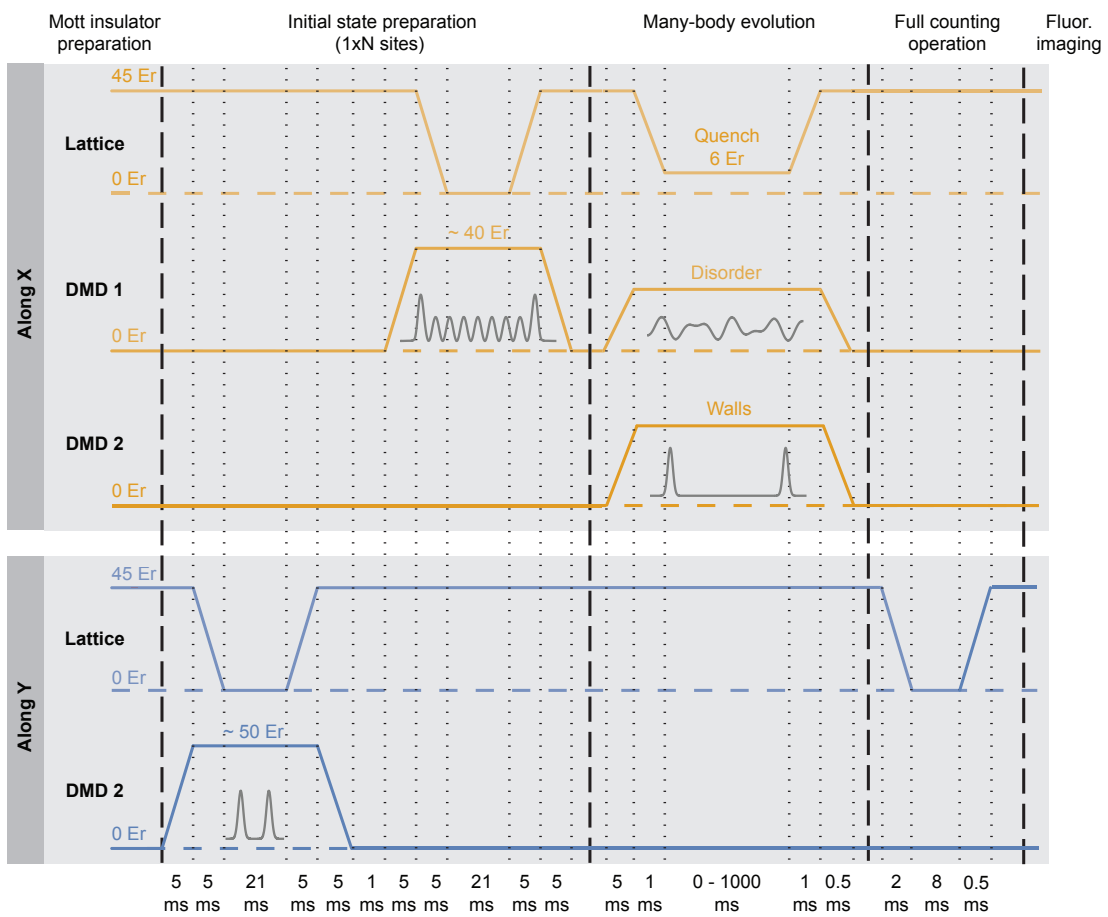


Figure C.2: Experimental sequence for probing many-body localization ¹¹⁸

D

Chapter I Calculations

D.1 OPTICAL LATTICE POTENTIAL FROM LASER LIGHT

Starting from two propagating plane waves, we can find the shape of the potential that is proportional to the intensity:

$$V_{Latt} \propto |e^{i(k_l x - \omega t)} + e^{i(k_l x + \omega t)}|^2 \propto \cos^2(k_l x) \propto \cos(2k_l x) \quad (\text{D.1})$$

Note, that we have left the potential as a function of the laser wavevector. This is important for the definition of the “recoil energy” of the lattice photons ($E_r = \frac{\hbar^2 k_l^2}{2m}$). The k_l defines the wavevector of the light projected into the plane of the lattice ($k_l = \frac{2\pi}{\lambda} \sin(\theta)$) where θ is the angle away from the normal vector to the plane. In a retro-reflecting lattice setup this is simply the bare photon wavevector $k_l = \frac{2\pi}{\lambda}$. To simplify calculations, we subtract off the mean energy of the lattice such that it has an amplitude V_o which we define as the lattice depth.

$$V_{Latt} = \frac{-V_o}{2} \cos(2k_l x) \quad (\text{D.2})$$

D.2 HARMONIC OSCILLATOR APPROXIMATION

In the deep lattice (or “tight-binding”) regime, the optical lattice can be approximated on-site as a harmonic potential:

$$V_{Latt} = \frac{-V_o}{2} \cos(2k_l x) \approx \frac{-V_o}{2} \left(1 - \frac{(2k_l x)^2}{2!} \right) \quad (\text{D.3})$$

By finding the on-site trap frequency ω , we can then construct the harmonic oscillator solutions shown in §I.2.2.

$$-V_o/2 + V_o k^2 x^2 \sim V_{HO}(x) = \frac{1}{2} m \omega^2 x^2$$

$$V_o k^2 = \frac{1}{2} m \omega^2$$

$$\hbar^2 \omega^2 = \frac{2V_o \hbar^2 k_l^2}{m} = 4V_o \frac{\hbar^2 k_l^2}{2m}$$

$$\omega = 2 \left(\frac{E_r}{\hbar} \right) \sqrt{\frac{V_o}{E_r}}$$

E

Chapter 2 Calculations

E.I Z-LATTICES FROM ANGLED REFLECTION

E.I.I FRESNEL COEFFICIENTS

The fresnel coefficients for illumination of a surface from a medium of refractive index n_1 to a surface of refractive index n_2 . They are defined in intensity as a function of illumination angle θ by:

$$R_s = \left| \frac{n_1 \cos(\theta) - n_2 \sqrt{1 - \left(\frac{n_1}{n_2} \sin(\theta) \right)^2}}{n_1 \cos(\theta) + n_2 \sqrt{1 - \left(\frac{n_1}{n_2} \sin(\theta) \right)^2}} \right|^2 \quad (\text{E.I})$$

$$R_p = \left| \frac{n_1 \sqrt{1 - \left(\frac{n_1}{n_2} \sin(\theta) \right)^2} - n_2 \cos(\theta)}{n_1 \sqrt{1 - \left(\frac{n_1}{n_2} \sin(\theta) \right)^2} + n_2 \cos(\theta)} \right|^2 \quad (\text{E.2})$$

where the subscripts “s” and “p” refer to the typical linear polarizations of light, $n_1 = 1$ for vacuum, and $n_2 \approx 1.45$ for fused silica.

E.I.2 LATTICE SPACING, CONTRAST, AND OFFSET

Interfering two lasers at a given angle θ and the wavelength λ the resultant lattice constant is $a = \frac{\lambda}{2 \sin(\theta)}$. The angle θ refers to the half-angle between the two lasers. For the x, y -lattices, the lattice wavelength is $\lambda \approx 758$ nm from a 3 nm broad light source $\theta \approx 34^\circ$.

We can use the reflection coefficients from above to determine the lattice parameters for both of the z -lattices. The “axial” lattice has a relatively steep angle of incidence with respect to the substrate ($\approx 75.6^\circ$). This produces a lattice with a lattice constant $a \approx 1.5\mu\text{m}$. This gives rise to a recoil

energy $E_r^{axial} \approx 2\pi \times 255\text{Hz}$. The lattice contrast is determined by the intensity reflectivity $R_s(\theta)$ by $\left(\frac{2\sqrt{R_s}}{1+R_s}\right)$. In the “axial” configuration this contrast is ≈ 0.9 . The lack of reflectivity additionally gives rise to a DC offset in the light potential at the nodes of the lattice which is determined by the minimum value in the potential versus the max-min depth of the lattice $\left(\frac{1-2\sqrt{R_s}+R_s}{4\sqrt{R_s}}\right)$. For the “axial” configuration, this offset is $\approx 0.056 \times V_o^{axial}$ where V_o^{axial} is the depth of the lattice in E_r^{axial} .

If we follow the same analysis for the “big” lattice configuration, we will find that the steeper angle of incidence ($\approx 88^\circ$) gives rise to the following lattice parameters: lattice constant $a \approx 9.2\mu\text{m}$, recoil energy $E_r^{big} \approx 2\pi \times 7\text{Hz}$, contrast of ≈ 0.997 , and a DC offset of $\approx 0.002 \times V_o^{big}$.

E.2 CALCULATIONS FOR DISORDER AND ZERO-POINT ENERGY

A simple model for estimating the disorder in a Bose-Hubbard system, the difference in the on-site potential energy change due to scatterers along the optical path can be estimated from the contrast imbalance due to loss from the scatterer. So the estimate for the ground state energy change comes from the energy felt by the atom due to two counter-propagating beams:

$$|V_1|^2 = \frac{1}{4} \left(\frac{V_o}{E_r} \right) E_r$$

$$|V_2|^2 = \frac{1}{4} (1 + \epsilon) \left(\frac{V_o}{E_r} \right) E_r$$

We can find the lattice potential $V(x) \sim (V_1^* + V_2^*) (V_1 + V_2)$ for a red detuned lattice: *

$$\begin{aligned}
V^{(red)}(x, \epsilon) &= -\frac{1}{4} \frac{V_o}{E_r} E_r \left(e^{-ik_l x} + \sqrt{(1+\epsilon)} e^{ik_l x} \right) \left(e^{ik_l x} + \sqrt{(1+\epsilon)} e^{-ik_l x} \right) \\
&= -\frac{1}{4} \frac{V_o}{E_r} E_r \left(2 + \epsilon + \sqrt{(1+\epsilon)} \left(e^{-i2k_l x} + e^{i2k_l x} \right) \right) \\
&= -\frac{1}{4} \frac{V_o}{E_r} E_r \left(2 + \epsilon + \sqrt{(1+\epsilon)} (2 \cos(2k_l x)) \right)
\end{aligned} \tag{E.3}$$

expand the $\cos(2k_l x)$ about $x = 0$ for both the red- and blue-detuned cases: †

$$V^{(red)}(x, \epsilon) = -\frac{1}{4} \frac{V_o}{E_r} E_r \left(2 + \epsilon + 2\sqrt{(1+\epsilon)} \left(1 - \frac{(2k_l x)^2}{2!} \right) \right) = V_{off}(\epsilon) + V_{HO}(x, \epsilon) \tag{E.4}$$

$$V^{(blue)}(x, \epsilon) = \frac{1}{4} \frac{V_o}{E_r} E_r \left(2 + \epsilon - 2\sqrt{(1+\epsilon)} \left(1 - \frac{(2k_l x)^2}{2!} \right) \right) = V_{off}(\epsilon) + V_{HO}(x, \epsilon) \tag{E.5}$$

Let us now evaluate the total offset (including the ground state energy shift from the harmonic oscillator) found as a function of ϵ for the red-detuned case:

$$V_{off}^{(red)}(\epsilon) = -\frac{1}{4} \frac{V_o}{E_r} E_r \left(2 + \epsilon + 2\sqrt{(1+\epsilon)} \right)$$

*We have assumed a phase of zero at $x=0$ for these beams since the fields are written as just the square root of the intensity assumed earlier.

†This takes care of the DC offset from either sitting at the nodes or anti-nodes of the optical lattice.

$$V_{HO}^{(red)}(x, \epsilon) = -\frac{V_o}{E_r} E_r (2\sqrt{(1+\epsilon)}) \frac{(k_l x)^2}{2} = \frac{1}{2} m \omega_{red}^2 x^2$$

$$\hbar^2 \omega_{red}^2 = -4 \frac{V_o}{E_r} E_r \sqrt{(1+\epsilon)} \frac{\hbar^2 k_l^2}{2m}$$

$$E_o^{(red)} = \frac{1}{2} \hbar \omega_{red} = 2 E_r \sqrt{\frac{V_o}{E_r}} (1+\epsilon)^{1/4}$$

$$E_g^{(red)}(\epsilon, V_o) = V_{off}^{(red)} + E_o^{(red)} = E_r \left[-\frac{(2+\epsilon+2\sqrt{1+\epsilon})}{4} \left(\frac{V_o}{E_r} \right) + 2 \sqrt{\frac{V_o}{E_r}} (1+\epsilon)^{1/4} \right] \quad (\text{E.6})$$

This can be modified easily for the blue-detuned case without much extra math:

$$V_{off}^{(blue)}(\epsilon) = \frac{1}{4} \frac{V_o}{E_r} E_r \left(2 + \epsilon - 2\sqrt{(1+\epsilon)} \right)$$

$$E_g^{(blue)}(\epsilon, V_o) = V_{off}^{(red)} + E_o^{(red)} = E_r \left[\frac{(2+\epsilon-2\sqrt{1+\epsilon})}{4} \left(\frac{V_o}{E_r} \right) + 2 \sqrt{\frac{V_o}{E_r}} (1+\epsilon)^{1/4} \right] \quad (\text{E.7})$$

However, considering that the deviation in local contrast due to deflected beam power is often

quite small from site-to-site, we can take the approximation of small ϵ :

$$E_g^{(red)}(\epsilon, V_o) \approx E_r \left[-\left(1 + \frac{1}{2}\epsilon\right) \left(\frac{V_o}{E_r}\right) + 2\sqrt{\frac{V_o}{E_r}} \left(1 + \frac{1}{4}\epsilon\right) \right] \quad (\text{E.8})$$

$$E_g^{(blue)}(\epsilon, V_o) \approx E_r \left[2\sqrt{\frac{V_o}{E_r}} \left(1 + \frac{1}{4}\epsilon\right) \right] \quad (\text{E.9})$$

By taking the derivative of the ground-state energies as a function of ϵ we can approximate the effective site-to-site change in ground-state energy due to local beam power deviation. This will allow us to compare the approximate site-to-site variation in the lattice detuning configurations as a function of lattice depth:

$$\frac{d}{d\epsilon} E_g^{(red)}(\epsilon, V_o) = \frac{E_r}{2} \left[-\left(\frac{V_o}{E_r}\right) + \sqrt{\frac{V_o}{E_r}} \right] \quad (\text{E.10})$$

$$\frac{d}{d\epsilon} E_g^{(blue)}(\epsilon, V_o) = \frac{E_r}{2} \left[\sqrt{\frac{V_o}{E_r}} \right] \quad (\text{E.11})$$

By taking the ratio of these two susceptibilities to beam-power deviation, we find that for almost all lattice depths ($V_o/E_r > 1$) are less susceptible in the blue-detuned lattice by the ratio given below:

$$\frac{1}{1 - \sqrt{V_o/E_r}}$$

F

Chapter 3 Calculations

F.I MAPPING: BOSE-HUBBARD MODEL TO TRANSVERSE ISING MODEL

$$\tilde{t} = t/J \quad (\text{F.1})$$

$$h_x = 2^{3/2}\tilde{t} \quad (\text{F.2})$$

$$h_z = 1 - \tilde{\Delta} \quad (\text{F.3})$$

$$\tilde{\Delta} = \Delta/J \quad (\text{F.4})$$

$$\Delta = E - U \quad (\text{F.5})$$

$$\delta_z^i = \delta E_i / J \quad (\text{F.6})$$

G

Chapter 4 Calculations

G.I PREDICTIONS FROM THERMODYNAMIC ENSEMBLES

ETH implies an equivalence between the local expectation values of a quenched many-body state and those of the thermal density matrix with the same average total energy as the many-body state. For the reported experiments, our system is initialized into the ground state, $|\psi_0\rangle$, of an initial Hamiltonian, \mathcal{H}_0 , in the atomic limit. At $t = 0$, we quench the system into a Hamiltonian, \mathcal{H}_q , after which the system is allowed to evolve for a variable amount of time. Comparing to the data at long times ($10 - 20$ ms, where we observe saturation), we can compute predictions for the expectation values of various local observables based upon different thermodynamic ensembles. These predictions are computed using the following procedures.

G.I.I MICROCANONICAL ENSEMBLE

The microcanonical ensemble is an equal probability statistical mixture of all the eigenstates that lie within an energy interval given by the initial state $|\psi_0\rangle$. In the quenched Hamiltonian, the initial state has an energy

$$E^{(0)} \equiv \langle \psi_0 | \mathcal{H}_q | \psi_0 \rangle$$

while the eigenstates of \mathcal{H}_q , $|\phi_i^{(q)}\rangle$, have energies $E_i^{(q)}$. The microcanonical ensemble is then composed of the N_{MC} number of eigenstates for which $|E_i^{(q)} - E^{(0)}| < \delta E$. For our numerical data, we have chosen $\delta E = 0.2J$, but the ensemble predictions are insensitive to the precise value of δE .

The microcanonical ensemble can be represented by the thermal density matrix

$$\rho_{ij}^{MC} = \begin{cases} \frac{1}{N_{MC}}, & \text{if } i = j \text{ and } |E_i^{(q)} - E^{(0)}| < \delta E \\ 0, & \text{else} \end{cases}.$$

G.I.2 CANONICAL ENSEMBLE

The canonical ensemble is a statistical mixture of all the eigenstates in the system weighted by each state's Boltzmann factor, $\exp(-E_i^{(q)}/k_B T)$. The temperature in the Boltzmann factor is fixed through the stipulation that the average energy of this thermal ensemble matches the energy of the initial state, i.e. we choose T such that

$$\text{Tr}(\mathcal{H}_q \rho^{CE}) = \langle \psi_0 | \mathcal{H}_q | \psi_0 \rangle,$$

where the thermal density matrix ρ^{CE} has the following construction,

$$\rho_{ij}^{CE} = \begin{cases} e^{-\frac{E_i^{(q)}}{k_B T}}, & \text{if } i = j \\ 0, & \text{else} \end{cases}.$$

G.I.3 SINGLE EIGENSTATE ENSEMBLE

Energy eigenstates of systems conforming to ETH are surmised to appear thermal in local observables. We numerically calculate the eigenstates of the quenched Hamiltonian and compare the experimentally observed local counting statistics to the prediction from the single full system eigenstate $\left| \phi_i^{(q)} \right\rangle$ that is closest in energy to the expectation value $E^{(0)}$. The expectation value in this case is given by,

$$\langle \mathcal{A} \rangle_{\text{SE}} = \left\langle \phi_i^{(q)} \middle| \mathcal{A} \middle| \phi_i^{(q)} \right\rangle.$$

G.I.4 DIAGONAL ENSEMBLE

The diagonal ensemble is a statistical mixture of all eigenstates of the full Hamiltonian \mathcal{H}_q , with the weights given by their amplitudes after quench.

$$\rho_{ij}^D = \begin{cases} |\langle \psi_0 | \phi_i^{(q)} \rangle|^2, & \text{if } i = j. \\ 0, & \text{else} \end{cases}$$

It carries all information about the amplitudes of the eigenstates but ignores all their relative phases.

G.I.5 GRAND CANONICAL ENSEMBLE

The grand-canonical ensemble requires calculating the temperature and chemical potential for the subsystem associated to the observable of interest. For example, the top (bottom) row of FIG. 6C pertains to the subsystem consisting of the third site (the first three sites) of the chain. We calculate

the temperature and chemical potential for the subsystem as follows. Because the energy and particle number within the subsystem are not conserved during the quench dynamics, we must compute the average energy $\langle E_A \rangle$ and average number $\langle N_A \rangle$ within the subsystem numerically. We time-evolve the full many-body state to the thermalized regime, then compute the reduced density matrix for the subsystem, with which we can calculate $\langle N_A \rangle$ and $\langle E_A \rangle$. We note that the average energy of nearly all the subsystems is very close to that of the full system (zero), while the average number is nearly consistent with unity particle density. For the single site subsystems, however, there is no tunneling term to offset the interaction energy, and therefore these subsystems have non-zero energy. We perform this full calculation to account for finite-size effects that cause small temporal energy and number fluctuations. If we neglect the energy fluctuations, the grand-canonical predictions (described below) are negligibly different.

After the above calculations, we can compute the chemical potential and temperature. Using each H_A^N , the subsystem Bose-Hubbard Hamiltonian with N particles, we compute the eigenstates ($|E_A^{N,i}\rangle$, where i indexes the eigenstate) and energies ($E_A^{N,i}$) for each particle sector. We seek T and μ such that,

$$\langle N_A \rangle = \langle N_{\text{GCE}} \rangle = \frac{1}{Z} \sum_{i,N} N e^{-(E_A^{N,i} - \mu N)/k_B T}$$

and,

$$\langle E_A \rangle = \langle E_{\text{GCE}} \rangle = \frac{1}{Z} \sum_{i,N} E_A^{N,i} e^{-(E_A^{N,i} - \mu N)/k_B T},$$

where for each particle number N , the index i is summed over all eigenstates within that number sector. The partition function, Z , is the overall normalization. These equations are numerically

solved to find μ and T . With these in hand, we arrive at the grand-canonical ensemble,

$$\rho_{\text{GCE}} = \frac{1}{Z} \sum_{i,N} |E_A^{N,i}\rangle \langle E_A^{N,i}| e^{-(E_A^{N,i} - \mu N)/k_B T}.$$

G.1.6 OBSERVABLES

For all statistical ensembles above, expectation values of an observable \mathcal{A} are calculated from the density matrix as

$$\langle \mathcal{A} \rangle = \text{Tr}(\mathcal{A}\rho),$$

where ρ is the full system density matrix corresponding to the appropriate ensemble.

G.2 ENTROPIES

G.2.1 RÉNYI ENTROPY

All entanglement entropy values discussed in the main text are defined as a function of the reduced density matrix of the subsystem. This applies also for the thermal entropies quoted in the main text, where we use the reduced density matrix of the canonical ensemble described above. The entropy metric used for comparison between the quantum system we measure and the canonical thermal ensemble is the Rényi entropy. In general, the n-th order Rényi entropy is defined for a reduced

density matrix of subsystem A as

$$S_n(\rho_A) = \frac{1}{1-n} \log (\text{Tr}[\rho_A^n]),$$

where the reduced density matrix ρ_A is defined by tracing out all degrees of freedom of the system that do not include subsystem A

$$\rho_A = \text{Tr}_B(\rho_{AB}).$$

Experimentally, we interfere two identical quantum states to obtain simultaneously the global and local purity ($\text{Tr}(\rho_A^2)$). Therefore the relevant order Rényi entropy is the second-order ($n = 2$) Rényi entropy which is defined for a density matrix of subsystem as

$$S_2(\rho_A) = -\log (\text{Tr}[\rho_A^2]),$$

and is also important qualitatively as a lower bound of the von Neumann entropy. When discussing the global purity as an entropy, we use the Rényi formulation in terms of the global density matrix ρ as opposed to a reduced density matrix ρ_A . Lastly, note that we use logarithms to base e throughout.

It is important to stress that the thermodynamic relations defined from statistical mechanics with the von Neumann definition do not directly apply for the Rényi definition. However, both quantities measure the incoherent diffusion in Hilbert space associated with entropy, and the Rényi entropy is directly accessible by our measurements.

H

Chapter 5 Calculations

H.I SCALING AND LIMITATIONS OF CONFIGURATIONAL CORRELATOR

The configurational correlator C studied in the text has a finite upper bound unlike the configurational entanglement entropy S_c . This can be seen from the inequality below:

$$\begin{aligned} C &= \sum_{n=0}^N p_n \sum_{\{A_n\}, \{B_n\}} |p(A_n \otimes B_n) + p(A_n)p(B_n)| \\ &\leq \sum_{n=0}^N p_n \sum_{\{A_n\}, \{B_n\}} |p(A_n \otimes B_n)| + |p(A_n)p(B_n)| = 2 \end{aligned} \quad (\text{H.I})$$

where the last equality is enforced by the normalization of the probability distributions. This bound of $C \leq 2$ can be shown to be a tight upper bound in large Hilbert space dimensions for a maximally mixed reduced density matrix, where the two probability distributions are perfectly correlated. Let us consider the maximally mixed reduced density matrix in the Schmidt basis, with $p_a^{(n)}, p_b^{(n)} = 1/N$ and $p_{a,b}^{(n)} \in \{1/N, 0\}$. For simplicity, let us consider the case where $p_n = 1$ for one n_0 and $p_n = 0$ for all other n . We therefore drop all superscripts of n .

$$\begin{aligned} C &= \sum_{\{A\}, \{B\}} |p(A \otimes B) - p(A)p(B)| \\ &\leq \sum_{a,b=1}^N \left| \frac{1}{N} - \frac{1}{N^2} \right| + \sum_{a,b=N+1}^{N^2} \left| 0 - \frac{1}{N^2} \right| \\ &= N \left(\frac{1}{N} \right) \left| 1 - \frac{1}{N} \right| + (N^2 - N) \frac{1}{N^2} \\ &= \frac{N-1}{N} + 1 - \frac{1}{N} = 2 \left(1 - \frac{1}{N} \right) \end{aligned} \quad (\text{H.2})$$

However, even with this bound, we find that the configurational entanglement entropy S_c and

C are remarkably linear when S_c is relatively small. It is also worth noting that the upper bound for the case shown above in entropy is also bounded by $\log(N)$. This temptingly suggests that in some cases a relationship could be made where perhaps $S_c \sim \log(1 - C/2)$.

I

Chapter 6 Calculations

I.I Δx : TIME SCALING BEHAVIOR (POWER LAW 12-SITES)

In order to quantify the transport distance of the particles, we defined the first moment of the two-point-density-correlation distribution, $\Delta x = 2 \sum_d G_2(d) \times d$ where $G_2(d) = \langle n_i n_{i+d} \rangle_{i,\phi} - \langle n_i \rangle_{i,\phi} \langle n_{i+d} \rangle_{i,\phi}$, i is the site index, and ϕ is the disorder realization. Numerical simulations were performed to determine time-scaling behavior of the first moment (Fig. I.1).

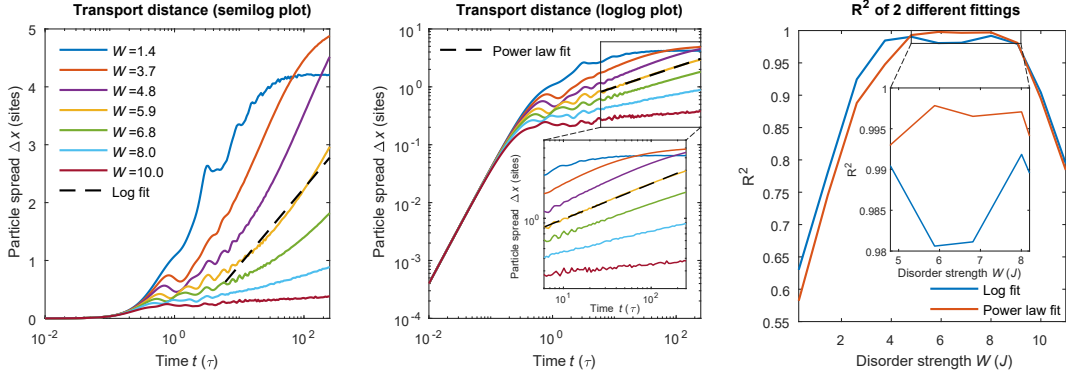
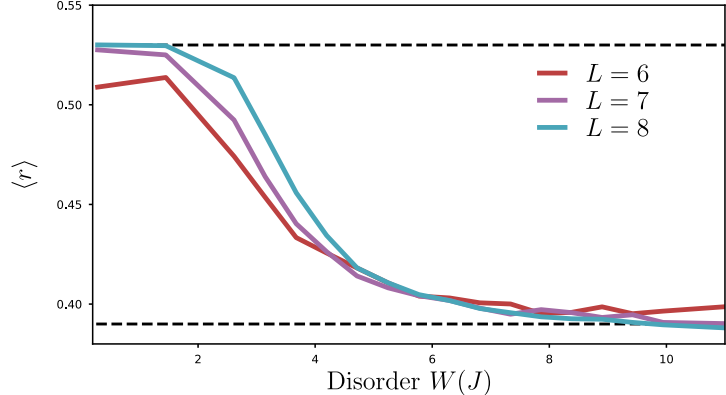


Figure I.1: Two different fittings for the time-dependence of the transport distance at various disorder strengths. The left panel and the center panels show the time dependence of the particle spread Δx in a 12-site system for various disorder strengths in semi-log and log-log scales. The dashed lines are sample least-square fits assuming logarithm and power-law time scaling, respectively. The right panel shows the R^2 values of each fit as a function of disorder strength. All simulations were performed by exact numerical integration of Schrödinger's equation, as described in the previous section.

To characterize the correct functional form of the temporal transport behavior of the system, we fit the first moment to either a logarithmically slow growth in time or a power-law growth in time. We look at times that avoid the initial transient dynamics in the system $t/\tau > L/2$ (the time for relaxation in the non-disordered, $W = 0$, case). Since we only experimentally measure up to a final evolution time of $t = 100\tau$, we restrict our fitting of the temporal transport behavior in the system to $L/2 < t/\tau \leq 100$. This time range was found to be robust to change in the exact endpoints. Additionally, we can see in Fig. I.1 that only disorder strengths $W \gtrsim 4.8J$ appear unaffected by the system's finite size at $t = 100\tau$. We therefore expect that comparing the fit quality in the critical disorder regime ($5 \lesssim W/J \lesssim 8$) is a good metric for determining which functional form of the temporal transport behavior. We find, by looking at the R^2 metric of the fits in this region, that the transport behavior more closely relates to a power-law rather than a logarithmically slow growth.

Figure I.2: Spectral Statistics. This shows the spectral statistics ratio, $\langle r \rangle \equiv \langle \frac{\min(\Delta_n, \Delta_{n+1})}{\max(\Delta_n, \Delta_{n+1})} \rangle$, for system sizes of $L=6$ and $L=8$. The approximate crossing point is $W \approx 5J$ which bounds the critical point from below $W_c \gtrapprox 5J$ and is consistent with the experimentally observed point of departure from thermalization.

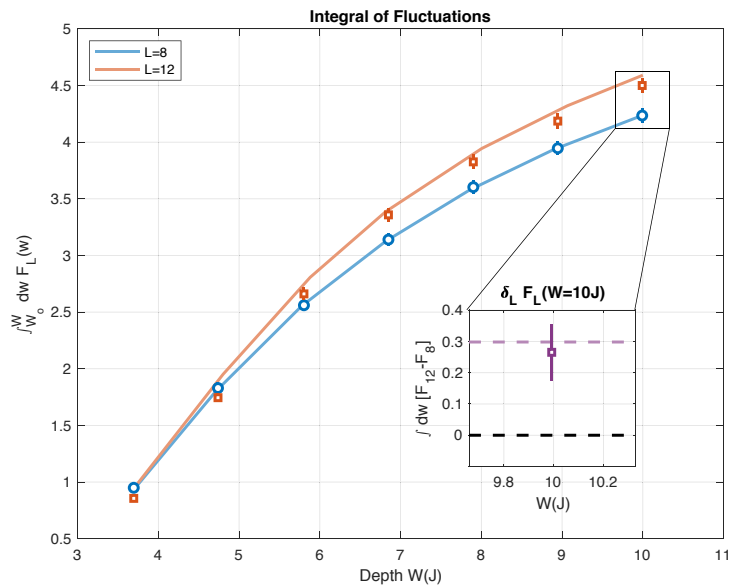


Hence, in this paper, we assumed a power-law time scaling of the particle spread to analyze the data.

I.2 SPECTRAL STATISTICS

The spectral statistics ratio (r) is a common metric used to determine the transition from the thermalizing to many-body-localized behavior. This ratio is defined as $r \equiv \min\{\Delta_n, \Delta_{n+1}\}/\max\{\Delta_n, \Delta_{n+1}\}$, where $\Delta_n = E_n - E_{n+1}$ is the spacing between eigenenergies in the system. This is then averaged over the eigenstates that do not lie close to the ends of the spectrum. In this case, we average over the middle $2/3$ of the eigenstates. This ratio is sensitive to the test of level repulsion of the system, which is a hallmark of a thermalizing system. This ratio approaches the Gaussian orthogonal ensemble (GOE) value of $r \approx 0.53$ in the thermalizing regime and approaches the Poisson value of $r \approx 0.39$ in the localized phase. We are able to compute these via exact diagonalization for system sizes up to $L=8$. The crossing point for successively larger system sizes is a typical method for helping estimate the lower bound for the critical point for the transition. With our experimental realization of the quasi-periodic potential, we see a cross point at $W \approx 5J$ which bounds the critical point in the

Figure I.3: Numeric Integration of Fluctuations 12 vs 8. This plot shows the integrated fluctuations of the exact numeric theory (solid lines) and measured data (points) for the curves from Fig. 2c. Only a subset of points were used that were measured at the same disorder value in both the twelve-site and eight-site experiments. The numerical integration was evaluated via the trapezoid rule. The relevant metric is the final point that incorporates the integral of all points along the curve and provides a robust metric for showing enhanced thermalization in the larger system. This integrated difference exceeds the null-hypothesis by more than two standard error bars of the mean.



thermodynamic limit from below $W_c \gtrapprox 5J^{101}$.

I.3 ENHANCED THERMALIZATION

The measured on-site number fluctuations plotted in §6 (Fig. 6.4) show enhanced thermalization in the larger system across an intermediate disorder range which we use to identify the critical regime.

To provide a more robust metric of the enhanced thermalization in the larger system-size, we numerically integrate the two curves and compare the difference in the fluctuations. This final integrated difference is plotted in Fig. I.3. The inset quantifies the systematically enhanced thermalization in the larger system size where it exceeds the null hypothesis by more than two standard errors of the mean.

I.4 SUBSYSTEM-SIZE FLUCTUATIONS SCALING

As discussed in §6, the subsystem-size scaling of particle-number fluctuations is a proposed probe for investigating the thermal-to-MBL transition. In the infinite temperature case (all Fock basis states contributing equally), the probability of fluctuations can be found easily by considering the number of states possible in a subsystem of size L_A with n_A particles:

$$\mathcal{D}_A = \binom{(n_A + L_A - 1)!}{n_A!(L_A - 1)!}$$

where its complement is given by $\{L_B = L - L_A, n_B = N - n_A\}$ where L is the total system size and N is the total atom number. This gives rise to the probability of having n_A atoms in subsystem size of L_A :

$$P(n_A, L_A, N)_L = \binom{(n_A + L_A - 1)!}{n_A!(L_A - 1)!} \binom{(N - n_A + L - L_A - 1)!}{(N - n_A)!(L - L_A - 1)!} / \binom{(N + L - 1)!}{N!(L - 1)!}$$

The fluctuations for such a distribution is then calculated as the second moment of n_A :

$$F(L_A, N)_L = \sqrt{\left(\sum_{n_A=0}^N P(n_A) n_A^2 \right) - \left(\sum_{n_A=0}^N P(n_A) n_A \right)^2} \quad (\text{I.I})$$

This reduces to the familiar form of the Bernoulli distribution with an additional enhancement

factor that derives from indistinguishable bosonic statistics:

$$F(L_A, N)_L/N = \left(\frac{(L - L_A) L_A}{L^2} \right) \left(\frac{1 + N/L}{1 + 1/L} \right) \quad (\text{I.2})$$

In the limit where we have integer filling, $N = \nu L$, we can see the scaling more easily for the fluctuations per particle $\tilde{\mathcal{F}}(l, \nu)_L$:

$$\tilde{\mathcal{F}}(L_A, \nu)_L = \left(\frac{(L - L_A) l}{L^2} \right) \left(\frac{1 + \nu}{1 + 1/L} \right) \quad (\text{I.3})$$

In the large $\{N, L_A, L\}$ limits, the probability of particle number becomes approximately Gaussian with a mean $\mu_{n_A} = N \times L_A / L$ and variance $\sigma_{n_A}^2 = N^2 \frac{(L_A)(L - L_A)}{L^2}$

This Gaussian relationship allows for a simple relationship to the number entropy that is approximately logarithmic in a given system size by evaluating the von Neumann entropy of particle number:

$$S_n(L_A) = - \sum_{n_A=0}^N P(n_A, L_A, N)_L \log[P(n_A, L_A, N)] \quad (\text{I.4})$$

The derivation of the Bernoulli distribution relies on particles being uniformly distributed throughout the system. This also means that the probability of a particle living in L_A is just given by:

$$P(L_A) = \int_{l=0}^{L_A} \frac{1}{L} dl$$

In the case that disorder is now applied to the lattice, this would have to be modified fundamentally since the particles then live in exponentially localized orbitals with a characteristic localization length ξ . We find phenomenologically that this modifies the probability of $P(n_A)$ from a Gaussian, but an exponential:

$$P(n_A, L_A, N)_L \sim e^{-(n_A - N \frac{L_A}{L})/\xi}$$

Due to this similarity, we attempted an approximation of fluctuations in the localized regime by $\sim \cosh[L_A/\xi]$. In the two extremes, ($\xi \rightarrow \infty, \xi \rightarrow 0$), this form provides the correct shapes of a parabola and a constant scaling for the particle-number fluctuations, respectively. This is shown qualitatively in Fig. I.4 as a function of time.

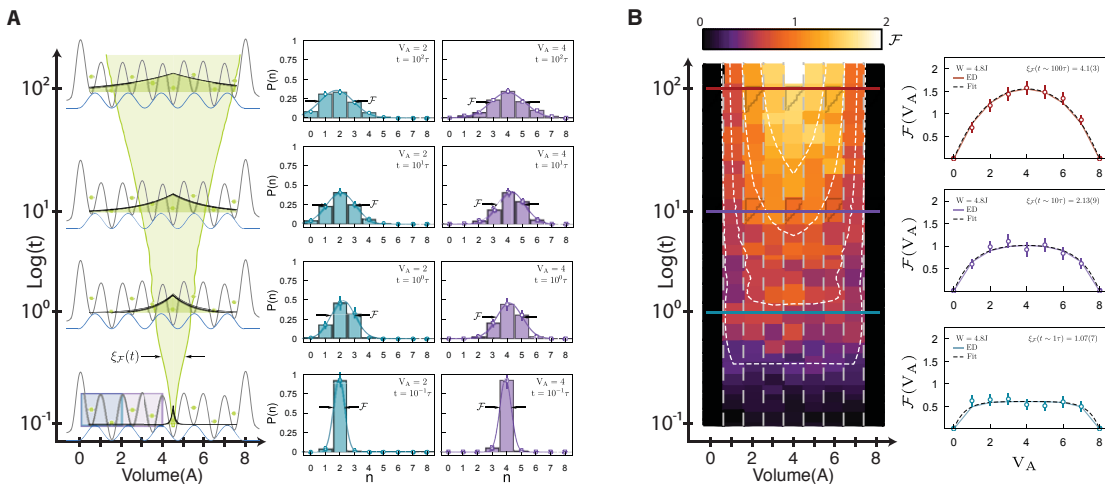


Figure I.4: Fluctuations Scaling Behavior. a) The probability of particle number n_A is plotted for both a subsystem size of two sites (teal) and four sites (purple). The relationship to the growth in the width of the particle number probability as a function of time is shown in the histograms as well as schematically by the shaded green triangle. b) The particle number fluctuations as a function of subsystem size and time in the color plot. Cross section of the fluctuations are plotted for three different evolution times: $t = 1\tau$ (blue), $t = 10\tau$ (purple), and $t = 100\tau$ (red).

References

- [1] Abanin, D. A., Altman, E., Bloch, I., & Serbyn, M. (2018). Ergodicity, Entanglement and Many-Body Localization.
- [2] Agarwal, K., Gopalakrishnan, S., Knap, M., Müller, M., & Demler, E. (2015). Anomalous diffusion and griffiths effects near the many-body localization transition. *Phys. Rev. Lett.*, 114, 160401.
- [3] Ahlbrecht, A., Alberti, A., Meschede, D., Scholz, V. B., Werner, A. H., & Werner, R. F. (2012). Molecular binding in interacting quantum walks. *New Journal of Physics*, 14(7), 073050.
- [4] Aidelsburger, M., Atala, M., Lohse, M., Barreiro, J. T., Paredes, B., & Bloch, I. (2013). Realization of the hofstadter hamiltonian with ultracold atoms in optical lattices. *Phys. Rev. Lett.*, 111, 185301.
- [5] Alet, F. & Laflorencie, N. (2018). Many-body localization: An introduction and selected topics. *Comptes Rendus Physique*, 19(6), 498–525.
- [6] Altshuler, B. L., Gefen, Y., Kamenev, A., & Levitov, L. S. (1997). Quasiparticle lifetime in a finite system: A nonperturbative approach. *Phys. Rev. Lett.*, 78, 2803–2806.
- [7] Amico, L., Fazio, R., Osterloh, A., & Vedral, V. (2008). Entanglement in many-body systems. *Reviews of Modern Physics*, 80(2), 517–576.
- [8] Anderson, P., W. (1958). Absence of Diffusion in Certain Random Lattices. *Physical Review*, 109(5), 1492–1506.
- [9] Anquez, M., Robbins, B. A., Bharath, H. M., Boguslawski, M., Hoang, T. M., & Chapman, M. S. (2016). Quantum kibble-zurek mechanism in a spin-1 bose-einstein condensate. *Phys. Rev. Lett.*, 116, 155301.
- [10] Ashkin, A. (1970). Acceleration and trapping of particles by radiation pressure. *Phys. Rev. Lett.*, 24, 156–159.

- [11] Aspect, A., Dalibard, J., & Roger, G. (1982). Experimental test of bell's inequalities using time-varying analyzers. *Phys. Rev. Lett.*, 49, 1804–1807.
- [12] Aspect, A., Grangier, P., & Roger, G. (1981). Experimental tests of realistic local theories via bell's theorem. *Phys. Rev. Lett.*, 47, 460–463.
- [13] Aubry, S. & André, G. (1980). *Ann. Isr. Phys. Soc.*, 3, 133.
- [14] Baier, S., Mark, M. J., Petter, D., Aikawa, K., Chomaz, L., Cai, Z., Baranov, M., Zoller, P., & Ferlaino, F. (2016). Extended bose-hubbard models with ultracold magnetic atoms. *Science*, 352(6282), 201–205.
- [15] Bakr, W. S., Gillen, J. I., Peng, A., Fölling, S., & Greiner, M. (2009). A quantum gas microscope for detecting single atoms in a Hubbard-regime optical lattice. *Nature*, 462(7269), 74–77.
- [16] Bakr, W. S. & Greiner, M. (2011). Microscopic Studies of Quantum Phase Transitions in Optical Lattices. *Thesis*, (May), 1–161.
- [17] Bakr, W. S., Peng, A., Tai, M. E., Ma, R., Simon, J., Gillen, J. I., Fölling, S., Pollet, L., & Greiner, M. (2010). Probing the superfluid-to-mott insulator transition at the single-atom level. *Science*, 329(5991), 547–550.
- [18] Bardarson, J. H., Pollmann, F., & Moore, J. E. (2012). Unbounded growth of entanglement in models of many-body localization. *Physical Review Letters*.
- [19] Basko, D. M., Aleiner, I. L., & Altshuler, B. L. (2006). Metal-insulator transition in a weakly interacting many-electron system with localized single-particle states. *Annals of Physics*, 321(5), 1126–1205.
- [20] Baumann, K., Guerlin, C., Brennecke, F., & Esslinger, T. (2010). Dicke quantum phase transition with a superfluid gas in an optical cavity. *Nature*, 464, 1301.
- [21] Bell, J. S. (1964). On the einstein podolsky rosen paradox. *Physics Physique Fizika*, 1, 195–200.
- [22] Billy, J., Josse, V., Zuo, Z., Bernard, A., Hambrecht, B., Lugan, P., Clément, D., Sanchez-Palencia, L., Bouyer, P., & Aspect, A. (2008). Direct observation of Anderson localization of matter waves in a controlled disorder. *Nature*, 453(7197), 891–894.

- [23] Blatt, R. & Roos, C. F. (2012). Quantum simulations with trapped ions. *Nature Physics*, 8, 277.
- [24] Bloch, I., Dalibard, J., & Nascimbène, S. (2012). Quantum simulations with ultracold quantum gases. *Nature Physics*, 8, 267.
- [25] Bloch, I., Dalibard, J., & Zwerger, W. (2008). Many-body physics with ultracold gases. *Rev. Mod. Phys.*, 80, 885–964.
- [26] Bordia, P., Lüschen, H., Schneider, U., Knap, M., & Bloch, I. (2017). Periodically driving a many-body localized quantum system. *Nature Physics*, 13, 460.
- [27] Bordia, P., Lüschen, H. P., Hodgman, S. S., Schreiber, M., Bloch, I., & Schneider, U. (2016). Coupling identical one-dimensional many-body localized systems. *Phys. Rev. Lett.*, 116, 140401.
- [28] Bouwmeester, D., Pan, J.-W., Daniell, M., Weinfurter, H., & Zeilinger, A. (1999). Observation of three-photon greenberger-horne-zeilinger entanglement. *Phys. Rev. Lett.*, 82, 1345–1349.
- [29] Bovino, F. A., Castagnoli, G., Ekert, A., Horodecki, P., Alves, C. M., & Sergienko, A. V. (2005). Direct measurement of nonlinear properties of bipartite quantum states. *Phys. Rev. Lett.*, 95, 240407.
- [30] Bruni, T. A. (2004). Measuring polynomial functions of states. *Quantum Information & Computation*, 4(5), 401–408.
- [31] Brydges, T., Elben, A., Jurcevic, P., Vermersch, B., Maier, C., Lanyon, B. P., Zoller, P., Blatt, R., & Roos, C. F. (2019). Probing rényi entanglement entropy via randomized measurements. *Science*, 364(6437), 260–263.
- [32] Calabrese, P. & Cardy, J. (2004). Entanglement entropy and quantum field theory. *Journal of Statistical Mechanics: Theory and Experiment*, (6).
- [33] Calabrese, P. & Cardy, J. (2005). Evolution of entanglement entropy in one-dimensional systems. *Journal of Statistical Mechanics: Theory and Experiment*, 2005(04), Po4010.
- [34] Cerf, N. J. & Adami, C. (1996). Quantum Information Theory of Entanglement and Measurement. (November 1996).

- [35] Cheuk, L. W., Nichols, M. A., Okan, M., Gersdorf, T., Ramasesh, V. V., Bakr, W. S., Lompe, T., & Zwierlein, M. W. (2015). Quantum-gas microscope for fermionic atoms. *Phys. Rev. Lett.*, 114, 193001.
- [36] Chin, C., Grimm, R., Julienne, P., & Tiesinga, E. (2010). Feshbach resonances in ultracold gases. *Rev. Mod. Phys.*, 82, 1225–1286.
- [37] Choi, J.-y., Hild, S., Zeiher, J., Schauß, P., Rubio-Abadal, A., Yefsah, T., Khemani, V., Huse, D. A., Bloch, I., & Gross, C. (2016). Exploring the many-body localization transition in two dimensions. *Science*, 352(6293), 1547–1552.
- [38] Choi, S., Choi, J., Landig, R., Kucsko, G., Zhou, H., Isoya, J., Jelezko, F., Onoda, S., Sumiya, H., Khemani, V., von Keyserlingk, C., Yao, N. Y., Demler, E., & Lukin, M. D. (2017). Observation of discrete time-crystalline order in a disordered dipolar many-body system. *Nature*, 543, 221.
- [39] Chu, S. (1998). Nobel lecture: The manipulation of neutral particles. *Rev. Mod. Phys.*, 70, 685–706.
- [40] Chu, S., Bjorkholm, J. E., Ashkin, A., & Cable, A. (1986). Experimental observation of optically trapped atoms. *Phys. Rev. Lett.*, 57, 314–317.
- [41] Clark, L. W., Feng, L., & Chin, C. (2016). Universal space-time scaling symmetry in the dynamics of bosons across a quantum phase transition. *Science*, 354(6312), 606–610.
- [42] Clos, G., Porras, D., Warring, U., & Schaetz, T. (2016). Time-Resolved Observation of Thermalization in an Isolated Quantum System. *Physical Review Letters*, 117(17), 1–6.
- [43] D'Alessio, L., Kafri, Y., Polkovnikov, A., & Rigol, M. (2016). From quantum chaos and eigenstate thermalization to statistical mechanics and thermodynamics. *Advances in Physics*, 65(3), 239–362.
- [44] Daley, A. J., Pichler, H., Schachenmayer, J., & Zoller, P. (2012). Measuring entanglement growth in quench dynamics of bosons in an optical lattice. *Physical Review Letters*, 109(2), 1–5.
- [45] Deissler, B., Zaccanti, M., Roati, G., Errico, C. D., Fattori, M., Modugno, M., Modugno, G., & Inguscio, M. (2010). Delocalization of a disordered bosonic system by repulsive interactions. *Nature Physics*, 6(5), 354–358.

- [46] DePue, M. T., McCormick, C., Winoto, S. L., Oliver, S., & Weiss, D. S. (1999). Unity occupation of sites in a 3d optical lattice. *Phys. Rev. Lett.*, *82*, 2262–2265.
- [47] D'Errico, C., Fattori, M., Zaccanti, M., Inguscio, M., Modugno, M., Modugno, G., Fort, C., Fallani, L., & Roati, G. (2008). Anderson localization of a non-interacting Bose–Einstein condensate. *Nature*, *453*(7197), 895–898.
- [48] Deutsch, J. M. (1991). Quantum statistical mechanics in a closed system. *Physical Review A*, *43*(4), 2046–2049.
- [49] Deutsch, J. M., Li, H., & Sharma, A. (2013). Microscopic origin of thermodynamic entropy in isolated systems. *Physical Review E - Statistical, Nonlinear, and Soft Matter Physics*, *87*(4), 1–5.
- [50] Dutta, O., Gajda, M., Hauke, P., Lewenstein, M., Lühmann, D.-S., Malomed, B. A., Sowiński, T., & Zakrzewski, J. (2015). Non-standard Hubbard models in optical lattices: a review. *Reports on Progress in Physics*, *78*(6), 066001.
- [51] Einstein, A., Podolsky, B., & Rosen, N. (1935). Can quantum-mechanical description of physical reality be considered complete? *Phys. Rev.*, *47*, 777–780.
- [52] Eisert, J., Cramer, M., & Plenio, M. B. (2010). Colloquium: Area laws for the entanglement entropy. *Reviews of Modern Physics*, *82*(1), 277–306.
- [53] Eisert, J., Friesdorf, M., & Gogolin, C. (2015). Quantum many-body systems out of equilibrium. *Nature Physics*, *11*(2), 124–130.
- [54] Ekert, A. K., Alves, C. M., Oi, D. K. L., Horodecki, M., Horodecki, P., & Kwek, L. C. (2002). Direct estimations of linear and nonlinear functionals of a quantum state. *Phys. Rev. Lett.*, *88*, 217901.
- [55] Endres, M., Cheneau, M., Fukuhara, T., Weitenberg, C., Schauß, P., Gross, C., Mazza, L., Bañuls, M. C., Pollet, L., Bloch, I., & Kuhr, S. (2011). Observation of correlated particle-hole pairs and string order in low-dimensional mott insulators. *Science*, *334*(6053), 200–203.
- [56] Endres, M., Fukuhara, T., Pekker, D., Cheneau, M., Schauß, P., Gross, C., Demler, E., Kuhr, S., & Bloch, I. (2012). The ‘Higgs’ amplitude mode at the two-dimensional superfluid/Mott insulator transition. *Nature*, *487*, 454.

- [57] Feynman, R. (1982). Can quantum-mechanical description of physical reality be considered complete? *International Journal of Theoretical Physics*, 21, 467–488.
- [58] Gadway, B., Pertot, D., Reeves, J., Vogt, M., & Schneble, D. (2011). Glassy behavior in a binary atomic mixture. *Physical Review Letters*, 107(14), 1–5.
- [59] Gadway, B., Pertot, D., Reimann, R., Cohen, M. G., & Schneble, D. (2009). Analysis of kapitza-dirac diffraction patterns beyond the raman-nath regime. *Opt. Express*, 17(21), 19173–19180.
- [60] Garanovich, I. L., Longhi, S., Sukhorukov, A. A., & Kivshar, Y. S. (2012). Light propagation and localization in modulated photonic lattices and waveguides. *Physics Reports*, 518(1), 1 – 79. Light propagation and localization in modulated photonic lattices and waveguides.
- [61] Garrison, J. R. & Grover, T. (2018). Does a Single Eigenstate Encode the Full Hamiltonian? *Physical Review X*, 8(2), 21026.
- [62] Geim, A. K. & Novoselov, K. S. (2007). The rise of graphene. *Nature Materials*, 6, 183.
- [63] Gillen, J. & Greiner, M. (2009). The Quantum Gas Microscope. *Thesis*, (October), 1–108.
- [64] Giustina, M., Versteegh, M. A. M., Wengerowsky, S., Handsteiner, J., Hochrainer, A., Pheilan, K., Steinlechner, F., Kofler, J., Larsson, J.-A., Abellán, C., Amaya, W., Pruneri, V., Mitchell, M. W., Beyer, J., Gerrits, T., Lita, A. E., Shalm, L. K., Nam, S. W., Scheidl, T., Ursin, R., Wittmann, B., & Zeilinger, A. (2015). Significant-loophole-free test of bell's theorem with entangled photons. *Phys. Rev. Lett.*, 115, 250401.
- [65] Gornyi, I. V., Mirlin, A. D., & Polyakov, D. G. (2005). Interacting electrons in disordered wires: Anderson localization and low-T transport. *Physical Review Letters*, 95(20), 1–4.
- [66] Greiner, M. (2003). Ultracold quantum gases in three-dimensional optical lattice potentials. *Thesis*.
- [67] Greiner, M., Mandel, O., Esslinger, T., Hänsch, T. W., & Bloch, I. (2002). Quantum phase transition from a superfluid to a Mott insulator in a gas of ultracold atoms. *Nature*, 415(6867), 39–44.
- [68] Grimm, R., Weidemüller, M., & Ovchinnikov, Y. B. (2000). Optical dipole traps for neutral atoms. 42, 95 – 170.

- [69] Grover, T. (2014). Certain General Constraints on the Many-Body Localization Transition. *V*(1), 1–7.
- [70] Gupta, S., Leanhardt, A., Cronin, A., & Pritchard, D. (2001). Coherent manipulation of atoms with standing light waves. *Comptes Rendus de l'Academie des Sciences - Series IV: Physics, Astrophysics*, 2(3), 479–495.
- [71] Häffner, H., Hänsel, W., Roos, C. F., Benhelm, J., Chek-al kar, D., Chwalla, M., Körber, T., Rapol, U. D., Riebe, M., Schmidt, P. O., Becher, C., Gühne, O., Dür, W., & Blatt, R. (2005). Scalable multiparticle entanglement of trapped ions. *Nature*, 438(7068), 643–646.
- [72] Haller, E., Hart, R., Mark, M. J., Danzl, J. G., Reichsöllner, L., Gustavsson, M., Dalmonte, M., Pupillo, G., & Nägerl, H.-C. (2010). Pinning quantum phase transition for a Luttinger liquid of strongly interacting bosons. *Nature*, 466, 597.
- [73] Haller, E., Hudson, J., Kelly, A., Cotta, D. A., Peaudecerf, B., Bruce, G. D., & Kuhr, S. (2015). Single-atom imaging of fermions in a quantum-gas microscope. *Nature Physics*, 11, 738.
- [74] Hartmann, T., Keck, F., Korsch, H. J., & Moessmann, S. (2004). Dynamics of Bloch oscillations. *New Journal of Physics*, 6.
- [75] Hauke, P., Heyl, M., Tagliacozzo, L., & Zoller, P. (2016). Measuring multipartite entanglement through dynamic susceptibilities. *Nature Physics*, 12, 778.
- [76] Hensen, B., Bernien, H., Dréau, A. E., Reiserer, A., Kalb, N., Blok, M. S., Ruitenberg, J., Vermeulen, R. F. L., Schouten, R. N., Abellán, C., Amaya, W., Pruneri, V., Mitchell, M. W., Markham, M., Twitchen, D. J., Elkouss, D., Wehner, S., Taminiau, T. H., & Hanson, R. (2015). Loophole-free Bell inequality violation using electron spins separated by 1.3 kilometres. *Nature*, 526, 682.
- [77] Herviou, L., Bera, S., & Bardarson, J. H. (2019). Multiscale entanglement clusters at the many-body localization phase transition. *Phys. Rev. B*, 99, 134205.
- [78] Heyl, M. (2018). Dynamical quantum phase transitions: A review. *Reports on Progress in Physics*, 81(5).
- [79] Hodgman, S. S., Khakimov, R. I., Lewis-Swan, R. J., Truscott, A. G., & Kheruntsyan, K. V. (2017). Solving the quantum many-body problem via correlations measured with a momentum microscope. *Phys. Rev. Lett.*, 118, 240402.

- [80] Horodecki, R. & Horodecki, M. (1996). Information-theoretic aspects of inseparability of mixed states. *Physical Review A - Atomic, Molecular, and Optical Physics*, 54(3), 1838–1843.
- [81] Horodecki, R., Horodecki, P., Horodecki, M., & Horodecki, K. (2007). Quantum entanglement. 81(June).
- [82] Houck, A. A., Türeci, H. E., & Koch, J. (2012). On-chip quantum simulation with superconducting circuits. *Nature Physics*, 8, 292.
- [83] Huang, K. (1963). *Statistical Mechanics*. John Wiley and Sons.
- [84] Huse, D. A., Nandkishore, R., & Oganesyan, V. (2014). Phenomenology of fully many-body-localized systems. *Physical Review B - Condensed Matter and Materials Physics*, 90(17).
- [85] Huse, D. A., Nandkishore, R., Oganesyan, V., Pal, A., & Sondhi, S. L. (2013). Localization-protected quantum order. *Phys. Rev. B*, 88, 014206.
- [86] Hyungwon, K. (2014). Quantum nonequilibrium dynamics: Transport, entanglement, and thermalization.
- [87] Imbrie, J. Z. (2016). *On Many-Body Localization for Quantum Spin Chains*, volume 163. Springer US.
- [88] Isakov, S. V., Hastings, M. B., & Melko, R. G. (2011). Topological entanglement entropy of a Bose–Hubbard spin liquid. *Nature Physics*, 7, 772.
- [89] Islam, R., Ma, R., Preiss, P. M., Eric Tai, M., Lukin, A., Rispoli, M., & Greiner, M. (2015). Measuring entanglement entropy in a quantum many-body system. *Nature*, 528(7580), 77–83.
- [90] Jaksch, D., Bruder, C., Cirac, J. I., Gardiner, C. W., & Zoller, P. (1998). Cold bosonic atoms in optical lattices. *Phys. Rev. Lett.*, 81, 3108–3111.
- [91] Jendrzejewski, F., Bernard, A., Müller, K., Cheinet, P., Josse, V., Piraud, M., Pezzé, L., Sanchez-Palencia, L., Aspect, A., & Bouyer, P. (2012). Three-dimensional localization of ultracold atoms in an optical disordered potential. *Nature Physics*, 8, 398.
- [92] Jensen, R. V. & Shankar, R. (1985). Statistical behavior in deterministic quantum systems with few degrees of freedom. *Phys. Rev. Lett.*, 54, 1879–1882.

- [93] Jiang, H.-C., Wang, Z., & Balents, L. (2012). Identifying topological order by entanglement entropy. *Nature Physics*, 8, 902.
- [94] Jo, G.-B., Lee, Y.-R., Choi, J.-H., Christensen, C. A., Kim, T. H., Thywissen, J. H., Pritchard, D. E., & Ketterle, W. (2009). Itinerant ferromagnetism in a fermi gas of ultracold atoms. *Science*, 325(5947), 1521–1524.
- [95] Jördens, R., Strohmaier, N., Günter, K., Moritz, H., & Esslinger, T. (2008). A Mott insulator of fermionic atoms in an optical lattice. *Nature*, 455, 204.
- [96] Kardar, M. (2012a). *Statistical Physics of Fields*. Cambridge: Cambridge University Press.
- [97] Kardar, M. (2012b). *Statistical Physics of Particles*. Cambridge: Cambridge University Press.
- [98] Kaufman, A. M., Lester, B. J., Reynolds, C. M., Wall, M. L., Foss-Feig, M., Hazzard, K. R. A., Rey, A. M., & Regal, C. A. (2014). Two-particle quantum interference in tunnel-coupled optical tweezers. *Science*, 345(6194), 306–309.
- [99] Kaufman, A. M., Tai, M. E., Lukin, A., Rispoli, M., Schittko, R., Preiss, P. M., & Greiner, M. (2016). Quantum thermalization through entanglement in an isolated many-body system. *Science*, 353, 794–800.
- [100] Keesling, A., Omran, A., Levine, H., Bernien, H., Pichler, H., Choi, S., Samajdar, R., Schwartz, S., Silvi, P., Sachdev, S., Zoller, P., Endres, M., Greiner, M., Vuletić, V., & Lukin, M. D. (2019). Quantum Kibble–Zurek mechanism and critical dynamics on a programmable Rydberg simulator. *Nature*, 568(7751), 207–211.
- [101] Khemani, V., Lim, S. P., Sheng, D. N., & Huse, D. A. (2017a). Critical properties of the many-body localization transition.
- [102] Khemani, V., Sheng, D. N., & Huse, D. A. (2017b). Two Universality Classes for the Many-Body Localization Transition. 075702(August), 1–6.
- [103] Kitaev, A. & Preskill, J. (2006). Topological entanglement entropy. *Phys. Rev. Lett.*, 96, 110404.
- [104] Kondov, S. S., McGehee, W. R., Xu, W., & Demarco, B. (2015). Disorder-induced localization in a strongly correlated atomic Hubbard gas. *Physical Review Letters*, 114(8).

- [105] Kondov, S. S., McGehee, W. R., Zirbel, J. J., & DeMarco, B. (2011). Three-dimensional anderson localization of ultracold matter. *Science*, 334(6052), 66–68.
- [106] Kozuma, M., Deng, L., Hagley, E. W., Wen, J., Lutwak, R., Helmerson, K., Rolston, S. L., & Phillips, W. D. (1999). Coherent splitting of bose-einstein condensed atoms with optically induced bragg diffraction. *Phys. Rev. Lett.*, 82, 871–875.
- [107] Lahini, Y., Avidan, A., Pozzi, F., Sorel, M., Morandotti, R., Christodoulides, D. N., & Silberberg, Y. (2008). Anderson localization and nonlinearity in one-dimensional disordered photonic lattices. *Physical Review Letters*, 100(1), 1–4.
- [108] Lahini, Y., Verbin, M., Huber, S. D., Bromberg, Y., Pugatch, R., & Silberberg, Y. (2012). Quantum walk of two interacting bosons. *Phys. Rev. A*, 86, 011603.
- [109] Landau, L. D. (1937). On the theory of phase transitions. *Zh. Eksp. Teor. Fiz.*, 7, 19–32.
- [110] Landig, R., Hruby, L., Dogra, N., Landini, M., Mottl, R., Donner, T., & Esslinger, T. (2016). Quantum phases from competing short- and long-range interactions in an optical lattice. *Nature*, 532, 476.
- [111] Léonard, J., Morales, A., Zupancic, P., Esslinger, T., & Donner, T. (2017). Supersolid formation in a quantum gas breaking a continuous translational symmetry. *Nature*, 543, 87.
- [112] Levin, M. & Wen, X.-G. (2006). Detecting topological order in a ground state wave function. *Phys. Rev. Lett.*, 96, 110405.
- [113] Lewenstein, M. (2012). *Ultracold atoms in optical lattices : simulating quantum many-body systems*. Oxford, U.K: Oxford University Press.
- [114] Liu, H.-C. (2016). High-order correlation of chaotic bosons and fermions. *Phys. Rev. A*, 94, 023827.
- [115] Luitz, D. J., Huvanees, F., & De Roeck, W. (2017). How a Small Quantum Bath Can Thermalize Long Localized Chains. *Physical Review Letters*, 119(15).
- [116] Luitz, D. J., Laflorencie, N., & Alet, F. (2016). Extended slow dynamical regime close to the many-body localization transition. *Phys. Rev. B*, 93, 060201.
- [117] Lukin, A. (2018). Entanglement Dynamics in One Dimension : From Quantum Thermalization to Many-Body Localization.

- [118] Lukin, A., Rispoli, M., Schittko, R., Tai, M. E., Kaufman, A. M., Choi, S., Khemani, V., Léonard, J., & Greiner, M. (2019). Probing entanglement in a many-body-localized system. *Science*, 364(6437), 256–260.
- [119] Lüschen, H. P., Bordia, P., Hodgman, S. S., Schreiber, M., Sarkar, S., Daley, A. J., Fischer, M. H., Altman, E., Bloch, I., & Schneider, U. (2017). Signatures of many-body localization in a controlled open quantum system. *Phys. Rev. X*, 7, 011034.
- [120] Lüschen, H. P., Bordia, P., Scherg, S., Alet, F., Altman, E., Schneider, U., & Bloch, I. (2017). Observation of Slow Dynamics near the Many-Body Localization Transition in One-Dimensional Quasiperiodic Systems. *Physical Review Letters*, 119(26), 1–6.
- [121] Ma, R. (2014). Engineered potentials and dynamics of ultracold quantum gases under the microscope A dissertation presented. (May).
- [122] Ma, R., Tai, M. E., Preiss, P. M., Bakr, W. S., Simon, J., & Greiner, M. (2011). Photon-assisted tunneling in a biased strongly correlated bose gas. *Phys. Rev. Lett.*, 107, 095301.
- [123] Ma, S. K. (1985). *Statistical Mechanics*. World Scientific.
- [124] Manouchehri, K. & Wang, J. (2014). *Physical Implementation of Quantum Walks*. Springer.
- [125] Melko, R. G., Herdman, C. M., Iouchtchenko, D., Roy, P. N., & Del Maestro, A. (2016). Entangling qubit registers via many-body states of ultracold atoms. *Physical Review A*, 93(4), 1–6.
- [126] Metcalf, H. J. & van der Straten, P. (1999). *Laser Cooling and Trapping*. New York: Springer-Verlag.
- [127] Miranda, M., Inoue, R., Okuyama, Y., Nakamoto, A., & Kozuma, M. (2015). Site-resolved imaging of ytterbium atoms in a two-dimensional optical lattice. *Phys. Rev. A*, 91, 063414.
- [128] Miyake, H., Siviloglou, G. A., Kennedy, C. J., Burton, W. C., & Ketterle, W. (2013). Realizing the harper hamiltonian with laser-assisted tunneling in optical lattices. *Phys. Rev. Lett.*, 111, 185302.
- [129] Moura Alves, C. & Jaksch, D. (2004). Multipartite entanglement detection in bosons. *Phys. Rev. Lett.*, 93, 110501.

- [130] Nandkishore, R., Gopalakrishnan, S., & Huse, D. A. (2014). Spectral features of a many-body-localized system weakly coupled to a bath. *Phys. Rev. B*, *90*, 064203.
- [131] Nandkishore, R. & Huse, D. A. (2015). Many-body localization and thermalization in quantum statistical mechanics. *Annual Review of Condensed Matter Physics*, *6*(1), 15–38.
- [132] Neill, C., Roushan, P., Fang, M., Chen, Y., Kolodrubetz, M., Chen, Z., Megrant, A., Barends, R., Campbell, B., Chiaro, B., Dunsworth, A., Je, E., Kelly, J., Mutus, J., Malley, P. J. J. O., Quintana, C., Sank, D., Vainsencher, A., Wenner, J., White, T. C., Polkovnikov, A., & Martinis, J. M. (2016). Ergodic dynamics and thermalization in an isolated quantum system. *12*(July), 1037–1041.
- [133] Nielsen, M. A. & Chuang, I. L. (2010). *Quantum Computation and Quantum Information: 10th Anniversary Edition*. Cambridge University Press.
- [134] Oganesyan, V. & Huse, D. A. (2007). Localization of interacting fermions at high temperature. *Physical Review B - Condensed Matter and Materials Physics*, *75*(15), 1–5.
- [135] Osborne, T. J. & Nielsen, M. A. (2002). Entanglement in a simple quantum phase transition. *Physical Review A - Atomic, Molecular, and Optical Physics*, *66*(3), 14.
- [136] Osterloh, A., Amico, L., Falci, G., & Fazio, R. (2002). Scaling of entanglement close to a quantum phase transition Classical phase transitions occur when a physical system reaches a state below a critical temperature characterized by macroscopic order. *416*(April), 0–2.
- [137] Ovchinnikov, Y. B., Müller, J. H., Doery, M. R., Vredenbregt, E. J. D., Helmerson, K., Rolston, S. L., & Phillips, W. D. (1999). Diffraction of a released bose-einstein condensate by a pulsed standing light wave. *Phys. Rev. Lett.*, *83*, 284–287.
- [138] Page, D. N. (1993). Average entropy of a subsystem. *Phys. Rev. Lett.*, *71*, 1291–1294.
- [139] Pal, A. & Huse, D. A. (2010). Many-body localization phase transition. *Physical Review B - Condensed Matter and Materials Physics*, *82*(17), 1–7.
- [140] Palmer, R. N., Moura Alves, C., & Jaksch, D. (2005). Detection and characterization of multipartite entanglement in optical lattices. *Physical Review A - Atomic, Molecular, and Optical Physics*, *72*(4), 1–11.

- [141] Parsons, M. F., Huber, F., Mazurenko, A., Chiu, C. S., Setiawan, W., Wooley-Brown, K., Blatt, S., & Greiner, M. (2015). Site-resolved imaging of fermionic ${}^6\text{Li}$ in an optical lattice. *Phys. Rev. Lett.*, 114, 213002.
- [142] Peng, A. W.-C. (2010). Quantum Gas Microscope With Optical Lattice. *PhD Thesis*, (May), 1–106.
- [143] Pethick, C. & Smith, H. (2002). *Bose-Einstein condensation in dilute gases*. . Cambridge: Cambridge University Press.
- [144] Pichler, H., Daley, A. J., & Zoller, P. (2010). Nonequilibrium dynamics of bosonic atoms in optical lattices: Decoherence of many-body states due to spontaneous emission. *Physical Review A - Atomic, Molecular, and Optical Physics*, 82(6), 1–15.
- [145] Planck, M. (1914). *The Theory of Heat Radiation*. Blakiston's Son & Co.
- [146] Polkovnikov, A. (2005). Universal adiabatic dynamics in the vicinity of a quantum critical point. *Phys. Rev. B*, 72, 161201.
- [147] Ponte, P., Laumann, C. R., Huse, D. A., & Chandran, A. (2017). Thermal inclusions : how one spin can destroy a many-body localized phase Subject Areas :.
- [148] Potter, A. C., Vasseur, R., & Parameswaran, S. A. (2015). Universal properties of many-body delocalization transitions. (pp. 1–12).
- [149] Preiss, P. M. (2015). Atomic Bose-Hubbard Systems with Single-Particle Control. *Thesis*.
- [150] Preiss, P. M., Becher, J. H., Klemt, R., Klinkhamer, V., Bergschneider, A., Defenu, N., & Jochim, S. (2019). High-contrast interference of ultracold fermions. *Phys. Rev. Lett.*, 122, 143602.
- [151] Preiss, P. M., Ma, R., Tai, M. E., Lukin, A., Rispoli, M., Zupancic, P., Lahini, Y., Islam, R., & Greiner, M. (2015). Strongly correlated quantum walks in optical lattices. *Science*, 347(6227), 1229–1233.
- [152] Raab, E. L., Prentiss, M., Cable, A., Chu, S., & Pritchard, D. E. (1987). Trapping of neutral sodium atoms with radiation pressure. *Phys. Rev. Lett.*, 59, 2631–2634.
- [153] Rigol, M., Dunjko, V., & Olshanii, M. (2008). Thermalization and its mechanism for generic isolated quantum systems. *Nature*, 452(7189), 854–858.

- [154] Rispoli, M., Lukin, A., Schittko, R., Tai, M. E., Léonard, J., & Greiner, M. (2018). Quantum critical behavior at the many-body-localization transition. *V*(1), 1–10.
- [155] Roati, G., D’Errico, C., Fallani, L., Fattori, M., Fort, C., Zaccanti, M., Modugno, G., Modugno, M., & Inguscio, M. (2008). Anderson localization of a non-interacting Bose–Einstein condensate. *Nature*, 453, 895.
- [156] Roeck, W. D. & Huveneers, F. (2017). Stability and instability towards delocalization in many-body localization systems. 155129, 1–14.
- [157] Roushan, P., Neill, C., Tangpanitanon, J., Bastidas, V. M., Megrant, A., Barends, R., Chen, Y., Chen, Z., Chiaro, B., Dunsworth, A., Fowler, A., Foxen, B., Giustina, M., Jeffrey, E., Kelly, J., Lucero, E., Mutus, J., Neeley, M., Quintana, C., Sank, D., Vainsencher, A., Wenner, J., White, T., Neven, H., Angelakis, D. G., & Martinis, J. (2017). Spectroscopic signatures of localization with interacting photons in superconducting qubits. *Science*, 358(6367), 1175–1179.
- [158] Sachdev, S. (2011). *Quantum phase transitions*. Cambridge: Cambridge University Press.
- [159] Sachdev, S., Sengupta, K., & Girvin, S. M. (2002). Mott insulators in strong electric fields. *Phys. Rev. B*, 66, 075128.
- [160] Sakurai, J. J. (1993). *Modern Quantum Mechanics*. Addison Wesley Longman.
- [161] Santos, L. F., Polkovnikov, A., & Rigol, M. (2012). Weak and strong typicality in quantum systems. *Physical Review E - Statistical, Nonlinear, and Soft Matter Physics*, 86(1), 2–6.
- [162] Schachenmayer, J., Lanyon, B. P., Roos, C. F., & Daley, A. J. (2013). Entanglement growth in quench dynamics with variable range interactions. *Phys. Rev. X*, 3, 031015.
- [163] Schmid, C., Kiesel, N., Wieczorek, W., Weinfurter, H., Mintert, F., & Buchleitner, A. (2008). Experimental direct observation of mixed state entanglement. *Phys. Rev. Lett.*, 101, 260505.
- [164] Schreiber, M., Hodgman, S. S., Bordia, P., Lüschen, H. P., Fischer, M. H., Vosk, R., Altman, E., Schneider, U., & Bloch, I. (2015). Observation of many-body localization of interacting fermions in a quasirandom optical lattice. *Science*, 349(6250), 842–845.
- [165] Schrödinger, E. (1926). Quantisierung als eigenwertproblem. *Annalen der Physik*, 384(4), 361–376.

- [166] Schwartz, T., Bartal, G., Fishman, S., & Segev, M. (2007). Transport and Anderson localization in disordered two-dimensional photonic lattices. *Nature*, 446(7131), 52–55.
- [167] Schweigler, T., Kasper, V., Erne, S., Mazets, I., Rauer, B., Cataldini, F., Langen, T., Gasenzer, T., Berges, J., & Schmiedmayer, J. (2017). Experimental characterization of a quantum many-body system via higher-order correlations. *Nature*, 545, 323.
- [168] Semeghini, G., Landini, M., Castilho, P., Roy, S., Spagnolli, G., Trenkwalder, A., Fattori, M., Inguscio, M., & Modugno, G. (2015). Measurement of the mobility edge for 3D Anderson localization. *Nature Physics*, 11, 554.
- [169] Serbyn, M., Papić, Z., & Abanin, D. A. (2013a). Local conservation laws and the structure of the many-body localized states. *Physical Review Letters*, 111(12), 1–5.
- [170] Serbyn, M., Papić, Z., & Abanin, D. A. (2013b). Universal slow growth of entanglement in interacting strongly disordered systems. *Physical Review Letters*, 110(26), 1–5.
- [171] Setiawan, F., Deng, D.-L., & Pixley, J. H. (2017). Transport properties across the many-body localization transition in quasiperiodic and random systems. *Phys. Rev. B*, 96, 104205.
- [172] Shalm, L. K., Meyer-Scott, E., Christensen, B. G., Bierhorst, P., Wayne, M. A., Stevens, M. J., Gerrits, T., Glancy, S., Hamel, D. R., Allman, M. S., Coakley, K. J., Dyer, S. D., Hodge, C., Lita, A. E., Verma, V. B., Lambrocco, C., Tortorici, E., Migdall, A. L., Zhang, Y., Kumor, D. R., Farr, W. H., Marsili, F., Shaw, M. D., Stern, J. A., Abellán, C., Amaya, W., Pruneri, V., Jennewein, T., Mitchell, M. W., Kwiat, P. G., Bienfang, J. C., Mirin, R. P., Knill, E., & Nam, S. W. (2015). Strong loophole-free test of local realism. *Phys. Rev. Lett.*, 115, 250402.
- [173] Sherson, J. F., Weitenberg, C., Endres, M., Cheneau, M., Bloch, I., & Kuhr, S. (2010). Single-atom-resolved fluorescence imaging of an atomic Mott insulator. *Nature*, 467, 68.
- [174] Simon, J., Bakr, W. S., Ma, R., Tai, M. E., Preiss, P. M., & Greiner, M. (2011). Quantum simulation of antiferromagnetic spin chains in an optical lattice. *Nature*, 472, 307.
- [175] Singh, R., Bardarson, J. H., & Pollmann, F. (2016). Signatures of the many-body localization transition in the dynamics of entanglement and bipartite fluctuations. *New Journal of Physics*, 18(2), 023046.
- [176] Smith, J., Lee, A., Richerme, P., Neyenhuis, B., Hess, P. W., Hauke, P., Heyl, M., Huse, D. A., & Monroe, C. (2016). Many-body localization in a quantum simulator with programmable random disorder. *Nature Physics*, 12(10), 907–911.

- [177] Srednicki, M. (1994). Chaos and quantum thermalization. *Physical Review E*, 50(2), 888–901.
- [178] Steck, D. A. (2015). Rubidium 87 d line data. [available online at <http://steck.us/alkalidata> (revision 2.1.5, 13 January 2015)].
- [179] Stenger, J., Inouye, S., Chikkatur, A. P., Stamper-Kurn, D. M., Pritchard, D. E., & Ketterle, W. (1999). Bragg spectroscopy of a bose-einstein condensate. *Phys. Rev. Lett.*, 82, 4569–4573.
- [180] Tai, M. E. (2017). Microscopy of interacting quantum systems.
- [181] Tai, M. E., Lukin, A., Rispoli, M., Schittko, R., Menke, T., Dan Borgnia, Preiss, P. M., Grusdt, F., Kaufman, A. M., & Greiner, M. (2017). Microscopy of the interacting Harper-Hofstadter model in the two-body limit. *Nature*, 546, 519.
- [182] Täuber, U. C. (2017). Phase transitions and scaling in systems far from equilibrium. *Annual Review of Condensed Matter Physics*, 8(1), 185–210.
- [183] Vidal, G., Latorre, J. I., Rico, E., & Kitaev, A. (2003). Entanglement in Quantum Critical Phenomena. *Physical Review Letters*, 90(22), 4.
- [184] Vidmar, L. & Rigol, M. (2017). Entanglement entropy of eigenstates of quantum chaotic hamiltonians. *Phys. Rev. Lett.*, 119, 220603.
- [185] Vosk, R., Huse, D. A., & Altman, E. (2015). Theory of the many-body localization transition in one-dimensional systems. *Physical Review X*, 5(3), 1–14.
- [186] Walborn, S. P., Souto Ribeiro, P. H., Davidovich, L., Mintert, F., & Buchleitner, A. (2006). Experimental determination of entanglement with a single measurement. *Nature*, 440(7087), 1022–1024.
- [187] Weinberg, S. (2015). *Lectures on Quantum Mechanics*. Cambridge University Press, 2 edition.
- [188] Weiner, J., Bagnato, V. S., Zilio, S., & Julienne, P. S. (1999). Experiments and theory in cold and ultracold collisions. *Rev. Mod. Phys.*, 71, 1–85.
- [189] White, M., Pasienski, M., McKay, D., Zhou, S. Q., Ceperley, D., & DeMarco, B. (2009). Strongly interacting bosons in a disordered optical lattice. *Phys. Rev. Lett.*, 102, 055301.
- [190] Wiseman, H. M. & Vaccaro, J. A. (2003). Entanglement of Indistinguishable Particles Shared between Two Parties. *Physical Review Letters*, 91(9), 097902.

- [191] Wolf, M. M., Verstraete, F., Hastings, M. B., & Cirac, J. I. (2008). Area laws in quantum systems: Mutual information and correlations. *Physical Review Letters*, 100(7), 1–4.
- [192] Zhang, S.-X. & Yao, H. (2018). Universal properties of many-body localization transitions in quasiperiodic systems. *Phys. Rev. Lett.*, 121, 206601.
- [193] Zhang, Y., Grover, T., & Vishwanath, A. (2011). Entanglement entropy of critical spin liquids. *Phys. Rev. Lett.*, 107, 067202.
- [194] Zupancic, P., Preiss, P. M., Ma, R., Lukin, A., Tai, M. E., Rispoli, M., Islam, R., & Greiner, M. (2016). Ultra-precise holographic beam shaping for microscopic quantum control. 24(13), 4170–4175.
- [195] Zupancic, P. P. J. (2013). Dynamic Holography and Beamshaping using Digital Micromirror Devices. *Master Thesis*, (pp.75).
- [196] Zurek, W. H., Dorner, U., & Zoller, P. (2005). Dynamics of a quantum phase transition. *Phys. Rev. Lett.*, 95, 105701.
- [197] Zvyagin, A. A. (2016). Dynamical quantum phase transitions (Review Article). *Low Temperature Physics*, 42(II), 971–994.



THIS THESIS WAS TYPESET using L^AT_EX,
originally developed by Leslie Lamport
and based on Donald Knuth's T_EX.

The body text is set in 11 point Egenolff-Berner Garamond, a revival of Claude Garamont's humanist typeface. The above illustration, *Science Experiment 02*, was created by Ben Schlitter and released under CC BY-NC-ND 3.0. A template that can be used to format a PhD dissertation with this look & feel has been released under the permissive AGPL license, and can be found online at github.com/suchow/Dissertate or from its lead author, Jordan Suchow, at suchow@post.harvard.edu.